SAPIENZA
UNIVERSITÀ DI ROMA

Search for high-mass resonances in final states with a boosted-dijet resonance in proton-proton collisions at $\sqrt{s} = 13$ TeV with the CMS detector

Facoltà di Scienze Matematiche, Fisiche e Naturali

Dottorato di Ricerca in Fisica – XXXIV Ciclo

Candidate

Claudio Quaranta

ID number 1546726

Thesis Advisors

Prof. Daniele del Re

Prof. Francesco Santanastasio

December 2021

Thesis not yet defended

Search for high-mass resonances in final states with a boosted-dijet resonance in proton-proton collisions at $\sqrt{s} = 13\,\text{TeV}$ with the CMS detector
Ph.D. thesis. Sapienza – University of Rome

This thesis has been typeset by LaTeX and the Sapthesis class.

Author's email: claudio.quaranta@cern.ch

Abstract

The Standard Model (SM) of particle physics provides the best description of the fundamental constituents of the universe and their interactions. It is a robust theory, tested by many experiments with a high level of precision. However, there are several reasons to believe that the SM is not a fundamental theory, since, for example, it does not explain the huge difference between the electroweak and Planck scale (which is related to the so called "hierarchy problem" of the SM) and the values of the measured fermion masses. This led to the conception of several theories Beyond the Standard Model (BSM), which often foresee the existence of new resonances that could be detected in experiments at particle colliders, such as the Large Hadron Collider (LHC) at CERN.

This thesis reports the first LHC search for high-mass hadronic resonances that decay to a parton and a second Lorentz-boosted resonance, which in turn decays into a pair of partons. Such resonances are predicted, for example, by BSM theories that foresee the existence of extra spatial dimensions, providing a solution to the open questions mentioned above. The search is based on data collected with the CMS detector in proton-proton collisions produced at the LHC at $\sqrt{s} = 13\,\text{TeV}$, corresponding to an integrated luminosity of $138\,\text{fb}^{-1}$. The boosted resonance is reconstructed as a single wide jet with substructure consistent with a two-body decay. The high-mass resonance is thus considered as a dijet system. The jet substructure information and the kinematic properties of resonance decays are exploited to disentangle the signal from the large quantum chromodynamics multijet background. The dijet mass spectrum is analyzed for the presence of new high-mass resonances, and is found to be consistent with the standard model background predictions. Results are interpreted in a warped extra dimension model where the high-mass resonance is a Kaluza–Klein gluon, the boosted resonance is a radion, and the final state partons are all gluons. Limits on the production cross section are set as a function of the Kaluza–Klein gluon and radion masses. These limits exclude at 95% confidence level models with Kaluza–Klein gluon masses in the range from 2.0 to 4.3 TeV and radion masses in the range from 0.20 to 0.74 TeV. By exploring a novel experimental signature, the observed limits on the Kaluza–Klein gluon mass are extended by up to about 1 TeV compared to previous searches.

Contents

Introduction

The Standard Model (SM) of particle physics is a very solid and elegant theory, verified by many independent experiments, that describes the fundamental particles and their interactions with a high degree of accuracy. Despite its great success, there are several reasons to believe that it is incomplete. For example, it does not explain the huge difference between the electroweak and Planck scale (which is related to the so called "hierarchy problem" of the SM), and the values of the measured fermion masses.

Several theories Beyond the Standard Model (BSM) have been proposed in the recent decades to answer these open questions. These BSM models foresee the existence of new particles with a mass at the TeV scale, which could be produced at the Large Hadron Collider (LHC) at CERN. Searches for new hadronic resonances are particularly important at the LHC, as any hypothetical particle produced via the strong interaction in pp collisions can decay into partons (quarks, antiquarks or gluons). Partons are colored particles and cannot be directly observed by the experiments. Instead, they generate streams of particles collimated with their original direction, which are called jets.

In the last decades several searches for hadronic resonances were performed assuming different production mechanisms: production of single resonances decaying to a pair of jets (dijet), production of dijet resonances in association with an initial state radiation jet, photon, or lepton, and pair production of resonances resulting in final states with four or more jets. Despite the many analysis efforts, no evidence for new physics has been found.

There is still the chance that signals from new hadronic resonances are hidden by the large amount of background events originating from quantum chromodynamics processes with jets in the final state (QCD multijet background), which typically affects these searches. This consideration led to the development of searches for high mass resonances that decay to pairs of heavy SM particles like top quark-antiquark pairs, or pairs of SM electroweak bosons or Higgs bosons. If the mass of the new resonance is much larger than that of the SM particles, the decay products of the latter particles are collimated and the new resonance is reconstructed again as a dijet system. Jets from the decay of top quarks, or electroweak/Higgs bosons can be distinguished from light-quark jets based on their mass and their substructure (i.e. the pattern of constituents forming the jet). The use of this additional informations is used to reduce significantly the QCD multijet background for these analyses.

The analysis presented here goes further along this direction by studying a new process, currently unexplored at the LHC. We consider the production of a new resonance (R_1) that decays into a parton (P_3) and a second resonance (R_2), which

in turns decays into two partons ($P_1 + P_2$) as in Fig. 0.1. The three partons in the final state generate jets.

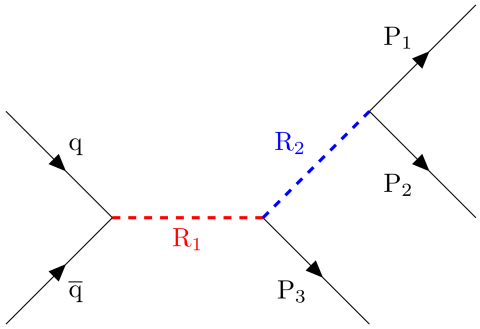

$$q\overline{q} \to R_1 \to R_2 + P_3 \to (P_1 + P_2) + P_3$$

Figure 0.1. Feynman diagram of leading order production of the process under study, which involves the cascade decay of two new massive resonances R_1 and R_2 to partons P_1, P_2, and P_3 in the final state.

The main difference with respect to previous hadronic searches is the presence of two resonances of unknown mass in the decay process. Different final state topologies are then allowed, depending on the ratio between the masses of the two resonances $\rho_m = m(R_2)/m(R_1)$. In this thesis we focus on a signal hypotheses where R_2 is much lighter than R_1 ($\rho_m \lesssim 0.2$). The resonance R_2 is then produced with a large Lorentz-boost, and its decay products are collimated and reconstructed as a single jet. The substructure properties of the R_2-jet are exploited to enhance the analysis sensitivity to the process under study. Resonances decaying in cascade as described above are foreseen by theoretical models that assume the existence of extra spatial dimensions. We focus in particular on a model with a warped extra dimension (WED), which we use as a benchmark model to interpret the results of this search.

The search uses data collected with the CMS experiment in proton-proton (pp) collisions produced at the CERN LHC at the center-of-mass energy of 13 TeV.

The Chapter 1 of this thesis presents a brief introduction of the strong sector of the SM, recalling the elements of QCD and its implications for the experimental measurements of hadronic interactions. Elements of the physics of pp interactions at hadron colliders are also introduced. The last two Sections of this Chapter are dedicated to describing two open questions within the SM: the hierarchy problem and the flavor puzzle.

Chapter 2 describes new physics models that foresee the existence of extra spatial dimensions, including the WED benchmark model.

Chapter 3 gives a summary of the past searches for hadronic resonances, focusing on the most recent results from the LHC experiments, and it ends with a description of the peculiar kinematic properties of the cascade decay studied in this thesis.

Chapter 4 is dedicated to the description of the experimental apparatus: the LHC is introduced, and the CMS detector is described in its various subdetectors.

The CMS jet reconstruction is described in Chapter 5, together with the procedure to calibrate the jet energy.

Chapter 6 introduces the data and simulation samples, and the criteria adopted for the event selection, which requires two high-p_{T} jets with an invariant mass (m_{jj}) at the TeV scale, compatible with the decay of an high-mass resonance like R_1. This Chapter also shows the distributions of jets kinematic variables in data, compared to the simulated ones.

Chapter 7 describes the analysis strategy. The signal sensitivity is optimized by dividing pp collision events into categories defined based on the masses and substructure observables of the jets. We reconstruct the spectrum of m_{jj} of the two jets with largest p_{T} of each event. The m_{jj} spectra are then analyzed to search for a peak, in correspondence of the R_1 mass, over the smoothly-decreasing QCD multijet background.

The analysis results are reported and discussed in Chapter 8, where they are interpreted as limits on the mass of the two resonances R_1 and R_2. This Chapter also include a comparison between this analysis and a previous CMS search.

Finally, Chapter 9 gives a summary of the analysis results and it is concluded by a paragraph about future analysis perspectives.

Chapter 1

The Standard Model and physics at colliders

1.1 The Standard Model of particle physics

The Standard Model (SM) of particle physics is the theory describing the physics of elementary particles in terms of quantum fields. The first step towards the SM was Sheldon Glashow's unification of the electromagnetic and weak interactions [1]. Few years later Steven Weinberg [2] and Abdus Salam [3] incorporated the Higgs mechanism into Glashow's electroweak interaction, giving to the theory its modern form. The SM describes in one coherent framework three of the four fundamental interactions: electromagnetic, weak and strong forces, therefore not including the gravity. The particles described by this theory can be divided into two groups:

- Fermions: Particles with half-integer spin obeying to the Fermi-Dirac statistics.
- Bosons: Particles with integer spin obeying to the Bose-Einstein statistics, mediators of the fundamental forces.

The fermions can be further divided into two groups: leptons and quarks, which are further organized into three generations of particles. A schematic view of the SM particles and their properties (mass, electric charge and spin) is reported in Fig. 1.1. Starting from the leptons, in the first generation we have the electron e and the electronic neutrino ν_e, which can interact via the weak interaction. Moreover, the electron can also interact through the electromagnetic interaction, since it has a charge of $-1.6 \times 10^{-19} C$, which is equivalent to -1 in natural units. The other two families both have a lepton with charge -1, respectively the muon μ and the tau τ, and a neutral lepton, respectively the muonic neutrino ν_μ and the tau neutrino ν_τ. The three generations shows increasing masses for the charged lepton, with a difference of four orders of magnitude between the electron and the tau.

Also the quarks are divided into three generations with different masses. Each generation has a quark with charge $+2/3$, respectively named up u, charm c and top t quarks, and a quark with charge $-1/3$, respectively named down d, strange s and bottom b quarks. The quark masses span a range of 5 orders of magnitude from the mass of the lightest up quark $m_u \approx 2.3\,\text{MeV}$ to the mass of the top

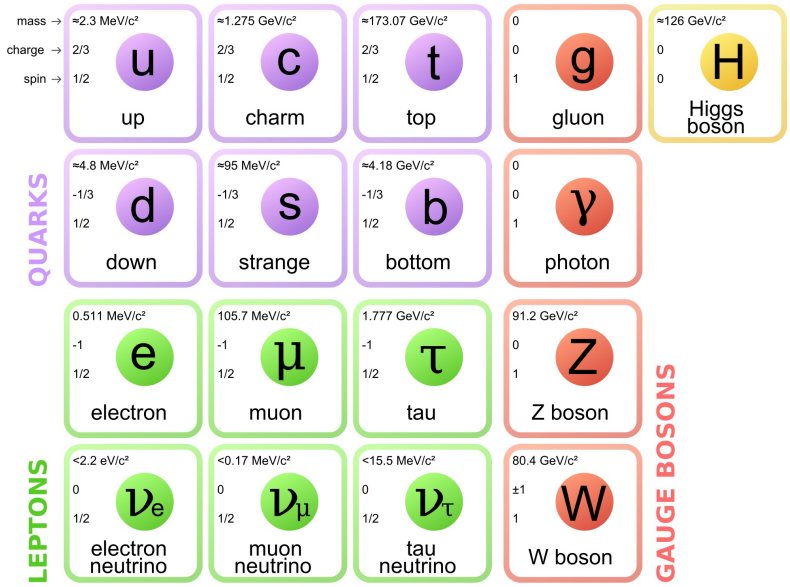

Figure 1.1. The Standard Model of elementary particles, with the three generations of fermions, the gauge bosons in the fourth column, and the Higgs boson in the fifth.

quark $m_t \approx 173.1\,\text{GeV}$, which is the heaviest fundamental particle of the SM. The large mass split between quarks and charged leptons belonging to the three generations, and their ordering, are not explained within the SM, originating the flavor puzzle described in Sec. 1.4. The quarks can interact, like the leptons, via the electromagnetic and weak interactions, but also via the strong interaction. The strong interaction is responsible for the formation of hadrons, which are bounded states of quarks. For example the up and down quarks can bond to form a proton or a neutron. Two features of the strong interactions are the confinement and the asymptotic freedom, which will be described in Sec. 1.1.1.

The interactions between the SM particles are mediated by the four vector bosons of spin 1 listed in the fourth column of Fig. 1.1. The gluon g is the carrier of the strong interaction, the photon γ is responsible for the electromagnetic interactions and the W and Z bosons are the carriers of the weak interaction.

The fields of the SM particles and their interactions are described in a quantum field theory by a Lagrangian that is invariant under the non-Abelian gauge symmetry group:

$$SU(3)_C \times SU(2)_L \times U(1)_Y \tag{1.1}$$

where $SU(3)_C$ indicates the color symmetry, preserved by strong interactions, while the invariance under $SU(2)_L \times U(1)_Y$ describes the unification between the electromagnetic and weak forces. The Lagrangian can be written as the sum of two contributes: one describing the strong interaction (quantum chromodynamics or QCD), and one the electroweak interactions (EW):

$$\mathcal{L}_{\text{SM}} = \mathcal{L}_{\text{QCD}} + \mathcal{L}_{\text{EW}} \tag{1.2}$$

Because of the symmetries of the model, the Lagrangian cannot contain explicit mass terms for the particles involved. This would lead to the conclusion, in contrast with the observations, that all fundamental particles are massless. This issue has been solved with the introduction of a scalar boson, as independently proposed by Brout and Englert [4], and Higgs [5]. The two papers describe how, with a mechanism called spontaneous symmetry breaking, the massive fermions and bosons acquire their masses through the interaction with the new scalar, called Brout-Englert-Higgs (or simply Higgs) boson. In Sec. 1.3, we will see how the introduction of a scalar field open the way to the hierarchy problem of the SM.

In the next Section we will focus on the QCD sector of the SM, which is mostly relevant for the search presented in this thesis.

1.1.1 Quantum Chromodynamics

The QCD is the theory which describes the strong interactions between quarks in terms of exchange of gluons which are the force carriers of the theory, like the photons are for the electromagnetic force in quantum electrodynamics. The gauge invariant QCD Lagrangian can be written as:

$$\mathcal{L}_{\text{QCD}} = \sum_i \overline{\text{q}}_{i,a} \left(i\gamma^\mu \partial_\mu \delta_{ab} - g_s \gamma^\mu t^A_{ab} G^A_\mu - m_i \delta_{ab} \right) \text{q}_{i,b} - \frac{1}{4} F^A_{\mu\nu} F^{\mu\nu,A} \tag{1.3}$$

where $\text{q}_{i,a}$ represents the quark spinor of flavor i and color $a = 1 \to 3$, G^A_μ is the gluon field associated with the generator t^A_{ab} ($A = 1 \to 8$), g_s is the gauge coupling and $F^A_{\mu\nu}$ is the gluon field tensor:

$$F^A_{\mu\nu} = \partial_\mu G^A_\nu - \partial_\mu G^A_\mu - g_s f_{ABC} G^B_\mu G^C_\nu \tag{1.4}$$

f_{ABC} are the structure constants satisfying the relation:

$$[t^A, t^B] = i f_{ABC} t^C \tag{1.5}$$

The QCD is characterized by two peculiar properties: the asymptotic freedom and the confinement [6]. Because of the asymptotic freedom, the bonds between strongly interacting particles become asymptotically weaker as the distance between them decreases. Quarks interact weakly for high colliding energies, when two quarks are closely pushed one against the other. These scenarios are referred as deep inelastic processes, where the hard-scattering of quarks and gluons can be described in a perturbative way. On the contrary, when the distance increase, the internal energy in the gluon field increase proportionally to the distance between two quarks. Above a certain distance, the internal energy is enough to create another quark pair. For this reason, a quark or a gluon cannot exist as free particles. They are "confined" in color-singlet states, which are the only that can be directly observed. An exhaustive description of these QCD effects can be found, for example, in Ref. [7]

1.2 Physics at colliders

In this Section we deal with the phenomenology of high-energy pp collisions, such the ones produced at the LHC. The first noticeable aspect of an high-energy pp collision is that the protons do not interact as elementary particles but as composite ones. This is a direct consequence of the asymptotic freedom. At high energies the hard scattering process takes place between the proton constituents, the partons.

A sketch illustrating what typically happens in a pp collision is shown in Fig. 1.2. The three horizontal green lines on the left and on the right of the figure represent the three quarks that make up each proton. Two of the initial quarks, one from each proton, interact through hard scattering (red circle), i.e. with a large portion of the momentum transferred between the two partons. The other partons interact at very low energy (magenta blob), and generate soft radiation that constitutes the "underlying event". The beam remnants go forward along the beam line (cyan blobs). The partons can radiate gluons or split, in both the initial and the final state of the interaction. Immediately after the interaction, any colored particles, because of the confinement, starts to produce streams of hadrons (red and magenta lines) that decay in stable particles (dark green blobs and lines) that can be detected in the experiments at colliders. This latter process is called hadronization and it will be the subject of Sec. 1.2.1.

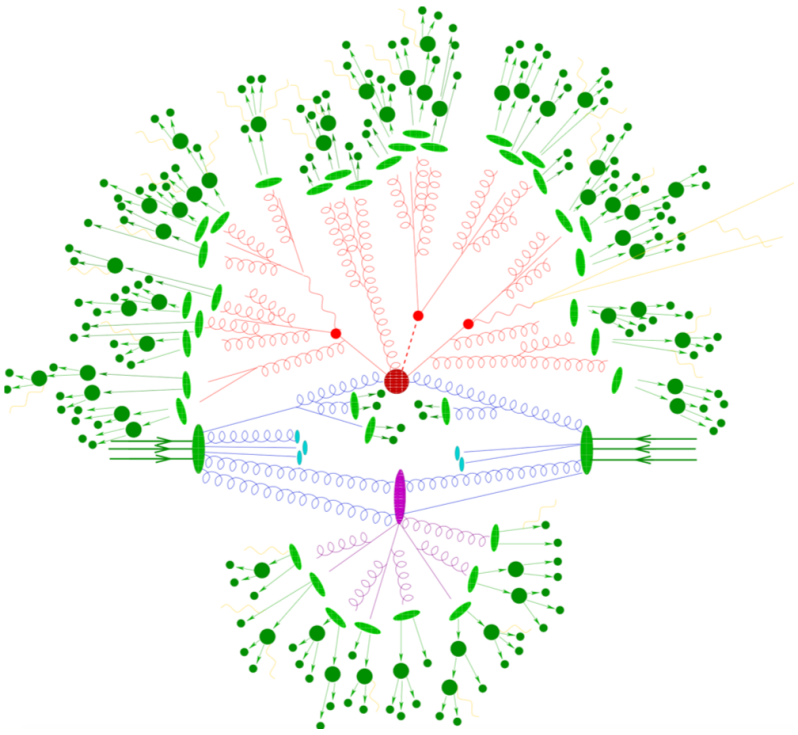

Figure 1.2. Sketch of a pp collision.

1.2.1 Hadronic jets

As a direct consequence of the confinement property of QCD, colored particles cannot be directly observed in nature. Hence, whenever a quark or a gluon is produced in an interaction, it radiates particles that mask its color charge to the observer. The result of the process is then a stream of particles collimated with the direction of the original parton, which is called jet.

The formation of a jet is composed by two stages. In the first stage, called *parton branching*, each parton has a finite probability to split in other two partons. The peculiarity of this process is that the two partons are emitted at small angles with respect to the originating parton, therefore this first step causes the collimation of the particles inside a jet. Another remarkable feature is that gluons have a larger probability to split, therefore jets originating from a gluon (gluon jets) tend to shower more than quark jets. After several parton splitting, the energy of the individual partons is reduced, and low-momentum interactions became dominant. In this phase, called *hadronization*, the partons originated in the parton branching recombine to form hadrons, which are color neutral. The hadrons can be enough stable to be directly detected or they can be unstable and decay into other hadrons, photons or leptons, both charged or neutral. On average, about 65% of the jet energy is carried by charged particles, detected by the tracker and the calorimeters, about 20% is composed by high-energy photons, detected by electromagnetic calorimeters, and the remaining part is made of neutral hadrons, mainly detected by hadronic calorimeters.

The formation of a jet is generally a non-perturbative process, which leads to the production of a large amount of particles. Therefore, the jet reconstructed by the detector is not a uniquely defined object, but the output of a clustering algorithm, which groups the jet constituents originating from the parton according to their kinematic properties. An overview of different clustering algorithms used to define a jet is given in Sec. 5.2. Despite the fact that the jets are complex objects, they can be used to infer the kinematical properties of the parton originating the shower, which are related to that of the resulting jet. However, the complexity of the processes involved in the jet formation introduce an intrinsic resolution of the hadronic jet properties with respect to the parton properties.

1.2.2 Kinematics variables of parton scattering

In this Section we discuss the general kinematical properties of a two-to-two parton scattering $p_1 + p_2 \to p_3 + p_4$, which constitutes the most relevant background of the search presented in this thesis. Most of the properties and of the variables that we will describe are relevant also for the signal process studied in this thesis, where the two initial partons produce two new particles in their interaction. A sketch of the two-to-two parton scattering is shown in Fig. 1.3, where the z-axis is oriented along the direction of the colliding partons.

In a two particle collision, the energy available for the interaction is given by the invariant mass $\sqrt{s}$, also called center-of-mass energy. Calling $\mathbf{P}$ the sum of the

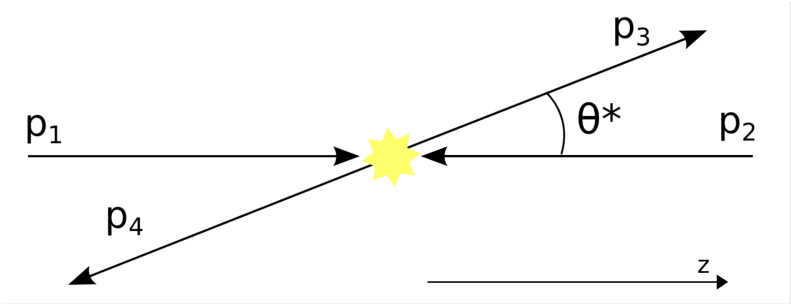

Figure 1.3. Scheme of the two-to-two parton scattering.

four-momenta of the incoming particles, the invariant mass is:

$$\sqrt{s} = \sqrt{\mathbf{P} \cdot \mathbf{P}} = \sqrt{\left(\sum_k E_k\right)^2 - |\sum_k \overrightarrow{p_k}|^2} \tag{1.6}$$

where E_k and $\overrightarrow{p_k}$ are respectively the energy and the momentum of the k-th incoming particle. In the equation above we used the natural units system where $c = 1$. The invariant mass is a relativistic invariant, therefore its value does not depend on the reference system. At the LHC, two protons are accelerated at the same energy E, which is much larger than their masses, and collide head-to-head. Under these conditions the center-of-mass energy of the two proton system is approximately $\sqrt{s} \simeq 2E = 2 \cdot 6.5\,\text{TeV} = 13\,\text{TeV}$.

Because of the asymptotic freedom, at such high energies the interaction happens between two partons inside each proton as if they were free particles. The partons carry only a fraction of the momentum of the whole proton. Hence, the center-of-mass energy available for the two-parton interaction is generally lower than 13 TeV.

The momentum fraction carried by a parton inside a proton is called Bjorken-x, simply indicated as x. Given the x of two partons (x_1 and x_2), the square of their invariant mass ($\hat{s}$) is related to that of the proton-proton system by:

$$\hat{s} = x_1 x_2 s \tag{1.7}$$

The probability of the parton to have a particular value of x is modeled by the parton distribution functions (PDFs), which depends on the energy of the proton. We will see later how the cross section of the process depends on the PDFs.

We introduce here two variables very useful when dealing with physics at colliders, the rapidity (y) and the pseudorapidity (η):

$$y = \frac{1}{2} ln \left(\frac{E + p_z}{E - p_z}\right) \tag{1.8}$$

$$\eta = \frac{1}{2} ln \left(\frac{|p| + p_z}{|p| - p_z}\right) \tag{1.9}$$

For ultrarelativistic particles, $|p| \gg m$, therefore $E \approx |p|$ and the rapidity is approximately equal to the pseudorapidity. The pseudorapidity can also be written

as a function of θ, the angle of the particle with respect to the z-axis:

$$y \simeq \eta \equiv \frac{1}{2} ln \left(\frac{|p| + p_z}{|p| - p_z} \right) = \arctan(\frac{p_z}{|p|}) = -\log \tan \frac{\theta}{2} \tag{1.10}$$

where η is the pseudorapidity that, being a function of θ, can be easily measured in the laboratory frame.

The rapidity is useful because it is connected with the scattering angle in the center-of-mass frame[1], θ^* in Fig. 1.3. In this frame the rapidities of the two decay products are opposite, i.e. $y_3^* = +y^*$ and $y_4^* = -y^*$. Hence we have:

$$\cos \theta^* = \tanh y^* \tag{1.11}$$

Since the difference between two rapidities is a invariant with respect to Lorentz boosts along the z–axis, the rapidities of the outgoing particles y_3 and y_4 in the laboratory frame are related to y^* by:

$$y^* = \frac{y_3 - y_4}{2} \tag{1.12}$$

therefore:

$$\cos \theta^* = \tanh \frac{y_3 - y_4}{2} \simeq \tanh \frac{\eta_3 - \eta_4}{2} = \tanh \frac{\Delta\eta}{2} \tag{1.13}$$

We then expressed $\cos \theta^*$, as a function of a quantity that can be easily measured in the laboratory frame, $\Delta\eta$, which is the difference between the pseudorapidities of outgoing partons. We will see in Sec. 6.3 how this quantity can be used to discriminate signal from background events.

1.2.3 Hadronic cross sections

The parton distribution functions (PDFs), introduced in the previous section and indicated with $f_i(x, \mu^2)$, allow the calculation of the probability of finding inside a hadron a certain kind of parton i carrying a momentum fraction x at a squared energy scale μ^2. The (arbitrary) factorization scale μ can be thought as the scale which separates the long and short-distance physics. The total cross section of the hard scattering processes can be factorized into a normalization part, based on the PDFs, and another part expressed by the parton-parton scattering cross section, $\hat{\sigma}_{ij}(x_1 p_A, x_2 p_B, \mu^2)$, where p_A and p_B are the momenta of incoming hadrons. It can be written then as:

$$\sigma_{\text{had}} = \sum_{ij} \int dx_1 dx_2 f_i(x_1, \mu^2) f_j(x_2, \mu^2) \hat{\sigma}_{ij}(x_1 p_A, x_2 p_B, \mu^2) \tag{1.14}$$

Partons with transverse momentum larger than μ participate in the hard scattering process with a short-distance partonic cross-section $\hat{\sigma}$.

It is often helpful in hadron collisions to factorize the effect of the parton distribution functions on the hadronic cross section by introducing the parton luminosity factor. This is defined as:

[1] In the following equations we mark with * the quantities evaluated in the center-of-mass frame, while the other quantities are evaluated in the laboratory frame.

$$\frac{dL_{ij}}{d\tau} = \int_0^1 \int_0^1 dx_1 dx_2 f_i(x_1, \mu^2) f_j(x_2, \mu^2) \delta(x_1 x_2 - \tau) \tag{1.15}$$

where $\tau = x_1 x_2 = \frac{\hat{s}}{s}$ (Eq. 1.7). The hadronic cross section of any process, can be expressed generally as a function of two terms:

$$\sigma_{\text{had}}(s) = \sum_{ij} \int \frac{d\tau}{\tau} \left[\frac{1}{s} \frac{dL_{ij}}{d\tau} \right] [\hat{s}\hat{\sigma}_{ij}] \tag{1.16}$$

The first term between brackets (the parton luminosity) depends on the PDFs and on the design parameter of the collider s. The second term depends from the physical parameters of the interaction: the square of the two-parton invariant mass ($\sqrt{\hat{s}}$) and the parton-parton cross section $\hat{\sigma}_{ij}$.

1.2.4 Definition of luminosity

The luminosity is a key parameter of a particle accelerator because it is a measure of the quantity of the pp interactions (or events) that the machine is able to produce. The number of expected events, N_{evt}, is the product of the hadronic cross section of interest, σ_{had}, and the time integral over the instantaneous luminosity L:

$$N_{\text{evt}} = \sigma_{\text{had}} \int L(t) dt \tag{1.17}$$

The unit of L is therefore $\text{cm}^{-2}\,\text{s}^{-1}$. The integrated luminosity that appears in Eq. 1.17, then, has the same unit of measure of the inverse of a cross section, therefore is measured in inverse barns b^{-1}, where:

$$1\,\text{b} = 10^{-24}\,\text{cm}^2 \tag{1.18}$$

More often submultiple of the inverse barn are used, like the inverse picobarn pb^{-1} or the inverse femtobarn fb^{-1}.

The luminosity for colliding beams experiment can be evaluated from the properties of the colliding beams. In a typical collider experiments, two beams travel in a circular path in opposite directions. The beams are formed by a certain number of bunches of particles, N_{b}, interspersed by empty space. Each bunch contains N particles (in the case of the LHC, protons) and circulates in the collider with a frequency f. Another important parameter for the evaluation of the luminosity is the density ρ of the N particles inside the volume occupied by the bunch. A schematic picture is shown in Fig. 1.4.

At fixed points of the accelerator, called interaction points, the path of the two beams are intersected, causing the bunches of the opposite beams to overlap, and the proton inside them to collide. The luminosity is proportional to the overlap of the bunches, which are moving through each other. The value of the overlap integral depends on the longitudinal position of the bunches s and the time of the mutual crossing t. In our integration we can use $s_0 = ct$ as "time" variable (see Fig. 1.4). Assuming that particles collide head-on with frequency f and that the two bunches meet at $s_0 = 0$, the luminosity (proportional to the overlap integral) is then:

$$L = 2N_1 N_2 N_{\text{b}} f \int\int\int\int_{-\infty}^{+\infty} \rho_1(x, y, s, s_0) \rho_2(x, y, s, s_0) dx dy ds ds_0 \tag{1.19}$$

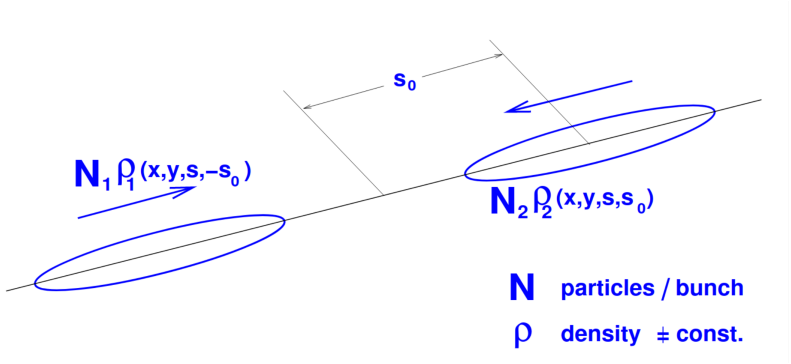

Figure 1.4. Schematic view of colliding bunches.

where $\rho_1(x, y, s, s_0)$ and $\rho_2(x, y, s, s_0)$ are the time dependent beam density distribution function. Assuming them to be identical in the transverse part, Gaussian and uncorrelated in x, y and z, the formula above can be rewritten as:

$$L = f\frac{N_1 N_2 N_\mathrm{b}}{4\pi\sigma_x\sigma_y} \tag{1.20}$$

where σ_x and σ_y characterize the RMS transverse beam sizes in the horizontal and vertical directions. The revolution frequency in a collider is accurately known and the number of particles or beam intensity is continuously measured with beam current transformers which reach an accuracy of ∼1% for LHC nominal beam parameters. The only unknown parameter that needs to be measured is the effective transverse area which depends on the density distribution of the two beams. This measurement is done with the Van Der Meer technique [8], that consists in scanning the LHC beams through one another to determine the size of the beams at their point of collision. For the experiments at the LHC these measurements, when combined with information on the number of circulating protons, allows the determination of an absolute luminosity scale, which in turn is used to calibrate the subdetectors of the experiments dedicated to the online luminosity measurements. The latest precision luminosity measurements at CMS [9, 10, 11] report a systematic uncertainty of 1.0, 1.5, and 2.1% on absolute calibration from the van der Meer scan respectively for the last three years of data-taking (2016, 2017, and 1028).

1.3 The hierarchy problem

The hierarchy problem is a theoretical issue connected with the radiative corrections to the Higgs boson (H) mass. The problem can be defined as follows: if there exists new physics above an energy scale Λ, which foresees new particles interacting with the Higgs boson, then the radiative corrections to the H mass (m_H) are of the order of Λ^2.

This poses serious questions when Λ is larger than m_H by even few order of magnitudes. In this case, in fact, the radiative corrections to m_H would be very large compared to the value of m_H itself. As a consequence, large parameters have to be introduced and fine-tuned in order to cancel the contribution from the radiative corrections, raising doubts on the naturalness of the model.

A description of the hierarchy problem is provided in Ref. [12]. The SM Higgs potential is of the form:

$$V(\mathrm{H}) = -\mu^2|H|^2 + \lambda|H|^4. \tag{1.21}$$

To evaluate the propagator of the Higgs boson in the vacuum, one should take into account for all the possible diagrams that start and end with an Higgs boson. An example of such diagrams with one order loops are shown in Fig. 1.5, involving, from left to right, a scalar bosons (like H itself), gauge bosons and fermions.

Figure 1.5. One loop contributions to the radiative corrections of Higgs boson mass in the SM. The three integrals associated to the diagrams are quadratically divergent for $\Lambda \to \infty$, therefore the radiative corrections to m_{H} are much larger than the value of m_{H} itself, leading to the hierarchy problem.

These diagrams will cause a contribution to the mass parameter μ, which can be decomposed in a square sum of two terms, the bare mass and the radiative corrections, $-\mu^2 \to -\mu_0^2 + \delta\mu^2$, where

$$\delta\mu^2 = \frac{\Lambda^2}{32\pi^2}\left[-6y_t^2 + \frac{1}{4}(9g^2 + 3g'^2) + 6\lambda\right] \tag{1.22}$$

In the equation above, Λ is the cutoff of the theory, i.e. the energy scale where the new physics take place, y_t is the top Yukawa coupling, g, g' are the $SU(2)$ and $U(1)$ gauge couplings and λ is the Higgs boson self-coupling. Since the Yukawa coupling of the Higgs to fermions is proportional to their mass, we can neglect the contributions from loops with other fermions. The minimum of the Higgs potential is at:

$$\langle H \rangle = \begin{pmatrix} 0 \\ \frac{v}{\sqrt{2}} \end{pmatrix}, \quad v^2 = \frac{\mu^2}{\lambda} \tag{1.23}$$

from the measured values of the W, Z masses we know $v \approx 246\,\mathrm{GeV}$. The physical Higgs mass, measured in the experiments is $m_{\mathrm{H}} = \sqrt{2}\lambda v \approx 125\,\mathrm{GeV}$ which implies $\lambda = 0.13 \sim 1/8$.

Since, from the equations above, $m_{\mathrm{H}} \sim v \sim \mu$, if $\Lambda \gg$ TeV the corrections to the mass parameter μ, $\delta\mu$, are several order of magnitude larger than the value of μ itself. The bare mass parameter μ_0, then, has to be fine-tuned in order to cancel the large radiative corrections to obtain a value of μ of the order of the Higgs mass.

The hierarchy problem arises especially when trying to construct a theory that includes both the SM and the gravity. In principle, the effect of the gravity at particle level should became relevant for energy above the Planck energy scale, which is proportional to the Planck mass M_{Pl}. The Planck mass is related to the Newton constant by $G_N \propto 1/{M_{\mathrm{Pl}}}^2$. Since $G_N \sim 10^{-39}\,\mathrm{GeV}^{-2}$, the value of the Planck mass is $M_{\mathrm{Pl}} \sim 10^{19}\,\mathrm{GeV}$. Under these assumptions we have:

$$\delta\mu \sim {M_{\mathrm{Pl}}}^2 \sim 10^{38}\,\mathrm{GeV}^2 \tag{1.24}$$

As a consequence, also μ_0^2 value should be $\sim 10^{38}\,\mathrm{GeV}^2$, and fine-tuned up to 34 digits in order to cancel with $\delta\mu$ almost exactly to obtain:

$$\mu^2 = \mu_0^2 + \delta\mu^2 \sim 10^4\,\mathrm{GeV}^2 \Rightarrow m_{\mathrm{H}} \sim \mu \sim 100\,\mathrm{GeV} \tag{1.25}$$

In addition to what we said on the hierarchy problem, it is important to note that it arises only in the presence of a scalar field like the Higgs field. The masses of the fermions and the SM gauge fields, in fact, are protected from quadratically divergent radiative corrections by the chiral or the gauge symmetry.

The hierarchy problem does not stand if the new physics exists around the TeV scale, therefore it has been one of the leading motivations for new physics within the energy scale of the LHC collisions.

In Ch. 2 we will discuss new physics theories assuming the presence of extra spatial dimensions. These theories solve the hierarchy problem caused by the large gap between the Planck and the Higgs masses, and foresee new resonances at the TeV scale. The new resonances can be observed by their cascade decays, which are the experimental signature we are interested in.

1.4 The flavor puzzle

The flavor puzzle is an open question within the SM that arises from its inability to predict the masses of the fundamental particles. In the SM the massive fermions acquire their masses through the Higgs mechanism and their resulting couplings with the Higgs boson, also called Yukawa couplings. The values of the Yukawa couplings are free parameters of the SM. Their values are set by the experiments that measure the fermion masses and couplings.

The SM does not predict the existence of a hierarchy between the particle masses. However, as shown in Fig. 1.6, the masses of charged fermions belonging to different generations appear to follow a hierarchical ordering. The heaviest charged particle of one generation has a mass below that of the lightest one of the generation after.

A similar hierarchical pattern appear also in the interactions between positive charged quarks (u-type) and negative charged quarks (d-type) mediated by the W boson (Fig. 1.7). Such interactions have the property to change the flavor of the quarks.

The flavor changing process depends on the parameters of the Cabibbo-Kobayashi-Maskawa (CKM) matrix, V_{CKM}, that can be written as follows:

$$V_{\mathrm{CKM}} = \begin{pmatrix} V_{ud} & V_{us} & V_{ub} \\ V_{cd} & V_{cs} & V_{cb} \\ V_{td} & V_{ts} & V_{tb} \end{pmatrix} \tag{1.26}$$

where V_{ij} is proportional to the strength of the transition between quarks $j \to i$. A puzzling question arises from the values of the V_{CKM} parameters, which are roughly:

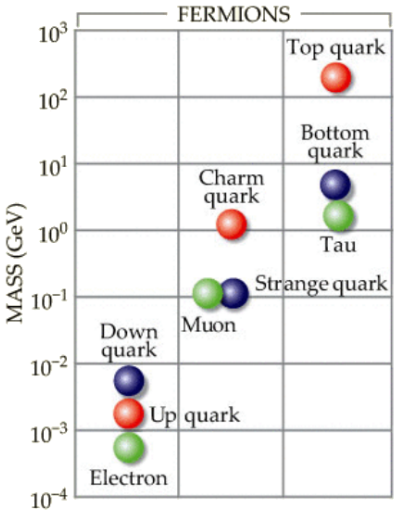

Figure 1.6. SM quarks and charged leptons, ordered by mass and generation.

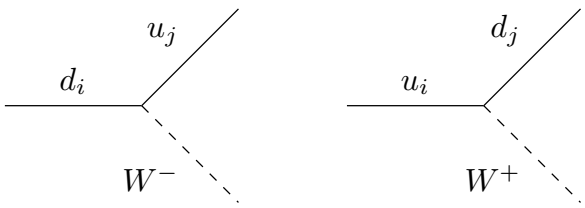

Figure 1.7. Transition between u-type and d-type quarks mediated by the W boson. The indexes i, j refer to the quark generations, numbered from 1 to 3.

$$V_{\text{CKM}} \sim \begin{pmatrix} 1 & 0.2 & 10^{-3} \\ 0.2 & 1 & 10^{-2} \\ 10^{-3} & 10^{-2} & 1 \end{pmatrix} \tag{1.27}$$

This means that W-mediated transitions between quarks within the same generation happens more frequently than transitions between two consecutive generations ($1 \leftrightarrow 2$, $2 \leftrightarrow 3$), and even more frequently than $1 \leftrightarrow 3$ transitions. This introduces a hierarchy in the interactions between quarks that is not explained by the SM principles.

The SM is able to accommodate the different masses of the fermions and the different interaction rates between quarks of different flavors by setting the relative parameters to match the experimental observations. However, the presence of hierarchical patterns, not foreseen by the SM, has given way to the development of new theories able to explain them. In Sec. 2.2 we will see an example of a theory beyond the SM that provides a possible explanation to the flavor puzzle.

Chapter 2

New resonances in models with a warped extra dimension

In this Chapter we will describe the theoretical context of the extra dimension (ED) model underlying our signal benchmark model.

In general, ED models have been introduced to solve the hierarchy problem that arises from the large gap between the Planck mass and the Higgs boson mass.

The Chapter starts with a digression on the Arkani-Hamed, Dimopoulos, and Dvali (ADD) model (Sec. 2.1). We will see how this model can solve the hierarchy problem by introducing one or more large and flat extra dimensions.

In Sec. 2.2, instead, we will explore an alternative theory by Randall and Sundrum (RS), where the single ED introduced is warped. The final part of this Chapter is dedicated to the new resonances foreseen by this model, which decay into the final state considered in this thesis.

2.1 Large extra dimensions

The first ED models proposed to solve the hierarchy problem assumed the extra dimensions to be large and flat. The general scheme is represented in Fig. 2.1. Two four-dimensional (4D) hypersurfaces, called branes, delimit the volume of space between them, called bulk, along the extra dimension. Depending on the model it is possible to have any number d of extra dimensions.

These models allows to create a framework where it is possible to avoid the hierarchy problem introduced in Sec. 1.3. The argument for the solution of this problem is described in the following. In a formulation of the general relativity in a $4+d$ flat dimensional space, the Einstein field equations can be obtained by applying the principle of least action to the Einstein-Hilbert action:

$$\begin{aligned} S_{(4+d)} &= -M_{(4+d)}^{2+d} \int d^{(4+d)}x \sqrt{g_{(4+d)}} \mathcal{R}_{(4+d)} \\ &= -M_{(4+d)}^{2+d} V_{(d)} \int d^{(4)}x \sqrt{g_{(4)}} \mathcal{R}_{(4)} + ... \end{aligned} \tag{2.1}$$

where $\mathcal{R}_{(4+d)}$ is the Ricci tensor and $g_{(4+d)}$ is the determinant of the metric tensor matrix $g_{\mu\nu}$, which in a 4+d space is a diagonal matrix with the elements on the

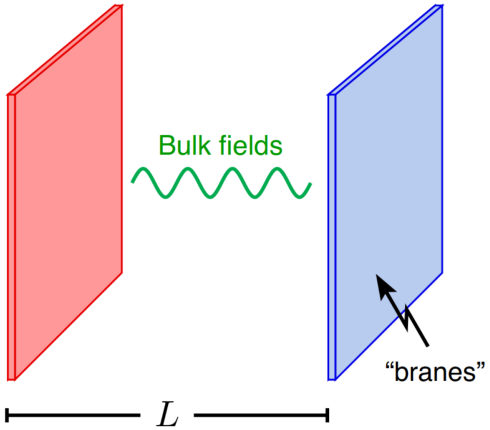

Figure 2.1. Representation of a space with a flat extra dimension. The extra dimension has a finite length L which is delimited by two 4 dimensional hypersurfaces called branes. The volume between branes is called the bulk.

diagonal corresponding to $\{x^0, x^1, x^2, x^3, ..., x^{3+d}\} = \{+1, -1, -1, -1, ..., -1\}$. The prefactor $M_{(4+d)}^{2+d}$ is introduced to keep the action dimensionless and in 4D it is equal to the square of the Planck mass $M_{\rm Pl}$. In the last term of Eq. 2.1 we integrated over the extra d dimensions using the relation $\mathcal{R}_{(4+d)} = \mathcal{R}_{(4)}$, true at linear order for flat extra dimensions. The result of the integration is $V_{(d)}$, i.e. the volume of the bulk. Matching Eq. 2.1 with the 4 dimensional Einstein-Hilbert action [13]

$$S_{(4)} = {M_{\rm Pl}}^2 \int d^{(4)}x \sqrt{g_{(4)}} \mathcal{R}_{(4)} \tag{2.2}$$

we obtain the relation:

$${M_{\rm Pl}}^2 = M_{(4+d)}^{2+d} V_{(d)} \tag{2.3}$$

This relation can be interpreted to solve the hierarchy problem. In fact, the large value of $M_{\rm Pl}$ may arise from a relatively small value of the real scale of the theory, $M_{(4+d)} \equiv M_*$, multiplied by a large volume from the extra dimensions. In this interpretation the gravitational interaction is apparently weak because its effects are diluted in the large volume of the bulk. By setting the value of M_* to few TeV, it is possible therefore to define a theory where the radiative correction to $m_{\rm H}$, which are of the order of M_*, and not $M_{\rm Pl}$, are not too large compared to the value of $m_{\rm H}$ itself.

However, a problem arises from this kind of models when considering that also the SM gauge fields can propagate in the bulk. If we assume so, also the gauge couplings of other fundamental forces are diluted. The 4D values of the couplings are related to the couplings in the $4 + d$ dimensional space by:

$$g_4^2 = \frac{g_{(4+d)}^2}{V_{(d)}} \tag{2.4}$$

In order to g_4 to be adimensional, $g_{(4+d)}$ should have dimension:

$$\left[g_{(4+d)}\right] = \left[L^{d/2}\right] \tag{2.5}$$

In a natural theory the parameter of scale, M_*, should set the order of magnitude of the couplings $g_{(4+d)}$. Since the dimensionality of M_* is $[M_*] = \left[L^{-1}\right]$, the relation between $g_{(4+d)}$ and M_* is:

$$g_{(4+d)} \sim M_*^{-d/2} \tag{2.6}$$

Combining 2.6 with 2.4 we obtain:

$$g_4^2 \sim \frac{M_*^{-d}}{V_{(d)}} \quad \Rightarrow \quad M_* \sim g_4^{-2/d} V^{-1/d} \tag{2.7}$$

which, replaced in Eq. 2.3 and considering that $V_{(d)} \sim L^d$, gives the relation:

$$L \sim \frac{1}{M_{\mathrm{Pl}}} g_4^{1+\frac{2}{d}} \tag{2.8}$$

The size of each of the extra dimensions is forced to be roughly Planck-length $L \sim \frac{1}{M_{\mathrm{Pl}}} = L_{\mathrm{Pl}}$. Thus, M_* is forced to be $M_* \sim M_{\mathrm{Pl}}$ because of Eq. 2.3. The propagation of both the SM gauge bosons and gravity in the bulk prevents to solve the hierarchy problem because it fixes both the scale M_* and the length of the d extra dimensions.

In 1998, the physicists Arkani-Hamed, Dimopoulos, and Dvali (ADD) proposed a solution to this problem using branes [14]. They postulated that all the SM fields are confined on one brane and only the gravity is allowed to propagate in the bulk. In this framework, the gauge couplings are no more diluted in an higher-dimensional volume, therefore they are not connected with M_*. Only the gravitational interaction is diluted, explaining why it is much weaker than the other fundamental forces. In fact its original couplings are not lower than that of other forces, but its effects are weaker because they are diluted in a much larger volume. As a side effect, the dilution of gravity should cause significant deviations of the gravitational force from the $1/r^2$ dependence of Newtonian gravity for distances below L, where L is the typical length of the extra dimensions.

If we assume $M_* \sim 1\,\mathrm{TeV}$ to solve the hierarchy problem, from Eq. 2.3 we obtain:

$$\begin{aligned} &{M_{\mathrm{Pl}}}^2 \propto M_*^{2+d} L^d \Rightarrow \\ &\Rightarrow L \propto \frac{1}{M_*} \left(\frac{M_{\mathrm{Pl}}}{M_*}\right)^{\frac{2}{d}} \propto \frac{1}{1\,\mathrm{TeV}} 10^{\frac{32}{d}} \sim 10^{\frac{32}{d}-17}\mathrm{cm} \end{aligned} \tag{2.9}$$

This allows to put some boundaries on L and d using results from experiments that test Einstein/Newton gravity:

- if $d = 1$, then $L \sim 10^{15}$cm, which is about the size of the solar system. Since we do not observe deviations at this scale the hypothesis of a single extra dimension is ruled out;
- if $d = 2$, then $L \sim 10^{-1}$cm, this hypothesis is ruled out by Cavendish-like experiments [15];
- if $d \geqslant 3$, then $L < 10^{-6}$cm, which evades the tests from the aforementioned experiments.

Besides providing an elegant solution to the hierarchy problem, the ADD model predicts also the existence of new particles, which could be a clear evidence of new physics.

In fact, the propagation of the gravity field in the extra dimensions gives birth to a tower of 4D massive fields that arise from the Kaluza–Klein (KK) decomposition of the $4 + d$ dimensional fields (see Appendix A), which is basically a quantization of the field along the extra dimensions. Each $4 + d$ dimensional field corresponds to an infinite tower of 4D fields (KK modes), which in turn correspond to particles with masses n/L, where $n = 0, 1, 2, ...$ is a positive integer corresponding to the n-th KK mode of the tower. If L is large with respect to the Planck length $L_{\mathrm{Pl}} \sim 1/M_{\mathrm{Pl}} \sim 10^{-35}\,\mathrm{m}$, like in the ADD model, the spectrum of KK graviton modes is quasi-continuous. As the interaction scale increases, more graviton modes are excited, leading the ADD model to predict, for example, a nonresonant excess of photon or lepton pairs at high diphoton or dilepton masses originating from the decay of virtual (KK) gravitons. These signatures are currently searched by the ATLAS and CMS analyses [16, 17, 18].

Another signature of the model would be the presence of Quantum Black Holes (QBH), i.e. black holes at microscopic level [19]. In this case the signature is represented by a nonresonant excess in the right tail of the distribution of the total sum of the transverse momentum (p_{T}) of the particles produced in pp interactions, or in the distribution of their invariant mass. The ATLAS and CMS experiments respectively exclude the presence of QBH below a mass threshold of 7.8 TeV for $d = 2$, or 7.4 TeV for $d = 6$ (ATLAS [20]); or 5.3, 5.5, and 5.6 TeV for ADD models with respectively $d = 4$, 5, 6 (CMS [21]).

In the next Section we will see an alternative ED model, where the typical length of the extra dimension is $L \sim 1\,\mathrm{TeV}^{-1}$, or $10^{-14}\,\mathrm{cm}$, much smaller than the dimensions of the ADD model. In this case, as we will see the KK modes have well separated mass values, originating resonant signatures.

2.2 Warped extra dimension model

In this section we provide a description of warped extra dimension (WED) models, focusing on how they solve the hierarchy problem. The first WED model was proposed by Randall and Sundrum (RS) in a seminal paper in 1999 [22, 23], where they showed that a metric for a space with a warped extra dimension can arise from a solution to the Einstein's equations. The metric of such space is:

$$ds^2 = \alpha(z)^2(\eta_{\mu\nu}dx^\mu dx^\nu - dz^2) \tag{2.10}$$

where $\eta_{\mu\nu}dx^\mu dx^\nu$ is the flat metric in 4D ($\eta_{\mu\nu}$ is a diagonal matrix with $\{1, -1, -1, -1\}$ on the diagonal) and z is the conformal coordinate along the extra dimension. $\alpha(z)$ is the warp factor, which is of the form:

$$\alpha(z) = \frac{R}{z} \tag{2.11}$$

where R^{-1} is the curvature of the space, which is usually set to $1/M_{\mathrm{Pl}}$. To show how the RS model can solve the hierarchy problem, we consider a space truncated

by two branes in the z direction, respectively at $z = R = 1/M_{\text{Pl}}$ and $z = R' > R$, where and $R' = O(\text{ TeV}^{-1})$. The two branes are respectively called ultraviolet (UV), or Planck brane, and infrared (IR), or weak brane.

We consider then a simplified model including only the Higgs field confined on the IR brane. The five-dimensional (5D) action for the Higgs field is then:

$$S_5 = \int d^5x \sqrt{-\hat{g}} \delta(z - R') \mathcal{L}_{\text{H}} \tag{2.12}$$

where $\hat{g}$ is the determinant of the tensor of the induced metric on the 4D IR brane ($\hat{g}_{\mu\nu}$), defined below, and $\mathcal{L}_{\text{H}}$ is the Higgs Lagrangian:

$$\mathcal{L}_{\text{H}} = \hat{g}^{\mu\nu} \partial_\mu \text{H}^* \partial_\nu \text{H} + \lambda \left(|\text{H}|^2 - \frac{v^2}{2} \right)^2 \tag{2.13}$$

The $\delta(z - R')$ function in Eq. 2.12 is introduced to confine the Higgs boson on the IR brane. For a field confined on the IR brane $z = R'$ and $dz = 0$. The induced metric for such field can be obtained from Eq. 2.10:

$$ds^2 = \left(\frac{R}{z} \right)^2 (\eta_{\mu\nu} dx^\mu dx^\nu - dz) = \left(\frac{R}{R'} \right)^2 \eta_{\mu\nu} dx^\mu dx^\nu \tag{2.14}$$

We can then define the induced metric tensor $\hat{g}_{\mu\nu}$ and its determinant $\hat{g}$:

$$\begin{aligned} \hat{g}_{\mu\nu} &\equiv \left(\frac{R}{R'} \right)^2 \eta_{\mu\nu} \\ \hat{g} &= det(\hat{g}_{\mu\nu}) = - \left(\frac{R}{R'} \right)^8 \end{aligned} \tag{2.15}$$

Plugging the expression of $\hat{g}$ in Eq. 2.12 we obtain:

$$S_5 = \int d^5x \left(\frac{R}{R'} \right)^4 \delta(z - R') \mathcal{L}_{\text{H}} \tag{2.16}$$

Keeping in mind the property of tensors:

$$\hat{g}_{\mu\nu} = \left(\frac{R}{R'} \right)^2 \eta_{\mu\nu} \quad \Rightarrow \quad \hat{g}^{\mu\nu} = \left(\frac{R'}{R} \right)^2 \eta^{\mu\nu} \tag{2.17}$$

We can replace $\hat{g}^{\mu\nu}$ in the expression of $\mathcal{L}_{\text{H}}$ in Eq. 2.13, and rewrite the 5D action as:

$$S_5 = \int d^5x \left(\frac{R}{R'} \right)^4 \delta(z - R') \left[\left(\frac{R'}{R} \right)^2 \eta^{\mu\nu} \partial_\mu \text{H}^* \partial_\nu \text{H} + \lambda \left(|\text{H}|^2 - \frac{v^2}{2} \right)^2 \right] \tag{2.18}$$

At energies below $1/R' \sim$ TeV, we are not sensitive to the extra dimension, so the physics should be adequately described by a 4D effective field theory (EFT). To get this EFT, all we have to do is integrate the action over the extra dimension. The action after the integration along z is then:

$$
\begin{aligned}
S_4 &= \int d^4x \mathcal{L}_{\mathrm{H}}^{4D} \\
&= \int d^4x \left(\frac{R}{R'}\right)^2 \partial_\mu \mathrm{H}^* \partial^\mu \mathrm{H} + \left(\frac{R}{R'}\right)^4 \lambda \left(|\mathrm{H}|^2 - \frac{v^2}{2}\right)^2
\end{aligned}
\tag{2.19}
$$

The Higgs kinetic term of the 4D effective Lagrangian is not canonically normalized. We can then rescale the Higgs field:

$$
\mathrm{H} \to \left(\frac{R}{R'}\right) \mathrm{H} \quad \Rightarrow \quad \mathcal{L}_{\mathrm{H}}^{4D} = \partial_\mu \mathrm{H}^* \partial^\mu \mathrm{H} + \lambda \left(|\mathrm{H}|^2 - \frac{\tilde{v}^2}{2}\right)^2 \tag{2.20}
$$

where $\tilde{v} = v\frac{R}{R'}$ is the 4D Higgs vacuum expectation value (VEV). $\tilde{v}$ is "warped down" by the factor $\frac{R}{R'}$ with respect to v, the 5D Higgs VEV. The value of v, to which μ is proportional (Eq. 1.23), can also be large, even $\sim M_{\mathrm{Pl}}$, and the small value of the Higgs mass would be a consequence of the warping.

To obtain the observed value of the Higgs mass, the value of $\frac{R}{R'}$ should be $\sim 10^{-18}$. Such a large difference between R and R' may sound unnatural, but the RS framework provide also a mechanism to naturally stabilize the distance between the two branes, known as the Goldberger and Wise mechanism [24]. This mechanism uses a bulk scalar field with a z-dependent VEV that generates a potential that stabilize the distance between R and R'. The potential causes the scalar field introduced by the KK theory, the radion (ϕ), to have a mass. With reasonable values for the scalar potential, the size of the extra dimension is large enough to solve the hierarchy problem.

In the next Sections we will introduce a realistic construction of a WED model which, besides solving the hierarchy problem, predicts the existence of new resonances decaying in the cascade process we are interested in.

2.2.1 Complete 2-branes WED model

In the previous section we introduced the fundamental ideas at the base of a WED model. We saw also, in a simplified model, how this approach can solve the hierarchy problem by confining the Higgs field on the IR brane while the gravity can propagate in the bulk. A realistic construction of a WED model, including all the SM fields and consistent with the electroweak precision constraints has been provided by Agashe, Delgado, May, and Sundrum in 2003 [25].

In this representation, each 4D SM field arises from a KK decomposition (see Appendix A) of a 5D field, like for the ADD model. All the SM fields have a profile in the extra dimension which indicates where the field is localized (Fig. 2.2): the Higgs and the top fields are assumed to be localized on the IR brane, the light fermions are localized on the UV brane and the SM gauge fields can propagate in the whole space.

This configuration solves the hierarchy problem since, as shown in the previous section, the Higgs field is confined on the IR brane, and its VEV is warped down by the $\frac{R}{R'}$ factor. The propagation of fermion fields in the bulk provides also an

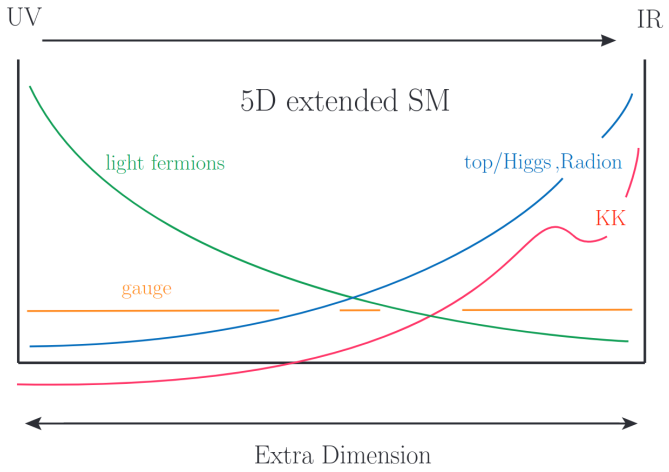

Figure 2.2. Schematic view of the propagation of particle fields in the bulk of a space with a warped extra dimension (figure from Ref [26]). The Higgs and top fields are localized on the IR brane, while the light fermion fields are localized on the UV brane, providing an explanation for the flavor puzzle. All the SM gauge fields can propagate in the bulk. The schematic shapes of extra-dimensional wavefunctions for a generic KK mode and for the radion are also shown.

explanation for the flavor puzzle (see Sec. 1.4). The different masses of fermions arise by the different overlap between the Higgs and the fermion fields in the extra dimension. The top field, localized on the IR brane, has a large overlap with the Higgs field, therefore the top quark mass is large (with respect to that of other fermions). The light fermions fields, instead, are localized on the UV brane, therefore their overlaps with the Higgs field are lower, and their masses are smaller.

From the KK decomposition of each of the 5D fields an infinite tower of particles (KK modes) is generated. The mass separation between two KK mode is proportional to $1/R'$, where ΔR is the distance between the two branes $\Delta R = R' - R$. The SM particles correspond to the lightest modes of this KK decomposition. Since $\Delta R \sim R'$ is such that $1/R' = O(\text{ TeV})$, the mass of first KK mode above the SM field is at the TeV scale. Because of their large masses, the 4D fields of the KK modes are localized near the IR brane like the Higgs field.

Finally, we have the additional massive scalar from the KK theory, the radion, which acquires a mass with the Goldberger and Wise mechanism. The radion is also localized near the IR brane, thus its mass is generically of the order of the IR brane scale. However, with mild tuning, the radion mass can be arranged to be a factor of few below the mass of the first KK mode: $O(0.1\,\text{TeV})$-$O(1\,\text{TeV})$.

The new KK particles can be, in principle, produced and detected in experiments at pp colliders like the LHC. The most striking signature would be the production of a KK gluon (G_{KK}), the KK mode of the SM gluon field, and its decay in the process $q\bar{q} \to G_{KK} \to q\bar{q}$ [26]. The production cross sections for the KK modes of W and Z bosons (W_{KK}, Z_{KK}) are lower with respect to the G_{KK} cross section by a factor g_Z/g_{QCD}.

The G_{KK} production cross section at the LHC, however, is still suppressed due to the small coupling of the G_{KK} to the proton constituents (up and down

quarks). The G_{KK} production cross section, from the assumptions made in Ref. [26], is $\sigma(q\bar{q} \to G_{KK}) \sim 0.1\,\text{pb}$ for $m(G_{KK}) \sim 3\,\text{TeV}$, while it decrease to $\sim 10\,\text{fb}$ for $m(G_{KK}) \sim 5\,\text{TeV}$. Moreover, since the top is peaked on the IR brane, the KK gluons decay almost exclusively to $t\bar{t}$ (ditop) with a Branching Ratio ($\mathcal{B}$) above 90%.

The constraints for the KK gluon come from both ditop [27, 28]) and dijet searches [29, 30] from ATLAS and CMS. In particular the ditop search provides the strongest limits, excluding a KK gluon with $m(G_{KK}) < 4.5\,\text{TeV}$, while the upper limit on $m(G_{KK})$ from the dijet search is at most $\sim$3.7 TeV.

Another signature from this RS model is the decay of the graviton into two partons, gg or $q\bar{q}$. In Sec. 3.1 we will see that this process is currently studied by dijet searches. However, the sensitivity to the graviton decay into two partons is drastically lower with respect to the sensitivity of the ditop search on the KK gluon decay.

2.2.2 Extended 3-branes WED model

The strong constraints on the masses of the G_{KK} and new particles, set by experiments at the LHC, could imply that the masses of the new particles are above the LHC reach. Alternatively, the new particles could be lighter than the LHC bounds, but they evade the searches in the dijet and ditop channels because they decay to other final states to which the current searches are not sensitive or not optimized for. Such a situation motivates dedicated searches for non-standard signals, like the one proposed in this thesis.

In particular, in an extension of the 2-branes WED model, proposed by Agashe et al. in 2017 [31], it is possible to get around with the bounds on KK gluon, and in general on KK gauge bosons from standard searches. The extension consists in the addition of an intermediate brane between the IR and the UV branes, as shown in Fig. 2.3.

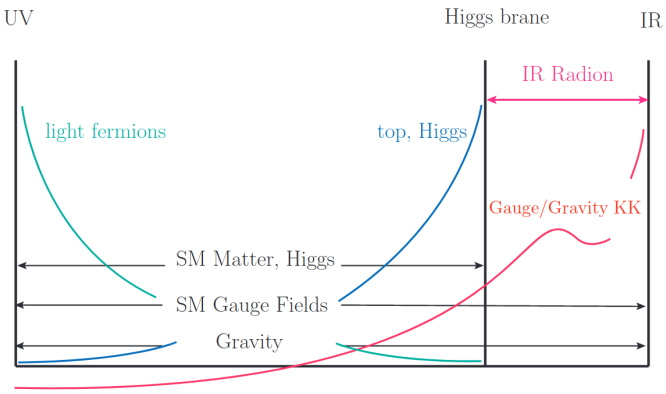

Figure 2.3. Warped extra-dimensional model with 3 branes along the extra dimension from Ref. [26]. Schematic shapes of extra-dimensional wavefunctions for various particles (zero mode SM fermions and gauge bosons, an IR radion, and gauge/gravity KK modes) are shown. The arrows indicate that the associated gauge fields propagate within the marked range in the extra dimension.

In this case the light fermions, the Higgs, and the top fields are allowed to

propagate only in the portion of the bulk within the UV brane and the intermediate brane, also called Higgs brane. The Higgs brane energy scale is set to $\Lambda' \gtrsim O(10\,\text{TeV})$, close to that of the IR brane of the standard scenario (remember that the distance in the extra dimension is connected with the energy scale by $R \sim 1/\Lambda$). Only the radion, the KK gauge fields, and the gravity are allowed to propagate in the extended bulk between the Higgs and the IR brane.

This setup retains the solution to the hierarchy and the flavor problems, but suppresses the overlap, and then the couplings, between the KK modes and the top/Higgs. As a consequence, the decay of G_{KK} to $\text{t}\bar{\text{t}}$ is suppressed, relaxing the constraints on the KK gluon from ditop and dijet limits. Another direct consequence of this extension is that a new class of processes becomes dominant, and offers new handles for the search for KK resonances at colliders.

These new processes consist in the production of a KK gauge boson A_{KK} which decays to a radion ϕ and a SM gauge boson A. The radion itself then decays to two SM gauge bosons. The process is then $\text{q}\bar{\text{q}} \to A_{\text{KK}} \to \phi + A \to AAA$, and it is shown in Fig. 2.4. For simplicity we refer to the $A_{\text{KK}} \to \phi A$ decay channel as the radion channel. The first SM boson from the A_{KK} decay can also be different from the pair of SM bosons from the radion decay.

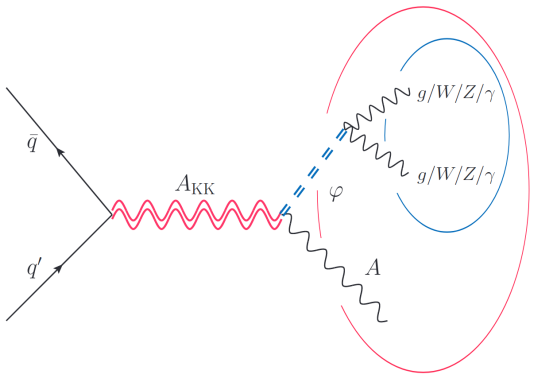

Figure 2.4. Feynman diagram for the cascade decay process in a 3-brane WED model (diagram from Ref [26]). The two new particles produced originates a final state with two resonances, highlighted by a blue (radion) and a red (KK gauge boson) circles. In the diagram A stands for any one among g, W, Z, γ.

As can be deduced from Fig. 2.4, three types of (new) couplings are relevant in the signal processes: (1) the KK gauge bosons coupling to SM quarks, (2) the KK gauge boson coupling to a radion and a SM gauge boson, and (3) the radion coupling to a pair of SM gauge bosons. The KK gauge boson coupling to SM fermions has the form:

$$\delta\mathcal{L}_{(1)} = Q_A^2 \frac{g_A^2}{g_{AKK}} A^\mu_{\text{KK}} \overline{\psi} \gamma_\mu \psi \tag{2.21}$$

where g_A and g_{AKK} are respectively the SM and KK gauge couplings for gauge bosons A and A_{KK}, and Q_A denotes the charge of the SM fermion ψ for the SM gauge field of A.

Second, the KK gauge boson coupling to a radion and a SM gauge boson is of the form:

$$\delta\mathcal{L}_{(2)} = \epsilon g_{\text{grav}} \frac{g_A}{g_{AKK}} \frac{\phi}{m_{\text{KK}}} A_{\mu\nu} A^{\mu\nu}_{\text{KK}} \tag{2.22}$$

where g_{grav} is the KK gravity coupling and m_{KK} is the mass of KK gauge boson, $A^{\mu\nu}_{\text{KK}}$ is the field strength tensor for the KK gauge boson A_{KK}. Finally, the radion coupling to a pair of SM gauge bosons has the structure of:

$$\delta\mathcal{L}_{(3)} = -\frac{1}{4}\left(\frac{g_A^2}{g_{AKK}}\right)^2 \frac{g_{\text{grav}}}{m_{\text{KK}}} \phi A_{\mu\nu} A^{\mu\nu} \tag{2.23}$$

In the equations above, g_{grav} and g_{AKK} couplings are free parameters of the theory. Their values have the following constraints from the theoretical assumptions described in [31]:

$$3 \lesssim g_{AKK} \lesssim 6 \quad 1 \lesssim g_{\text{grav}} \lesssim 6. \tag{2.24}$$

As mentioned above, A_{KK} can be any of the KK gauge bosons: a KK photon (γ_{KK}), a KK gluon (G_{KK}), a KK W (W_{KK}) or a KK Z (Z_{KK}). Each of them can decay via the radion channel, but also into two fermions or two SM bosons, depending on the type of the KK boson. The latter decays are covered by standard searches at the LHC, and sets limits on the masses of the new particles. The decay channels that provide the strongest limits on the KK boson masses are summarized in Tab. 2.1.

Table 2.1. Limits on KK gauge boson masses from searches in decays into two SM particles.

KK gauge boson	**decay channel**	**current limit**
γ_{KK}	dilepton	$m_{\gamma\text{KK}} \gtrsim 2\,\text{TeV}$ for $g_{\gamma\text{KK}} \sim 3$
G_{KK}	ditop	$m(\text{G}_{\text{KK}}) \sim 2\,\text{TeV}$ for $g_{\text{GKK}} \sim 3.5$
W_{KK}	$\text{W}_{\text{KK}} \to l\nu$	$m_{\text{WKK}} \gtrsim 2.5\,\text{TeV}$ for $g_{\text{WKK}} \sim 3$
Z_{KK}	dilepton	$m_{\text{ZKK}} \gtrsim 2.5\,\text{TeV}$ for $g_{\text{ZKK}} \sim 5$ & $m_{\text{ZKK}} \gtrsim 3\,\text{TeV}$ for $g_{\text{ZKK}} \sim 3$

In the 3-branes model the branching fraction of the radion channel is dominant, with $\mathcal{B} \sim 40 - 80\%$ for $g_{\text{grav}} > 3$, depending on the KK particle considered. This motivates dedicated searches for KK gauge bosons decays in this channel. The new experimental signature, with two resonances produced, offers new opportunities to develop dedicated strategies to disentangle the signal from the large background that typically characterize standard searches.

Additional constraints to this 3-branes model come from the bounds on the radion mass. The radion can be produced in pp collisions via gluon fusion and can decay to a pair of SM gauge bosons. To leading order, the radion decay width to a couple of vector bosons is given by:

$$\Gamma(\phi \to AA) = N_A g_{\text{grav}}^2 \left(\frac{g_A}{g_{AKK}}\right)^4 \left(\frac{m(\phi)}{m(A_{\text{KK}})}\right)^2 \frac{m(\phi)}{64\pi} \tag{2.25}$$

where $m(\phi)$ is the radion mass and N_A is number of degrees of freedom of SM gauge boson: 8 for gluon, 2 for W, and 1 for γ and Z. The radion decay branching fractions are determined by the relative size of KK gauge couplings. Numerically, the branching fractions to, $\gamma\gamma$, ZZ, WW, and gg are roughly $O(0.1)\%$, $O(1)\%$, $O(1)\%$, and $O(95)\%$ assuming $g_{\gamma\text{KK}} \sim 2$ and $g_{\text{gKK}} = g_{\text{WKK}} = 6$ (like in the SM, the value of g_{ZKK} depends on the other KK couplings). Although the diphoton channel has the smallest branching ratio in most of the parameter space of interest, the cleaner nature of photonic final states with respect to that of diboson or dijet ones leads to the most stringent bounds for the radion. The diphoton searches [32, 33] performed by the ATLAS and CMS Collaborations sets upper limits on the production cross section of a radion to 0.7 (0.4) fb for a radion mass of 1 (1.5) TeV. These limits exclude radion masses below ∼1 TeV.

Nevertheless, the hypothesis of a light radion, below 1 TeV, cannot be fully excluded. In the next Section we will see an alternative 3-brane model, for which the results of the diphoton searches cannot be applied to the radion, allowing it to be lighter than the aforementioned limit.

2.2.3 Extended 3-branes WED model: only QCD in extended bulk

In a later formulation of the 3-brane model, proposed by Agashe et al. in Ref. [34], the limits on the radion mass from diphoton searches are bypassed by assuming that only QCD (i.e. the SM gluon field) can propagate in the extended bulk, as in Fig. 2.5. Since the radion is confined in the extended bulk, in this case it can only couple with gluons. The decay of the radion in two photons is not allowed, and $\mathcal{B}(\phi \to \text{gg}) = 100\%$.

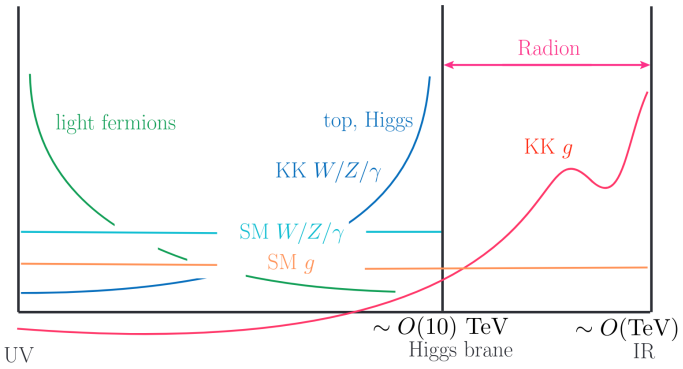

Figure 2.5. Alternative version of an RS model with 3 branes along the extra dimension. Unlike the model shown in Fig. 2.3, only the SM gluon field can propagate in the extended bulk. In this framework, the decay $\phi \to \gamma\gamma$ is not allowed, and the constraints on ϕ mass from diphoton searches does not hold anymore.

In the rest of the paper we will focus on this extension of the model, and in particular on the KK gluon, which has only three decay channels, the radion, the dijet and ditop channels, with the following decay widths:

$$\Gamma(\mathrm{G_{KK}} \to \phi \mathrm{g}) \approx \left(\epsilon \mathrm{g_{grav}} \frac{\mathrm{g_g}}{\mathrm{g_{GKK}}}\right)^2 \left[1 - \left(\frac{\mathrm{m}(\phi)}{\mathrm{m}(\mathrm{G_{KK}})}\right)^2\right]^3 \frac{\mathrm{m}(\mathrm{G_{KK}})}{24\pi} \tag{2.26}$$

$$\Gamma(\mathrm{G_{KK}} \to \mathrm{q\overline{q}}) \approx \left(\frac{\mathrm{g_g^2}}{\mathrm{g_{GKK}}}\right)^2 \frac{\mathrm{m}(\mathrm{G_{KK}})}{24\pi} \tag{2.27}$$

where $\mathrm{q\overline{q}}$ in Eq. 2.26 refers to either a pair of light quarks-antiquarks or to a top-antitop pair, since in this extension of the model the $\mathrm{G_{KK}}$ coupling is the same for all the SM quarks. The values of the couplings g_{grav} and g_{GKK}, which are bounded as in Eq. 2.24, modify the the decay widths and the branching fractions ($\mathcal{B}$) of the various channels. An increase of g_{grav} enhances the $\mathcal{B}$ of the $\mathrm{G_{KK}}$ decay to ϕg, while an increase of g_{GKK} reduces the decay width in both the equations above, without altering the branching fractions. Since g_{GKK} also appears in the denominator of the $\mathrm{G_{KK}}$ coupling to quarks (Eq. 2.21), the $\mathrm{G_{KK}}$ production cross section is inversely proportional to g_{GKK}. The dependence of the cross section σ of the process $\mathrm{q\overline{q}} \to \mathrm{G_{KK}} \to \phi\mathrm{g}$ from the g_{GKK} and g_{grav} couplings is shown in Fig. 2.6, for a specific choice of the other couplings of the model.

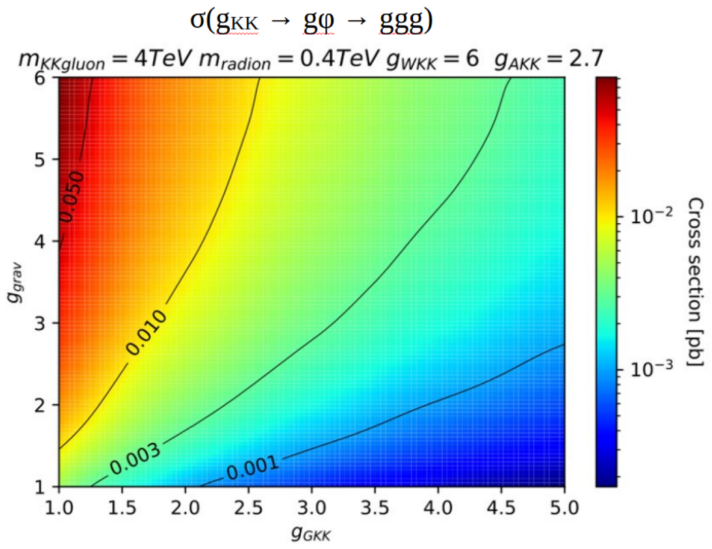

Figure 2.6. Cross section of the process $\mathrm{q\overline{q}} \to \mathrm{G_{KK}} \to \phi\mathrm{g}$ as a function of the couplings g_{grav} and g_{GKK}. The values are obtained for a specific choice of the other couplings of the theory and of the $\mathrm{G_{KK}}$ and ϕ masses.

For the benchmark model adopted for our search we use the following set of couplings:

$$g_{\mathrm{grav}} = 6.0 \quad g_{\mathrm{GKK}} = 3.0 \quad g_{\mathrm{WKK}} = 6.0 \quad g_{\gamma\mathrm{KK}} = 2.7 \tag{2.28}$$

which is a configuration that maximize the production of $\mathrm{G_{KK}}$ and the branching fraction of its decay in the radion channel $\mathcal{B}(\mathrm{G_{KK}} \to \phi\mathrm{g})$ assuming the constrains mentioned above. For this choice of couplings $\mathcal{B}(\mathrm{G_{KK}} \to \phi\mathrm{g})$ is between 50 and 60%

for all the values of $m(\mathrm{G_{KK}})$ and $m(\phi)$ considered, while the rest of the decays are $\mathrm{G_{KK}} \to \mathrm{q\overline{q}}$.

In this particular extension of the model considered, since the radion can only decay into two gluons, the final state is formed by three gluons. The peculiar decay kinematics of this process can generate different final state topologies, depending on the ratio (ρ_{m}) between the masses of the radion and the KK gluon: $\rho_{\mathrm{m}} = m(\phi)\,/m(\mathrm{G_{KK}})$. The different topologies will be described in detail in Sec. 3.3. The characteristics of the final state can be exploited to enhance the sensitivity of our search to $\mathrm{G_{KK}}$ signals, with respect to the dijet and ditop searches. Chapter 7 is dedicated to the illustration of our analysis strategy, expressly designed for this purpose.

The search proposed here covers only one of the possible signatures that can arise from WED models. Currently, there are ongoing efforts within the CMS experiment to search for other exotic signatures from WED models. In particular, here we mention the recently published CMS results [35, 36], which consider a 3-branes model, like the one shown here, but allowing only the electroweak (EW) gauge bosons to propagate in the extended bulk. These analyses then set limits on the production cross section of a KK W boson studying the decay $\mathrm{W_{KK}} \to \phi + \mathrm{W} \to \mathrm{WWW}$, and explore an extension of the WED model that is complementary to the one considered in this thesis.

Chapter 3

Searches for hadronic resonances at the LHC

In this Chapter we discuss the experimental context of searches for hadronic resonances at the LHC.

The experimental signature of a resonance is generally represented by a peak in the distribution of the reconstructed invariant mass of its decay products. The position of the peak in the distribution corresponds approximately to the resonance mass, while its width is given by the convolution between the "natural" resonance width and the instrumental resolution.

Hadronic resonances interacts via the strong force, are directly coupled with quarks and gluons, and decay into final states with jets. In Sec. 3.1 we will show the latest results from CMS and ATLAS searches for resonances decaying into two jets (dijet). As we will see, this is a "golden" channel for the search for hadronic resonances.

In Sec. 3.2 we will report the latest results from searches for resonances decaying to a $t\bar{t}$ pair. These searches, besides setting limits on the 2-branes WED model presented in Sec. 2.2.1, are an example of how the characteristics of the jets allow us to distinguish between signal and background events, reducing the large QCD multijet background which typically affects dijet searches.

In the last Section, 3.3, we will describe the kinematic of the signal process under study, which involves the production of two new hadronic resonances that decay in cascade. We will also define the final-state topology of signals searched by our analysis. Such new experimental signatures derive from models of new physics addressing the hierarchy problem, like the WED model introduced in Sec. 2.2.3.

3.1 Dijet searches

Dijet searches are strongly relevant for physics at the LHC, mainly because any new particle that can be produced through the interaction of two partons can also decay into two partons, which hadronize to form two jets detectable by the experiments. It is possible to fully reconstruct the new particle mass from the invariant mass of the two-jet system, the dijet mass (m_{jj}). As mentioned above, the presence of a new dijet resonance would produce a striking signature, represented by a bump on the smoothly falling dijet mass spectrum that arises from SM QCD multijet processes (Fig. 3.1). For these reason dijet resonances have been widely searched at the LHC, in a mass range from ∼100 GeV to several TeV.

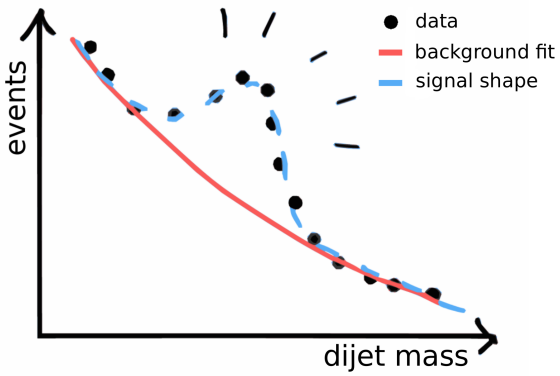

Figure 3.1. Sketch of a typical signature from a dijet resonance.

Another advantage of dijet searches is that, by analyzing a relatively simple signature with only two jets in the final state, it is possible to test a wide range of theories Beyond the Standard Model (BSM). Examples of BSM dijet resonances are: excited quarks [37], axigluons and colorons [38, 39], color-octet scalars [40], new Z' and W' gauge bosons [41], scalar diquarks [42], string resonances [43], Randall–Sundrum (RS) gravitons and Kaluza–Klein (KK) gauge bosons (from the WED model introduced in Sec. 2.2), and Dark matter (DM) mediators [44, 45, 46].

The dijet mass spectrum has been extensively studied in recent decades, from the UA1 and UA2 experiments in the '80s, which used data from the $p\bar{p}$ collisions at the CERN $Sp\bar{p}S$ collider ($\sqrt{s} = 0.63$ TeV), to the searches in the 0.1–1 TeV mass range with the CDF and D0 experiments at the Fermilab Tevatron ($\sqrt{s} = 1.8$ and 1.96 TeV), to the current searches at the TeV mass scale and above with the CMS and ATLAS experiments at the CERN LHC ($\sqrt{s} = 13$ TeV). The basic feature of the analysis technique has remained very similar over the years, consisting in the scan of the dijet mass spectrum looking for resonance peaks.

In Secs. 3.1.1 and 3.1.2, we will report the latest ATLAS and CMS dijet searches, respectively for high ($\gtrsim$1 TeV) and low ($\lesssim$1 TeV) mass resonances. We will discuss some innovations introduced in the analysis techniques with respect to previous analyses, and will summarize the analyses results.

3.1.1 High-mass range

The latest ATLAS and CMS searches for high mass dijet resonances, respectively reported in Refs. [29] and [30], use the full LHC Run 2 dataset corresponding to an integrated luminosity of $\sim$140 fb^{-1} of pp collisions at a center-of-mass energy of 13 TeV. This is currently the largest dataset available with the highest collision energy, therefore it is the most suitable to search for high-mass resonances.

The analysis technique is similar for the two analyses. The final state partons are reconstructed as jets using the technique that we will describe in Sec. 5.2. The events are selected, among all the events produced in an LHC bunch crossing, by triggers requiring the presence of one or more jets with high transverse momentum, p_{T}, typically above several hundreds of GeV.

The two jets in the event with the largest p_{T} are defined as the leading jets. An offline selection is also applied to events, requiring the jets $\vec{p}_{\mathrm{T}}$ to be back-to-back, as consistent with a two-body decay. In addition to this, the requirement $|\Delta\eta_{\mathrm{jj}}| \lesssim 1.1\text{-}1.2$ is applied to reduce the background from QCD multijet processes, which is mostly concentrated at large values of $|\Delta\eta_{\mathrm{jj}}|$. The dijet mass of the two jets is also required to be above a certain threshold, which is $m_{\mathrm{jj}} > 1.5$ TeV for the CMS search and $m_{\mathrm{jj}} > 1.1$ TeV for the ATLAS one. This selection is necessary because the trigger requirements on the jets p_{T} reduce the efficiency at low m_{jj}, significantly reducing the analysis sensitivity for m_{jj} below $\sim$1 TeV.

The m_{jj} spectra of events from signal processes (the signal shapes) are usually modeled with Monte Carlo (MC) simulations. The smoothly-falling spectrum in m_{jj} from the QCD multijet background, instead, is estimated with data-driven methods. The data-driven approach for the background modelling is robust, insensitive to the theoretical uncertainty that affects the simulation, and agnostic with respect to the theoretical model underlying the m_{jj} distribution of background events. The most common method for the background estimation, which will be used also in the search presented in this thesis, consists in parameterizing the m_{jj} distribution of QCD multijet background events with an empirical function describing a smoothly-decreasing spectrum. For both the searches described here the function chosen is:

$$\frac{d\sigma}{dm_{\mathrm{jj}}} = \frac{p_0(1-x)^{p_1}}{x^{p_2+p_3\ln(x)}} \tag{3.1}$$

where $x = m_{\mathrm{jj}}/\sqrt{s}$ and p_0, p_1, p_2, p_3 are free parameters. A fit using this background parameterization and the signal shape obtained from the simulation is performed directly on data, where the four background parameters are treated as unconstrained nuisance parameters and the empirical function is then adapted to data. The compatibility of the data with the background-only description is shown by fits to the m_{jj} spectrum under only the background hypothesis, which are shown in Fig. 3.2 for the two analyses here considered.

The resonances foreseen in the theoretical model described above can decay into three possible final states: quark-quark (qq), quark-gluon (qg) and gluon-gluon (gg). The signals from the three decays are separately considered in the CMS analysis, because the resonance peak has different shapes in the three cases. The signal shape of a gg resonance is wider with respect to that of a qq one, because gluons have

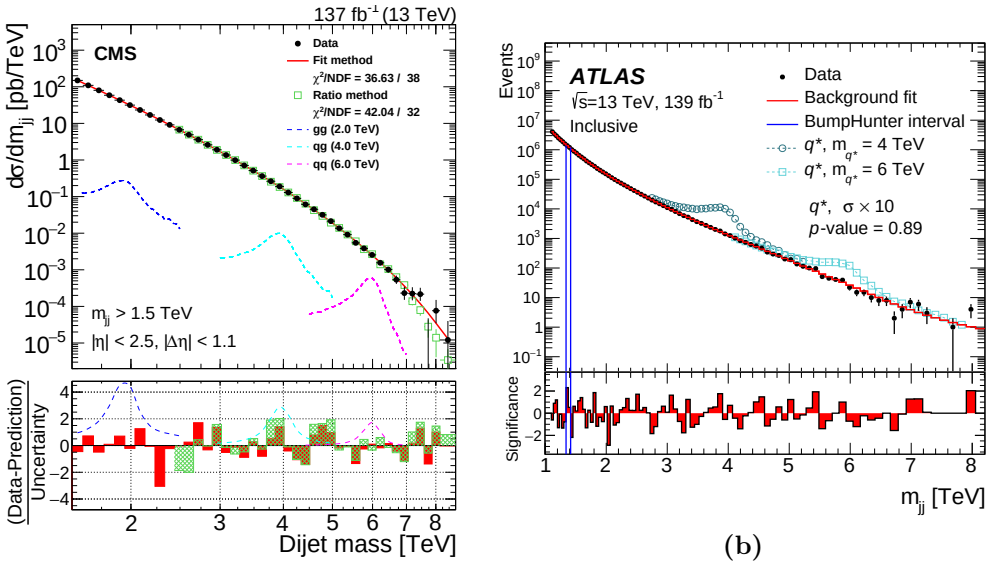

Figure 3.2. Dijet mass spectrum (points) compared to the background predictions from fits (solid line) for the latest (a) CMS [30] and (b) ATLAS [29] high-mass dijet searches. The lower panels show the difference between the data and the background predictions, divided by the statistical uncertainty in the data. For the CMS search, the background prediction from the ratio method is shown with green squares, together with examples of predicted signals from narrow qq, qg, and gg resonances. For the ATLAS search, signals from the decay of an excited quark (q^*) are shown for a cross section 10 times larger than the expected one, σ, while vertical lines mark the interval with the most significative local excess (not compatible in this case with a resonance hypothesis), evaluated with the BumpHunter algorithm [47, 48].

larger probability to split during the parton branching phase with respect to quarks, leading to a worse jet energy resolution. The qg resonance peak has an intermediate width between the first two.

Moreover, the CMS analysis uses an additional data-driven method to fit the background, called ratio method. A signal region (SR) and a control region (CR) are defined applying an event selection based on $|\Delta\eta_{jj}|$. The prediction for the QCD multijet background in the SR is then obtained by multiplying the data in the CR by a transfer factor determined from the QCD multijet background simulation. The ratio method yields similar results with respect to the fit method.

Besides performing the standard dijet search, the ATLAS analysis also define event categories selecting jets originating from the decay of a hadron containing a b quark (b-hadron), using a technique called b-tagging. We will discuss this kind of searches in Sec. 3.1.3.

No significant excesses are observed in data and the analyses set 95% Confidence Level (CL) upper limits on the cross sections times the branching fraction and the acceptance for dijet signals. Figure 3.3a shows the CMS limits obtained for quark-quark, quark-gluon and gluon-gluon resonances using the fit method for $m_{jj} \leq 2.4\,\text{TeV}$ and the ratio method for $m_{jj} > 2.4\,\text{TeV}$. The cross sections expected from several new physics models are superimposed, in order to produce mass exclusion limits. The

limits from the ATLAS search on a signal with a generic Gaussian shape, instead, are reported in Fig. 3.3b with various relative widths of the Gaussian peak σ_X/m_X.

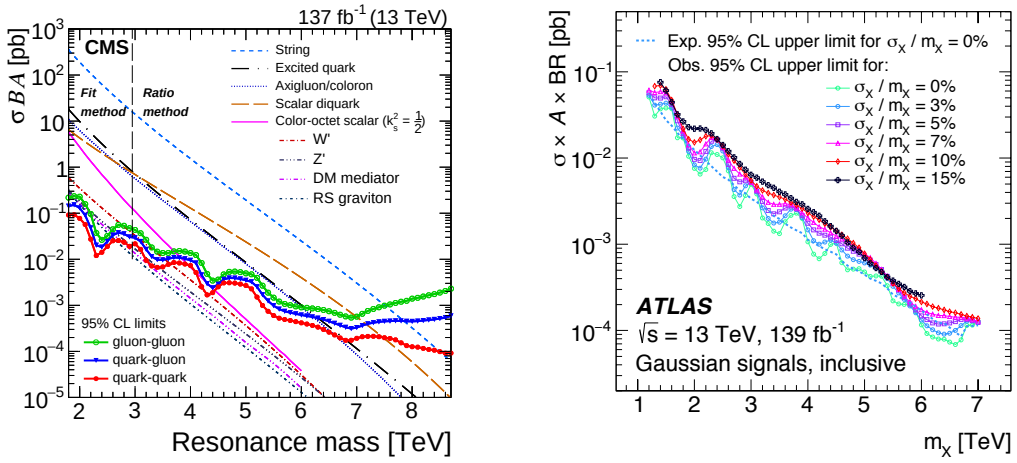

(a) (b)

Figure 3.3. (a) Observed 95% CL upper limits on the product of the cross section σ, branching fraction $\mathcal{B}$, and acceptance A for qq, qg, and gg type dijet resonances, from CMS analysis [30]. Limits are compared to predicted cross sections for the new resonances models mentioned above. The vertical dashed line indicates the boundary between the regions where the fit method and the ratio method are used to estimate the background. (b) The 95% CL upper limit on the cross-section times kinematic acceptance times branching ratio for resonances with a generic Gaussian shape, as a function of the Gaussian mean from ATLAS search [29]. Different widths, from 0% up to 15% of the signal mass, are considered. For a Gaussian-shaped signal with a relative width of 15%, the limits are truncated at high mass when the broad signal starts to overlap the upper end of the m_{jj} spectrum.

3.1.2 Low-mass range

The standard dijet analysis at the LHC are limited by the trigger requirements on the jets p_T, which reduce the trigger efficiency below a certain value of m_{jj}, which is $m_{jj} \lesssim 1.5$ and 1.1 TeV respectively for the CMS and ATLAS analyses discussed in the previous Section.

The trigger requirements are introduced because the limited bandwidth available (i.e. the data transfer rate to disk) does not allow to record all the events produced at the LHC. Moreover, the prompt reconstruction of an event, combining the information from the CMS subdetectors, takes time. For these reasons the CMS trigger (see Sec.4.2.7) selects only events with high-energetic jets, which are more interesting for high-mass searches, paying the price of a reduced efficiency for events with low m_{jj}.

In order to study also the low m_{jj} range, it is possible to get around this problem by reducing the size of the data recorded for each event. The CMS collaboration introduced in 2011 the "data scouting" technique [49, 50], where only the four-momenta of jets and leptons in each event are stored, reducing the average event

size from 500 kB to ∼5–10 kB. Later, also the ATLAS and LHCb collaborations developed similar techniques. The technique implemented by ATLAS is called trigger-object-level analysis (TLA). Only the four-momentum of each jet and a set of calorimeter variables associated with it are saved. The event size of these events is less than 0.5% of the size of full event. Due to the reduction of the event size, these techniques allow to lower the thresholds on jets p_{T} and increasing the efficiency at low m_{jj}.

The latest ATLAS and CMS dijet searches using these techniques can be found in Refs. [51] and [52] respectively. In these analyses, similar event reconstruction and fit methods of the corresponding high mass searches are used. The two datasets analyzed correspond respectively to an integrated luminosity of 29.3 and 27 fb^{-1}. The background-only fit to the dijet mass spectra from the two searches are shown in Fig. 3.4 in the m_{jj} ranges: $0.45 < m_{\mathrm{jj}} < 1.8$ TeV (ATLAS) and $0.6 < m_{\mathrm{jj}} < 1.6$ TeV (CMS).

ATLAS performs its search using two version of the event selection. In the standard selection the two jets are required to have $0.7 < m_{\mathrm{jj}} < 1.8$ TeV and $|\Delta\eta_{\mathrm{jj}}| < 1.2$ ($|y^*| < 0.6$). In the alternative selection, applied to a small portion of the data (3.6 fb^{-1}), events with $0.45 < mjj < 1.8$ TeV and $|\Delta\eta| < 0.6$ ($|y^*| < 0.3$) are selected. The more stringent choice of $|y^*| < 0.3$ selects higher-p_{T} jets at a given invariant mass and thus provides a mass distribution that is unbiased by the leading-jet selection from $m_{\mathrm{jj}} = 450$ GeV

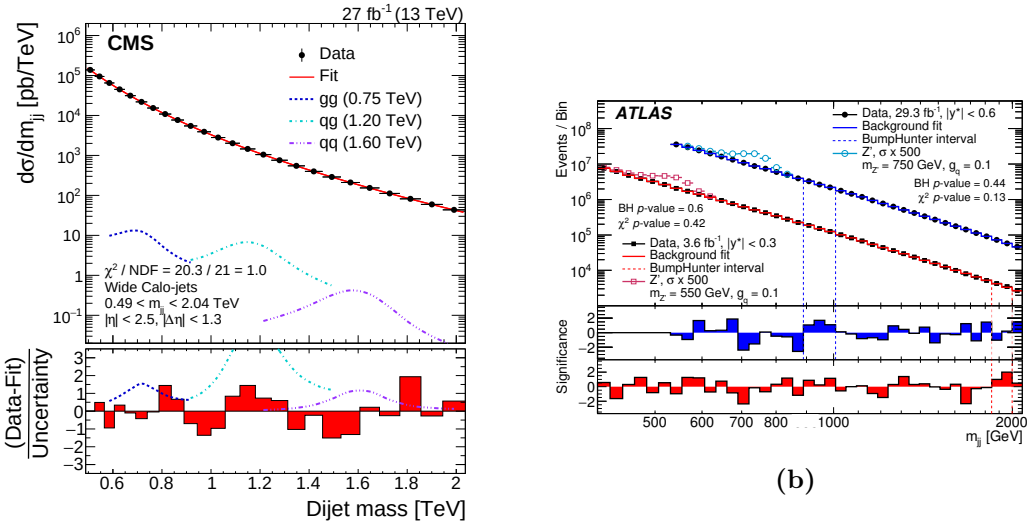

(a) (b)

Figure 3.4. Dijet mass spectra (points) compared to a fitted parameterization of the background (solid curve) for the low-mass search from (a) CMS [52] (b) and ATLAS [51]. The lower panels show the difference between the data and the fitted parameterization, divided by the data statistical uncertainty. For the CMS search, examples of predicted signals from narrow qq, qg, and gg with cross sections equal to the observed upper limits at 95% CL are shown. For the ATLAS search the most relevant excess found from the BumpHunter algorithm is delimited by the vertical lines.

With the two special datasets analyzed, the dijet searches are extended in the low-mass range. This is shown in Fig. 3.5, which compare limits from various dijet analysis on the universal coupling g_q' between a leptophobic Z′ boson and quarks.

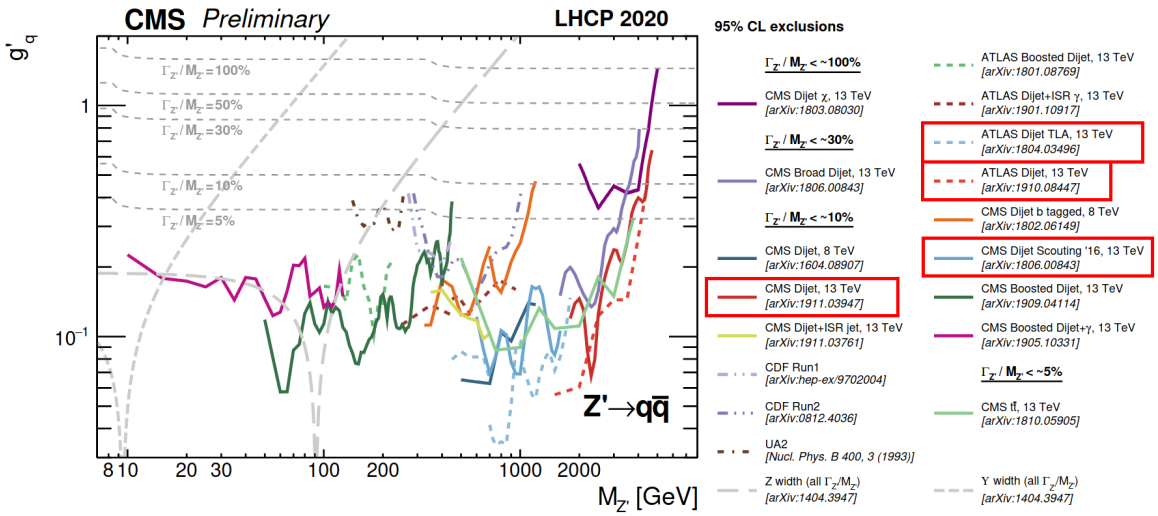

Figure 3.5. Limits on the universal coupling g_q' between a leptophobic Z′ boson and quarks [53] from various dijet analyses from CMS, ATLAS, CDF, and UA2. The expected limits are shown in dashed lines, and the corresponding observed limits are shown in solid lines. The hashed areas show the direction of the excluded area from the observed limits. The grey dashed lines show the g_q' values at fixed values of $\Gamma_{Z'}/M_{Z'}$, where $\Gamma_{Z'}$ is the decay width of the Z' and $M_{Z'}$ is its mass. The red boxes mark the dijet analyses reported in this Chapter.

3.1.3 Dijet searches with b-jets

Jets originating from the hadronization of a b-quark (b-jets) have peculiar features that distinguish them from jets originated by light quarks. The identification of b-jets (b-tagging) can significantly enhance the sensitivity to new resonances with a sizeable coupling to b-quarks, which decays into bg or $b\bar{b}$ pairs.

The b-hadrons contained in b-jets, in fact, have sufficient lifetime to travel some distance from the primary interaction vertex before decaying, producing a secondary vertex like in Fig. 3.6. It is possible, then, to identify b-jets by the displacement of this secondary vertex from the primary vertex.

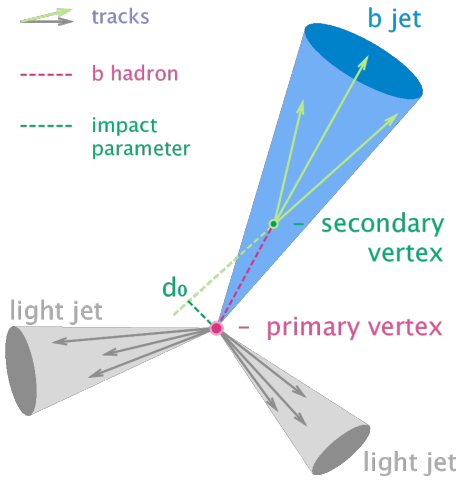

Figure 3.6. Diagram showing the common principle of identification of jets initiated by b-hadron decays. The secondary vertex is displaced with respect to the primary vertex.

The events can then be divided in categories requiring the presence of one or more b-tagged jets, reducing the background from SM QCD processes, which mostly produce jets from light quarks. The already mentioned ATLAS dijet search [29] also includes an event categorization based on the b-tagging, while the latest CMS search that apply this technique can be found in Ref. [54]. The two searches analyze the whole Run 2 dataset and adopt similar strategies for the event reconstruction and selections as the corresponding high-mass dijet searches. In Fig. 3.7 and 3.8 we report respectively the dijet mass spectra for the ATLAS and the CMS searches, for event categories requiring at least 1 b-tagged jet ($\geq$1 b-tag) or exactly 2 b-tagged jets (2 b-tag). The background is estimated through the same fit method used in high-mass dijet searches.

The CMS search separately analyzes events of the different years of data-taking, performing the fits with different fit functions. In Fig. 3.8, we show just the spectra for 2018 data.

The two analysis did not observe significant excesses with respect to the SM predictions, therefore they set limits on the couplings and masses of several resonances decaying to final states with one or more b-quarks.

To compare the b-tagged analysis with the inclusive dijet analysis, we show in Fig. 3.9 the limits from the ATLAS search on the production cross section of a Z' boson times its branching fraction into $b\bar{b}$, times the acceptance. The comparison

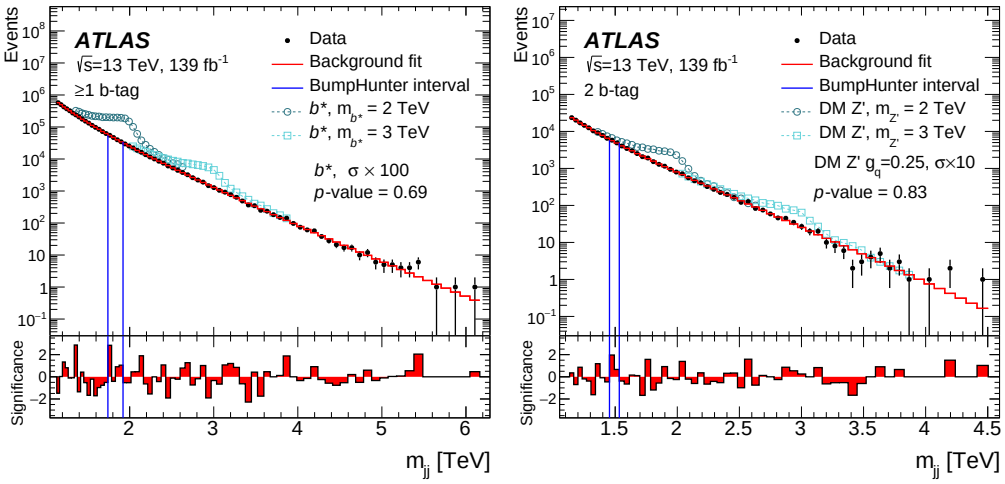

(a) (b)

Figure 3.7. Dijet invariant mass distributions from multiple categories of the ATLAS search of Ref. [29]: (a) dijet events with at least one b-tagged jet, (c) dijet events with both jets b-tagged. The vertical lines indicate the most discrepant interval identified by the BumpHunter test, for which the p-value is stated in the figure.

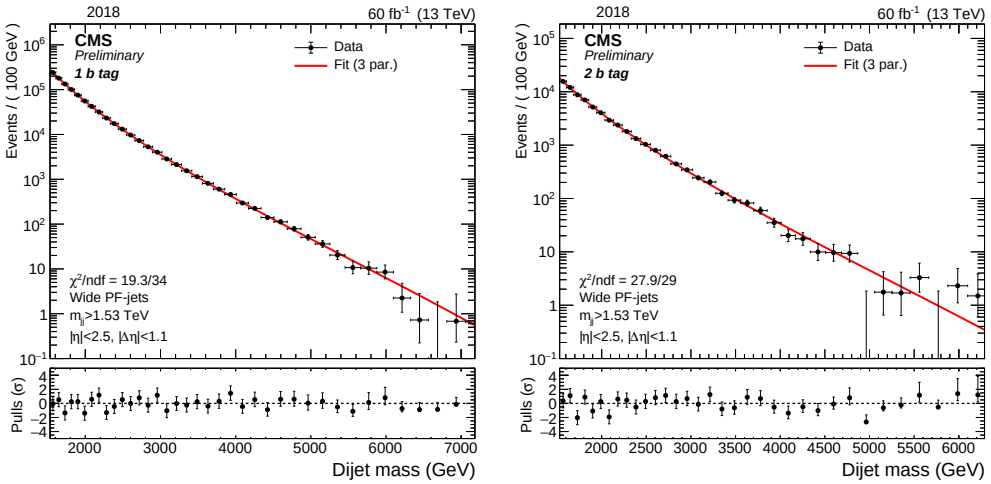

(a) (b)

Figure 3.8. Dijet mass distributions for 2018 data (points) for two categories: (a) dijet events with at least one b-tagged jet, (c) dijet events with both jets b-tagged. The background prediction from the fit with the 3-parameter function is also shown (red solid line). Spectra for 2016 and 2017 data (together with the plot reported here) can be found in Ref. [54].

with the theory exclude Z' masses below ∼3 TeV, for a value of the Z' coupling to SM quarks of $g_q = 0.25$. The ATLAS inclusive dijet search, reported in the same paper, excludes Z' up to ∼3.9–4.0 TeV for $g_q = 0.25$ (Fig. 3.9b).

The inclusive search puts a stronger constraint on the Z' mass with respect to the search with b-tagged jets. This effect arises from the drop of the b-tagging performance with the increase of the resonance mass. At high mass, in fact, also the p_T of the jets increases, and the b-jet tend to look like a jet from a light quark. For this reason, at high mass limits from b-tagged and inclusive searches are similar. However, it should be considered that the inclusive analysis is sensitive to all the possible decays of the Z' into two quarks, while the other considers only $Z' \to b\bar{b}$. Therefore the latter shows a similar sensitivity to Z' decays even if it analyzes a decay channel with a lower branching fraction. For new states with a larger branching ratio into b-quark final states, the b-tagged categories will have greater sensitivity.

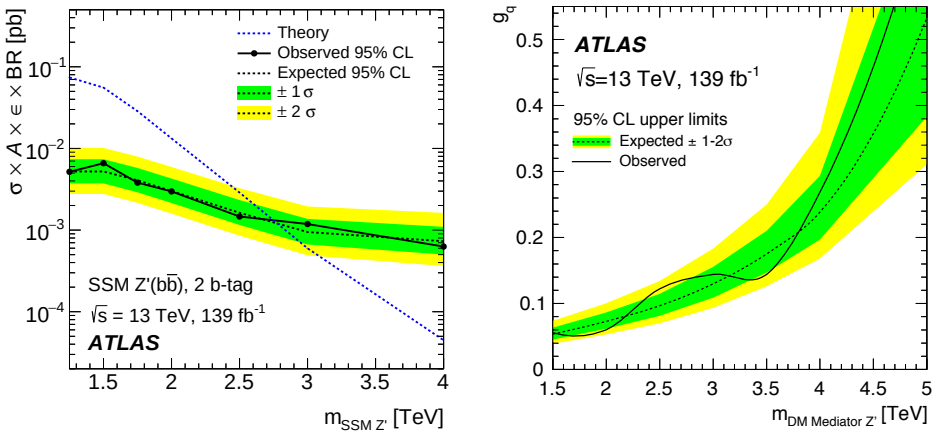

(a) 95% CL upper limit on the cross-section times acceptance times branching fraction of $Z' \to b\bar{b}$ from the ATLAS search [29] in the m_{jj} spectra of the 2 b-tag category.

(b) Upper limits on the Z' signal at 95% CL from the ATLAS inclusive dijet search [29]. The 95% CL upper limits are set on the universal quark coupling g_q as a function of the Z' mass.

Figure 3.9. Limits on the DM mediator Z' model from the dijet ATLAS search reported in Ref. [29]. The observed limits (solid) and expected limits (dashed) with $\pm 1\sigma$ and $\pm 2\sigma$ uncertainty bands are shown.

3.2 Ditop searches

In this Section we report the latest results from ATLAS and CMS searches for resonances decaying in a $t\bar{t}$ pair (ditop) [27, 28]. These searches are a good example of how the properties of the jets in the final state can be exploited to enhance the analyses sensitivity to a specific class of new physics signals with respect to standard dijet searches (in this case ditop resonances).

Such resonances, like dijet resonances, are foreseen by a large number of models. Examples of $t\bar{t}$ resonances are: the KK gluon (G_{KK}) from the 2-branes WED model introduced in Sec. 2.2.1, TeV scale color singlet Z' bosons [55, 56], pseudoscalar Higgs bosons [57], and leptophobic topcolor Z' bosons [58].

The decay to $t\bar{t}$ offers a wide range of possible final states. The top quark predominately decays to a W boson and a b-quark. Each of the two W bosons in the event can decay to either a lepton and its corresponding neutrino or to hadrons. Therefore, three decay channels can be considered for the $t\bar{t}$ system, depending on the decay modes of the W bosons:

- in the dilepton channel, both W bosons decay to an e or μ and a ν. The reconstructed dilepton final state consists then of two leptons ($\mu\mu$, ee, or μe) collimated with two b-jets with high p_T, and missing transverse momentum (p_T^{miss}) from the undetected neutrinos. The b-jets and the leptons are collimated because of the large Lorentz boost of the top quarks;

- the single-lepton channel consists of one lepton (μ or e), at least two high-p_T jets, and p_T^{miss}. The decay products of the $t\bar{t}$ pairs are also collimated for this channel;

- the fully hadronic channel contains events with a dijet topology, because the decay products of both the t-quarks are collimated and reconstructed as two large radius jets, with a distance parameter[1] of $R = 0.8$.

The CMS search, in particular, includes three independent sub-analyses for the three decay channels, while the ATLAS search reported above is focused only on the fully hadronic channel.

The QCD multijet background is generally lower for the dilepton and single-lepton channel, with respect to the fully hadronic channel, because the requirement of one or two leptons in the final state drastically reduces this background. Moreover, the remaining SM backgrounds can be modeled with appropriate precision with Monte Carlo simulations.

For the fully hadronic channel, it is still possible to reduce the QCD multijet background, which is irreducible for the standard dijet searches, by identifying jets from t-quark decays (t-jets). The t-jets have a mass compatible with that of a t-quark and a substructure formed by three sub-jets: two from the hadronic W decay and one from the hadronization of the b-quark.

The trajectories of the constituents of the jets and their masses are used, by the ATLAS and CMS searches, to design a t-tagging algorithm to identify t-jets in the

[1] see Sec. 5.2 for the definition of the distance parameter.

final state. The data can then be further divided into categories requiring a certain number of t-jets enhancing the searches sensitivity to ditop resonances.

The $t\bar{t}$ invariant mass ($m_{t\bar{t}}$) distributions of the categories are then scanned to search for excesses with respect to the background prediction. In Figs. 3.10 and 3.11 we report the fit to the $m_{t\bar{t}}$ spectra respectively from the ATLAS and the CMS search in the fully hadronic channel, for the categories requiring 1 or 2 b-tagged jets.

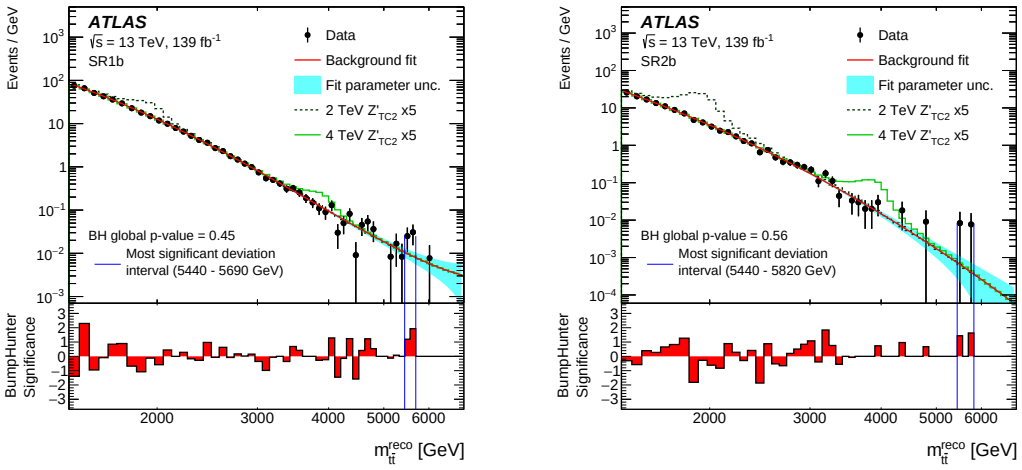

Figure 3.10. Observed $m_{t\bar{t}}$ distributions in data (points) for the 1 b-tag (left) and the 2 b-tag (right) categories from the ATLAS $t\bar{t}$ search [27]. The background prediction (solid line) is also shown, with signal shapes from 2 and 4 TeV mass resonances superimposed. The lower panel shows the significance of excesses in data with respect to the background prediction. Two vertical lines delimit the most significant deviation interval.

Also in this case, no excesses above the SM predictions has been found and the analyses set limits on the cross sections of various models. Here in particular we report the limits on the production cross section of a KK gluon from the CMS analysis, which exclude G_{KK} masses below 4.5 TeV.

The plot of Fig. 3.5 shows also the limits on the universal coupling g'_q between a leptophobic Z' boson and quarks from the CMS $t\bar{t}$ analysis. The $t\bar{t}$ analysis shows a similar sensitivity to Z' boson with respect to the inclusive CMS and ATLAS dijet searches. This is a good result since the branching fraction of the $Z' \to t\bar{t}$ decay is lower than the sum of the branching fraction of the Z' decay to the other quark/antiquark pairs, which are the final states searched by the dijet search. For new states with a larger branching ratio into t-quark final states, the t-tagged search will have greater sensitivity. Moreover the CMS $t\bar{t}$ analysis is also sensitive to lower masses of the Z' boson than the CMS dijet search.

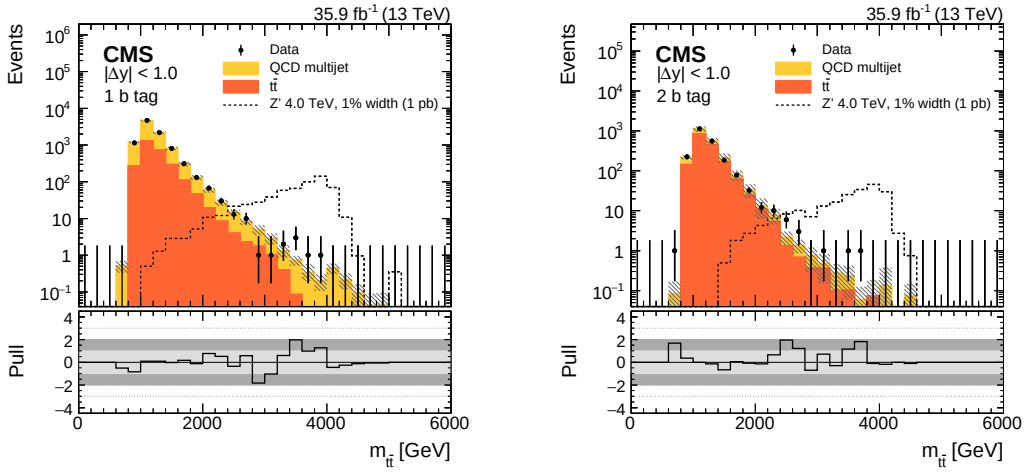

Figure 3.11. $t\bar{t}$ mass distributions for 2016 data (points) for two categories from the CMS search [28]: (left) $t\bar{t}$ events with at least one b-tagged jet, (right) $t\bar{t}$ events with both jets b-tagged.

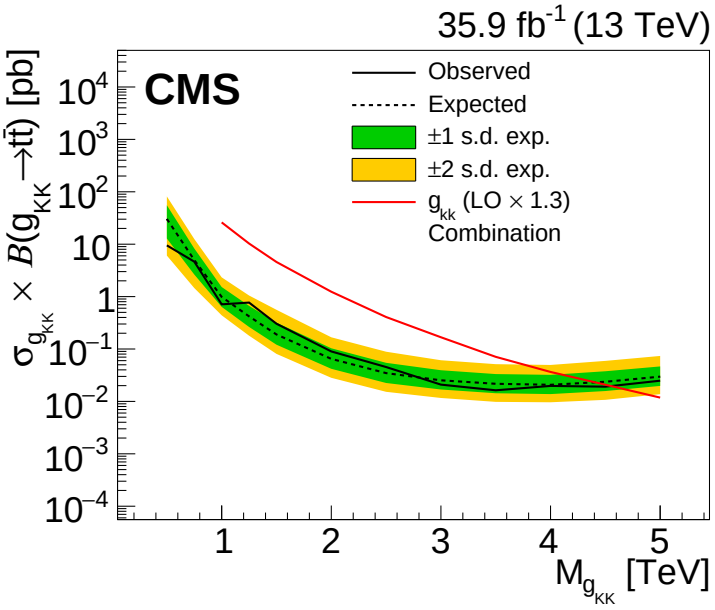

Figure 3.12. Observed and expected limits at 95% CL for on the production cross section times the branching fraction for the G_{KK} (right) hypotheses considered in the CMS analysis [28].

3.3 Trijet: unexplored final state

The dijet and ditop searches shown in the previous Sections set strong limits on new hadronic resonances, in both the low (500 GeV–1 TeV) and high (>1 TeV) mass ranges. However, signals from new hadronic resonances may be hidden by the large amount of background events from QCD multijet processes. In this case, it is possible to develop further searches for hypothetical new hadronic resonances by exploring other production/decay channels besides the dijet and the ditop ones. The exploration of these channels can then increase the sensitivity of the searches to these new resonances, eventually leading to their discovery.

For this reason, both the ATLAS and CMS collaborations searched for new hadronic resonances produced in association with an initial state radiation jet [59, 60, 61], photon [62, 63], or lepton [64], and pair production of resonances resulting in final states with four or more jets [65, 66, 67, 68].

Furthermore, following the lead of the $t\bar{t}$ searches, the CMS and ATLAS collaboration searched also for new resonances decaying into heavy SM objects, like a pair of vector bosons WW, ZZ, WZ [69, 70], or a pair of Higgs bosons HH [71, 72], or an Higgs and a SM vector bosons [73, 74, 75].

The search presented in this thesis aims to further extend this reasoning by considering an unexplored process where a new resonance R_1 decays into a second new resonance R_2 and a SM object, following the cascade decay (Fig. 0.1):

$$q\bar{q} \to R_1 \to R_2 + P_3 \to (P_1 + P_2) + P_3. \tag{3.2}$$

The presence of two new resonances in the process is unusual with respect to previous searches, which often assumes that only one new resonance, or pairs of the same new resonance, could be produced at the LHC.

Such new resonances are foreseen, for example, by the warped extra dimension (WED) model we introduced in Sec. 2.2.2. In our analysis we focus on this benchmark model assuming R_1 to be a KK gluon (G_{KK}), R_2 to be a radion (ϕ) and P_1, P_2 and P_3 to be all gluons.

The masses of the two resonances, $m(R_1)$ and $m(R_2)$, are unknown. The process under study can then produce final states with different jet topologies depending on the assumptions made on their values. The kinematics of the decay depends in fact on the mass ratio:

$$\rho_m = \frac{m(R_2)}{m(R_1)} \tag{3.3}$$

In the approximation of R_1 produced at rest in the laboratory reference system, and assuming P_1, P_2, and P_3 to be massless, the minimum angle between P_1 and P_2 (α_{min}) is related to ρ_m by:

$$\alpha_{min} = \frac{4\rho_m}{1 + \rho_m^2} \tag{3.4}$$

Hence, the lower is ρ_m, the lower will be the angle between P_1 and P_2. This effect is clearly visible in Fig. 3.13, which shows the distribution of the angular separation:

$$\Delta R(\mathrm{P_1P_2}) = \sqrt{(\phi(\mathrm{P_1}) - \phi(\mathrm{P_2}))^2 + (\eta(\mathrm{P_1}) - \eta(\mathrm{P_2}))^2} \tag{3.5}$$

from simulations of signal events corresponding to different hypotheses of ρ_m and $m(\mathrm{R_1})$ values. In the Equation above ϕ and η are respectively the angular coordinate and the pseudorapidity in the CMS coordinate system (Sec. 4.2.1). The ΔR is a measure of angular separation between the trajectories of $\mathrm{P_1}$ and $\mathrm{P_2}$, which is invariant with respect to Lorentz boosts along the beam axis (the z-axis of the CMS coordinate system).

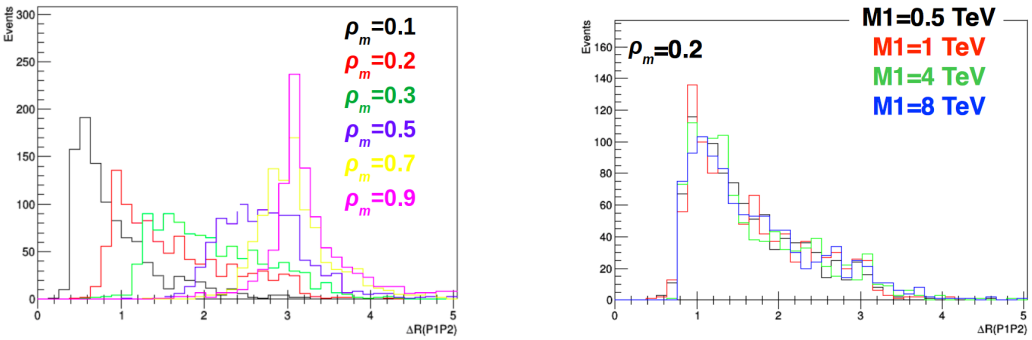

Figure 3.13. Simulated distribution of ΔR between $\mathrm{P_1}$ and $\mathrm{P_2}$ for $m(\mathrm{R_1}) = 1\,\mathrm{TeV}$ at different values of ρ_m (left), and for $\rho_\mathrm{m} = 0.2$ at different values of $m(\mathrm{R_1})$ (right).

The right plot of Fig. 3.13 shows that $\Delta R(\mathrm{P_1P_2})$ does not depend on the value of $m(\mathrm{R_1})$, as expected from Eq. 3.4.

The signal process can then result in different final states depending on the assumed value of ρ_m (Fig. 3.14):

- **resolved dijet:** for values of ρ_m close to unity ($\rho_\mathrm{m} \gtrsim 0.9$), the $\mathrm{P_3}$ parton has low p_T and may not pass the offline selection. The resulting final state has two leading jets coming from the decay of $\mathrm{R_2}$.

- **resolved trijet:** for intermediate ρ_m values, the three partons from the cascade decay chain are spatially well separated and they can be reconstructed as three resolved;

- **boosted dijet:** if $m(\mathrm{R_2})$ is significantly lighter than $m(\mathrm{R_1})$ ($\rho_\mathrm{m} \lesssim 0.2$–$0.3$), $\mathrm{R_2}$ is produced with large Lorentz boost and its decay products $\mathrm{P_1}$ and $\mathrm{P_2}$ are collimated. The partons $\mathrm{P_1}$ and $\mathrm{P_2}$ can be reconstructed within a single jet with a cone size about $\Delta R = 1.5$, which is of the same order of that of jets used in CMS searches. The final state presents then only two reconstructed jets: a regular jet coming from $\mathrm{P_3}$ and a second jet containing both $\mathrm{P_1}$ and $\mathrm{P_2}$ with a jet mass corresponding to $m(\mathrm{R_2})$;

Existing searches for dijet resonances at collider experiments, as those reported in Sec. 3.1, are sensitive to the first scenario, but are not optimized for the other two.

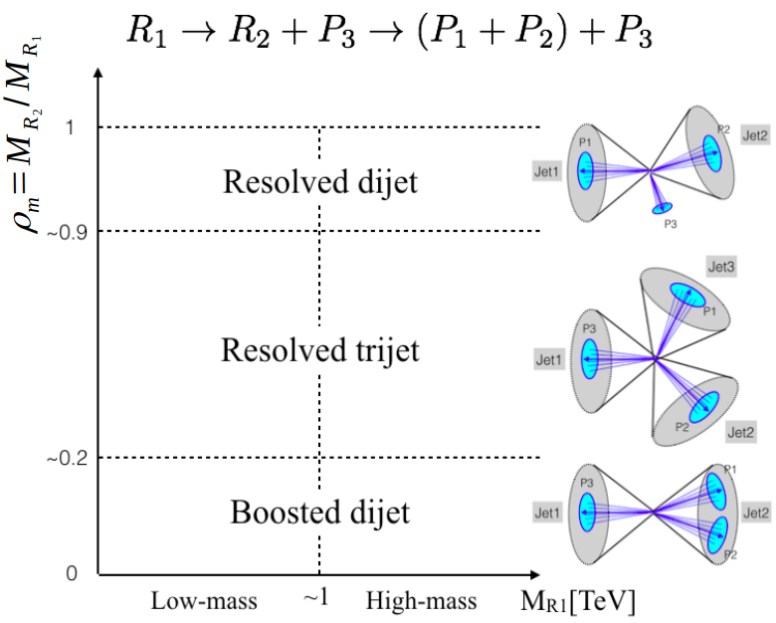

Figure 3.14. Experimental signatures for trijet resonances in the plane ρ_{m} vs $m(\mathrm{R}_1)$.

In the resolved trijet scenario, the expected signature would be a peak corresponding to $m(\mathrm{R}_1)$ in the distribution of the invariant mass of three jets. There are currently no published searches considering this channel.

In the boosted dijet scenario, analyses like the last CMS dijet analysis [30], which use wide jets, could fully reconstruct the R_1 mass, but their results would be suboptimal because the information from the R_2 decay would not be used. Therefore, new analysis approaches can be developed to optimize the search for this processes.

The rest of the thesis will then be focused on this final state, corresponding to $\rho_{\mathrm{m}} \lesssim 0.2$, where the study of jet substructure has a central role. In Sec. 5.5, we will introduce the jet structure variables, which will allow us to identify massive jets from R_2 decays by jets originating from the hadronization of single quarks/gluons. Then, in Ch. 7, we will see how these variables can be used to design a strategy to reduce the QCD multijet background and enhance the search sensitivity to trijet resonances in the boosted dijet scenario. In this analysis the two resonances are assumed to be narrow, i.e., with small peak widths compared to the experimental resolution.

Chapter 4

The CMS experiment at the CERN LHC

4.1 The Large Hadron Collider

The Large Hadron Collider (LHC) is the world's largest and most powerful particle accelerator. It measures 27 km of length and it is capable to generate pp collisions at a center-of-mass energy $\sqrt{s} = 13\,\text{TeV}$. It has been installed in the underground tunnel previously occupied by the Large Electron Positron collider (LEP), active until the year 2000. The LHC first started up on 10 September 2008, and remains the latest addition to CERN's accelerator complex (Fig. 4.1). Each step of the chain pre-accelerates the protons at increasing energies before the injection in the LHC.

The protons, after being extracted from an hydrogen source, are first accelerated by a linear accelerator, the LINAC 4, to an energy of 160 MeV. The Proton Synchrotron Booster (PSB), then, increases the proton energy up to 2 GeV before injecting them in the Proton Synchrotron (PS), where they are further accelerated to 26 GeV. The Super Proton Synchrotron (SPS), a circular accelerator with a radius of 1 km, is the final stage of this preliminary acceleration where the protons reach an energy of 450 GeV. The protons are then ready to be injected in the LHC, where

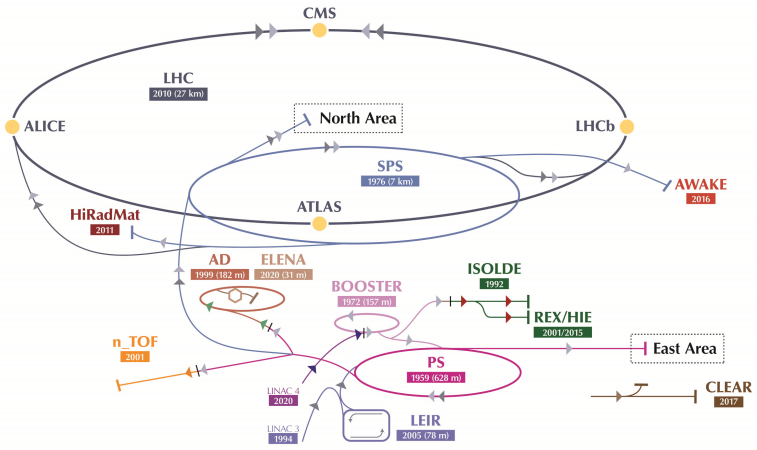

Figure 4.1. Schematic view of CERN accelerator complex

they reach the final energy of 6.5 TeV per beam.

The protons circulate in the LHC ring into two separate pipes in opposite directions. To maintain them in such circular path, the LHC employs 1232 superconducting, 14.2 m long, Niobium-Titanium dipole magnets, cooled down to 1.9 K by means of super-fluid Helium. Each magnet creates a bending magnetic field of about 8.3 T, which is oriented in opposite direction in the two pipes, in order to bend the protons circulating in the two beams.

The LHC beams are crossed in four interaction points, generating pp interactions with a maximum instantaneous luminosity of $2 \times 10^{34}\,\mathrm{cm}^{-2}\,\mathrm{s}^{-1}$.

The interactions produced are analyzed by the four LHC experiments located in correspondence of the interaction points. The ATLAS (A Toroidal LHC ApparatuS) [76] and CMS (Compact Muon Solenoid) [77] detectors are designed for a large program of physics analyses. They mainly analyze data from pp interactions exploiting different technical solution for the detection of the interaction products. ALICE (A Large Ion Collider Experiment)[78] addresses the physics of the quark-gluon plasma at extreme values of energy density and temperature in nucleus-nucleus collision, and LHCb (Large Hadron Collider beauty) [79] is optimized for studies on matter-antimatter asymmetry and CP violation through analyses involving b quarks.

The first LHC research run (Run 1) took place between March 2010 and February 2013 at an initial center-of-mass energy of 7 TeV (with 3.5 TeV colliding beams), increased to 8 TeV from 2012. With the data collected in the Run 1 the collaborations of the ATLAS and CMS experiments discovered the Higgs boson in 2012 [80, 81].

After a shutdown of ∼3 years for planned upgrades, the LHC started its second research run, Run 2. Between 2016 and 2018, the LHC delivered to the experiments pp collisions for an integrated luminosity of $\sim 140\,\mathrm{fb}^{-1}$ recorded by ATLAS and CMS. This dataset is still the largest dataset available of pp collisions at the highest center-of-mass energy ever recorded.

The accelerator was then shut down again for 3 years, for the maintenance of the components of both the accelerator and the detectors.

The LHC is now preparing for its Run 3, which will start on April 2022 and will last ∼3 years. The experiments expect to collect data for an integrated luminosity of $\sim 190\,\mathrm{fb}^{-1}$ at $\sqrt{s} = 13.6\,\mathrm{TeV}$. On 19th October 2021, two pilot beams where injected at the energy of 450 GeV and the very same day the CMS and ATLAS detector successfully recorded data and passed all the required tests. The new dataset, although characterized by a modest increase of the center-of-mass energy, in combination with the Run 2 dataset will improve the searches for very high-mass resonances, the observation of rare SM physics processes (like the production of multiple vector bosons), and the characterization of the Higgs boson properties by differential analyses of its cross section.

4.2 The Compact Muon Solenoid

The Compact Muon Solenoid (CMS) experiment [77] is designed for a wide range of physics analyses: from the search for the Higgs boson, to the precision measurements of SM phenomena, to searches for physics beyond the Standard Model (SM). The overall layout of CMS is shown in Fig. 4.2. It has a cylindrical shape and it is formed by many layers of different components. Starting from the interaction point, the outgoing particles encounter the CMS components in the following order:

- the tracking system;
- the electromagnetic calorimeter;
- the hadronic calorimeter;
- the superconductive magnet;
- the muon system.

Each component of CMS, except for the magnet, is a subdetector designed for the measurement of a specific particle property (the energy, the momentum, the trajectory,...). The components are described in the following sections, after an introduction of the CMS coordinate system convention (Sec. 4.2.1).

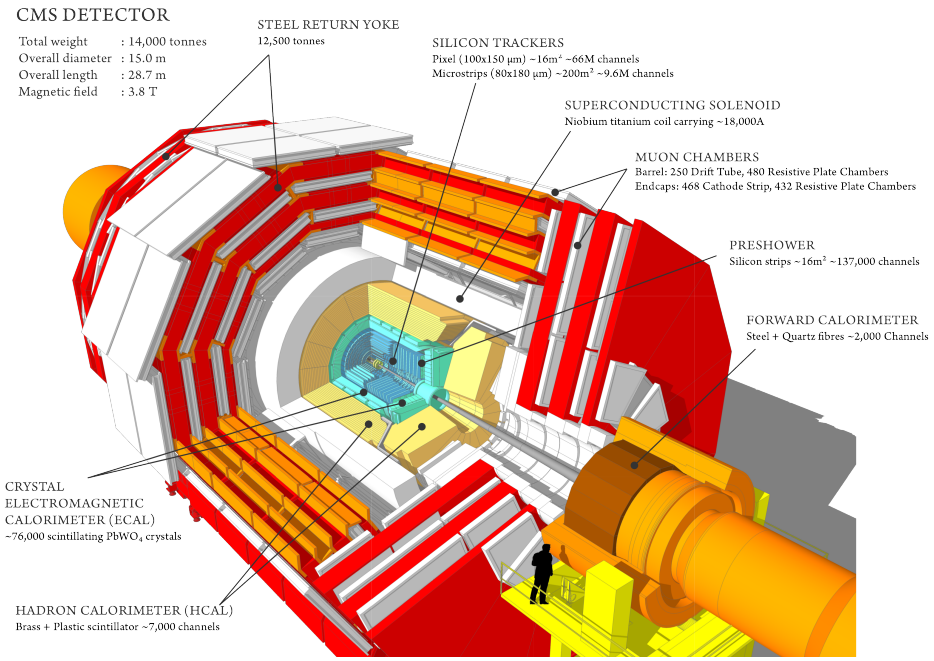

Figure 4.2. The CMS detector and its layers.

4.2.1 Coordinate system

CMS adopts the right-handed Cartesian coordinate system shown in Fig. 4.3, with the origin at the nominal interaction point (IP) at the center of the detector.

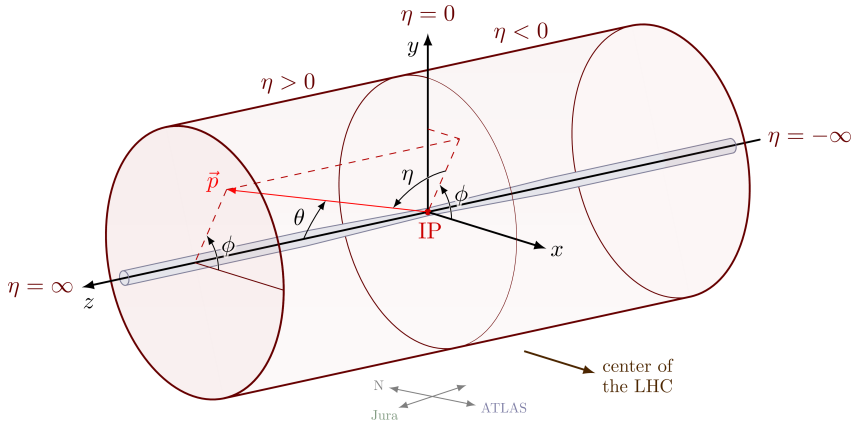

Figure 4.3. CMS coordinate system

The x-axis points to the center of the LHC, the y-axis points upwards, perpendicular to the LHC plane, and the z-axis along the anticlockwise-beam direction. Given the cylindrical system, it is also useful to define some variables in a angular reference system. The polar angle, θ, is measured from the positive z-axis and the azimuthal angle, ϕ, lies in the x-y plane. Transverse energy and momentum (p_{T} and E_{T}), i.e. the particle's energy (E) and momentum (p) in the transverse plane, are therefore defined as $p_{\mathrm{T}} = p\sin(\theta)$ and $E_{\mathrm{T}} = E\sin(\theta)$. The polar angle is usually expressed using the pseudorapidity η, which is related to θ by the relation of Eq. 1.10.

The main advantage of this convention is that, for ultrarelativistic particles ($|p| \gg E$), η is approximately equal to the rapidity y (Sec. 1.2.2). Since the difference of rapidities is invariant with respect to Lorentz-boosts along the z–axis, it is possible to define a measure of angular separation between particles which also is invariant:

$$\Delta R^2 \equiv (\Delta\eta)^2 + (\Delta\phi)^2. \tag{4.1}$$

where we used the approximation $\Delta y \simeq \Delta\eta$.

4.2.2 Magnet

The CMS experiment is primarily designed to be a high performance and compact muon system. In order to obtain an high resolution on the measurement of muons momenta, a strong bending power is needed, which is provided by the intense magnetic field developed by the CMS magnet [82].

This is composed by a superconducting cylindrical Niobium-Titanium solenoid, which provides a uniform magnetic field of 3.8 T at its center, carrying a current of 18 kA and a total stored magnetic energy of 2.4 GJ. In order to ensure good momentum resolution also in the forward region of the detector, a large enough length/radius ratio is also demanded. The length of the solenoid is then 13 m, while its diameter is 5.9 m, enough to contain the tracker and the calorimeters. In the external part of the solenoid the magnet field is returned by a saturated iron yoke, which also works as mechanical support of the detector. Figure 4.4 shows the designed magnetic field intensity and direction on a longitudinal section of the CMS detector [83].

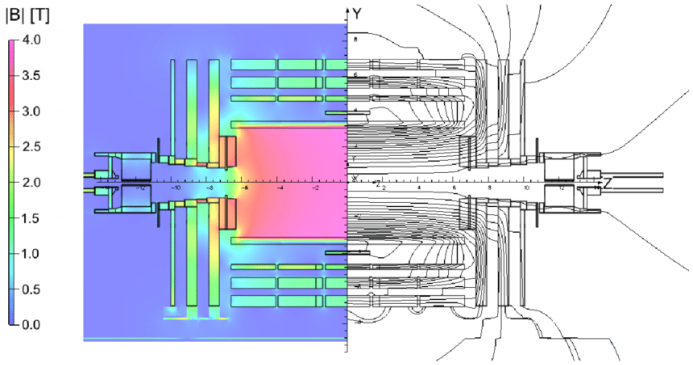

Figure 4.4. Design values of the magnetic field $|B|$ (left) and field lines (right) for a longitudinal section of the CMS detector, for a central magnetic flux density of 3.8 T. Each field line represents a magnetic flux increment of 6 Wb.

4.2.3 Tracker

The CMS tracker [84] reconstructs the trajectories of charged particles produced in pp interactions (tracks), together with the interaction points (vertices). The vertices are reconstructed by the intersection of track directions that overlaps in the same point of the z–axis. The evaluation of the curvature of the tracks, bended by the magnetic field, allows for the precision measurement of the particle momenta.

The CMS tracker is the innermost component of the CMS detector, the closest to the beam pipe and the interaction point. It is composed by several layers of silicon detectors, which register the position of a charged particle that passes through them (hit). The tracks are then reconstructed by connecting the hits from the different layers.

The layout of the CMS tracker is shown in Figure 4.5. It is divided into three parts, each one that can be decomposed into a cylindrical part (the barrel) and two disks (the endcaps). The use of silicon detectors has been chosen in order to provide good radiation hardness, high granularity and large hit redundancy to perform a good pattern recognition. The innermost part is formed by layers of pixel detectors with a small size necessary for the resolution of close tracks and the vertex reconstruction. The middle and the outer part of the tracker are composed by microstripes with a coarser segmentation since the particle flux is lower in this region.

The total area of the silicon detectors provide coverage up to $|\eta| = 2.5$. The material budget of the tracker needs to be controlled in order to contain the degradation of the measure of the particle energies by the calorimeters. The "thickness" of the tracker increases from 0.4 radiation length (X_0) at $\eta = 0$ to around $1X_0$ at $|\eta| = 1.6$, before decreasing to $0.6X_0$ at $|\eta| = 2.5$.

The spacial resolution of the tracker is of the order of 15 μm, resulting in a momentum resolution below 2% (6%) in the barrel (endcap) for muons with $20\,\text{GeV} < p_\text{T} < 100\,\text{GeV}$,and better than 10% for p_T up to 1 TeV.

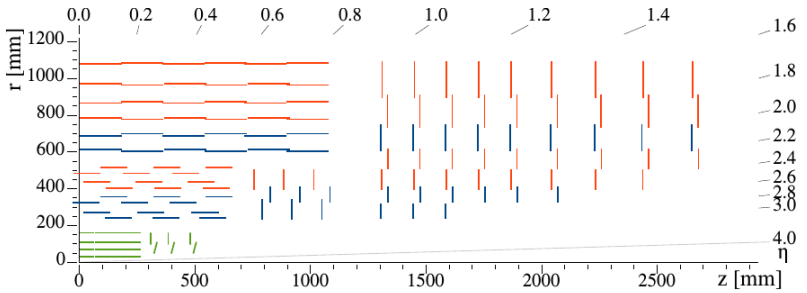

Figure 4.5. Layout of the tracker detector.

4.2.4 Electromagnetic calorimeter

The CMS electromagnetic calorimeter (ECAL) [85] is an hermetic, homogeneous detector composed by over 75.000 scintillating lead-tungstate ($PbWO_4$) crystals. It is designed to measure the energy of incoming electrons, positrons and photons with an high resolution.

The ECAL is important for a large variety of analyses, and it played an essential role in the Higgs boson discovery in the decay channel $H \to \gamma\gamma$. Consequently, the construction of an high performance electromagnetic calorimeter has been one of the principal CMS design objectives.

To match the requirements on the energy resolution, ECAL has been designed as an homogeneous calorimeter with high granularity, i.e. entirely composed by sensitive material. After an intensive initial R&D programme, the $PbWO_4$ has been chosen for the realization of the crystals because it met all the requirements for the building of ECAL:

- its radiation length X_0 is short, meaning that it is possible to realize a compact calorimeter that allows the containment of almost all the energy of the incoming particle;
- the small Molière radius (2.2 cm) ensures lateral shower containment and, therefore, allow for the realization of a detector with high granularity, which is needed for π_0–γ separation and angular resolution;
- the $PbWO_4$ is a fast scintillator: the scintillation decay time is of the same order of magnitude as the LHC bunch crossing time (25 ns), enabling ECAL to measure the particles energy with a little overlap between signals from different bunch crossing;
- it has a fairly good resistance to radiation damage, which is essential for its operation in the harsh environment of the LHC. However, as we will see in Appendix B, the crystal transparency loss caused by the radiation damage produces non-negligible effect which are corrected using many different approaches.

The $PbWO_4$ light output is relatively low: about 4.5 photoelectrons per MeV. This low value limits the choice of photodetectors to those which provide an internal amplification of the small signal from the collected scintillation light. The barrel mounts a couple of avalanche photo-diodes (APDs) on each crystal while the endcaps mounts vacuum photo-triodes (VPTs).

The ECAL detector is placed between the tracker and the hadronic calorimeter, and it is divided in a central cylindrical region (barrel) closed by two end caps (Fig. 4.6). The ECAL barrel (EB) covers the pseudorapidity range $|\eta| < 1.479$, while the ECAL endcaps (EEs) extends the coverage to $|\eta| < 3.0$.

Each EB crystal has the form of a truncated pyramid 230 mm long (25.8 X_0) with the smaller face of $22 \times 22\,\text{mm}^2$ facing the interaction point. The crystals are mounted in a a semi-projective geometry forming a 3°angle with respect to the nominal interaction point in order to avoid incoming photons to fall in the zone between two crystals.

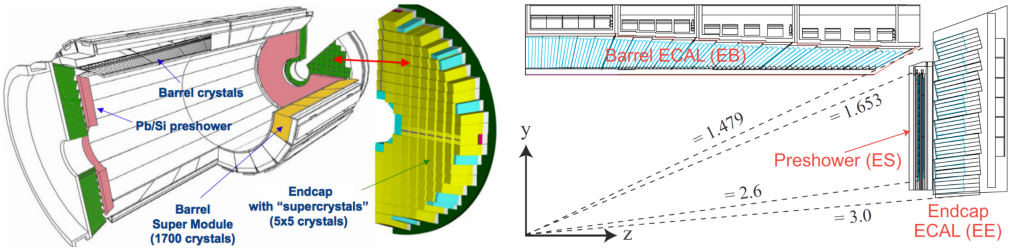

Figure 4.6. Left: sketch of ECAL and its parts: barrel, endcaps, supermodules and supercrystals. The identical supercrystals of the half of an endcap are marked in yellow, while those with different shapes are marked in light blue. Right: longitudinal section of a quarter of the ECAL detector showing the crystals orientation.

The EB is organized in a modular structure: it is divided into two halves in the $\eta\phi$–plane, each one composed by 18 supermodules. Each supermodule subtends a 20° angle in ϕ, and contains 1700 crystals divided into four modules (500 in one module and 400 in the remaining three). The total number of EB crystals is then 61.200.

The two EEs are made of crystals with front-face dimensions $28.6 \times 28.6\,\mathrm{mm}^2$ and a length of 220 mm (24.7 X_0). They are grouped together into 268 identical supercrystals with 25 crystals each, plus 64 supercrystals with different shapes placed at the contours of the endcaps, for a total of 14648 crystals.

The EEs are also equipped with a preshower detector (ES), covering the region $1.7 < |\eta| < 2.6$, which is a two-layer sampling calorimeter made of lead and silicon strips. The preshower is used to obtain a better spatial resolution in the endcaps in order to separate photons from boosted π_0s.

The energy resolution of ECAL, as for any homogeneous calorimeter, is a function of the energy (E) of the incoming electrons and photons. It can be parameterized as a squared sum of three terms:

$$\left(\frac{\sigma_E}{E}\right)^2 = \left(\frac{S}{\sqrt{E}}\right)^2 + \left(\frac{N}{E}\right)^2 + C^2 \tag{4.2}$$

The stochastic term (S) depends on the stochastic fluctuations of the number of detected photons from the scintillation process, the noise term (N) is due to the electronics noise, and the constant term (C) depends on lateral containment, non uniformity of response and intercalibration. The values of these parameters have been measured at a beam test at a single-crystal level and were found to be $S = 2.8\%\,\mathrm{GeV}^{1/2}$, $N = 124\,\mathrm{MeV}$ and $C = 0.3\%$ where E is expressed in GeV. The energy resolution for photons with $E_T \simeq 60\,\mathrm{GeV}$ varies between 1.1% and 2.6% over the solid angle of the ECAL barrel, and from 2.2% to 5% in the endcaps. The ECAL energy resolution for electrons with $E_T \simeq 45\,\mathrm{GeV}$ from $\mathrm{Z} \to \mathrm{ee}$ decays is better than 2% for $|\eta| < 0.8$, and is between 2% and 5% elsewhere. For low-bremsstrahlung electrons, where 94% or more of their energy is contained within a 3×3 array of crystals, the energy resolution improves to 1.5% for $|\eta| < 0.8$.

4.2.5 Hadronic calorimeter

The hadronic calorimeter (HCAL) [86] measures the energy of hadrons produced in pp collisions and, in combination with ECAL, also the missing transverse energy flow. The design of HCAL originates from the necessity of containing the hadronic shower inside the volume of the detector, which occupies the limited space between the ECAL and the solenoid.

Thus, as opposed to ECAL, the HCAL is a sampling calorimeter formed by layers of absorbing material alternating to layers of active material. The energy deposited by particles in the absorbing material is not measured by the detector. For this reason a sampling calorimeter generally has lower energy resolution than an homogeneous calorimeter, but it is also more compact in order to absorb the radiation from hadronic showers.

The absorbing layers of HCAL are made of brass, while the active material is composed by plastic scintillators that produce a rapid light pulse when a particle passes through them. Brass has been chosen because it has a reasonably short interaction length, good mechanical properties and is non-magnetic, so it does not interfere with the CMS magnetic field. The light from the scintillators is collected with wavelength-shifting fibers.

The HCAL is divided into six parts: the barrel (HB), two endcaps (HE), two forward (HF) sections and an additional layer in the barrel region outside the magnetic coil (HO). The longitudinal section of the HCAL components is shown in Fig. 4.7.

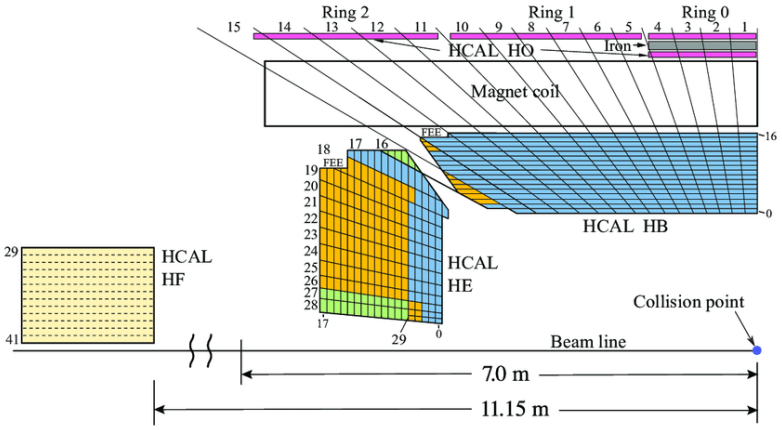

Figure 4.7. Longitudinal section of a quarter of HCAL, showing HCAL parts in the zη-plane.

The HB covers a region of $|\eta| < 1.4$ and is segmented in towers of $\Delta\eta \times \Delta\phi = 0.087 \times 0.087$ to help the reconstruction of the crossing point of the incoming particle and its direction from the analysis of the resulting shower. The two HEs cover a region of $1.3 < |\eta| < 3.0$ with a similar granularity in $\Delta\eta \times \Delta\phi$ of the HB. The HO layer has been inserted to correct for escaping hadron showers from particles with transverse energies above 500 GeV, which could interfere with the muon chambers measurements. It is composed by plastic scintillators, with the same granularity of HB, which adds one radiation length to the calorimeter. The forward region of

$3.0 < |\eta| < 5.0$ is covered by the steel/quartz fiber HF calorimeter, which is made by different materials since it is far from the center of the CMS magnetic field and it receives a very high flux of particles from pp interactions at shallow angles.

The combined energy resolution of the HCAL for single pions is:

$$\left(\frac{\sigma}{E}\right) = \left(\frac{52.9\%}{\sqrt{E(GeV)}}\right)^2 + (5.7\%)^2 \tag{4.3}$$

where the noise term is negligible. The HCAL energy resolution is much larger than the ECAL resolution (Eq. 4.2), therefore it dominates in the combination of HCAL and ECAL measured energies.

4.2.6 Muon system

The muon system [87] detects muons, the only charged particles that pass through the calorimeters without being absorbed. The paths of the muons are reconstructed from the energy that they deposit in the four layers of measuring station of the detector, placed outside the magnet coil. They are imbedded in the iron yoke, where the return flux of the magnetic field is of about 1.5 T. The return field bends muons in the opposite direction with respect to the bending in the tracker. The muon track is then reconstructed matching the information of the muon system and the tracker in a trajectory with two curves in opposite directions in the transverse plane. This peculiar trajectory is a clear sign that identifies the muon.

The muon system use different technologies for its measuring stations in different regions of the detector (Fig. 4.8):

- drift tubes (DT) for $|\eta| < 1.2$;
- resistive plate chambers (RPC) for $|\eta| < 1.6$ (in both barrel and endcaps);
- cathode strip chambers (CSC) for $0.9 < |\eta| < 2.4$.

The DT and the CSC provide an excellent spatial resolution ($\approx$100 μm) for the measurement of the momentum, while the RPC are mainly used for trigger purposes, thanks to their excellent time resolution (3 ns).

4.2.7 Trigger

The LHC produces bunch crossings with a rate of 40 MHz, i.e. one every 25 ns. The CMS is able to store the data from pp interactions with a maximum bandwidth of $\sim$2 GB/s that, considering an average event size of $\sim$2 MB, is equivalent to an event rate of $\sim$1 kHz.

Thus, it would be impossible for CMS to record the data from all the collisions produced. Moreover, the vast majority of them would be soft collisions, useless for the physics program of CMS. Hence, a trigger system is needed to select only the relatively rare interesting events from hard parton-parton interactions.

The CMS trigger system [88] reduces then the event rate from 40 MHz to $\sim$1 kHz using a two-level system:

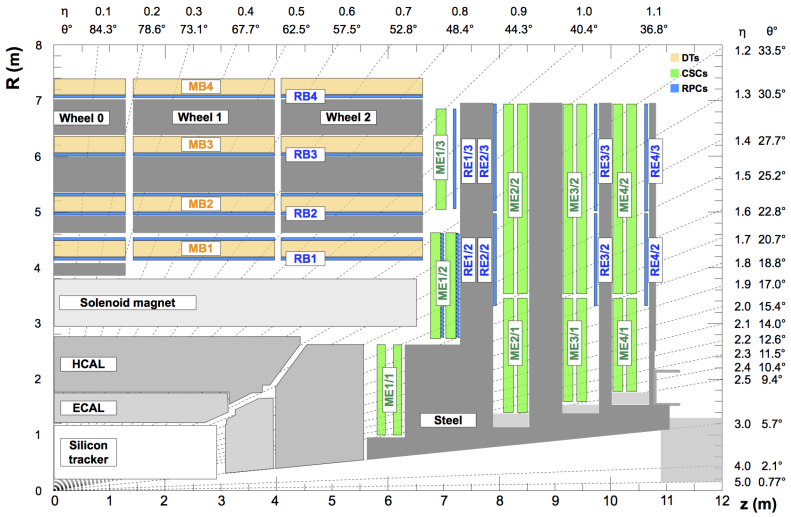

Figure 4.8. Longitudinal view of a quarter of the muon system in the zη-plane.

- the Level-1 (L1) trigger is made by hardware processors that perform fast logical operations on the signals generated by the subdetectors;
- the high level trigger (HLT) is a software system implemented in a multiprocessor computer farm. It takes decisions analyzing the reconstructed quantities for a given object.

The L1 trigger reduces the initial event rate to ∼100 kHz, operating selections in a time interval (latency) of 3.2 μs. It uses only coarsely segmented data from the calorimeters and muon detectors, while holding all the high-resolution data in pipeline memories in the front-end electronic. The L1 features several algorithms (L1 bits, or seeds) to store a general description of the event content that, if the event is accepted, are passed to the HLT for further event processing.

The HLT reduces the output rate to about 1 kHz. It is a software system organized in a set of algorithms (known as HLT "paths") which are designed to select specific event topologies. Each path is composed by steps (modules) that reconstruct high-level objects and operates decisions based on their properties. Each path can be modified by changing its modules or defining new ones, giving to the software the maximum flexibility.

The guiding principles for the construction of HLT paths are regional reconstruction and fast event veto. The reconstruction is regional because it focuses only on the detector regions that the L1 seeds report as interesting, avoiding as much as possible the the complete event reconstruction. Fast event veto means that uninteresting events are discarded as soon as possible for time optimization.

At the end of this chain the selected events are stored in different Primary Dataset (PD) to be used for offline data analysis. A PD collects events with similar topology and it is generally fed by more than one HLT paths. For example, an event is saved in the `JetHT` data if it contains a jet with a p_{T} enough high to be selected by any of the HLT paths requiring an high-p_{T} jet, or if the scalar sum of the jets p_{T} of the event (H_{T}) is above a certain threshold.

Chapter 5

Jet reconstruction

The analysis presented in this thesis searches for resonances that decay into final states with quarks and/or gluons. They, as described in Sec. 1.1.1, hadronize to form jets, which can be detected by the experiments. This Chapter is dedicated to the jet reconstruction in CMS, which is a complex operation due to the composite nature of these objects.

The reconstruction of a jet starts from its constituents: the particles detected by the CMS subdetectors. To reconstruct the individual particles, the CMS collaboration employs the Particle Flow (PF) reconstruction algorithm, described in Sec. 5.1. It combines all the information from the subdetectors to identify the particles and produce objects, called PF Candidates, which contains all the relevant information of the particles. The PF Candidates are then grouped into jets using a jet clustering algorithm. Different algorithms can be used for the jets clustering, and some of them are discussed in Sec. 5.2.

The four-momenta of the reconstructed jet would be ideally equal to that of the originating parton. However, several effects alter the reconstructed energy and momentum of jets, and have to be corrected. These effects are the inclusion in the jet of particles not coming from the primary interaction (pileup) and the non-uniformity of the jet energy response across the detector. The mitigation of pileup effects and the jet energy calibration procedure used in CMS analyses are respectively discussed in Secs. 5.3 and 5.4.

In the analysis presented here, the final state of signal processes (Sec. 3.3) is formed by two jets: the first from the hadronization of a parton, and the second (R_2-jet) from the decay of the boosted R_2 resonance into two partons. Variables that quantify the substructure properties of a jet make it possible the identification of an R_2-jet from quark/gluon jets. In Sec. 5.5, we will then define the two substructure variables used in this thesis: the soft drop mass and the N-subjettiness ratio.

5.1 The Particle Flow algorithm

The CMS experiment reconstructs all the stable particles produced in a pp collision using the Particle Flow (PF) [89] algorithm. With this algorithm, information from all CMS subdetectors are exploited to their full granularity in order to optimize particle reconstruction and identification.

A schematic view of the CMS apparatus and the various particles that it can detects are shown in Fig. 5.1. At first, the tracks of charged particles are reconstructed from the points of their trajectory recorded by the silicon tracker. The tracker also combines the tracks information to reconstruct the points (vertices) where the pp interactions took place. The vertex with most high-energetic tracks associated is called primary (or leading) vertex. A 3.8 T magnetic field generated by the CMS solenoidal magnet bends the particle trajectories. The bending of the tracks allow precise measurement of the p_{T} of charged particles for values as low as 150 MeV. The energies of photons and electrons is measured by the electromagnetic calorimeter (ECAL), with excellent resolution, while the energy of hadrons is measured by the CMS hadronic calorimeter (HCAL), with a contribution of ECAL for charged hadrons. Muons, besides the neutrinos, are the only particles that escape the calorimeters and their track is reconstructed in the muon chambers.

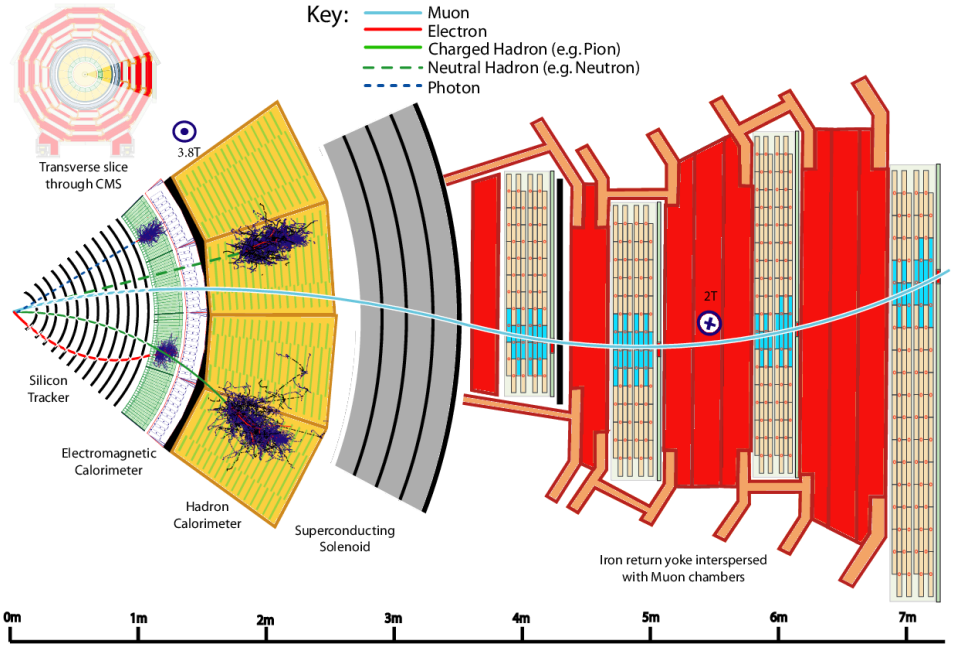

Figure 5.1. Schematic view of a transversal slice of the CMS apparatus. A graphical representation of the different particles and their interactions with the subdetectors is also shown.

The PF algorithm analyzes the raw data independently from each of these subdetectors and creates a list of basic reconstructed elements (blocks): charged tracks in the tracker and muon chambers, and clusters of energy deposits in the calorimeters. The blocks are then topologically matched to build PF particle candidates (PF Candidates). The type of a PF Candidate depends on the type of

blocks involved in its reconstruction:

- electron PF Candidates arise from the matching between a charged track and one or more ECAL clusters, provided a specific set of criteria is satisfied;
- charged tracks matched to any number of calorimeter (ECAL or HCAL) clusters, which do not pass electron selection criteria, are classified as charged hadron candidates;
- ECAL energy deposits not compatible with charged tracks give way to photon candidates;
- energy deposits in the hadronic forward (HF) calorimeters are reconstructed as HF hadronic or electromagnetic particle candidates, depending on the depth at which the energy is released;
- muon candidates are reconstructed and identified with very large efficiency and purity from a combination of the tracker and muon chamber information.

The formation of the PF Candidate list represents the Particle Flow interpretation of a given proton-proton collision in CMS, as it attempts to mirror the true particle composition of the event to the best of our knowledge. All the information on the momentum and the energy of the PF Candidates are saved and available for the analyses.

The jets can be reconstructed by grouping the PF Candidates using different clustering algorithms, as those discussed in Sec. 5.2. The reconstructed jets have to be corrected to account for several effects that modify their energy and p_{T}. We will discuss these effects and the strategies adopted for their mitigation in Secs. 5.3 and 5.4.

For a precise measurement of the jet p_{T} and energy, an adequate calibration of all the CMS subdetectors is needed. Charged hadron and photons inside a jet constitute $\sim$85% of its energy. The charged hadrons are reconstructed mainly by their tracking information, while the photon energy is measured by the ECAL detector. Therefore, the measurement of jet kinematic properties is sensitive to the ECAL calibration. The calibration of an high-granularity detector like ECAL is a complex task, mostly because the detector ages with time due to the radiation damage. Hence, a constant work of calibration is needed. A study on the calibration of the forward endcaps is reported in Appendix B.

5.2 Jet clustering algorithms

Jets observed by the detectors are not physical objects, but streams of particles. Therefore, there is some arbitrariness in their definition, as different algorithms can be used to cluster the reconstructed particles, the PF Candidates, to form a jet. The jet properties, like the momentum, the energy or the size, depend to some extent on the choice of the clustering algorithm.

In the ideal case, the four-momentum associated to the jet is exactly identical to that of the parton generating the shower. Although this is only true to some approximation, there are several theoretical and experimental criteria adopted for the construction of a clustering algorithm that matches as close as possible the jet properties with that of the generating parton.

Two fundamental requirements for a "good" clustering algorithm are the infrared and collinear (IRC) safety. "Infrared safety" means that the presence of soft gluons emitted in the hadronization process should not change the result of the jet clustering, while an algorithm is "collinear safe" if, splitting one parton into two partons (e.g. a gluon splitting into two quarks), the result of the jet clustering does not change. Sketches showing the effects of non-infrared and non-collinear safe algorithm are represented in Figs. 5.2 and 5.3.

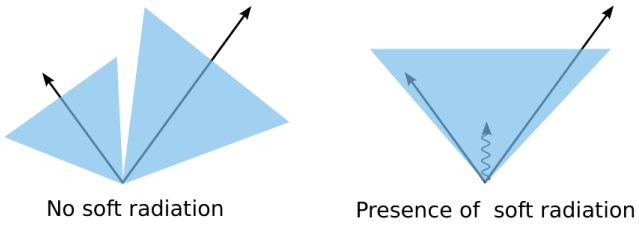

Figure 5.2. Illustration of a non-infrared-safe algorithm: the emission of a soft gluon changes the number of jets.

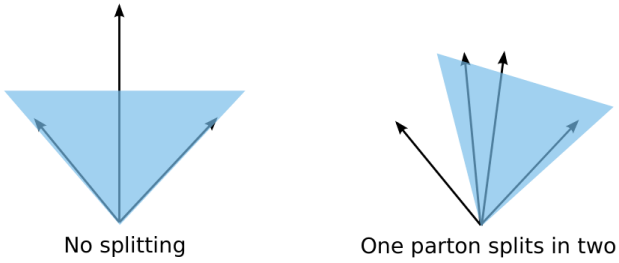

Figure 5.3. Illustration of a non-collinear-safe algorithm: the collinear splitting changes the direction of the jet.

A whole family of IRC algorithms are the sequential recombination jet algorithms, which includes k_{T} [90], Cambridge/Aachen [91] and anti-k_{T} [92] algorithms. In general these algorithms combine two particles if an opportunely defined "distance", which is a function of the transverse momentum (k_{T}), is less than a given threshold. Two kind of distances are introduces: the first between two input particles i and j

(d_{ij}), and the second between the particle i and the beam[1] (d_{iB}). They are defined as:

$$\begin{aligned} d_{ij} &= \min(k_{Ti}^{2p}, k_{Tj}^{2p}) \frac{\Delta R_{ij}^2}{R^2} \\ d_{iB} &= k_{\mathrm{T}i}^{2p} \end{aligned} \tag{5.1}$$

where $\Delta R_{ij} = (y_i - y_j)^2 + (\phi_i - \phi_j)^2$ and $k_{\mathrm{T}i}$, y_i and ϕ_i are respectively the transverse momentum, rapidity and azimuth of particle i. R and p are two parameters of the algorithm. In general, sequential recombination algorithms work as follows:

- for each particle and for each couple of particles, the distances d_{iB} and d_{ij} are evaluated;
- the minimum among all the d_{iB} and d_{ij} is labeled $d_{\min}$;
- if $d_{\min}$ is a d_{ij}, the particles are merged into a single entity called protojet by summing their four-momenta;
- if $d_{\min}$ is a d_{iB}, the particle is isolated and non-mergeable, therefore it is removed from the list and the process is repeated with the new list of particles;
- the algorithm is iterated using the protojets from the previous step as inputs, until only non-mergeable entities are left.

The result of the algorithm is then a list of jets with their four-momenta obtained by the merging process.

The parameter R in Eq. 5.1 is called distance parameter, and it is connected with the size of the jet. A larger value of R reduce the distances d_{ij} with respect to d_{iB}, therefore more objects, even with a larger ΔR separation, will be merged. The radius of the resulting jet in the $\eta\phi$-plane is then similar to the distance parameter R used for the jet clustering.

The value of the parameter p, instead, determines the type of the algorithm: for $p = 1$ we obtain the standard k_{T} algorithm; $p = 0$ corresponds to the Cambridge/Aachen algorithm; and for $p = -1$ the distances depend on the inverse of the k_{T}, therefore the algorithm is called anti-k_{T}.

In the k_{T} algorithm the softer particles are clustered first, and then the others are added in increasing energy, while in the anti-k_{T} this scheme is reversed. The Cambridge-Aachen algorithm, having $p = 0$, is a purely geometric clustering algorithm. The behaviors of different jet algorithms are illustrated in Fig. 5.4, which shows that the anti-k_{T} jet algorithm gives the jets with the most definite shape. In general, the behavior of algorithms with $p > 0$ is similar to the k_{T} algorithm, while for $p < 0$ the behavior is similar to the anti-k_{T} algorithm.

Standard jets used in CMS analyses are reconstructed using the anti-k_{T} algorithm with $R = 0.4$ (AK4) or $R = 0.8$ (AK8). Since the PF algorithm saves all the

[1] the sequential recombination jet algorithms have been designed for jet reconstruction at collider experiments, therefore they assume a reference system with one axis (the beam direction) and a transverse plane for the evaluation of the transverse momentum of jets constituents

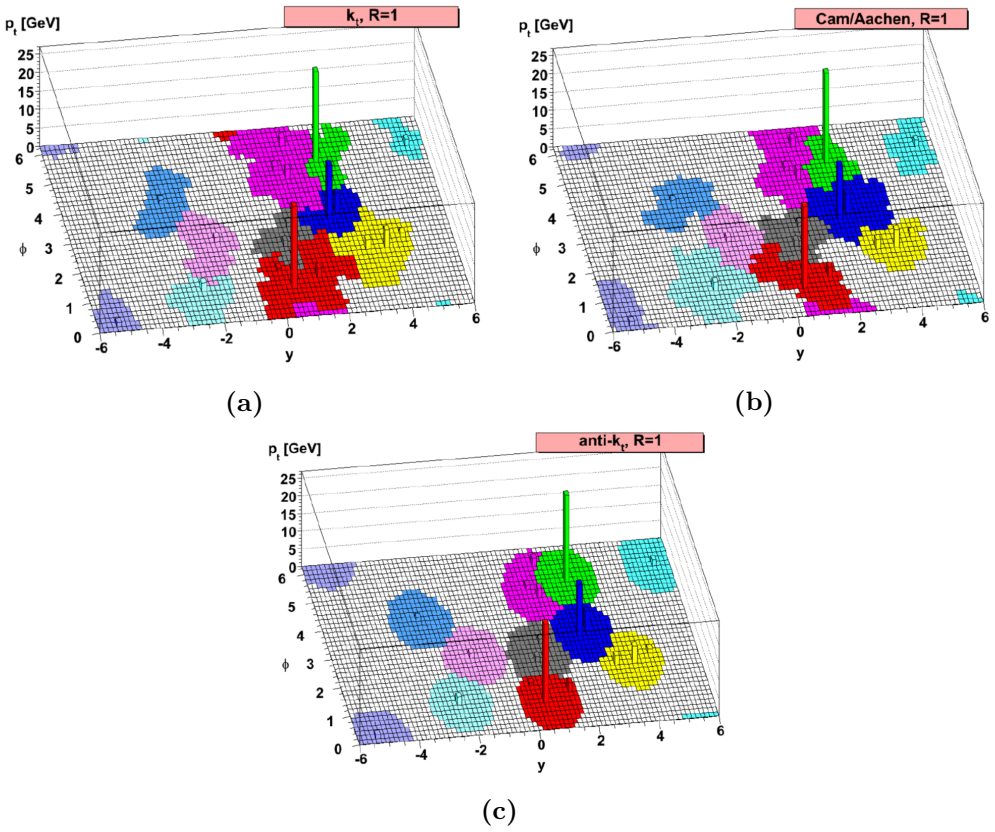

Figure 5.4. Illustration of different jet clustering algorithms. Figure from Ref. [92]

properties of jet constituents, the jets can also be reconstructed offline using a different clustering algorithm or a different distance parameter. The software used for the jet clustering with k_T algorithms is the FastJet package [93].

In our analysis we will use the AK4 and AK8 jets only for the event trigger and for the evaluation of the systematic uncertainty, as will be described respectively in Secs. 6.1 and 8.2.1. For the rest of the analysis we will use anti-k_T jets with $R = 1.5$, because they improve the reconstruction of the resonances under study, as shown in Sec. 6.3.

5.3 Jet pileup corrections

Jets reconstructed clustering PF Candidates also include particles produced in other pp interactions occurring in the same bunch crossing of the primary interaction. These particles alter the four-momenta of the resulting jet, causing an effect called pileup (PU).

The pileup particles are associated to vertices of pileup interactions, therefore we can use algorithms to identify them and correct for the pileup effect. Jets used for the analysis presented here are corrected for the PU using a dedicated algorithm called pileup per particle identification (PUPPI) [94]. The CMS implementation of the PUPPI algorithm is schematically shown in Fig. 5.5, and it is composed by the

following steps [95]:

- the tracks of the charged particles are used to associate them to the leading vertex (LV) or to a pileup vertex (PUV). A weight is assigned to the particles, which is respectively 1 or 0 in the two cases (i.e. they are removed from the jet if associated to a PUV);
- a variable α is defined, which has a different distribution for particles originating from PUV or particles originating from the LV;
- the distribution of α for particles originating from a PUV is evaluated for charged particles only, because their reconstructed tracks allow to assign them to the LV or to the PUV;
- the distribution of α for neutral particles, instead, is assumed to be similar to that of charged particles, with small corrections to be applied if necessary;
- the median (α_{med}) and the RMS (σ_α) of the α distribution are evaluated;
- the α value for each neutral particle i of the event (α_i) is evaluated, and a weight (w_i) is assigned by comparing α_i to α_{med}.
- if α_i is near to α_{med} in units of σ_α, the weight w_i is small. The four-momentum of particle i is then rescaled by w_i, therefore pileup particles, having a small weight, will have little contribution to the jet four-momentum.

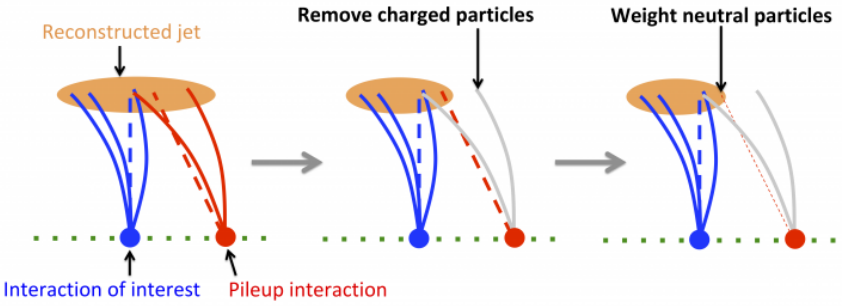

Figure 5.5. General scheme of the CMS PUPPI algorithm.

The α variable used for the PUPPI algorithm is:

$$\alpha_i = \log \sum_{j \in event} \frac{p_{\mathrm{T}_j}}{\Delta R_{ij}} \times \Theta(R_{\text{min}} \leq \Delta R_{ij} \leq R_0) \tag{5.2}$$

where ΔR_{ij} is the distance between particles i and j in $\eta\phi$-plane, and $\Theta(R_{min} \leq \Delta R_{ij} \leq R_0)$ is a shorthand notation for $\Theta(\Delta R_{ij} - R_{min}) - \Theta(R_0 - \Delta R_{ij})$, with Θ being the Heaviside step function. The function $\Theta(R_{min} \leq \Delta R_{ij} \leq R_0)$ is then equal to 1 for $R_{min} \leq \Delta R_{ij} \leq R_0$, and 0 otherwise. Therefore, only particles with ΔR_{ij} between R_{min} and R_0 are considered in the sum. In the equation above, p_{Tj} is the transverse momentum of the j-th particle in the events, and R_0 is the cone size

around each particle i, so that only particles within the cone enter the calculation of α_i. Particles closer to i than R_{min} are discarded from the sum, with R_{min} effectively serving as a regulator for collinear splittings of particle i.

The α_i distributions for charged particles from the PUV or the LV are shown in Fig. 5.6, from a simulated sample of pp $\rightarrow$ dijet events. For the simulated events it is also possible to evaluate the α_i distributions of neutral particles from the PUV or the LV, and they are close to the corresponding ones of charged particles.

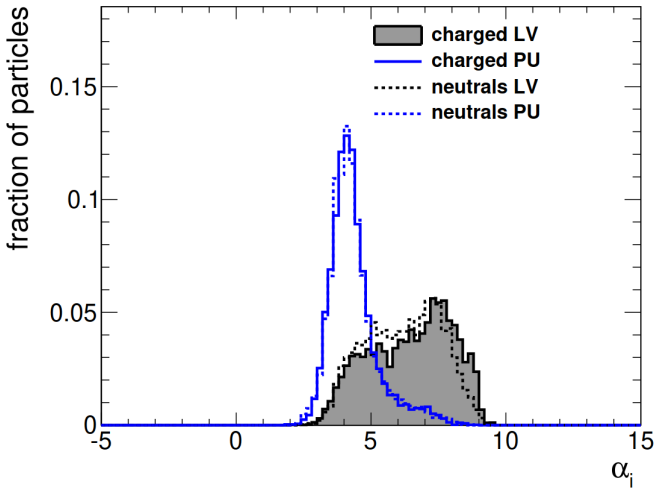

Figure 5.6. The distribution of α_i, over many simulated events, for particles i from the leading vertex (gray filled) and particles from pileup (blue) in a dijet sample (from Ref. [94]). Dotted and solid lines refer to neutral and charged particles respectively.

The performances of the PUPPI algorithm have been evaluated for CMS data at $\sqrt{s} = 13\,\text{TeV}$ [95].

Another source of PU are pp collisions occurred in the bunch crossings preceding and following that of the primary vertex. This effect arises because of the scintillation decay time of the ECAL crystals and HCAL plastic scintillators+fibers (see Secs. 4.2.4 and 4.2.5), which is comparable with the time between two consecutive bunch crossings. Hence, the calorimeters can associate a fraction of the energy deposited during the previous or the following bunch crossing to the primary interaction of the bunch crossing under study. This effect is called out-of-time pileup (OOT PU). The amount of OOT PU is reduced at the detector level by shortening the time integration window of the signal produced by the calorimeters and using the information on the signal pulse shape to subtract a varying pedestal. Both ECAL and HCAL use a fit to the pulse shape to remove OOT PU. For a detailed discussion of the OOT PU we refer to Ref. [96].

Some false signals can pass the aforementioned filters and affect the PF reconstruction. To further reject noise after detector signal processing and jet clustering, a set of criteria on the PF candidates within a jet are applied, called Jet ID criteria. The criteria are based on jet constituent energy fractions and multiplicities. A detailed list of the most recent Jet ID criteria can be found in Ref. [95].

5.4 Jet energy calibration

In this Section we introduce the jet energy corrections (JEC), which are a set of tools to correct the jet energy for the many effects that modify it, first above all the non-linearity of the response of CMS calorimeters.

The CMS collaboration adopted a factorized solution to the problem of JECs, where each level of correction takes care of a different effect. Each level consists in a scaling of the jet four-momentum with a scale factor (correction) which depends on jets p_{T} and η. The levels of correction are applied sequentially (the output of each step is the input to the next) and with fixed order, following the scheme shown in Fig. 5.7:

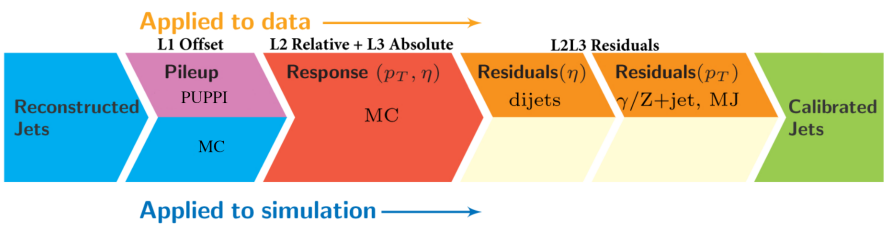

Figure 5.7. Consecutive stages of jet energy corrections, for data (upper row) and simulation (lower row). All the corrections marked with MC are derived from Monte Carlo simulation, and MJB (MultiJet Balance) refers to the analysis of multijet events (Sec. 5.4.2).

- **Level 1 (L1) corrections** purpose is to estimate and subtract the energy not associated with the hard scattering interaction. The energy in excess includes contributions from pileup interactions. We already described in Sec. 5.3 the PUPPI method, adopted for the mitigation of pileup effects in our analysis;

- **Level 2 and Level 3 (L2L3) MC-truth corrections** use simulated samples of QCD multijet events to correct for the response of the detector;

- **L2L3 residual corrections** correct the residual difference between data and simulation after the application of the other corrections;

The methods used to obtain the L2L3 MC-truth and residual JEC are described in in Secs. 5.4.1 and 5.4.2. For further details on the JEC evaluation methods and on the performances on 13 TeV data the reader can refer to Refs. [97] and [98]. The jet energy corrections are usually evaluated by a group of experts within the CMS collaboration for jets reconstructed with a limited number of clustering algorithms. As will be described in Sec. 6.3, we will use the anti-k_{T} algorithm with $R = 1.5$ (AK15) for the jet reconstruction, for which energy corrections are not calculated. However, as we will show later in Sec. 8.2.1, AK15 jets shows similar performances as the AK8 jets, which are officially calibrated. We will apply the JEC for AK8 jets also to AK15 jets used in this search.

5.4.1 Level 2-Level 3 MC-truth corrections

After being corrected for the pileup, the jet four-momenta are also corrected for the non linearity of the detector response versus the η and p_{T} of jets. These corrections are called Level L2L3 MC-truth corrections[2], as their evaluation relies entirely on Monte Carlo (MC) simulated samples of QCD dijet events.

The detector response to jet is evaluated by comparing the jet p_{T} to that of the particle-level jet. The latter is a jet obtained by applying the clustering algorithm to all the stable particles generated in the simulation (except neutrinos), whereas the first is a regular jet formed by the reconstructed PF Candidates of the simulated particles. The response is then defined as:

$$R_{\mathrm{ptcl}}\left(\langle p_{\mathrm{T}}\rangle, \eta\right) = \frac{\langle p_{\mathrm{T}}\rangle}{\langle p_{\mathrm{T,ptcl}}\rangle}\left[p_{\mathrm{T,ptcl}}, \eta\right], \tag{5.3}$$

where $\langle p_{\mathrm{T}}\rangle$ and $\langle p_{\mathrm{T,ptcl}}\rangle$ are the average values of the transverse momenta of the jet and of the particle-level jet respectively, and η is the pseudorapidity of the jet. The L2L3 corrections make the response uniform over these two variables. As an example, Fig. 5.8 shows the L2L3 MC-truth correction factors (the inverse of R_{ptcl}) for anti-k_{T} PUPPI jets with $R = 0.8$, as a function of η for three p_{T} values. As mentioned above, we apply the L2L3 corrections for AK8 jets also to the AK15 jets used for the analysis presented here. The L2L3 corrections in the barrel ($|\eta| \lesssim 1.4$) are of the order of 10–20%, with a flat profile in η, while in the forward region the correction factor may rise up to a factor 2. The discontinuity at $|\eta| = 3$ is due to the limited ECAL and HCAL coverage, which extends only up to $|\eta| = 3$.

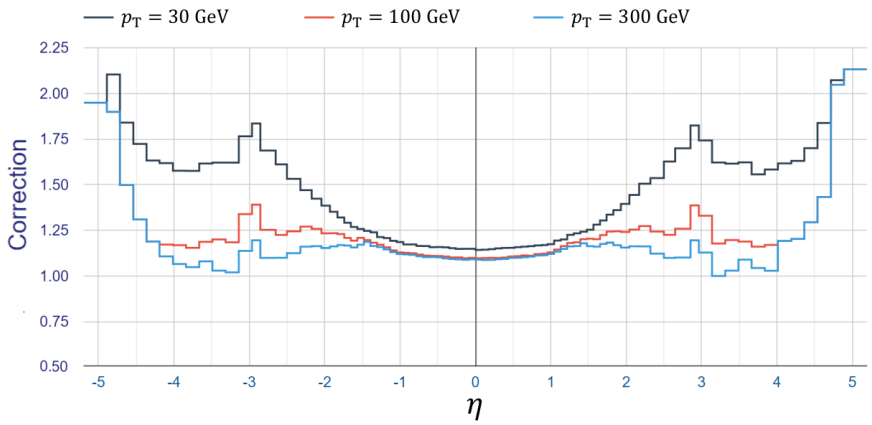

Figure 5.8. L2L3 MC-truth jet energy corrections for an anti-k_{T} PUPPI jets with $R = 0.8$ as a function of η, for three values of $p_{\mathrm{T}} = 30$, 100, 300 GeV

[2]The composite name depends on an old version of the JEC procedure, where the L2 and L3 jet corrections were two distinct levels.

5.4.2 L2L3 residual corrections

The L2 and L3 residual corrections are meant to correct for remaining small differences (of the order of few %) between jet response for data and MC. These are determined after correcting jets for pileup and having applied the L2L3 MC-truth corrections. The procedure is composed by two steps:

- the L2 residual corrections are first determined with a high statistics sample of dijet events, where the response of jets over a wide range of p_{T} is corrected relative to that of jets in the central part of the detector ($|\eta| < 1.3$). This gives a relative scale factor (i.e. relative to jets) as a function of jet pseudorapidity;
- in the second step L3 absolute corrections (i.e. they do not depend on the jet pseudorapidity) are then evaluated with a simultaneous fit to $Z(\rightarrow \mu\mu) + jet$, $Z(\rightarrow \mathrm{ee}) + jet$, $\gamma + jet$, and multijet data, for jets with $|\eta| < 1.3$ and a p_{T} between 30 GeV and 1 TeV.

The basic idea, for both the two steps and for all the considered topologies, is to exploit the p_{T} balance, at hard-scattering level, between the jet to be calibrated and a reference object: another jet, a photon, or an electron-positron (muon-antimuon) pair from a Z decay. If the detector response to jet energy is still different from unity after the application of the L2L3 MC corrections, the p_{T} of the reconstructed objects of the event is not balanced. The residual corrections are then derived by balancing the jet p_{T} with respect to that of the reference object. The L3 residual corrections, in particular, are derived using both the p_{T} balance and the MPF (missing transverse momentum projection fraction) methods [99].

It is beyond the purpose of this thesis to give a detailed description of all these methods, since each of these techniques is a stand-alone analysis. For a more complete treatment of the jet energy corrections derivation in CMS the reader can refer to Ref. [97].

The residual JECs are necessary because the data/MC ratio of responses is not equal to unity and it is p_{T} dependent. This is shown in Fig. 5.9, where the ratio between the L3 responses evaluated on data/MC is shown for collision data. The global fit to the points highlights the increasing trend of the ratio vs. the p_{T}, which is non-negligible with respect to the statistic and systematic uncertainties.

5.4.3 Jet energy scale uncertainties

The uncertainty on the L2L3 residual corrections is shown in Fig. 5.10 as a function of η for jets with $p_{\mathrm{T}} = 30$ GeV, and as a function of the p_{T} for jets with $|\eta| = 0$.

The jets relevant for this analysis are restricted in the central region of CMS, $|\eta| < 2.5$, and have a p_{T} above several hundreds of GeV. Hence, it is safe to assume an uncertainty on the jet energy scale of the 2%. In Sec. 8.2.1 we will see the effect of this uncertainty on the analysis results.

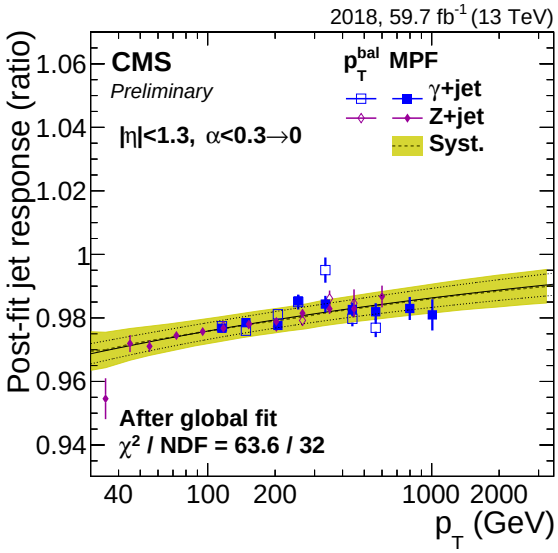

Figure 5.9. Global fit to the ratio of the jet response (line with yellow band) using the contribution of (γ+jets) (blue markers) and Z +jets (red markers) for 2018 data, from Ref. [98].

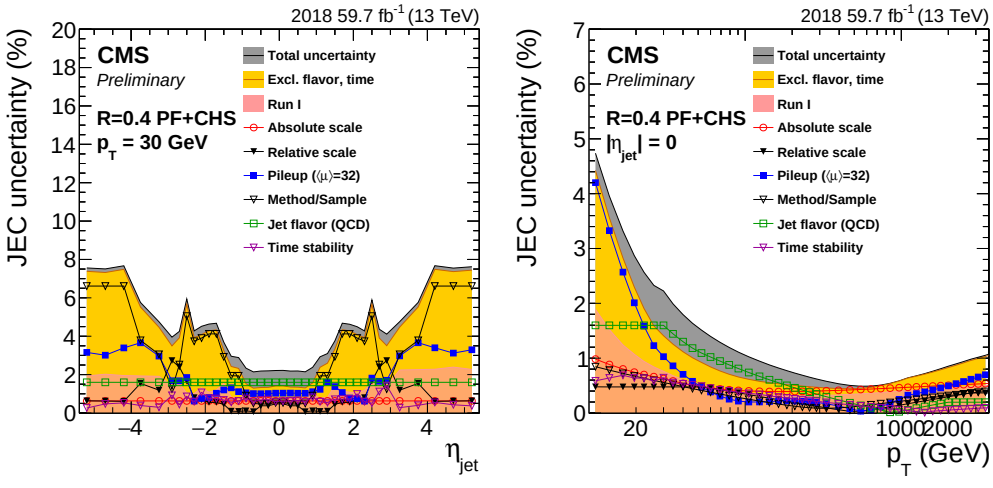

Figure 5.10. The uncertainties (from Ref. [98]) of L2 Residuals corrections versus η at $p_{\mathrm{T}} = 30\,\mathrm{GeV}$ (left),and L3 Residual corrections versus p_{T} at $\eta = 0$ (right).

5.5 Jet substructure variables

Jets produced by interactions at the LHC can be originated by boosted objects (t-quark, W, Z) that decay into quarks or gluons. Because of the Lorentz-boost, the quarks or gluons produced in the decay are collimated with respect to the p_{T} of the originating particle. Their resulting jets can be then reconstructed as a single jet, which shows a substructure formed by multiple subjets. Substructure variables are defined to quantify the properties of such jets, like their mass or the pattern of their constituents.

As introduced in Sec 3.3, the final state under study is formed by two jets, as schematically shown in Fig. 5.11. One of the two jets is originated by a parton (P_3) while the second from the decay of a new resonance (R_2) that decays into two partons (P_1 and P_2). In the assumption of the model under study the R_2 resonance is produced with large Lorentz-boost, and the two jets from the hadronization of P_1 and P_2 are reconstructed as a single jet.

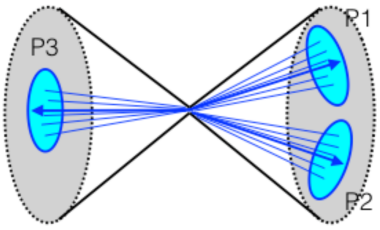

Figure 5.11. Jets topology of the final state of the process under study.

The aforementioned substructure variables can then be used to enhance the analysis sensitivity to this final state by identifying the jet from the R_2 decay among the large background populated by light-quark jets. In this Section we introduce two variables, the soft drop mass (m_{SD}) and the N-subjettiness ratio (τ_{21}), which are used in the analysis for this purpose.

5.5.1 Soft drop mass

The jets from the decay of a boosted object are characterized by a mass distribution which peaks at the value of the object mass. In our particular case, the boosted object originating the jet is the R_2 resonance in our signal model, which mass is much larger than the mass of a light quark. Hence, a jet from R_2 decay (R_2-jet) can be distinguished from a QCD jet using the jet mass.

If a jet is originated by a boosted object, the invariant mass of its constituents corresponds to the mass of the originating object. The mass of a QCD jet, instead, should be near to that of the originating parton. However, soft gluon radiation produced in the hadronization process can modify the reconstructed mass of the jet, giving it an average mass larger than that of the originating parton. The use of methods that remove the softer radiation, called jet grooming methods, corrects the jet mass of QCD jets, while maintaining the jet mass of other jets close to the mass of the originating boosted object.

In this thesis we apply the soft drop declustering algorithm [100] for the grooming of the jets. Like any grooming method, soft drop declustering mitigates the effects of jet contamination from initial state radiation, underlying event and pileup.

The soft drop criteria is based on the p_{T} and angular separation (ΔR) of the jet constituents. Assuming one jet with distance parameter R_0 formed by only two constituents, the softer constituent is removed unless:

$$\frac{\min(p_{\mathrm{T}1}, p_{\mathrm{T}2})}{p_{\mathrm{T}1} + p_{\mathrm{T}2}} > z_{cut} \left(\frac{\Delta R_{12}}{R_0} \right)^{\beta} \tag{5.4}$$

where $p_{\mathrm{T}i}$ are the transverse momenta of the constituents with respect to the beam, and ΔR_{12} is their angular separation. z_{cut} and β are two parameters of the model, respectively called soft drop threshold and angular exponent, which are set to the values $z_{cut} = 0.1$ and $\beta = 0$ in our analysis. These values optimize the algorithm results for standard searches at CMS.

The starting point for soft drop declustering is a jet with a characteristic radius (or distance parameter) R_0. In our analysis we will always consider jets defined with the anti-k_{T} (AK) algorithm, while the soft drop algorithm is based on jets defined with the Cambridge/Aachen (CA) algorithm. Therefore, the first step of the algorithm is the clustering of the original AK jet constituents with the CA algorithm. The constituents of the resulting jet are then organized in subjets as a pairwise clustering tree with an angular-ordered structure, as shown in Fig. 5.12 (left side).

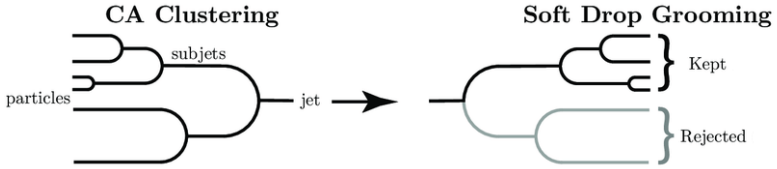

Figure 5.12. Scheme of the soft drop grooming algorithm.

The soft drop declustering procedure (Fig. 5.12, right) is implemented as follows:

- the jet j is divided into two subjets by undoing the last stage of CA clustering;
- if the subjets pass the soft drop condition of Eq. 5.4, j is the final soft drop jet;
- otherwise, j is redefined to be equal to subjet with larger p_{T} and the procedure is iterated;
- if j is reduced to be a single object without substructure, then j is removed from the list of jets.

The effect of the application of the soft drop algorithm to an MC simulated sample of R_2-jets and QCD jets is reported in Fig. 5.13. As can be seen, the algorithm "shifts" the QCD peak towards lower values and improves the resolution of the R_2 peak with respect to the scenario where the algorithm is not applied. The Fig. 5.13 (left) shows also an increase in the distribution of the R_2-jet soft drop mass at low mass values. This effect is caused by a small fraction of events where the soft drop algorithm removes a large part of the constituents from one of the two gluons

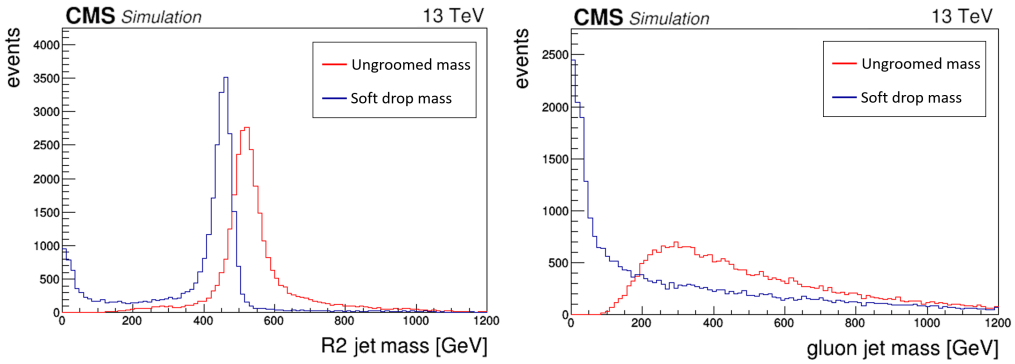

Figure 5.13. Distribution of the jet mass for R_2 (left) and QCD jets (right) from simulations. The blue and red distributions are respectively evaluated with and without the application of the soft drop algorithm.

from the R_2 decay. The resulting R_2-jet mass is then similar to that of a QCD jet for these events.

5.5.2 N-subjettiness ratio

The jets from the decay of a boosted object are characterized by a substructure in the patterns of particles inside the jet. For example, in the case of the R_2 resonance under study, particles produced by the hadronization of partons P_1 and P_2 have trajectories that are clustered around two axis, forming a dipolar substructure inside the jet, as shown in Fig. 5.14 (left).

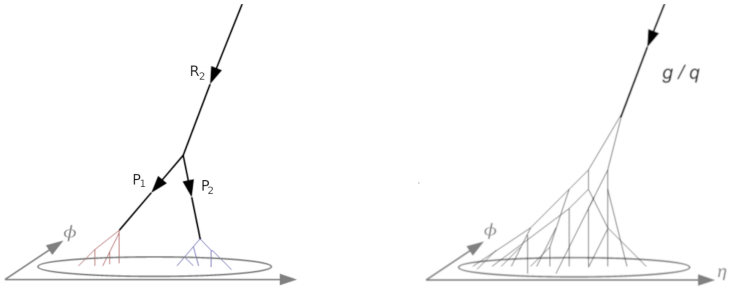

Figure 5.14. Schematic of the pattern of the particles inside a jet from the decay of a resonance R_2 into two partons (left), compared to that of a jet from the hadronization of a quark/gluon (right). In the first case a dipolar substructure, where the particle trajectories are clustered around two axis of partons P_1 and P_2, is clearly shown.

The substructure of a jet can be identified using variables defined for this purpose. In this analysis we use a variable which has a strong discrimination power and is, at the same time, easy to understand. The N-subjettiness variable [101] aims to quantify how it is likely that one jet has a substructure formed by N subjets by exploiting the p_{T} and trajectory information of particles inside the jet. At first, N subjet candidates are identified within a jet, using the exclusive-k_{T} clustering algorithm [102, 103], forcing it to return exactly N jets. The N-subjettiness (τ_N) is then defined as:

$$\tau_N = \frac{1}{d_0} \sum_k p_{\mathrm{T},k} \min \Delta R_{1,k}, \Delta R_{2,k}, ..., \Delta R_{N,k} \tag{5.5}$$

where k runs over the constituent particles in a given jet, $p_{\mathrm{T},k}$ are their transverse momenta, and $\Delta R_{J,k} = \sqrt{(\Delta\eta)^2 + (\Delta\phi)^2}$ is the distance in the $\eta\phi$-plane between a candidate subjet J and a constituent particle k. The normalization factor d_0 is:

$$d_0 = \sum_k p_{\mathrm{T},k} R_0 \tag{5.6}$$

where R_0 is the jet distance parameter used in the original jet clustering algorithm.

It is straightforward to see, from the definition of τ_N, that jets formed by N subjets correspond to $\tau_N \approx 0$, since they have all their radiation aligned with the candidate subjet directions. Jets with $\tau_N \gg 0$ have a large fraction of their energy distributed away from the candidate subjet directions and therefore tend to have at least $N + 1$ subjets. In our particular case, where we want to identify a jet from a two-body decay from a QCD jet, the N-subjettines variable of interest are τ_1 and τ_2.

They can be combined in a single variable that has a better discriminating power with respect to the two variables taken individually, the N-subjettiness ratio:

$$\tau_{21} = \frac{\tau_2}{\tau_1} \tag{5.7}$$

As a consequence of the τ_2 and τ_1 definitions, the τ_{21} values for jets with a dipolar substructure tend to be lower than those of a QCD jet. The τ_{21} distributions for an R_2-jet and a QCD jet are reported in Fig. 5.15. The simulated R_2 and the gluon jets have a p_T of ~2.5 TeV and the value of the R_2 mass is $m(R_2) = 1$ TeV. The R_2 is produced by the decay of a resonance R_1 with a mass of $m(R_1) = 5$ TeV, therefore $\rho_m = m(R_2)/m(R_1) = 0.2$. The difference between the two distributions shows the discriminating power of the τ_{21} variable. The criterion for the jets identification used in our analysis, based on τ_{21}, is described in Sec. 7.1.

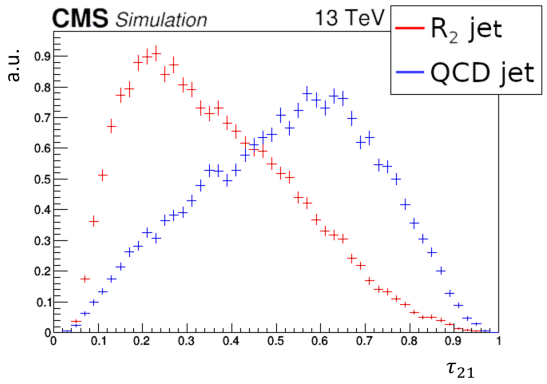

Figure 5.15. Distributions of τ_{21} for simulated jets from R_2 decay (R_2-jets) and from the hadronization of a gluon (QCD-jets). The simulated R_2 and the gluon jets have a p_T of ~2.5 TeV and the value of the R_2 mass is $m(R_2) = 1$ TeV. Each distribution is normalized to its integral. As expected, the τ_{21} distribution of R_2-jets peaks at lower values with respect to that of QCD jets.

Chapter 6

Data samples and event selection

6.1 Dataset and trigger selection

The analysis presented in this thesis uses pp collision data at a center-of-mass energy of 13 TeV collected with the CMS detector at the LHC in 2016, 2017, and 2018, corresponding to an integrated luminosity of $138\,\text{fb}^{-1}$.

We search signals in final states with a dijet-like signature, characterized by two jets with p_T above few hundreds of GeV which have a back-to-back topology in the plane transverse to the beam axis. In addition to that, one of the two jet originates from the decay of a boosted dijet resonance R_2, from the cascade resonance decay described in Sec. 3.3. Dijet-like events are mostly collected in the `JetHT` primary dataset [104], which is defined by the OR of all the high-level trigger (HLT) paths that require jets in the final state (Sec. 4.2.7).

The `JetHT` dataset is divided into three subdatasets corresponding to the three yeas of data-taking, with integrated luminosity of 36.3, 41.5 and $59.7\,\text{fb}^{-1}$, respectively for the 2016, 2017 and 2018 datasets. The LHC conditions are different among the three years. For example, the average instantaneous luminosity was smaller in 2016 than in the other years. Moreover, the calibration of the CMS subdetectors is performed independently for each year, as they age with the radiation damage. However, as we will see in Sec. 6.4, after the application of the jet energy corrections, the distributions of the reconstructed jet variables are similar across the three years. Hence, the data can be merged and analyzed as a single dataset.

Events are selected from the `JetHT` dataset applying a trigger strategy similar to that of CMS inclusive dijet analyses at $\sqrt{s} = 13\,\text{TeV}$ (Sec. 3.1). The selected triggers are designed to collect most of the events at high dijet mass (m_jj), interesting for our analysis. They require an AK4 or AK8 jet with a p_T above few hundreds of GeV, or a value of H_T above $\sim$1 TeV, where H_T is the scalar sum of the p_T of all jets in the event with $p_\text{T} > 30\,\text{GeV}$ and $|\eta| < 3.0$.

For our analysis, where one of the two jet is a massive jet from the decay of a resonance, we also include triggers which, in addition to requirements on p_T and H_T, also require the jet to have a mass above $\sim$50 GeV. In this case the mass of a jet, called trimmed mass (m_trim), is evaluated after the application of the trimming

algorithm [105], which is a grooming algorithm similar to the soft drop algorithm described in Sec. 5.5.1. The trimming algorithm is faster from a computational point of view, so it is more suitable to be applied to the jets used at the HLT.

The trigger paths and their definitions are summarized in Tab. 6.1. The p_{T} and H_{T} thresholds are different for the different years of data taking, mainly because the instantaneous luminosity was higher during 2017 and 2018. Hence, higher thresholds has been necessary to keep the trigger rate at an acceptable level, rejecting events with softer interactions.

Table 6.1. Jet triggers and their definition.

Year	Trigger path	definition
2016	`HLT_PFJet500_v*`	one AK4 jet with $p_{\mathrm{T}} > 500\,\mathrm{GeV}$
	`HLT_AK8PFJet500_v*`	one AK8 jet with $p_{\mathrm{T}} > 500\,\mathrm{GeV}$
	`HLT_PFHT900_v*`	$H_{\mathrm{T}} > 900\,\mathrm{GeV}$
	`HLT_AK8PFJet360_TrimMass30_v*`	one AK8 jet with $p_{\mathrm{T}} > 360\,\mathrm{GeV}$ and $m_{\mathrm{trim}} > 30\,\mathrm{GeV}$
	`HLT_AK8PFHT800TrimMass50_v*`	$H_{\mathrm{T}} > 800\,\mathrm{GeV}$ for AK8 jets with $m_{\mathrm{trim}} > 50\,\mathrm{GeV}$
2017 and 2018	`HLT_PFJet550_v*`	one AK4 jet with $p_{\mathrm{T}} > 550\,\mathrm{GeV}$
	`HLT_AK8PFJet550_v*`	one AK8 jet with $p_{\mathrm{T}} > 550\,\mathrm{GeV}$
	`HLT_PFHT1050_v*`	$H_{\mathrm{T}} > 1050\,\mathrm{GeV}$
	`HLT_AK8PFJet420_TrimMass30_v*`	one AK8 jet with $p_{\mathrm{T}} > 420\,\mathrm{GeV}$ and $m_{\mathrm{trim}} > 30\,\mathrm{GeV}$
	`HLT_AK8PFHT900TrimMass50_v*`	$H_{\mathrm{T}} > 900\,\mathrm{GeV}$ for AK8 jets with $m_{\mathrm{trim}} > 50\,\mathrm{GeV}$

The thresholds on the jets p_{T} and H_{T}, in fact, reduce the trigger efficiency for events below a certain dijet mass threshold, causing a distortion of the dijet mass spectrum. This effect is known as trigger "turn on". It is important then to study the trigger efficiency curve versus m_{jj}, in order to decide where we can start to fit the m_{jj} distribution in data without being affected by the turn on.

The trigger efficiency can be measured using a reference data sample and a reference trigger uncorrelated with the `JetHT` dataset. For this study we use the `SingleMuon` datasets with `HLT_Mu50_v*` as reference trigger. This dataset contains all the events that pass triggers requiring one or more muons, while the `HLT_Mu50_v*` trigger specifically requires at least one muon with $p_{\mathrm{T}} > 50\,\mathrm{GeV}$. Muon datasets and triggers provide a good reference for jet triggers because the request of a muon is completely independent from the jets in the event.

We can then measure the efficiency of the jet triggers as:

$$\varepsilon = \frac{N(\mu \cap jets)}{N(\mu)} \tag{6.1}$$

where:

- $N(\mu)$ is the number of events in the `SingleMuon` dataset that satisfy both the reference trigger `HLT_Mu50_v*` AND the selection criteria we apply in our analysis (Sec. 6.3);

- $N(\mu \cap jets)$ is the number of events in the `SingleMuon` dataset that satisfy the same requirements of the denominator AND of any of the dijet triggers from Tab. 6.1.

We then obtain the curves of the ε as a function of m_{jj}, for the different years of data taking (Fig. 6.1). The curves show that the trigger reaches the full efficiency for $m_{jj} > 1.6\,\text{TeV}$ for all the three years. In our analysis the we select only events with $m_{jj} > 1.6\,\text{TeV}$ in order to avoid the turn on effect. The use of the same m_{jj} threshold for the three years allows us to analyze all the data together. We chose then to fit only in m_{jj} ranges where the trigger is fully efficient, because the modeling of the turn on effect of the m_{jj} spectra would be a delicate procedure that could easily introduce biases in the fit. The calculation of upper limits on the cross sections starts from R_1 masses of 2 TeV, because, for signals with lower R_1 masses, a large portion of the signal shape in m_{jj} would be truncated by the fit range, introducing biases in the fit procedure.

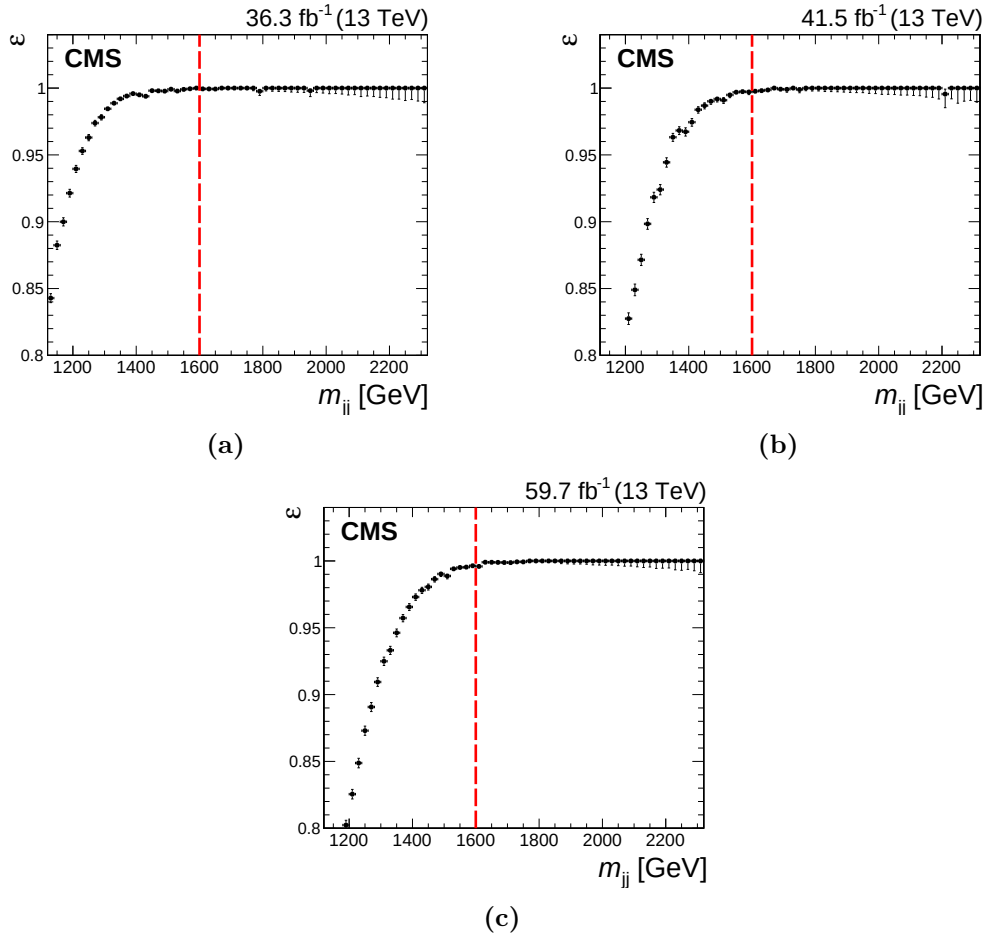

Figure 6.1. Trigger efficiency as function of m_{jj}, for the three years of data-taking: (a) 2016, (b) 2017, (c) 2018. The red dashed line marks the m_{jj} minimum threshold where the trigger is fully efficient for each of the three years: $m_{jj} = 1.6\,\text{TeV}$

6.2 Monte Carlo simulation

6.2.1 Signal samples

We consider, as benchmark model of our analysis, the cascade decay of a KK gluon (G_{KK}) in a SM gluon (g) and a radion (ϕ), which in turns decay into two gluons (Sec. 2.2.2). The overall decay chain is: $q\bar{q} \to G_{KK} \to \phi + g \to ggg$.

The Monte Carlo (MC) simulations of the signal samples have been produced for different values of the KK gluon mass ($m(G_{KK})$) and of the mass ratio $\rho_m = m(\phi)/m(G_{KK})$, where $m(\phi)$ is the radion mass. The specific choice of coupling parameters used in the generation does not affect the decay kinematic distributions but only modifies the signal cross section. For this reason, the signal selection efficiencies and distributions of kinematic observables, estimated using the simulated samples, are valid for all the possible choices of coupling parameters. A total of 24 MC samples has been generated, for 8 $m(G_{KK})$ values:2, 3, 4, 5, 6, 7, 8, and 9 TeV, and for three values of ρ_m = 0.1, 0.2, 0.3. In order to perform the analysis on intermediate $m(G_{KK})$ and ρ_m values, the signal shapes obtained from the simulated samples have been interpolated as described in Secs. 7.3.3.1 and 7.3.3.2. The interpolation steps are 100 GeV wide in $m(G_{KK})$ and 0.01125 wide in ρ_m.

The signal MC simulated samples are generated with MadGraph5_aMC@NLO v. 2.4.3 [106], using the next-to-next-to-leading order (NNLO) set of parton distribution functions (PDF) NNPDF3.1 [107]. Parton branching and hadronization are simulated with pythia 8.205 [108] with the CP5 [109] underlying event tune. All simulated samples are processed with the full simulation of the CMS detector based on the Geant4 [110] software, and they are reconstructed with the same suite of programs used for collision data.

The samples used have been generated in the 2017 production campaign, using the conditions of the 2017 data-taking. As we will see in Sec. 6.4.2, the differences between 2016, 2017 and 2018 data are negligible with respect to the statistical and systematic uncertainties. This justifies the use the 2017 signal MC samples for the analysis of the full Run 2 dataset.

6.2.2 Background samples

The only relevant background for the search here presented arises from SM QCD processes with multiple jets in the final state (QCD multijet background). Samples of the QCD multijet background are simulated with pythia 8.205 with the same set of PDFs, the same tune, and the same simulation of the CMS detector used for signal samples. The MC simulated samples for the QCD multijet background are produced for different bins of $\hat{p_T}$, the transverse momentum of the hard scattering process. The list of simulated background datasets with the corresponding cross section, number of events, and equivalent integrated luminosity is reported in Tab. 6.2.

As in standard CMS dijet searches, the simulation is not used to estimate the QCD multijet background, which is derived directly from a fit to data, as described in Sec. 7.3. Hence, QCD simulated samples are only used to perform checks on the overall quality of the data (Sec. 6.4), and to test the fit strategy before its application to data.

The analysis procedure followed a blinding policy during its early stages. The analysis strategy and the fit procedure, both described in Ch. 7, have been applied first to the simulated sample of QCD multijet events and then to data, after several tests of the fit performances and checks for the presence of bias or other issues.

The QCD multijet background samples, like the signal samples, are simulated assuming the 2017 conditions. Since the differences between the three years in data are relatively small, it is possible to compare the 2017 QCD simulated sample also with data from other years.

Table 6.2. The MC simulated samples of QCD multijet events used in the analysis. The linear order (LO) cross section, the number of generated events and the equivalent integrated luminosity are also reported for each sample.

dataset p_{T} bin (GeV)	LO cross section [pb]	number of events	Equiv. $\mathcal{L}_{\mathrm{int}}[\,\mathrm{fb}^{-1}\,]$
QCD $300 < p_{\mathrm{T}} < 470$	7475	53798780	7.2
QCD $470 < p_{\mathrm{T}} < 600$	587	27881028	47.5
QCD $600 < p_{\mathrm{T}} < 800$	167	66134964	396
QCD $800 < p_{\mathrm{T}} < 1000$	28.25	39529008	1399
QCD $1000 < p_{\mathrm{T}} < 1400$	8.195	19631814	2396
QCD $1400 < p_{\mathrm{T}} < 1800$	0.7346	5685270	7739
QCD $1800 < p_{\mathrm{T}} < 2400$	0.102	2923941	$28.7\ 10^3$
QCD $2400 < p_{\mathrm{T}} < 3200$	0.00644	1910526	$29.7\ 10^4$
QCD $p_{\mathrm{T}} > 3200$	0.000163	757837	$46.5\ 10^5$

6.3 Selection criteria

Events in data and in simulated samples are reconstructed using jets defined with the anti-k_{T} clustering algorithm introduced in Sec. 5.2 with $R = 1.5$ (AK15 jets). The value of R chosen is larger compared to those commonly used in CMS analyses in order to better reconstruct the final state of the process under study (Sec. 3.3). The jet width has been chosen to be large enough to collect the products of R_2 decay within the same jet, and also to collect more effectively the radiation emitted from the parton P_3 in its hadronization. This improves the resolution of the reconstructed R_1 resonance mass ($m(\mathrm{R}_1)$), as shown in Fig. 6.3 at the end of this Section.

An event selection is applied to all events of the `JetHT` dataset and of the simulated samples that match the trigger requirements. This selection aims to remove spurious events with poorly reconstructed jets and to filter background events enhancing the signal-to-background ratio.

To pass the selection, the two AK15 jets with highest p_{T} (leading jets) in the event have to satisfy the following requirements:

- both jets have to satisfy jet quality criteria ("jet ID") that remove spurious jets associated with calorimeter and/or readout electronics noise (see Ref. [95] for the latest jet ID criteria);
- both jets should have $p_{\mathrm{T}} > 100\,\mathrm{GeV}$ and $|\eta| < 2.5$;

- their dijet mass has to be $m_{\mathrm{jj}} > 1.6\,\mathrm{TeV}$ in order to avoid the distortion of the m_{jj} spectrum caused by the trigger turn on (Sec. 6.1);
- the pseudorapidity separation between the two jets $\Delta\eta_{\mathrm{jj}} = |\eta_{j1} - \eta_{j2}|$ is required to be $\Delta\eta_{\mathrm{jj}} < 1.3$.

The latter requirement suppresses the QCD multijet background, which mainly populates the region at high $\Delta\eta_{\mathrm{jj}}$ since it originates from t-channel processes, while the distribution of signal events decreases with increasing $\Delta\eta_{\mathrm{jj}}$ because it is formed by s-channel processes (see Fig. 6.2). This requirement also makes the trigger efficiency in Fig. 6.1 rise quickly, reaching a plateau at 100% for relatively low values of dijet mass. This is because the jet p_{T} threshold of the trigger at a fixed dijet mass is more easily satisfied at low $|\Delta\eta|$, as seen by the approximate relation $m_{\mathrm{jj}} \approx 2p_{\mathrm{T}} \cosh|\Delta\eta|/2$. This requirement on $\Delta\eta_{\mathrm{jj}}$ has been found to maximize the sensitivity of previous searches for dijet resonances in the presence of QCD multijet background [52]. The analysis of simulated samples shows that the $\Delta\eta_{\mathrm{jj}}$ requirement reduces the background by the ∼80% with respect to the number of events passing the other requirements.

The signal efficiency for all the kinematic requirements is between 40 and 50% for all signal hypotheses considered.

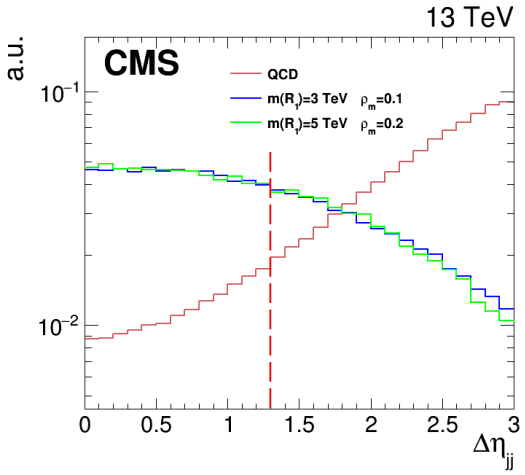

Figure 6.2. Distribution of $\Delta\eta_{\mathrm{jj}}$ for a simulated samples of background events (red line) and two simulated samples of signal events (green and blue) with different $m(\mathrm{R}_1)$ and ρ_{m} values.

In Figure 6.3 we show the m_{jj} distribution for a simulated signal sample with $m(\mathrm{R}_1) = 3\,\mathrm{TeV}$ and $m(\mathrm{R}_2) = 0.6\,\mathrm{TeV}$, obtained after the event selection described above. The figure shows also the m_{jj} distributions evaluated using anti-k_{T} jets with different values of the distance parameter. The AK15 jets show better performances in terms of resolution of the R_1 peak with respect to jets with a smaller distance parameter. In the following, unless otherwise stated, we will refer to AK15 jets simply as jets.

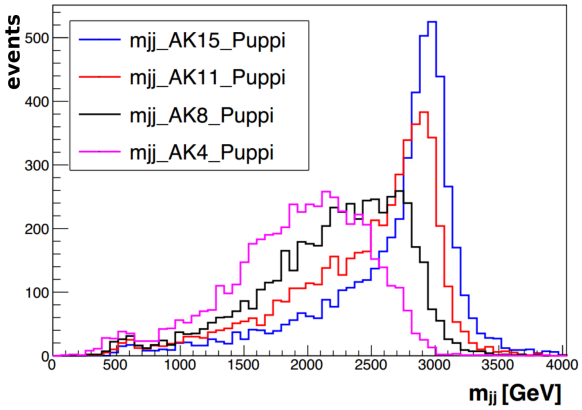

Figure 6.3. Distributions of the dijet mass from a simulation of signal events with $m(\mathrm{R}_1) = 3\,\mathrm{TeV}$ and $m(\mathrm{R}_2) = 0.6\,\mathrm{TeV}$. The different distributions are obtained with anti-k_T jets with different values of the distance parameter: $R = 0.4$, 0.8, 1.1, 1.5. The AK15 jets with $R = 1.5$ show the best resolution for the R_1 peak.

6.4 Data control plots

We performed detailed data quality checks on events passing the selection. They include the comparison between data from different years and the comparison between the data and the simulation. The results of these checks are reported in the following sections.

6.4.1 Comparison between data from different years

In this section we compare the distributions of the various kinematic variables for the data collected over the different years. The selection of events described in Sec. 6.3 is applied to each dataset.

Figures from 6.4 to 6.6 show the comparisons for the distributions in data of the dijet mass (m_{jj}) of the two leading jets in p_T (j_1 and j_2), their absolute η separation $\Delta\eta_{\mathrm{jj}} = |\eta_{j1} - \eta_{j2}|$, and their absolute ϕ separation $\Delta\phi_{\mathrm{jj}} = |\phi_{j1} - \phi_{j2}|$. The distributions for 2016 and 2018 data are rescaled to the luminosity of the 2017 dataset ($41.5\,\mathrm{fb}^{-1}$) and compared with it.

In Fig. 6.4 we observe, as expected, that the number of dijet events produced decrease smoothly as a function of the dijet mass. Comparison plots show an overall good agreement for all the distributions considered. Hence, we can merge datasets from different years and analyze them all at once. The difference in the m_{jj} distributions of the 2017 with respect to the other two years are contained within the uncertainty on the jet energy scale, which is of $\sim$2%.

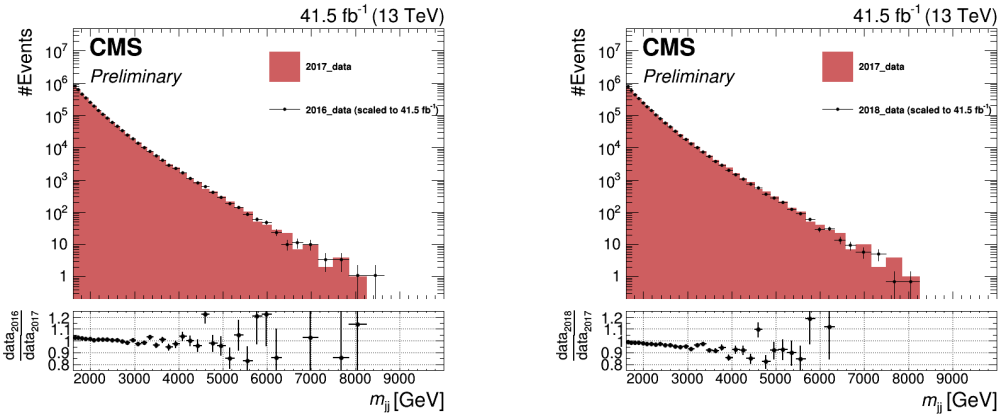

Figure 6.4. Distributions of m_{jj}: comparison between 2016, 2017 and 2018 data (scaled to 2017 luminosity).

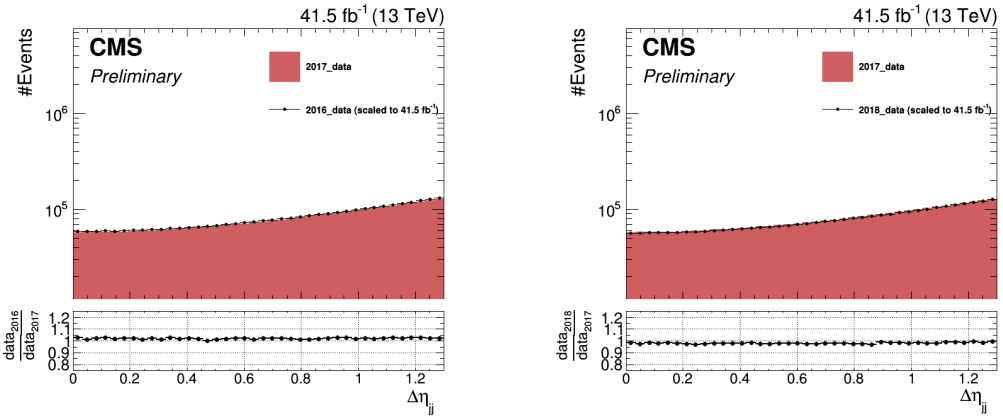

Figure 6.5. Distribution of $\Delta\eta_{jj}$: comparison between 2016, 2017 and 2018 data (scaled to 2017 luminosity).

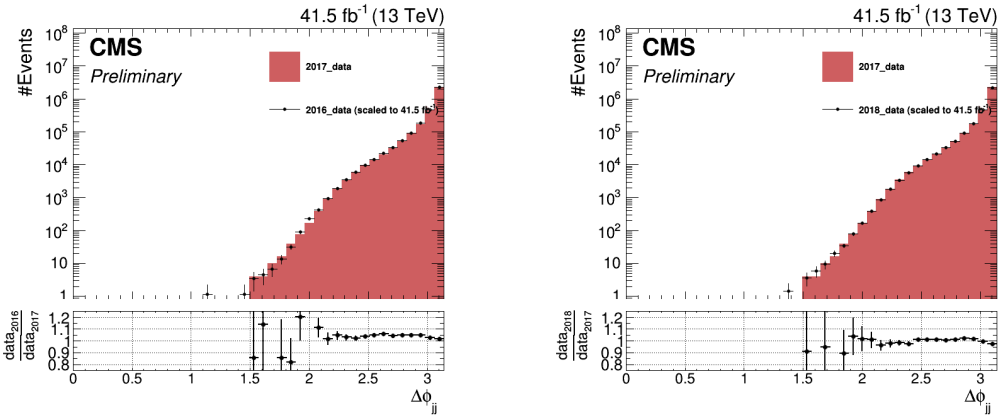

Figure 6.6. Distribution of $\Delta\phi_{jj}$: comparison between 2016, 2017 and 2018 data (scaled to 2017 luminosity).

6.4.2 Comparison between data and simulation

In this Section we compare the distributions of the various kinematic variables for the data with the simulated sample of QCD multijet background processes.

Figure 6.7 shows the distributions of several kinematic variables for the full Run 2 dataset. Each data distribution is compared to the corresponding one from the QCD simulated sample. The distributions for two examples of simulated signal samples are also shown. Each simulated sample is generated with the 2017 conditions and it is scaled to match the Run 2 integrated luminosity because, as seen in Sec. 6.4.1, data from different years shows similar distributions. The event distributions in data show an acceptable level of agreement to those from simulated QCD samples in most of the cases, ensuring that the data sample is not affected by pathologies.

The m_{jj} distribution (Fig. 6.7a) shows in particular the expected smoothly decreasing trend, which is in acceptable agreement with the background prediction. The variable-sized binning of the m_{jj} spectrum is chosen in order to have the bin size is similar to the experimental resolution at the mass value of the bin center (see Appendix D). The two signal samples shown correspond to a cross section of 1 pb, about 100–1000 times the expected limit. The $\Delta\eta_{\mathrm{jj}}$ and $\Delta\phi_{\mathrm{jj}}$ distributions also behave as expected (Figs. 6.7b and 6.7c). The discrepancy between data and simulation for the $\Delta\phi_{\mathrm{jj}}$ distribution does not have impact on the analysis, since the background is not modeled with simulated events when testing for a signal. This distribution ensures that the vast majority of the events follows the dijet topology, with two jets which are back-to-back in the x–y plane.

Figure 6.7d shows the overall distributions of the p_{T} of the two leading jets (labeled as j_1 and j_2). The distribution of p_{T} shows some discrepancy with respect to the simulation. However, also in this case it does not affect the analysis since because the simulation is not used to model the background. The η distribution (Fig. 6.7e) is the overall distributions of the η coordinate of the two leading jets. It shows a deficit in the data with respect to the simulation for $|\eta| > 2$. This effect is due to a slowly developing shift in the shape of the ECAL pulses, caused by radiation damage, which reduced the L1 trigger efficiency in data for jets with $|\eta| > 2$. This effect is known as ECAL prefiring, and we refer to Ref. [111] for further details. We do not correct for this effect in our analysis, since the prefiring affects only a small portion of events in a region of η with very low signal yield.

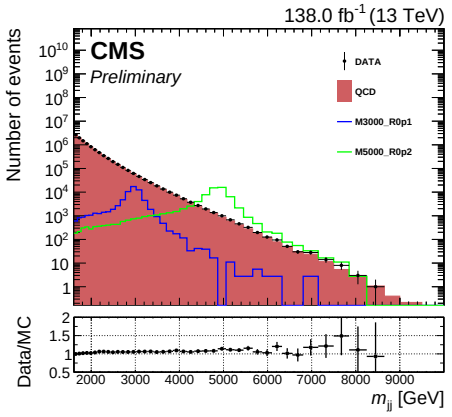

(a) m_{jj}

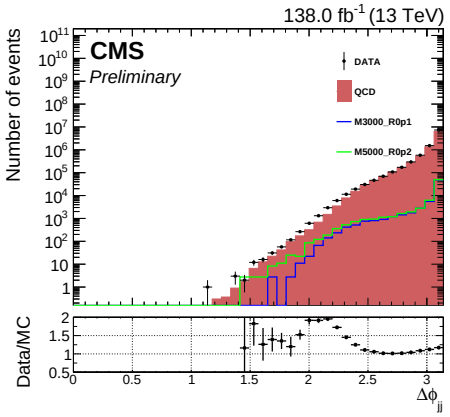

(b) $\Delta\phi_{jj}$

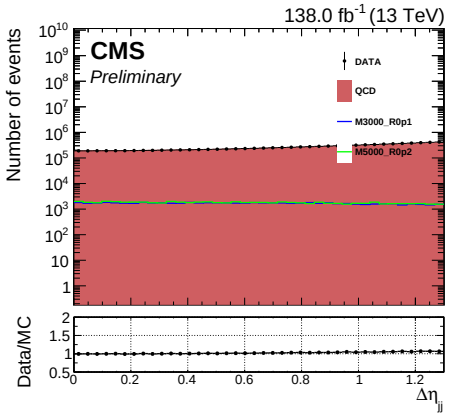

(c) $\Delta\eta_{jj}$

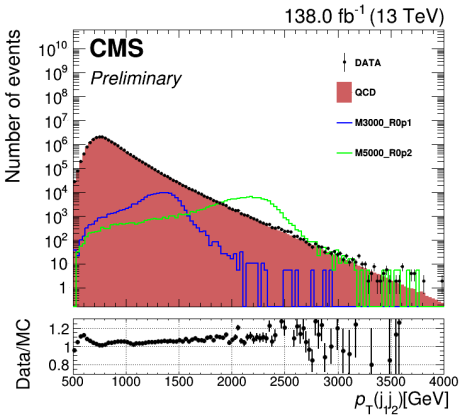

(d) $p_{\mathrm{T}}(j_1, j_2)$

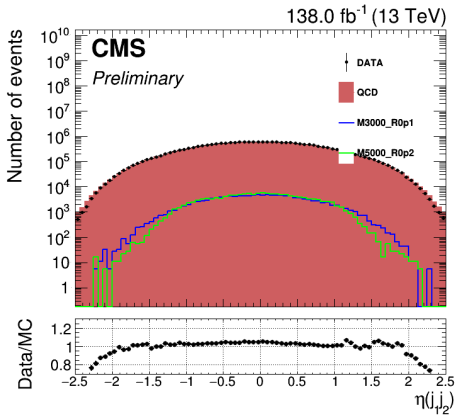

(e) $\eta(j_1, j_2)$

Figure 6.7. Comparison between all years data and simulated samples for the distributions of the dijet mass m_{jj}, $\Delta\eta_{\mathrm{jj}}$, $\Delta\phi_{jj}$. The distributions of two simulated signal samples are also shown. They correspond to signal hypotheses with $m(\mathrm{R}_1) = 3\,\mathrm{TeV}$ and $\rho_{\mathrm{m}} = 0.1$ (M3000_R0p1), and $m(\mathrm{R}_1) = 5\,\mathrm{TeV}$ and $\rho_{\mathrm{m}} = 0.2$ (M5000_R0p2). The simulated signal cross section is of 1 pb, which is two–three orders of magnitude larger than the expected cross section limit of this search.

Chapter 7

Analysis strategy

The search strategy described in this Chapter is oriented to get the best sensitivity for new resonances (R_1) decaying into a jet and a second resonance (R_2) in the process described in Sec. 3.3.

The final state topology we are interested in is characterized by two high p_T jets. The invariant mass of the two jets (m_{jj}), is compatible with $m(R_1)$, and one of the two jets has a dipolar substructure and a mass compatible with $m(R_2)$. The peculiar properties of this final state topology are exploited to discriminate the signal from the background events.

The jet from R_2 decay (R_2-jet) is identified from its substructure properties. The events are then divided into categories applying selections based on the masses of the two reconstructed jets, according to the hypothesis that one of the two jets has a mass compatible with $m(R_2)$. We then search for a peak corresponding to the R_1 resonance in the m_{jj} spectra of all the event categories, which are mostly populated by events from the QCD multijet background.

The next Sections will describe then the categories definition and the method used for the fit to the m_{jj} spectra, reporting also the fit quality checks performed.

7.1 Jets identification

The N-subjettiness ratio (τ_{21}), introduced in Sec. 5.5.2, is evaluated for each jet in each selected event and the jet with the lower value of τ_{21}, among the two jets with highest p_T, is labeled as the R_2-jet candidate, while other is labeled as P_3-jet.

In Fig. 7.1 , we report the distribution of the R_2-jet and P_3 jet masses for the data, the simulated QCD multijet background, and two signal samples. The jet masses are evaluated after the application of the soft drop grooming algorithm (m_{SD}) described in Sec. 5.5.1. As expected, the R_2-jet mass distribution of signal events is characterized by a peak at $m(R_2)$. However, a smaller peak corresponding to $m(R_2)$ appears also the P_3-jet mass distribution of signal events. The latter peak arises from events where the two jets are wrongly identified by the criterion described above.

The frequency of the errors in the identification method is estimated by analyzing the Monte Carlo (MC) simulations of signal events (listed in Sec. 6.2). The fractions of simulated events where the two jets are correctly matched with the method

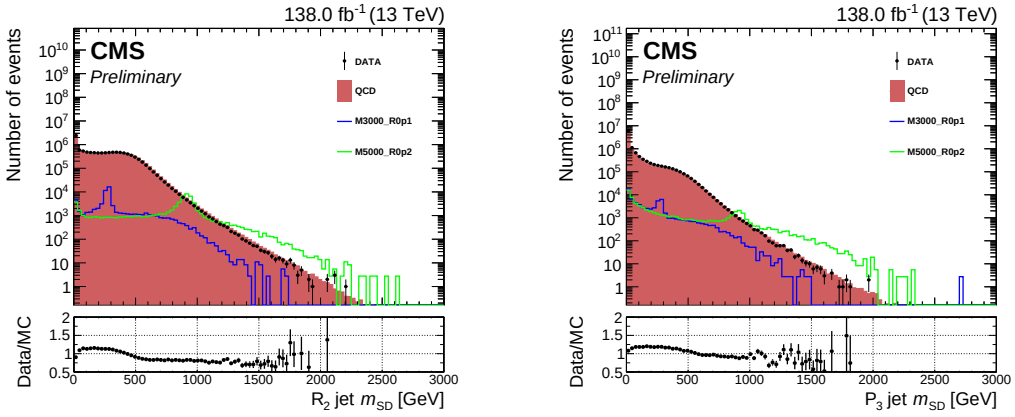

(a) R_2-jet soft drop mass **(b)** P_3-jet soft drop mass

Figure 7.1. Comparison between all years data and simulated samples for the distributions of the jet soft drop masses. The distributions of two simulated signal samples are also shown. They correspond to signal hypotheses with $m(R_1) = 3\,\text{TeV}$ and $\rho_m = 0.1$ (M3000_R0p1), and $m(R_1) = 5\,\text{TeV}$ and $\rho_m = 0.2$ (M5000_R0p2). The simulated signal cross section is of 1 pb, which is two–three orders of magnitude larger than the expected cross section limit of this search. The Figure on the left shows a peak in the distribution of signal events at $m(R_2)$ formed by events where the two jets are correctly matched. The peak in the distribution of signal events in the right plot, instead, arises from events where the two jets are wrongly identified by the τ_{21} based algorithm.

described above is reported in Fig. 7.2. The values range from 0.62 to 0.72 for the different values of $m(R_1)$ and ρ_m. This means that the algorithm wrongly identifies the jets about 30-40% of the times.

We also studied the performance of an alternative identification method where the R_2-jet is defined as the jet with the greatest mass among the two leading jets. This method has similar performances as the previous one. The jets are correctly matched in a fraction of events ranging from 0.58 to 0.75 for the various signal hypotheses. We decided to use the τ_{21} based identification method since it does not depend on the jet mass, which is the variable used to divide event into categories as explained in Sec. 7.2.

It could be possible to use the jet substructure variables to design more sophisticated algorithms for the jet identification. For this analysis, which is the first to explore the decay process with two new hadronic resonances, we decided to use the simple method described above. The effect of the identification errors is then mitigated by the analysis strategy, as described in the following.

The effect of the identification errors is visible in Fig. 7.3, which shows the distribution of the simulated signal events in the m_{Rjet} vs. m_{Pjet} plane, where m_{Rjet} and m_{Pjet} are respectively the reconstructed masses of the R_2-jet and the P_3-jet, for a particular signal hypothesis with $m(R_1) = 5\,\text{TeV}$ and $\rho_m = 0.1$. The blue and the red dots represent respectively the events with correct and incorrect jet assignment.

As expected, the blue distribution is concentrated at $m_{\text{Rjet}} \approx m(R_2)$ and $m_{\text{Pjet}} \approx 0$. This is consistent with an R_2-jet from the decay of the R_2 resonance and a P_3-jet from the hadronization of a parton. The red distribution, instead, arises from

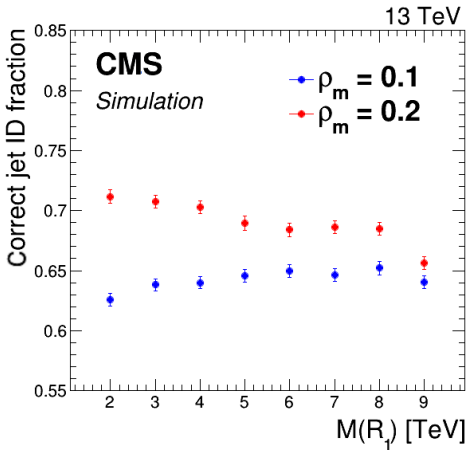

Figure 7.2. Fractions of events where the two jets with highest p_T are correctly matched with R_2 and P_3, from simulated signal samples with $m(R_1)$ between 2 and 9 TeV and ρ_m = 0.1; 0.2.

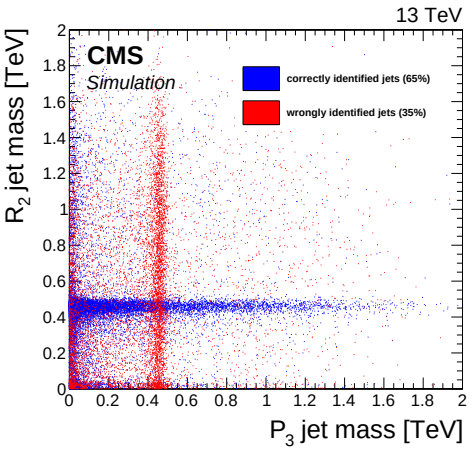

Figure 7.3. Distribution of events with correctly and wrongly identified jets in the m_{Rjet} vs. m_{Pjet} plane, for a simulated signal sample with $m(R_1)$ = 5 TeV and $\rho_m = 0.1$.

events where the two jets are wrongly identified, therefore the P_3-jet has a mass $m_{Pjet} \approx m(R_2)$.

The event categories, defined in Sec. 7.2, are designed following the signal cross pattern of Fig. 7.3. This choice takes advantage of the particular distribution of signal events in the m_{Rjet} vs. m_{Pjet} plane to distinguish the signal from the background, as will be further explained in the next Section.

In Fig. 7.4 we show the τ_{21} distributions for the two jets. The identification method, based on τ_{21}, clearly produces different τ_{21} distributions for the two jets. The discrepancies between the two distributions in the data and in the simulation suggest that the patterns of the particles produced in jet showering are not described by the simulation with the necessary precision. Based on the smearing necessary to remove the discrepancy between τ_{21} distributions in data and simulation, we associated to τ_{21} a relative systematic uncertainty of 10%. The effect of this uncertainty on the analysis results will be described in Sec. 8.2.1.

7.2 Event division in categories

After the identification of the jets, the events are divided into categories which are designed to enhance the analysis sensitivity to trijet resonances. The definition of the categories is based on the different patterns that signal and background distributions show in the m_{Rjet} vs. m_{Pjet} plane. For the reason described in Sec. 7.1, most of the signal events are clustered around a cross-shaped pattern in the plane (simply called "cross" in the following), as shown in Fig. 7.5. On the contrary, the background event distribution, shown in Fig. 7.6, is smooth in the plane, with little correlation between the two variables, and is concentrated at low values of the jet masses.

This observation leads to the conclusion that a large fraction of background

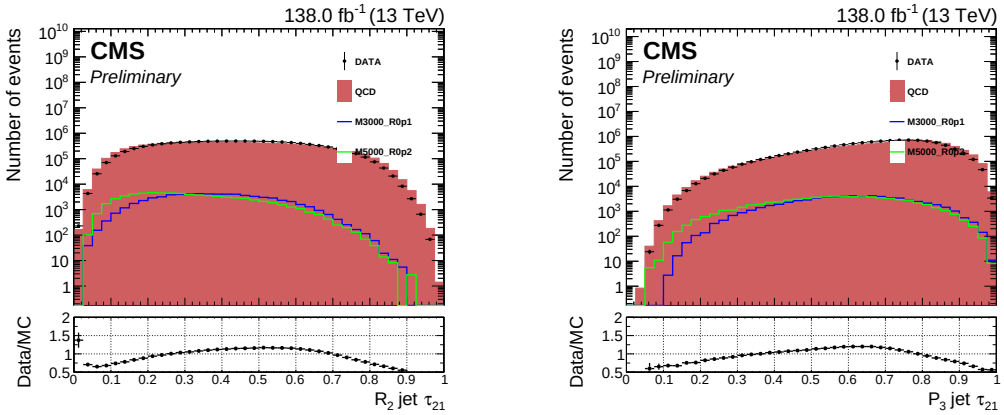

(a) R_2-jet τ_{21} **(b)** P_3-jet τ_{21}

Figure 7.4. Comparison between all years data and simulated samples for the distributions of τ_{21} of the two jets. The distributions of two simulated signal samples are also shown. They correspond to signal hypotheses with $m(\mathrm{R}_1) = 3\,\mathrm{TeV}$ and $\rho_\mathrm{m} = 0.1$ (M3000_R0p1), and $m(\mathrm{R}_1) = 5\,\mathrm{TeV}$ and $\rho_\mathrm{m} = 0.2$ (M5000_R0p2). The simulated signal cross section is of 1 pb, which is two–three orders of magnitude larger than the expected cross section limit of this search.

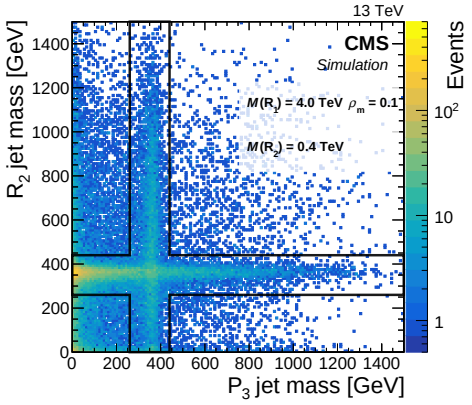

Figure 7.5. Distribution of signal events in the m_Rjet vs. m_Pjet plane for a simulated signal sample with $m(\mathrm{R}_1) = 4\,\mathrm{TeV}$ and $\rho_\mathrm{m} = 0.1$.

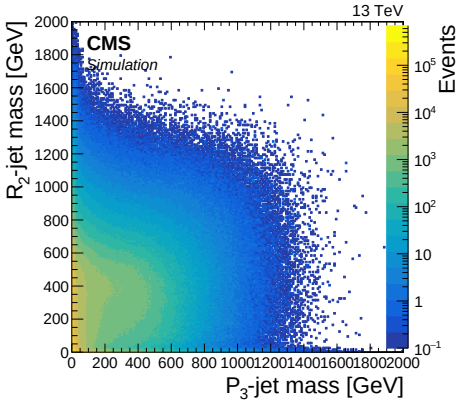

Figure 7.6. Distribution of signal events in the m_Rjet vs. m_Pjet plane for the simulated background from QCD processes.

events can be rejected by requiring them to fall inside the cross delimited in Fig. 7.5 by black lines. Furthermore, the cross is divided into categories, enhancing the analysis sensitivity by separating events belonging to regions of the cross with different signal-to-background ratio.

The values of $m(\mathrm{R}_1)$, $m(\mathrm{R}_2)$, and therefore ρ_m are in principle unknown. In our analysis we scan a wide range of $m(\mathrm{R}_1)$ and ρ_m values, with $m(\mathrm{R}_1)$ ranging from 2 to 9 TeV with 100 GeV wide steps, and ρ_m ranging from 0.1 to 0.2 with 0.0125 wide steps. As a consequence, the $m(\mathrm{R}_2)$ values range from 0.2 to 1.8 TeV with steps with variable width. The position of the cross changes accordingly to the value of $m(\mathrm{R}_2)$ considered, therefore it is not fixed in the m_Rjet vs. m_Pjet plane. For each signal hypothesis we then define a specific set of categories, centered at $m(\mathrm{R}_2)$. The event selection is then repeated every time, sorting the event in the categories for the corresponding $m(\mathrm{R}_2)$ value. In general, the width of each band of the cross is designed in order to be about $\sim$9 times the resolution of the $m(\mathrm{R}_2)$ peak in m_Rjet. This value of the width is found to maximize the analysis sensitivity, collecting a large fraction of signal events from the cross. As a consequence, the width of the two bands is much larger than the distance between two consecutive $m(\mathrm{R}_2)$ tested, therefore the corresponding sets of categories overlap in the m_Rjet vs. m_Pjet plane. The two signal hypotheses, then, share the same events in adjacent categories. This causes a correlation between signal hypotheses corresponding to similar $m(\mathrm{R}_2)$ values that will affect the analysis results, as we will show in Ch. 8.

In our analysis we use three schemes to divide the cross, with different numbers of categories, depending on $m(\mathrm{R}_2)$:

- 22 categories for $m(\mathrm{R}_2) \leqslant 0.6\,\mathrm{TeV}$.
- 9 categories for $0.6\,\mathrm{TeV} < m(\mathrm{R}_2) \leqslant 1.2\,\mathrm{TeV}$.
- a single cross shaped category for $m(\mathrm{R}_2) > 1.2\,\mathrm{TeV}$.

The choice of a variable number of categories is necessary because, when $m(\mathrm{R}_2)$ increases beyond a certain threshold, harder cuts are imposed on the jet masses and a lower number of events in data passes the selection. As a consequence, the number of categories has to be reduced in order to have enough events to ensure the fit to be stable for each category while still providing an optimal sensitivity to trijet signals. The three possible schemes for the sets of categories are described in detail in Sections from 7.2.1 to 7.2.3 and are shown in Figs. from 7.7 to 7.9.

7.2.1 22 categories set

The 22 categories of this set (Fig. 7.7) are defined in the m_Rjet vs. m_Pjet plane in order to enhance the fit sensitivity and exploit all information from jet mass distributions:

- the horizontal and vertical arms of the cross contains m_Rjet and m_Pjet values ranging from 65 to 110% of $m(\mathrm{R}_2)$ for all m_Pjet and m_Rjet values, respectively. The window is asymmetric with respect to $m(\mathrm{R}_2)$ because the soft drop jet mass algorithm reconstructs a peak mass that is about 10% lower than the nominal R_2 mass. The window chosen optimizes the search sensitivity to a

narrow resonance. For the optimization we evaluated the analysis sensitivity using different choices for the window width;

- the low m_{Pjet} region of the horizontal arm of the cross is the region with the highest fraction of signal events and the largest background. We exploit the differences in m_{Rjet} vs. m_{Pjet} correlations between signal and background events to improve the analysis sensitivity by dividing this region into nine horizontal slices based on m_{Rjet}, with a width approximately equal to the jet mass resolution (about 5% of $m(\mathrm{R}_2)$). This approach allows us to exploit the line shape of the signal jet-mass distribution;

- as a result of the analysis optimization, each of the aforementioned slices is further divided in two sub-categories, separating events with values of m_{Pjet} below or above 0.25 $m(\mathrm{R}_2)$. This allows to further separate categories with a high signal-over-background ratio (near the R_2-jet mass peak) from the other categories with lower sensitivity;

- the remaining region, corresponding to the vertical arm and the high m_{Pjet} region of the horizontal arm of the cross, is divided in four categories. The jet mass range of these latter categories is wider in order to retain a sufficient number of events in data to perform the fit.

The detailed rules for the definition of the category boundaries according to the value of $m(\mathrm{R}_2)$ in the signal hypothesis considered are listed in Tab. 7.1.

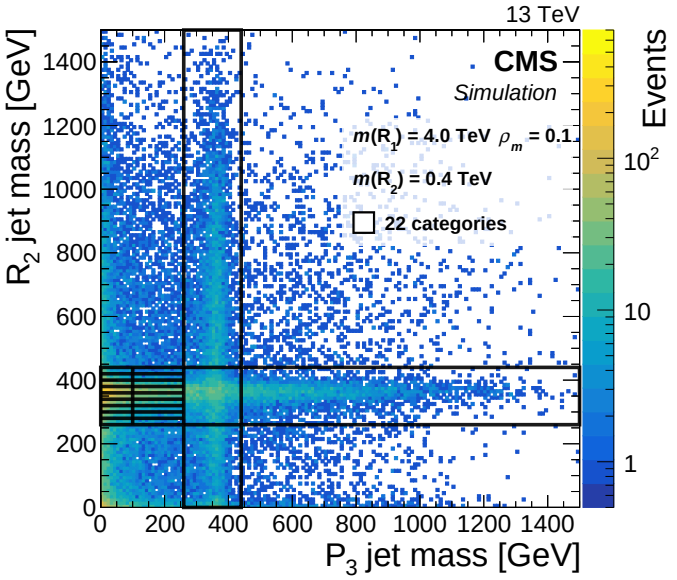

Figure 7.7. Event categories in m_{Rjet} vs m_{Pjet} plane for a set with 22 categories. The two arms of the cross are centered around the value of $m_{\mathrm{Rjet}} = m(\mathrm{R}_2)$ (horizontal) and $m_{\mathrm{Pjet}} = m(\mathrm{R}_2)$ (vertical). In this case $m(\mathrm{R}_1) = 4\,\mathrm{TeV}$, $\rho_{\mathrm{m}} = 0.1$ and $m(\mathrm{R}_2) = 0.4\,\mathrm{TeV}$. The z axis represents the number of signal events expected per bin, for a signal sample with a cross section of 1 pb.

Table 7.1. Selections on m_{Pjet} and m_{Rjet} for the set with 22 categories. The selections depend on the value of $m(\mathrm{R}_2)$ of the signal hypothesis. The categories are identified by the progressive index i_{cat}.

i_{cat}	m_{Pjet} and m_{Rjet} boundaries (multiples of $m\left(\mathrm{R}_2\right)$)	i_{cat}	m_{Pjet} and m_{Rjet} boundaries (multiples of $m\left(\mathrm{R}_2\right)$)
1	[0; 0.25] & [0.65; 0.7]	2	[0; 0.25] & [0.7; 0.75]
3	[0; 0.25] & [0.75; 0.8]	4	[0; 0.25] & [0.8; 0.85]
5	[0; 0.25] & [0.85; 0.9]	6	[0; 0.25] & [0.9; 0.95]
7	[0; 0.25] & [0.95; 1.0]	8	[0; 0.25] & [1.0; 1.05]
9	[0; 0.25] & [1.05; 1.1]	10	[0.25; 0.65] & [0.65; 0.7]
11	[0.25; 0.65] & [0.7; 0.75]	12	[0.25; 0.65] & [0.75; 0.8]
13	[0.25; 0.65] & [0.8; 0.85]	14	[0.25; 0.65] & [0.85; 0.9]
15	[0.25; 0.65] & [0.9; 0.95]	16	[0.25; 0.65] & [0.95; 1.0]
17	[0.25; 0.65] & [1.0; 1.05]	18	[0.25; 0.65] & [1.05; 1.1]
19	[0.65; 1.1] & [0; 0.65]	20	[0.65; 1.1] & [0.65; 1.1]
21	[0.65; 1.1] & [1.1; ∞)	22	[1.1; ∞) & [0.65; 1.1]

7.2.2 9 categories set

When the value of $m(\mathrm{R}_2)$ is over 0.6 TeV, the categories defined inside the cross falls in regions of the plane where the number of events in data is very low. In this condition the simultaneous fit to the dijet mass spectra of the 22 categories is not stable. For this reason, when $m(\mathrm{R}_2) > 0.6\,\mathrm{TeV}$, the set with 9 categories, shown in Fig. 7.8, is defined. The category boundaries in this case follows the definitions listed in Tab. 7.2.

Table 7.2. Selections on m_{Pjet} and m_{Rjet} for the set with 9 categories. The selections depend on the value of $m(\mathrm{R}_2)$ of the signal hypothesis. The categories are identified by the progressive index i_{cat}.

i_{cat}	m_{Pjet} and m_{Rjet} boundaries (multiples of $m\left(\mathrm{R}_2\right)$)	i_{cat}	m_{Pjet} and m_{Rjet} boundaries (multiples of $m\left(\mathrm{R}_2\right)$)
1	[0; 0.25] & [0.65; 0.7]	2	[0; 0.25] & [0.7; 0.75]
3	[0; 0.25] & [0.75; 0.8]	4	[0; 0.25] & [0.8; 0.85]
5	[0; 0.25] & [0.85; 0.9]	6	[0; 0.25] & [0.9; 0.95]
7	[0; 0.25] & [0.95; 1.0]	8	[0; 0.25] & [1.0; 1.1]
9	[0.65; 1.1] OR [0.65; 1.1] (with additional request $m_{\mathrm{Pjet}} > 0.25$)		

7.2.3 Single category.

When the value of $m(\mathrm{R}_2)$ is above 1.2 TeV, the number of events in data passing the selection is further reduced, and the fit is unstable even using the set with 9 categories. Hence, for these signal hypotheses the cross is no more divided in categories (Fig. 7.9) and the only selection applied to the masses of the two jets is given by the cross boundaries (Eq. 7.1).

$$m_{\mathrm{Pjet}} \in [0.65\, m(\mathrm{R}_2)\,; 1.1\, m(\mathrm{R}_2)] \text{ OR } m_{\mathrm{Rjet}} \in [0.65\, m(\mathrm{R}_2)\,; 1.1\, m(\mathrm{R}_2)] \tag{7.1}$$

Table 7.3. Selections on m_{Pjet} and m_{Rjet} for the single category. The selections depend on the value of $m(\mathrm{R}_2)$ of the signal hypothesis. The categories are identified by the progressive index i_{cat}.

i_{cat}	m_{Pjet} and m_{Rjet} boundaries (multiples of $m\left(\mathrm{R}_2\right)$)
1	[0.65; 1.1] OR [0.65; 1.1]

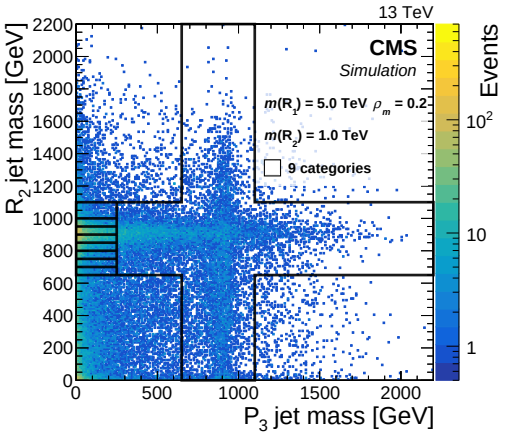

Figure 7.8. Set with 9 categories in m_{Rjet} vs m_{Pjet} plane for $m(\mathrm{R}_2) > 0.6\,\mathrm{TeV}$. In this case $m(\mathrm{R}_1) = 5\,\mathrm{TeV}$, $\rho_{\mathrm{m}} = 0.2$ and $m(\mathrm{R}_2) = 1.0\,\mathrm{TeV}$.

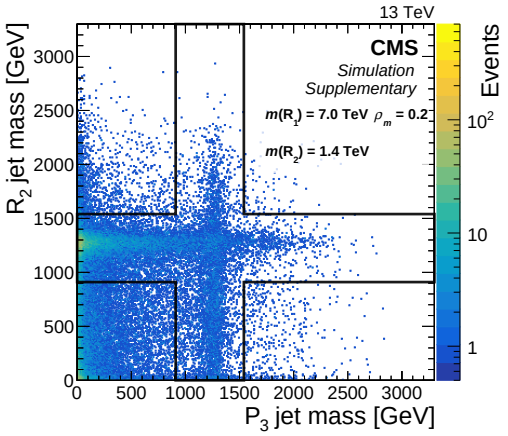

Figure 7.9. Set with a single category in m_{Rjet} vs m_{Pjet} plane for $m(\mathrm{R}_2) > 1.2\,\mathrm{TeV}$. In this case $m(\mathrm{R}_1) = 7\,\mathrm{TeV}$, $\rho_{\mathrm{m}} = 0.2$ and $m(\mathrm{R}_2) = 1.4\,\mathrm{TeV}$.

7.3 Fit method

The fit method used in this analysis analyzes simultaneously the dijet mass distributions of the event categories searching for a signal peak from a narrow R_1 resonance over the smoothly decreasing distribution originating from QCD multijet background events.

The fit performed is a maximum likelihood fit to all the binned dijet mass spectra from the different categories. We use a variable-sized binning for the dijet mass, with the bin width corresponding approximately to the mass resolution (see Appendix D). For each category c the fit uses a function of m_{jj} that has two components:

- a smooth, monotonicly decreasing function for background modeling $B_c(m_{\mathrm{jj}})$;
- a double-tailed crystal-ball function, $S_c(m_{\mathrm{jj}})$, describing a narrow resonance.

The likelihood to maximize in the fit is:

$$L = \prod_{c=1}^{n_c} \prod_{i=1}^{n_b} Poisson(x_{ic}|\lambda_{ic}) = \prod_{c=1}^{n_c} \prod_{i=1}^{n_b} \frac{\lambda_{ic}^{x_{ic}} e^{-\lambda_{ic}}}{x_{ic}!} \tag{7.2}$$

where i is an index running on the bin number (n_b) of the m_{jj} spectrum and c is an index running on the category number (n_c), while x_{ic} and λ_{ic} are respectively the data yield and the expected number of events in the i^{th} bin of the c^{th} category. In particular, λ_{ic} it is made of two terms:

$$\lambda_{ic} = \mu s_{ic} + b_{ic} \tag{7.3}$$

where:

- $b_{ic} = N_{ic}(B) = \int_{m_{ic,low}}^{m_{ic,high}} B_c(m_{\mathrm{jj}}) dm_{\mathrm{jj}}$ is the number of expected background events, and it is obtained with an integral to the background function in the dijet mass bin range;
- $s_{ic} = N_{ic}(S) = \sigma_{br} \cdot \int_{m_{ic,low}}^{m_{ic,high}} S_c(m_{\mathrm{jj}}) dm_{\mathrm{jj}}$ is the number of signal events, obtained with an integral to the signal function in the dijet mass bin range, multiplied by the product of the signal cross section for the branching fraction of the channel under study, referred as σ_{br};
- μ is the *signal strength modifier*, which is a positive factor that modify the signal cross section by multiplying it for μ.

In the fit, the value of σ_{br} is set to 1 pb, while the fit parameter of interest (POI) is the signal strength modifier, μ. With this choice, the post-fit value of μ corresponds to signal cross section times the branching fraction equal to μ expressed in pb. A μ value significantly above 0 would imply the observation of a signal in data. We will quantify the significance of the obtained values of μ in Sec. 8.1

In Secs. 7.3.1 and 7.3.3 we will discuss in detail the background estimation and the signal model, respectively. In Sec. 7.3.4, instead, we report the results of the tests on fit quality and performances.

7.3.1 Background estimation

In each category, the MC simulations of the dijet mass spectra from QCD processes show a decreasing and smooth profile. Therefore the fit function used to model the background in each category is the 3-parameters function defined in Eq. 7.4, which is also smoothly decreasing:

$$B_c(m_{\mathrm{jj}}) = f_1(m_{\mathrm{jj}}) = \frac{p_0 \left(1 - \frac{m_{\mathrm{jj}}}{\sqrt{s}}\right)^{p_1}}{\left(\frac{m_{\mathrm{jj}}}{\sqrt{s}}\right)^{p_2}} \tag{7.4}$$

This function is derived from the 4-parameters function (Eq. 7.5), which has been used in many previous CMS dijet analyses at $\sqrt{s} = 13\,\mathrm{TeV}$ [30, 52], 8 TeV [112] and 7 TeV [113].

$$f_{\mathrm{dijet}}(m_{\mathrm{jj}}) = \frac{p_0 \left(1 - \frac{m_{\mathrm{jj}}}{\sqrt{s}}\right)^{p_1}}{\left(\frac{m_{\mathrm{jj}}}{\sqrt{s}}\right)^{p_2 + p_3 \log\left(m_{\mathrm{jj}}/\sqrt{s}\right)}} \tag{7.5}$$

We chose a fit function with fewer parameters because the number of background events that populates each category is lower than the background of the single m_{jj} spectrum analyzed by inclusive dijet searches by a few order of magnitudes. Hence, fewer parameters are needed to model the background in each category.

We performed a Fisher F-test comparing the performances of the fits performed with f_1, f_{dijet} and a 2-parameter function derived from f_1. The results of the test, reported in Appendix C, show that the 3-parameters function is suitable to fit the m_{jj} spectra per category.

The three parameters of function f_1 are floating, independently in each category, in the fit in a wide range with flat priors. The background shape in each category is then fitted to the data together with the signal strength μ, which multiplies the signal shape in the m_{jj} spectra. This procedure, called signal+background fit, may originate a bias on the signal extraction, eventually absorbing the excess from the signal. The presence of bias has been checked by the test reported in Sec. 7.3.4.2.

The analysis followed a strict blinding policy, therefore the use of this fit function has been preliminarily tested by performing background-only fits on MC simulations (i.e. with μ set to 0) of the QCD multijet background. An example of such fits is reported in Fig. 7.10 for a selection of categories from a signal hypothesis with $m(\mathrm{R}_1) = 5\,\mathrm{TeV}$ and $\rho_{\mathrm{m}} = 0.1$.

These plots show that the fitted background shape follows correctly the expected background events distribution. The overall p-value of the fit is 0.13, and it is evaluated using the goodness of fit test described in Sec. 7.3.4.1. In the final fit, the background function is fitted to the data, providing a fully data-driven background prediction. A full display of the fit for two different signal hypothesis is shown in Sec. 8.1, while robust and detailed tests on the fit performances are reported in in Sec. 7.3.4.

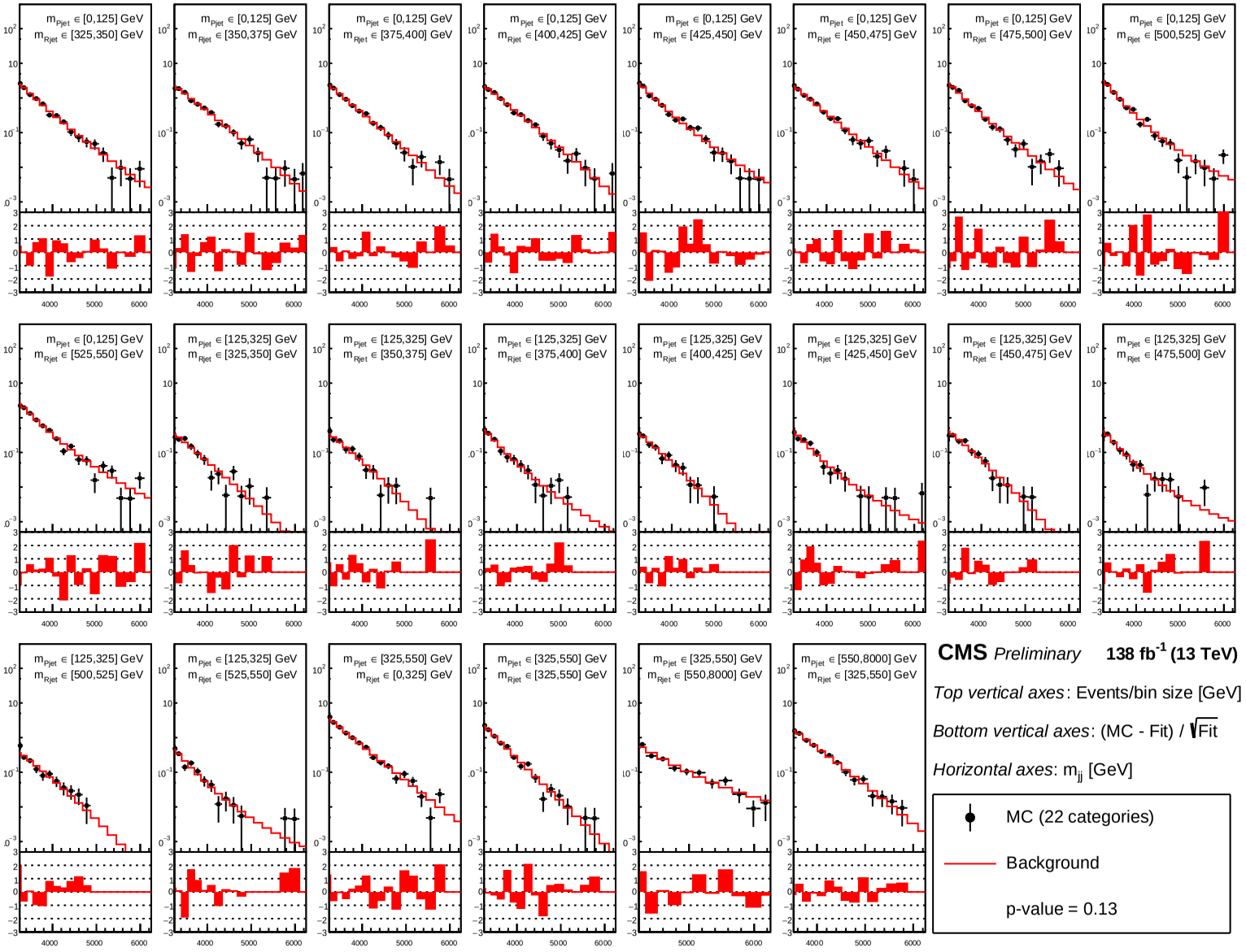

Figure 7.10. m_{jj} spectra (black points) from an MC simulated sample of QCD background events, for the 22 categories corresponding a to signal hypothesis with $m(\mathrm{R}_1) = 5\,\mathrm{TeV}$ and $\rho_{\mathrm{m}} = 0.1$. The resulting background-only fit is also shown (red line). The horizontal axis shows the value of m_{jj} in GeV. The vertical axis shows, in the top part of each plot, the bin event content divided by the bin width, and, in the bottom part, the difference between the simulated spectra and the fit divided by the statistical uncertainty in each bin.

7.3.2 Fit ranges

The categories defined in Sec. 7.2 divide the events applying cuts on the masses of the two jets: m_{Rjet} and m_{Pjet}. This selection determines a side effect that originates from the correlation between m_{Rjet}, m_{Pjet} and the dijet mass, m_{jj} observed for background events. Since the QCD jet mass is correlated with their p_{T}, by requiring the jet masses to be above a certain value, the distribution of m_{jj} (which depends on the jets p_{T}) is sculpted and develops a rising trend at low m_{jj}. This effect is clearly shown in Fig. 7.11, where the inclusive m_{jj} distribution from simulated background events (left) is compared to the m_{jj} distribution of the selection of events that falls inside one category of a particular signal hypothesis (right).

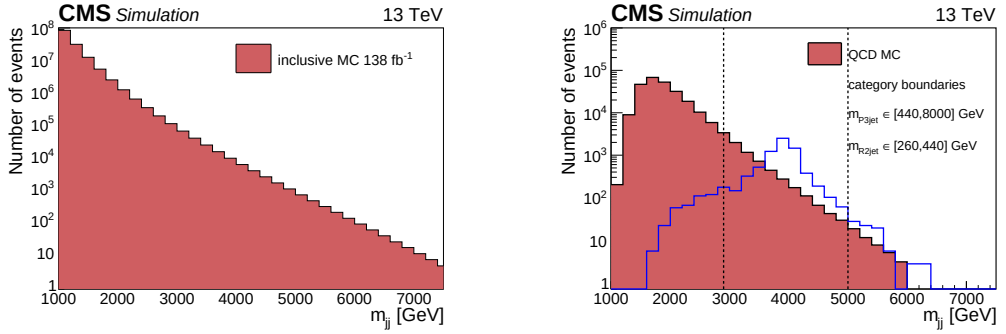

Figure 7.11. Left: inclusive m_{jj} spectrum from the simulated QCD multijet background. Right: the same spectrum for a category with $m(\mathrm{R}_1) = 4\,\mathrm{TeV}$, $\rho_{\mathrm{m}} = 0.1$, $m_{\mathrm{Pjet}} \in [440, \infty]\,\mathrm{GeV}$, $m_{\mathrm{Rjet}} \in [260, 440]\,\mathrm{GeV}$. The turn on effect of the requirements on the jet masses is visible at low m_{jj}. The vertical dashed lines mark the begin and the end of the fit window (defined in the text).

The rising part of the m_{jj} spectrum cannot be modeled by the function we chose for the fit, f_1. Nevertheless, an alternative fit with a combination of functions, able to model the local maximum of the background, could easily interpret a signal as background in that region, introducing a strong bias. We then decided to use f_1 for the background modeling, and start the fit at higher m_{jj} values. To do this, a jet-mass-dependent minimum m_{jj} threshold ($m_{\mathrm{jj}}^{\mathrm{thr}}$) is applied, which is specific to each category. The threshold is evaluated from simulated background samples as follows. For each category, we compute the ratio between the m_{jj} spectra of the category (for example, Fig. 7.11, right) and the inclusive spectrum (Fig. 7.11, left). This ratio can be thought of as an efficiency of the selection of background events made for a category (ϵ_{cat}). An example of ϵ_{cat} for a category is shown in Fig. 7.12, as a function of m_{jj}. The plot shows an increasing trend and a maximum before decreasing, and the same behavior is observed in both data and simulation. The rising part of the efficiency is correlated to the developing of the rising trend in the m_{jj} spectrum in data. The presence of a decreasing trend of the efficiency, instead, does not alter the m_{jj} spectrum of the category with respect to the inclusive distribution, which is still decreasing in that portion of the m_{jj} range.

We set then $m_{\mathrm{jj}}^{\mathrm{thr}}$ to be 15% higher than the position of the maximum, in order to be sure to perform the fit only in the undistorted portion of the m_{jj} distribution.

The $m_{\mathrm{jj}}^{\mathrm{thr}}$ then is the lowest value of m_{jj} where it is possible to start the fit with

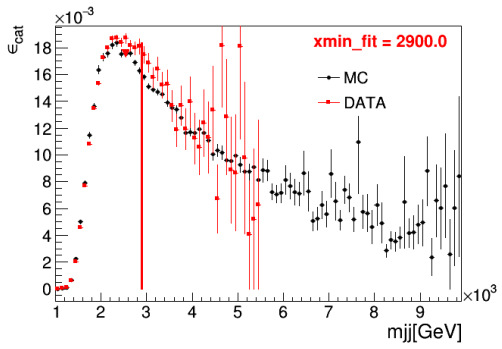

Figure 7.12. Ratio between the two m_{jj} distribution in Fig. 7.11. The numerator is the spectrum for the category with $m(\mathrm{R}_1) = 4\,\mathrm{TeV}$, $\rho_{\mathrm{m}} = 0.1$, $m_{\mathrm{Pjet}} \in [440, \infty]\,\mathrm{GeV}$, $m_{\mathrm{Rjet}} \in [260, 440]\,\mathrm{GeV}$ (Fig. 7.11, right), while the denominator is the inclusive m_{jj} spectrum (Fig. 7.11, left). The plot obtained from the QCD MC shows a good agreement with data.

the function f_1. The actual fit range in m_{jj} is centered around the signal peak. It is defined as: $m_{\mathrm{jj}}^{\mathrm{min}} < m_{\mathrm{jj}} < m_{\mathrm{jj}}^{\mathrm{max}}$, where $m_{\mathrm{jj}}^{\mathrm{min}}$ is the greater of $m_{\mathrm{jj}}^{\mathrm{thr}}$ and $0.65\,m(\mathrm{R}_1)$, and $m_{\mathrm{jj}}^{\mathrm{max}} = 1.25 m(\mathrm{R}_1)$. With this choice the left fit range is always above $m_{\mathrm{jj}}^{\mathrm{thr}}$, and its distance from the peak is not larger than $0.35 m(\mathrm{R}_1)$, which is about 7 times the peak resolution ($\sim$5% of $m(\mathrm{R}_1)$). The upper fit range, $m_{\mathrm{jj}}^{\mathrm{max}}$, is chosen in order to avoid the presence of signal biases in the fit, which arise if the fit range is extended far above the signal peak.

In some cases, $m_{\mathrm{jj}}^{\mathrm{thr}}$ (therefore $m_{\mathrm{jj}}^{\mathrm{min}}$) can be very close to the peak, which is truncated. When this happens a bias can arise in the fit. For this reason if $m_{\mathrm{jj}}^{\mathrm{thr}} > 0.9 m(\mathrm{R}_1)$ the corresponding category is removed from the analysis. The Fig. 7.11 (right) shows an example of one category passing the $m_{\mathrm{jj}}^{\mathrm{thr}}$ requirement, displaying the fit range position with respect to the peak. Figure 7.13, instead, shows a category that is removed from the analysis. In the latter case the left fit range is too close to the $m(\mathrm{R}_1)$ peak position.

In Fig. 7.14, we show the fraction of categories that are used in the final fit versus the ρ_{m} and $m(\mathrm{R}_1)$ of the corresponding signal hypothesis. The fraction is evaluated with respect to the total number of categories, which is respectively 22, 9 or 1 for the signal hypotheses with $m(\mathrm{R}_2)$ in the range $[0; 0.6]\,\mathrm{TeV}$, $[0.6; 1.2]\,\mathrm{TeV}$, $[1.2\,\mathrm{TeV}, \infty)$. In the top left region of the ρ_{m} vs. $m(\mathrm{R}_1)$ plane, a lower fraction of categories passes the aforementioned requirements on $m_{\mathrm{jj}}^{\mathrm{thr}}$. The total signal efficiency is then reduced in that region (shown below in Fig. 7.22), with a consequent reduction of the analysis sensitivity to the corresponding signal hypotheses.

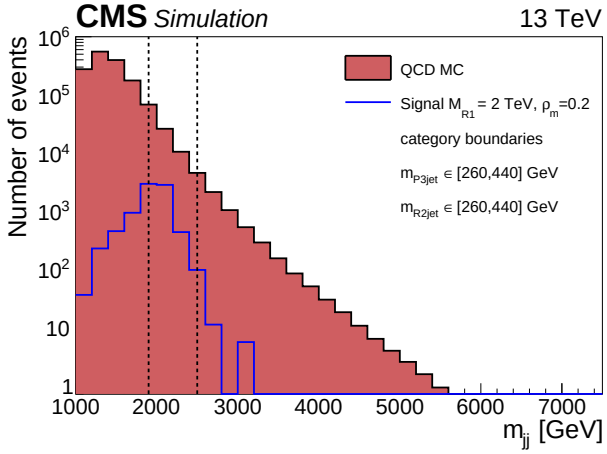

Figure 7.13. m_{jj} spectrum from a simulated sample of QCD multijet events for a category with $m(\mathrm{R}_1) = 2\,\mathrm{TeV}$, $\rho_{\mathrm{m}} = 0.2$, $m_{\mathrm{Pjet}} \in [260, 440]\,\mathrm{GeV}$ and $m_{\mathrm{Rjet}} \in [260, 440]\,\mathrm{GeV}$. This category is excluded from the final fit because $m_{\mathrm{jj}}^{\mathrm{thr}} > 0.9m(\mathrm{R}_1)$.

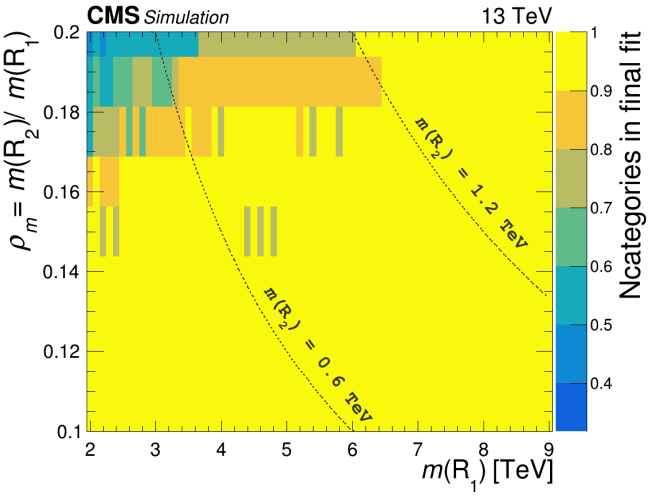

Figure 7.14. Fraction of categories used in the final fit as a function of ρ_{m} and $m(\mathrm{R}_1)$. The fraction is evaluated with respect to the total number of categories of the corresponding signal hypotheses. The two hyperboles mark in the plane the transition between 22 and 9 categories ($m(\mathrm{R}_2) = 0.6\,\mathrm{TeV}$), and 9 and 1 category ($m(\mathrm{R}_2) = 1.2\,\mathrm{TeV}$). The plot shows signal hypotheses up to $\rho_{\mathrm{m}} = 0.2$, which has been chosen as the maximum ρ_{m} value for the analysis because of the observations reported in Sec. 7.3.3.2.

7.3.3 Signal model

The signal shape of the R_1 peak in the dijet mass spectra is derived from the signal MC simulated samples listed in Sec. 6.2, for 8 values of G_{KK} (R_1) masses ($m(R_1) = 2, 3, 4, 5, 6, 7, 8, 9\,\text{TeV}$) and for 3 values of ρ_m ($\rho_m = 0.1, 0.2, 0.3$). Signal events from each sample are divided into the event categories defined in Sec. 7.2. The signal model parameters are then obtained by fitting the resulting m_{jj} signal event distributions with a double-sided Crystal Ball (f_{CB}) [114, 115], a peak-shaped function defined by Eq. 7.6:

$$f_{CB}(x;\mu_{CB},\sigma_{CB},\alpha_1,n_1,\alpha_2,n_2) = N\cdot\begin{cases} e^{-\frac{\alpha_1^2}{n_1}}\left(1-\frac{\alpha_1}{n_1}\left(\alpha_1+\frac{x-\mu}{\sigma}\right)\right)^{-n_1} & x \le -\alpha_1 \\ e^{-\left(\frac{x-\mu}{2\sigma}\right)^2} & -\alpha_1 < x < \alpha_2 \\ e^{-\frac{\alpha_2^2}{n_2}}\left(1-\frac{\alpha_2}{n_2}\left(\alpha_2-\frac{x-\mu}{\sigma}\right)\right)^{-n_2} & x \ge \alpha_2 \end{cases} \tag{7.6}$$

.

Here $x = m_{jj}/\sqrt{s}$, μ_{CB} and σ_{CB} are respectively the mean and the standard deviation of the Gaussian core, α_1 and α_2 are the starting point for the exponential tails in units of σ_{CB}, and n_1 and n_2 are parameters of the exponential functions. Examples of fits to signal distributions for some categories for a signal hypothesis with $m(R_1) = 3\,\text{TeV}$ and $\rho_m = 0.1$ are reported in Figs. 7.15.

The signal samples are simulated for a limited number of $m(R_1)$ and ρ_m values. To search for signal hypotheses corresponding to intermediate values of $m(R_1)$ and ρ_m with respect to those generated, the corresponding signal shapes can be obtained from an interpolation of the shapes from MC simulated samples. For each signal sample we have 22, 9 or 1 signal shapes according to the number of categories defined for that signal hypothesis. The interpolation of a variable number of shapes is a complex task, therefore, instead of using one shape for each category, we used an average shape for the signal in each category. The average shape is then defined as a double-sided Crystal Ball with parameters fixed to the average values of each parameter across the categories. This simplified approach is possible because the signal shape is quite stable across the categories, as it is shown in Fig. 7.16, where the 22 shapes of a signal with $m(R_1) = 3\,\text{TeV}$ and $\rho_m = 0.1$ are normalized to unity and compared.

The parameters μ_{CB} and σ_{CB} have a non-negligible variance across the categories, which depends on the statistical error of the fit. This introduces a systematic uncertainty on the value of the two parameters, which is taken into account in the fit as discussed in detail in Sec. 8.2.1.

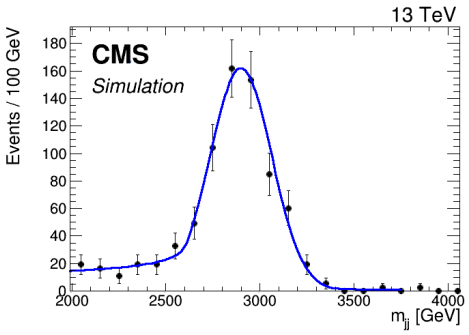

(a) $m_{\mathrm{Pjet}} \in [0, 75]$ GeV
$m_{\mathrm{Rjet}} \in [225, 240]$ GeV

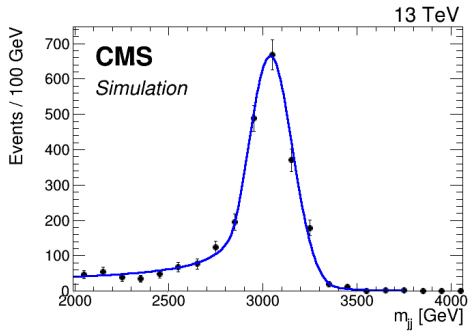

(b) $m_{\mathrm{Pjet}} \in [0, 75]$ GeV
$m_{\mathrm{Rjet}} \in [285, 300]$ GeV

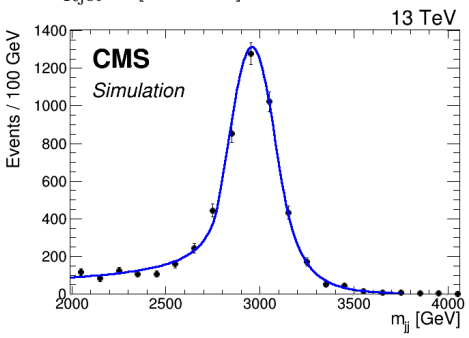

(c) $m_{\mathrm{Pjet}} \in [195, 330]$ GeV
$m_{\mathrm{Rjet}} \in [195, 330]$ GeV

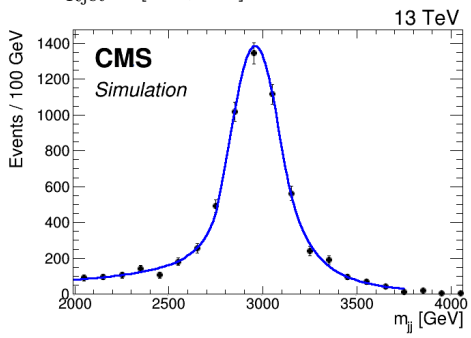

(d) $m_{\mathrm{Pjet}} \in [330, \infty)$ GeV
$m_{\mathrm{Rjet}} \in [195, 330]$ GeV

Figure 7.15. Examples of the R_1 peak in the m_{jj} spectra of 4 categories for $m(\mathrm{R}_1) = 3$ TeV and $\rho_{\mathrm{m}} = 0.1$. The black dots represent the distribution of the simulated signal samples for a cross section of 1 pb. The blue line is the shape obtained from the fit.

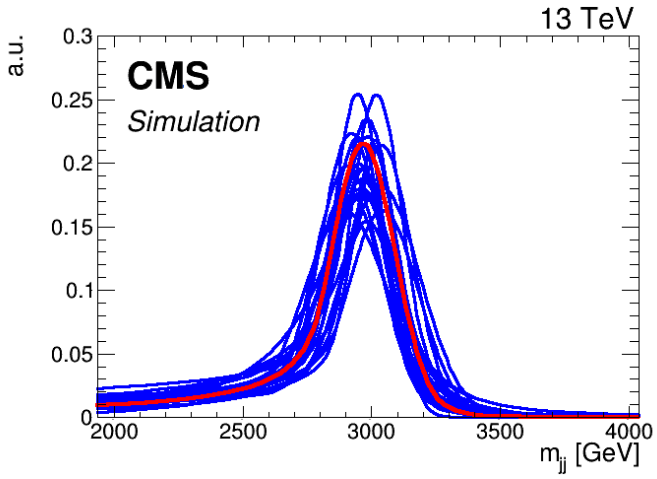

Figure 7.16. Comparison of the signal shapes (blue lines) for the 22 categories of a signal sample with $m(\mathrm{R}_1) = 3$ TeV and $\rho_{\mathrm{m}} = 0.1$. The integral of each shape is normalized to unity. The average shape is represented by a red line.

7.3.3.1 Signal shape interpolation

The average shapes for each simulated signal sample are interpolated to obtain the signal shapes for the intermediate $m(\mathrm{R}_1)$ and ρ_m values. The interpolation is performed using the linear interpolation algorithm described in Ref. [116].

At first, the average shapes are interpolated between $\rho_\mathrm{m} = 0.1, 0.2$ and 0.3 for fixed values of $m(\mathrm{R}_1) = 2, 3, 4, 5, 6, 7, 8, 9\,\mathrm{TeV}$, with 0.0125 wide steps in ρ_m. The intermediate shapes obtained are reported in Fig. 7.17 for a selection of $m(\mathrm{R}_1)$ values. The shapes are very similar for different ρ_m values, therefore they overlap in the plots. The shapes from this first step are then interpolated between the $m(\mathrm{R}_1)$ points, at fixed ρ_m, with 100 GeV steps. Figure 7.18 shows the shapes obtained after this second step for five different ρ_m values.

Signal shapes for $\rho_\mathrm{m} > 0.2$ were evaluated and examined in the preliminary steps of the analysis to investigate the possibility to extend its range up to $\rho_\mathrm{m} = 0.3$. This possibility has been excluded after the observations reported in Sec. 7.3.3.2. The corresponding shapes are not shown in this thesis.

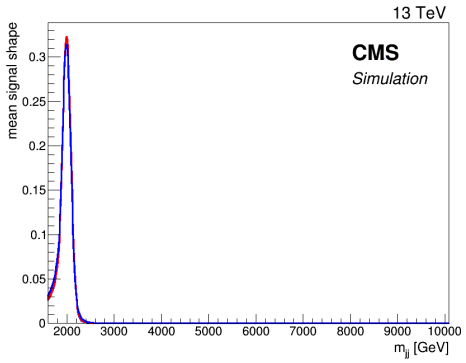

(a) $m(\mathrm{R}_1) = 2\,\mathrm{TeV}$.

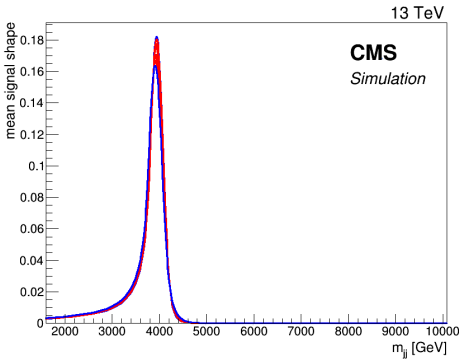

(b) $m(\mathrm{R}_1) = 4\,\mathrm{TeV}$.

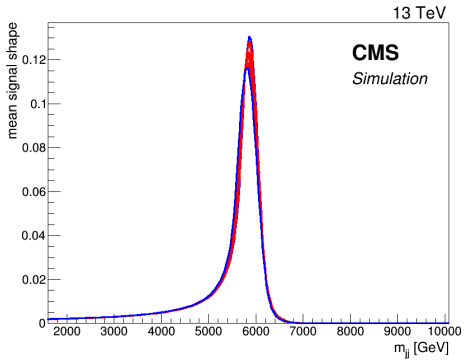

(c) $m(\mathrm{R}_1) = 6\,\mathrm{TeV}$.

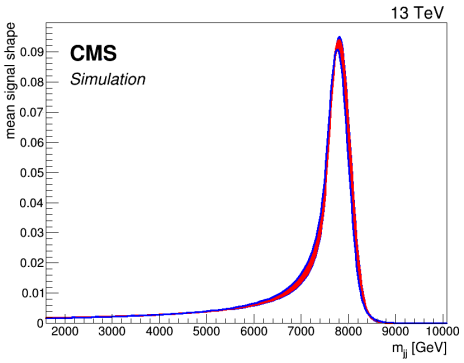

(d) $m(\mathrm{R}_1) = 8\,\mathrm{TeV}$.

Figure 7.17. Generated (blue) and interpolated (red) mean signal shapes, from the interpolation between $\rho_\mathrm{m} = 0.1$ and 0.2, at fixed $m(\mathrm{R}_1)$, with steps of 0.0125 in ρ_m.

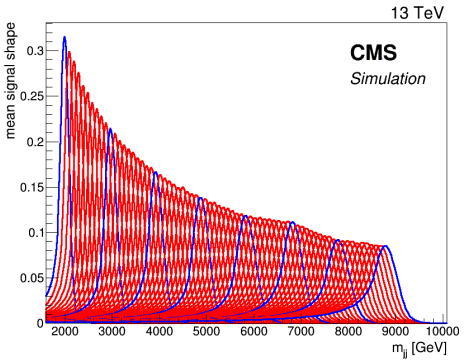

(a) $\rho_{\mathrm{m}} = 0.1$.

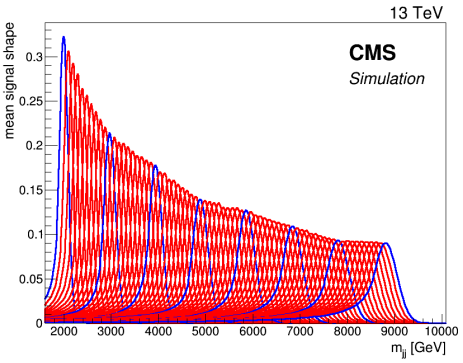

(b) $\rho_{\mathrm{m}} = 0.125$.

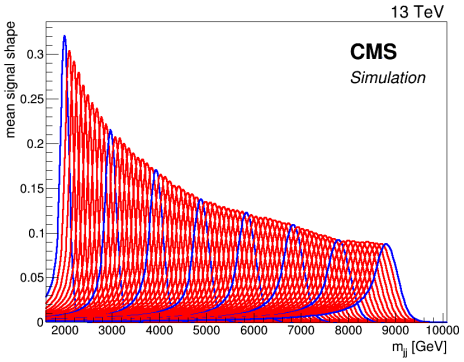

(c) $\rho_{\mathrm{m}} = 0.15$.

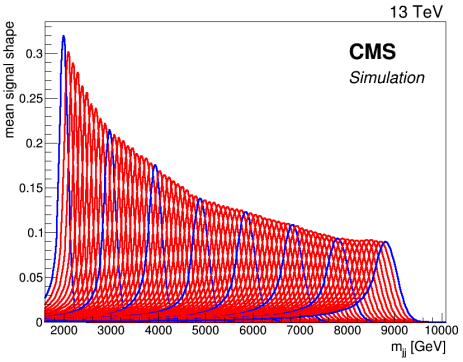

(d) $\rho_{\mathrm{m}} = 0.175$.

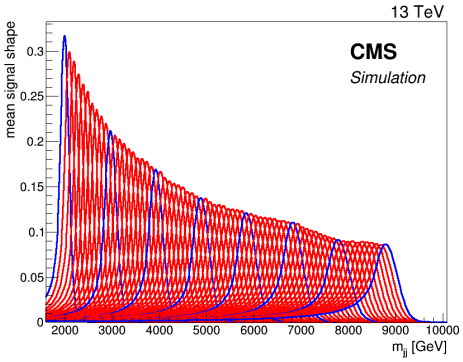

(e) $\rho_{\mathrm{m}} = 0.2$.

Figure 7.18. Generated and interpolated mean signal shapes, for the interpolation between $m(\mathrm{R}_1) = 2$, 3, 4, 5, 6, 7, 8 and 9 TeV, at fixed ρ_{m}, with steps of 100 GeV in $m(\mathrm{R}_1)$. The interpolated shapes are shown in red. For $\rho_{\mathrm{m}} = 0.1$ and 0.2 the generated signal shapes are shown in blue, while for $\rho_{\mathrm{m}} = 0.125$, 0.15, and 0.175 the blue shapes are obtained after the first step of the interpolation along ρ_{m}.

7.3.3.2 Signal efficiency interpolation

As for the signal shapes, also the signal efficiencies in each category have been interpolated for the intermediate $m(\mathrm{R}_1)$ and ρ_{m} points. We define the signal efficiency in the *i-th* category as:

$$\epsilon_i = \frac{N_{icat}}{N_{gen}} \tag{7.7}$$

where:

- N_{icat} is the number of signal events in the i-th category, defined as the integral of the signal shape between the m_{jj} fit ranges defined in Sec. 7.3.2.
- N_{gen} is the number of the generated signal events.

By the previous definition of N_{icat}, ϵ_i can be factorized as the product of two efficiencies:

$$\epsilon_i = \epsilon_i^{sel} \cdot \epsilon_i^{fit} \tag{7.8}$$

where:

- ϵ_i^{sel} is the efficiency of the basic event selection (described in section 6) and the selection introduced by the category boundaries.
- ϵ_i^{fit} is the efficiency of the cuts introduced by the fit ranges.

We studied the variation of ϵ_i^{sel} along $m(\mathrm{R}_1)$ and ρ_{m} for the available signal samples. An example of this study is shown in Figs. from 7.19 to 7.21.

We performed a linear interpolation of ϵ_i^{sel} between two consecutive points in the ρ_{m} vs $m(\mathrm{R}_1)$ plane, first along the ρ_{m} axis, then along the $m(\mathrm{R}_1)$ axis. The interpolation has been made independently for each category. The linear approximation is fairly good for along the $m(\mathrm{R}_1)$ direction. The plots at the top of Figs. 7.19, 7.20, and 7.21, show that he efficiency is roughly constant for different $m(\mathrm{R}_1)$ values considering the systematic uncertainty on ϵ_i^{sel}. The value of the uncertainty is represented by the vertical bars on the points of the plot, and it is about 20% of ϵ_i^{sel}. This value arises from the uncertainty on the jet masses, that will be described in more detail in Sec. 8.2.1. The linear approximation is fairly good also along ρ_{m} (Figs. 7.19c, 7.20c, 7.21c).

The categories 21 and 22 of Fig. 7.19c, show large variations in ϵ_i^{sel} between $\rho_{\mathrm{m}} = 0.1$, 0.2, and 0.3. These variations are much larger than the uncertainty on ϵ_i^{sel}. They are the most external categories of the cross and, when ρ_{m} increase, these region of the plane are less populated than the others. However, as we will describe below, in the final analysis we only consider signal hypotheses below $\rho_{\mathrm{m}} = 0.2$, therefore the large drop in efficiency above 0.2 is not a problem for our analysis. We then used the linear interpolation to evaluate ϵ_i^{sel} for intermediate $m(\mathrm{R}_1)$ and ρ_{m} values also for these two categories.

After the linear interpolation, we evaluate the component ϵ_i^{fit} for each category evaluating the integral of the signal shape inside the category fit range.

With this method we are able to perform a better interpolation of the efficiencies, because the linear interpolation is performed for the smoothly varying component

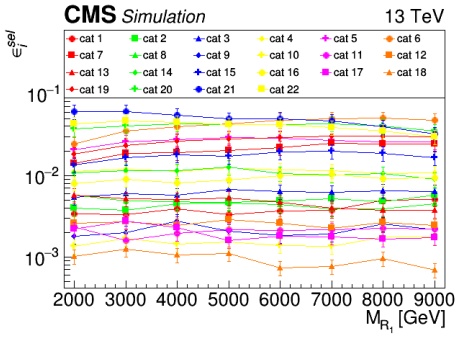

(a) 22 categories efficiencies vs $m(\mathrm{R}_1)$ at $\rho_\mathrm{m} = 0.1$

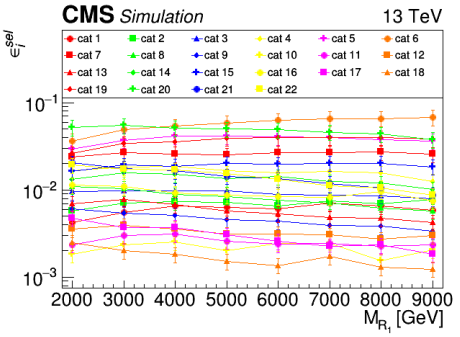

(b) 22 categories efficiencies vs $m(\mathrm{R}_1)$ at $\rho_\mathrm{m} = 0.2$

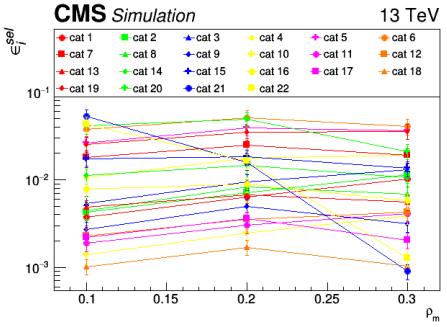

(c) 22 categories efficiencies vs ρ_m at $m(\mathrm{R}_1) = 4\,\mathrm{TeV}$

Figure 7.19. Plots of signal efficiencies ϵ_i^{sel} for the 22 categories set. The vertical bars represent the 20% uncertainty on the signal efficiency. The top plots shows that ϵ_i^{sel} is approximately flat (within the uncertainty) as a function of $m(\mathrm{R}_1)$. The bottom plot shows that this is also valid for ϵ_i^{sel} as a function of ρ_m, except for categories 21 and 22 (details in the text).

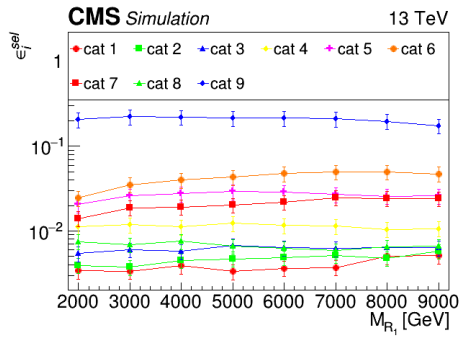

(a) 9 categories efficiencies vs $m(\mathrm{R}_1)$ at $\rho_\mathrm{m} = 0.1$

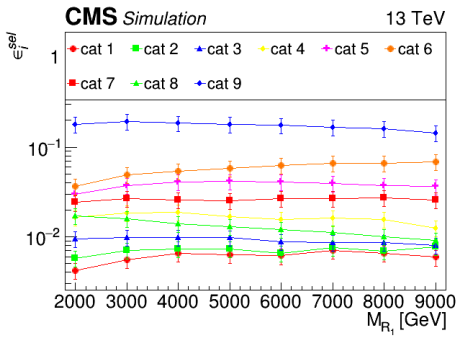

(b) 9 categories efficiencies vs $m(\mathrm{R}_1)$ at $\rho_\mathrm{m} = 0.2$

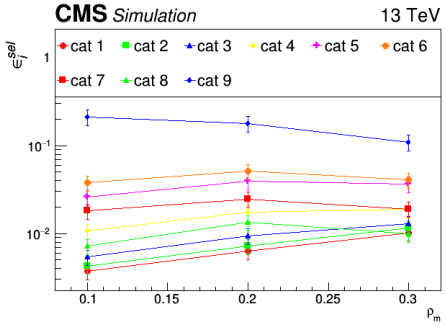

(c) 9 categories efficiencies vs ρ_m at $m(\mathrm{R}_1) = 4\,\mathrm{TeV}$

Figure 7.20. Plots of signal efficiencies ϵ_i^{sel} for the 9 categories set. The vertical bars represent the 20% uncertainty on the signal efficiency. The top and bottom plots shows that ϵ_i^{sel} is approximately flat (within the uncertainty) as a function of both $m(\mathrm{R}_1)$ and ρ_m.

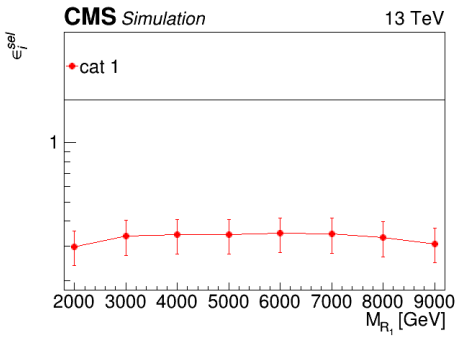

(a) 1 category efficiency vs $m(\mathrm{R}_1)$ at $\rho_\mathrm{m} = 0.1$

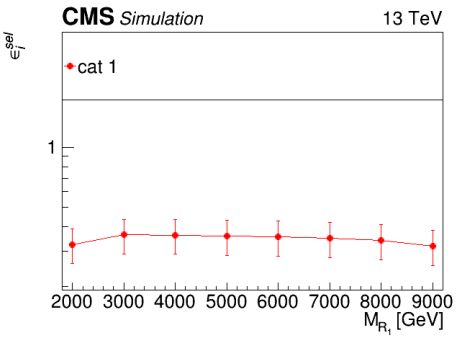

(b) 1 categories efficiencies vs $m(\mathrm{R}_1)$ at $\rho_\mathrm{m} = 0.2$

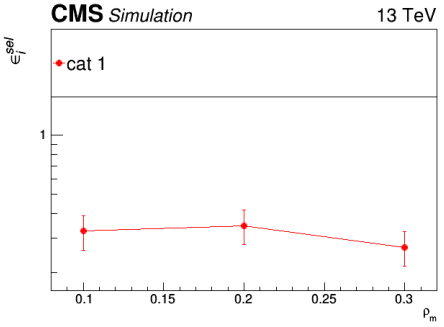

(c) 1 category efficiency vs ρ_m at $m(\mathrm{R}_1) = 4\,\mathrm{TeV}$

Figure 7.21. Plots of signal efficiencies ϵ_i^{sel} for the singe category. The vertical bars represent the 20% uncertainty on the signal efficiency. The top and bottom plots shows that ϵ_i^{sel} is approximately flat (within the uncertainty) as a function of both $m(\mathrm{R}_1)$ and ρ_m.

ϵ_i^{sel}, while the efficiency of the cut introduced by the fit ranges is evaluated exactly with the integral of the signal shape.

After the interpolation, the total signal efficiency has been evaluated for all the signal hypotheses considered in this study. The total signal efficiency is defined as:

$$\epsilon_{tot} = \sum_i \epsilon_i = \frac{\sum_i N_{icat}}{N_{gen}} = \frac{N_{AllCat}}{N_{gen}} \tag{7.9}$$

The figure 7.22 shows that the total efficiency decreases for $\rho_{\mathrm{m}} > 0.2$. This effect is due to the fit ranges, which eventually cut-off the signal at high $m(\mathrm{R}_1)$, and to the removal of categories from final fit, which is described in section 7.3.2. This limits the range of application of the analysis at $\rho_{\mathrm{m}} \leqslant 0.2$.

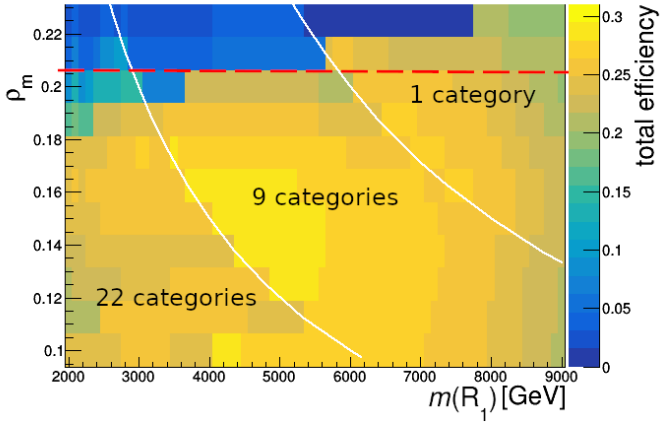

Figure 7.22. Total signal efficiency in the plane ρ_{m} vs $m(\mathrm{R}_1)$. The total signal efficiency is defined as the number of events falling in the cross-shaped categories region (N_{AllCat}) divided by the total number of generated events (N_{gen}). The total efficiency is evaluated for the three different sets of categories. The white lines define the area of application in the plane for each set of categories. Above $\rho_{\mathrm{m}} = 0.2$, the efficiency drops significantly because the lower fit range truncates the signal in a significant fraction of the categories is removed because of the requirements of Sec. 7.3.2. The range of application of the analysis is then limited to $\rho_{\mathrm{m}} \leqslant 0.2$ (red line).

7.3.4 Fit quality tests

The fit procedure described in this chapter has been checked performing goodness of fit and bias tests. The two tests verify respectively that the background fit function is suitable to describe the QCD multijet background in data, and that it does not introduce a significant bias in the signal extraction procedure. The Secs. 7.3.4.1 and 7.3.4.2 report the details and the results of these tests.

7.3.4.1 Goodness of fit test

For the goodness of fit test, the m_{jj} spectra of the event categories are fitted with the function f_1, in the hypothesis that only background events are present in data (background-only fit). Then, pseudodata distributions are generated from the f_1 functions resulting from the fit, assuming Poissonian fluctuation in each bin.

The pseudodata distribution are then fitted again in the background-only hypothesis. The procedure has been repeated 100 times for each signal hypothesis (with different $m(\mathrm{R}_1)$ and ρ_{m} values) and for each iteration the test statistic q (Eq. 7.10) has been evaluated. q is a generalization of the χ^2 test statistics, therefore it is applicable also when bin fluctuations are not Gaussian (low bin content).

The test statistic is defined as the likelihood ratio between the fit to the data and the *saturated* model [117], which is defined as the model where the expected content in each bin of the histogram is equal to the data observed in that bin:

$$q = -2\log\frac{\prod_{c=1}^{n_c}\prod_{i=1}^{n_b} Poisson(x_{ic}|\lambda_{ic})}{\prod_{c=1}^{n_c}\prod_{i=1}^{n_b} Poisson(x_{ic}|x_{ic})} = 2\sum_{c=1}^{n_c}\sum_{i=1}^{n_b}\left[\lambda_{ic} - x_{ic} + \frac{x_{ic}}{\lambda_{ic}}\right] \tag{7.10}$$

here the symbols have the same meaning as in Eq. 7.2.

The distribution of q obtained from the fit to the pseudodata distributions is roughly Gaussian for each signal hypothesis. The value of q is then evaluated also for the fit to the data (q_{data}), and it is compared with the mean value of q from the pseudodata (toy experiments). For the comparison, we define a *p-value* that is the number of toy experiments with $q > q_{\mathrm{data}}$, divided by the number of toys (n_{toys}), as in Eq. 7.11.

$$p\text{-}value = \frac{n_{q>q_{\mathrm{data}}}}{n_{\mathrm{toys}}} \tag{7.11}$$

Figure 7.23 shows the q distributions, the q_{data} and the resulting *p-values* obtained for a selection of signal hypotheses.

A *p-value* close to 0 would be a sign of discrepancies between the data and the model, suggesting that the chosen fit function fits data much worse than the toy, therefore it is not suitable for the fit. On the other hand, a value close to 1 could be a sign of *overfitting*, a situation that happens when the fit has too many degrees of freedom that cannot be constrained by the data.

The goodness of fit test described above has been systematically applied to the different signal hypotheses. The resulting *p-value* are shown in Fig. 7.24 (left). The *p-values* are mostly well above 0.05, except for some sporadic signal hypotheses.

The hyperbolic patterns shown in the figure are expected because they correspond to regions of the plane with similar values of $m(\mathrm{R}_2)$. In fact, the category selections

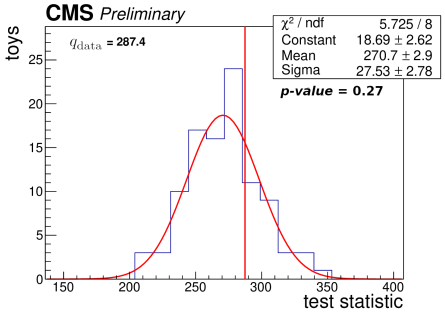

(a) $m(\mathrm{R}_1) = 3\,\mathrm{TeV}$, $\rho_\mathrm{m} = 0.1$

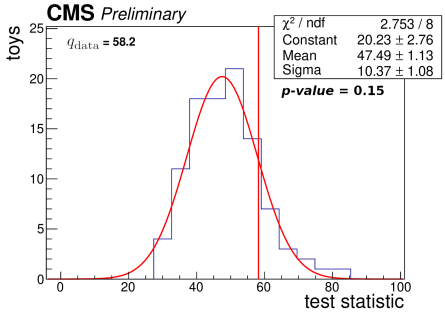

(b) $m(\mathrm{R}_1) = 3\,\mathrm{TeV}$, $\rho_\mathrm{m} = 0.2$

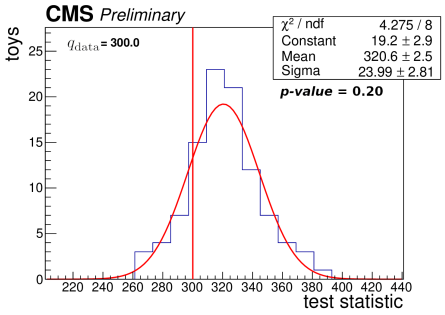

(c) $m(\mathrm{R}_1) = 5\,\mathrm{TeV}$, $\rho_\mathrm{m} = 0.1$

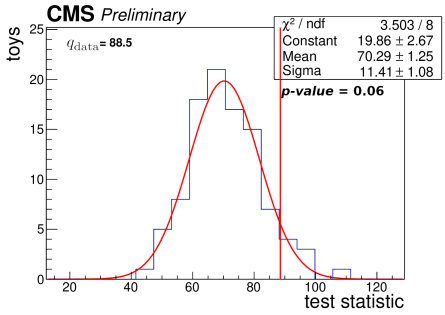

(d) $m(\mathrm{R}_1) = 5\,\mathrm{TeV}$, $\rho_\mathrm{m} = 0.2$

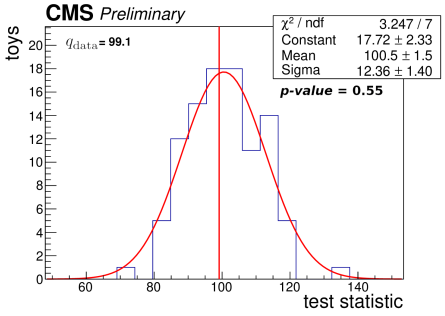

(e) $m(\mathrm{R}_1) = 7\,\mathrm{TeV}$, $\rho_\mathrm{m} = 0.1$

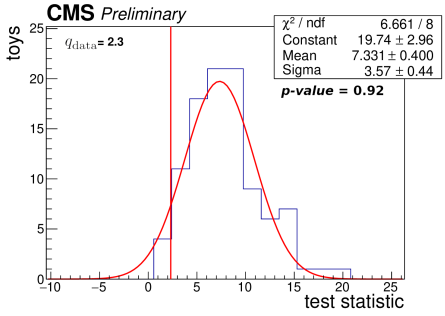

(f) $m(\mathrm{R}_1) = 7\,\mathrm{TeV}$, $\rho_\mathrm{m} = 0.2$

Figure 7.23. Distributions of the test statistic (q) obtained from 100 toy experiments for signal hypotheses with different $m(\mathrm{R}_1)$ and ρ_m values. The red curves represent the Gaussian fits to the distributions. The red vertical lines mark the values of the test statistic evaluated from data (q_data).

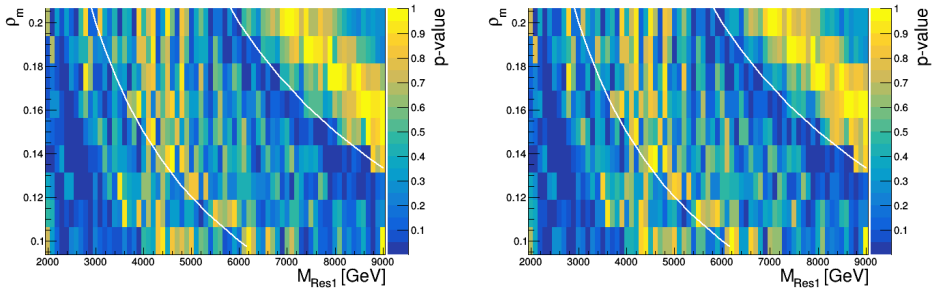

(a) background-only fit with function f_1 **(b)** background-only fit with function f_2

Figure 7.24. Goodness of fit *p-value* for the different signal hypothesis considered in the analysis. The two white hyperboles, corresponding to the values of $m(\mathrm{R}_2) = 0.6$ and 1.2 TeV, mark the transitions from 22 to 9 categories and from 9 to 1 category respectively. The hyperbolic patterns in the *p-value* distribution are expected, because signal hypothesis with the same value of $m(\mathrm{R}_2)$ share the same fraction of events.

defined in Sec. 7.2 depends on the value of $m(\mathrm{R}_2)$, and signal hypotheses belonging to the same hyperbole in the ρ_m vs. $m(\mathrm{R}_1)$ plane share the same event selection, therefore the fit results are similar in these cases. Because of this effect, the *p-value* for the different signal hypotheses are correlated and the resulting *p-value* distribution is not uniform contrary to what would be expected.

We can identify two regions of the plane where the *p-value* is below 0.05, respectively around $(m(\mathrm{R}_1), \rho_\mathrm{m}) \approx (2.7\,\mathrm{TeV}, 0.14)$ and $\approx(8\,\mathrm{TeV}, 0.14)$. We performed a dedicated test for the signal hypotheses corresponding to these two regions. We evaluated the single χ^2 of the fits to the m_jj spectra of each category, and removed the category with the lowest value. The fit has been repeated and the q distribution, the q_data value and the *p-value* have been re-evaluated. The new *p-values* are shown to be similar or larger than 0.05. This test shows that the low *p-values* in the two regions of the plane are due to statistical fluctuation in data and not to the specific choice of the background fit function.

The right part of Fig. 7.24 shows the result of the same goodness of fit test performed fitting the data with the alternative function f_2:

$$f_2(m_\mathrm{jj}) = \frac{p_0 e^{-p_1\left(\frac{m_\mathrm{jj}}{\sqrt{s}}\right)}}{\left(\frac{m_\mathrm{jj}}{\sqrt{s}}\right)^{p_2}} \tag{7.12}$$

This function, which also fits well the data, is used to test for the presence of bias in the fit, following the procedure described in Sec. 7.3.4.2.

7.3.4.2 Bias test

The background estimation is obtained with a fit to data, using the empirical function f_1 of Eq. 7.4. The true functional form of the m_{jj} distribution of QCD multijet background events is unknown, therefore f_1 is not the only possible choice for the fit. For example, we showed that the f_2 function of Eq. 7.12 can fit the data with the same performance as f_1. Moreover, in presence of signal, the fit function could absorb the bump, introducing a bias in the signal extraction. For these reasons we tested for the presence of bias in the fit, comparing also the bias for the functions f_1 and f_2. We adopted the following procedure:

- A sample of 100 pseudodata distributions is generated for all signal hypothesis considered, using one of the two background functions, with parameters fixed to the values from the best fit to collision data. A signal is injected in the pseudodata distributions, assuming a cross section equal to the expected upper limit resulting from the analysis (described in Sec. 8.2).
- The distributions are fitted with the same generation function or with the other one, following the same fit method used for the analysis of actual data. The signal cross section resulting from the fit is obtained, along with its standard deviation.
- The extracted value of the signal cross section is compared with the injected one and the signal bias (defined below) is evaluated.

The procedure described above is repeated also without the injection of a signal. To evaluate the bias for each signal hypothesis, we defined the pulls of the signal cross section as the difference between the injected signal cross section (σ_{inj}) and the fitted signal cross section (σ_{fit}) divided by the error on the standard deviation (σ_{err}) of the fit[1]

$$\text{pull} = \frac{\sigma_{\text{fit}} - \sigma_{\text{inj}}}{\sigma_{\text{err}}} \tag{7.13}$$

Figure 7.25 shows the pull distributions obtained for 6 different signal hypothesis, for the test performed both generating and fitting with f_1. The mean of the histograms gives our estimation of the bias in units of σ_{err}. In this case σ_{inj} is equal to the 95% CL expected limit for each signal hypothesis.

The Figures reported in the next Paragraphs show the measured bias as a function of ρ_{m} and $m(\text{R}_1)$ for the considered signal hypotheses. The results are reported for all the tests performed with different configurations of functions (generation with f_1 and fit with f_1, generation with f_2 and fit with f_1, etc.), with and without the injection of a signal.

In general, an absolute value of the bias below 0.5 is considered negligible. In this case, in fact, the total uncertainty on the signal cross section from the combination of the bias and the fit uncertainty would be:

$$\sigma_{\text{err}}^{\text{tot}} = \sqrt{\sigma_{\text{err}}^2 + (0.5\sigma_{\text{err}})^2} \sim 1.1\sigma_{\text{err}} \tag{7.14}$$

[1] In the figures of this section we use a different notation: $\sigma_{\text{fit}} = r_{\text{fit}}$, $\sigma_{\text{inj}} = r_{\text{inj}}$, and $\sigma_{\text{err}} = r_{\text{err}}$

The increase due to the bias on the total uncertainty would be about 10% of the fit uncertainty, therefore it can be neglected.

Generation and fit with f_1

The pulls reported in Figs. 7.26 and 7.27 are obtained using f_1 for both the generation and the fit, respectively with and without the injection of a signal. This test is used as a "closure" test for the fit with f_1. The right plot of each Figure shows the histogram of the bias values obtained. The results shows that the average bias is well below 0.5 and can then be neglected.

The top regions of Figs. 7.26a and 7.27a, show the largest bias. This increase in the bias can be caused by the left fit range, which may cut a portion of the left tail of the signal peak. However ,the effect is moderate. Figs. 7.26b and 7.27b show, in fact, that also in this region the bias is about 0.6-0.7.

The region of Fig. 7.27a for $m(\mathrm{R}_1) > 7\,\mathrm{TeV}$ shows only positive values for the bias. This is because σ_{fit} is forced to be positive in that region. At such high values of $m(\mathrm{R}_1)$, in fact, the m_{jj} distribution is poorly populated, and a negative fluctuation of σ_{fit} would cause the signal+background distribution to be negative, which is unrealistic. As a consequence the bias in that region can only be positive. This does not happen in Fig. 7.26 because the injection of a signal populates the spectra at high m_{jj} values, and the total distribution is always positive. In this case negative value of the bias arise when $\sigma_{\mathrm{fit}} < \sigma_{\mathrm{inj}}$ on average.

Generation with f_2 and fit with f_1

The bias test has been performed also generating pseudodata using f_2 and fitting with f_1. Figures. 7.28 and 7.29, respectively produced with and without the injection of a signal, show that also in this case the bias is negligible. This test ensures that the function f_1 is flexible enough to model the background, even if it originates from a different functional form (that also fits well the data).

Also in this case the top region shows the largest bias, and the region corresponding to $m(\mathrm{R}_1) > 7\,\mathrm{TeV}$ shows only positive bias (see previous paragraph).

Generation with f_1 and fit with f_2

We also performed the test inverting the two functions, i.e. using f_1 to generate pseudodata and f_2 for the fit. The results are reported in Figs. 7.30 and 7.31. The fit with f_2 shows in general larger (absolute) value of the bias and less uniformity in the ρ_{m} vs. $m(\mathrm{R}_1)$ plane with respect to the fit with f_1.

We can conclude that f_1 is the function that introduces the smaller bias between the two, and for this reason we choose it for the fit.

Generation and fit with f_2

We performed on f_2 a similar closure test as that performed for f_1. Figures. 7.32 and 7.33 show the bias obtained by generating and fitting the pseudodata distributions with f_2. Also in this case the bias distribution is less uniform across the ρ_{m} vs. $m(\mathrm{R}_1)$ plane with respect to that from the fit with f_1.

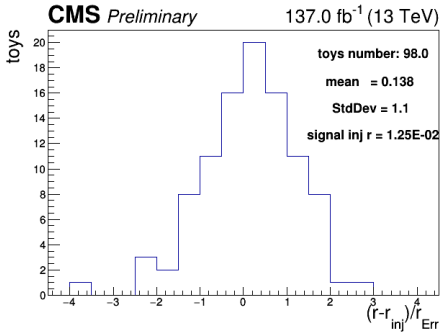

(a) $m(\mathrm{R}_1) = 3\,\mathrm{TeV}$ $\rho_\mathrm{m} = 0.1$

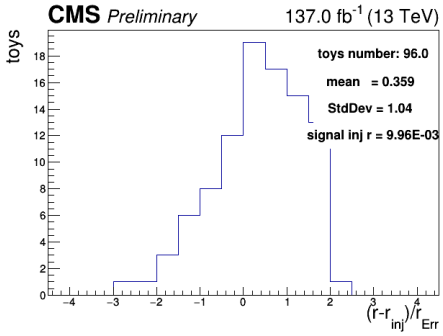

(b) $m(\mathrm{R}_1) = 3\,\mathrm{TeV}$ $\rho_\mathrm{m} = 0.2$

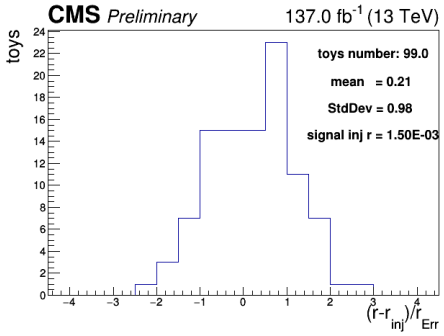

(c) $m(\mathrm{R}_1) = 5\,\mathrm{TeV}$ $\rho_\mathrm{m} = 0.1$

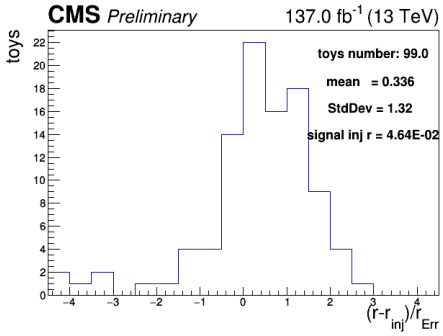

(d) $m(\mathrm{R}_1) = 5\,\mathrm{TeV}$ $\rho_\mathrm{m} = 0.2$

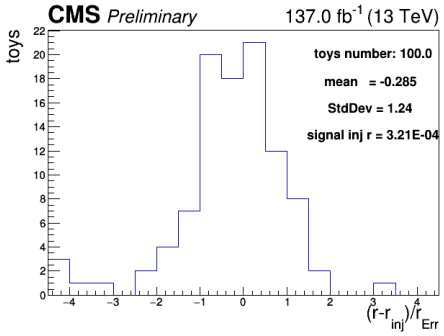

(e) $m(\mathrm{R}_1) = 7\,\mathrm{TeV}$ $\rho_\mathrm{m} = 0.1$

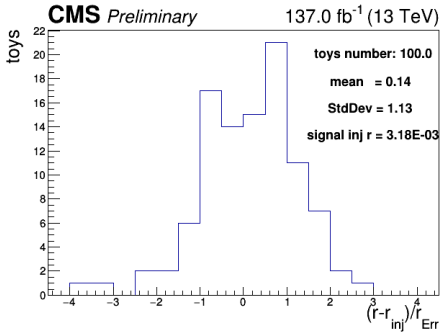

(f) $m(\mathrm{R}_1) = 7\,\mathrm{TeV}$ $\rho_\mathrm{m} = 0.2$

Figure 7.25. Pull distribution plots of fitted signal strength parameter (**r**) from 100 toys both generated and fitted with function f_1, for different signal hypothesis (different set of categories). In these plots the injected signal cross section is equal to the expected upper limit for each signal hypothesis. In the z-axes of the plots the signal cross section, σ, is indicated with r

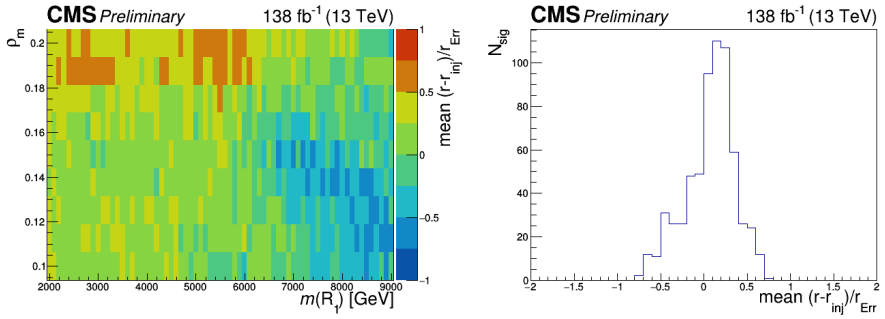

(a) $\sigma_{\text{inj}} = 95\%$ CL expected upper limit. **(b)** bias histogram

Figure 7.26. Left: bias versus ρ_{m} and $m(\text{R}_1)$ from pseudodata both generated and fitted with function f_1. A signal is injected with a cross section equal to the expected limit. Right: 1D histogram of the bias (N_{sig} = # of signal hypotheses). The position of the peak of the distribution, around 0.2, shows the presence of a small bias which can be considered negligible.

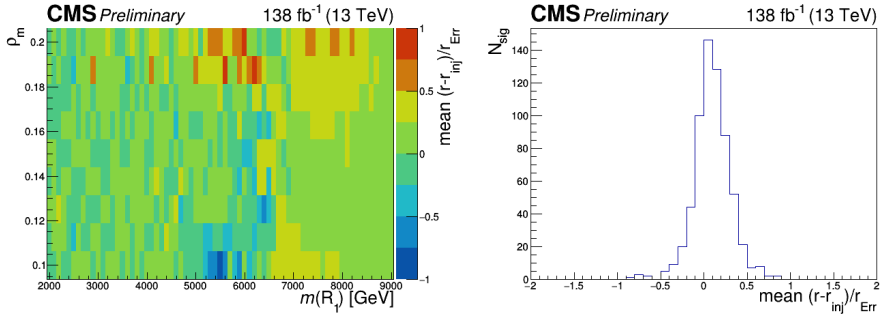

(a) No signal injection **(b)** bias histogram

Figure 7.27. Same as Fig. 7.26, but for test performed without the signal injection.

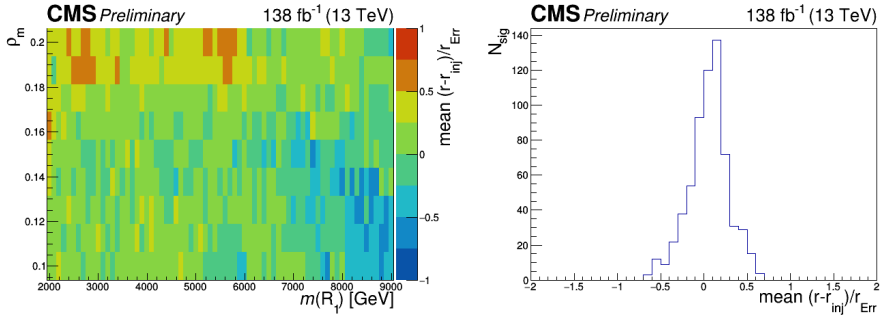

(a) $\sigma_{\text{inj}} = 95\%$ CL expected upper limit. **(b)** bias histogram

Figure 7.28. Left: bias versus ρ_{m} and $m(\text{R}_1)$ from pseudodata generated with f_2 and fitted with f_1. A signal is injected with a cross section equal to the expected limit. Right: 1D histogram of the bias (N_{sig} = # of signal hypotheses).

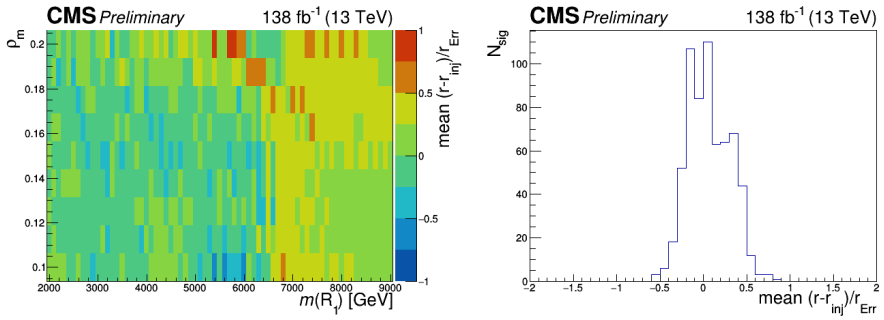

(a) No signal injection **(b)** bias histogram

Figure 7.29. Same as Fig. 7.28, but for test performed without the signal injection.

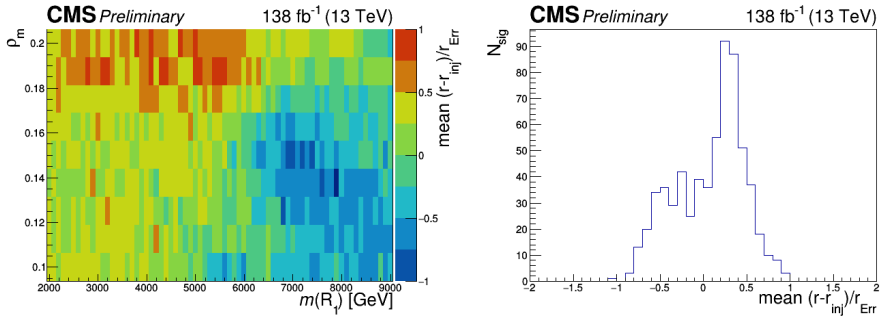

(a) $\sigma_{\text{inj}} = 95\%$ CL expected upper limit. **(b)** bias histogram

Figure 7.30. Left: bias versus ρ_{m} and $m(\text{R}_1)$ from pseudodata both generated and fitted with f_2. A signal is injected with a cross section equal to the expected limit. Right: 1D histogram of the bias (N_{sig} = # of signal hypotheses).

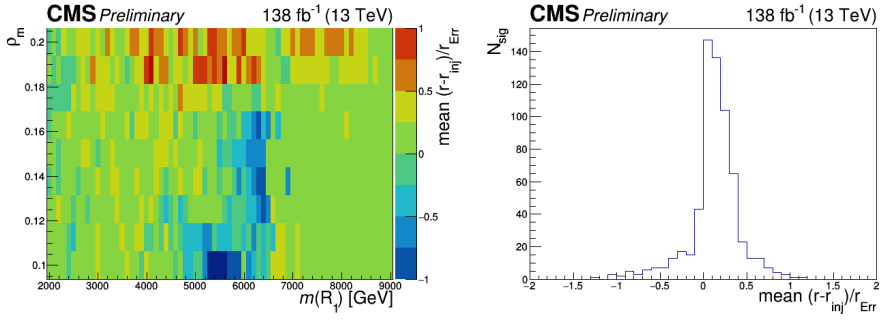

(a) No signal injection **(b)** bias histogram

Figure 7.31. Same as Fig. 7.30, but for test performed without the signal injection.

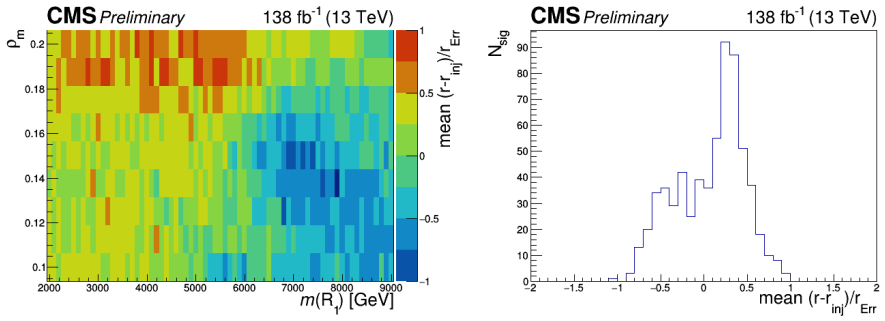

(a) $\sigma_{\text{inj}} = 95\%$ CL expected upper limit. **(b)** bias histogram

Figure 7.32. Left: bias versus ρ_{m} and $m(\text{R}_1)$ from pseudodata both generated and fitted with f_2. A signal is injected with a cross section equal to the expected limit. Right: 1D histogram of the bias (N_{sig} = # of signal hypotheses).

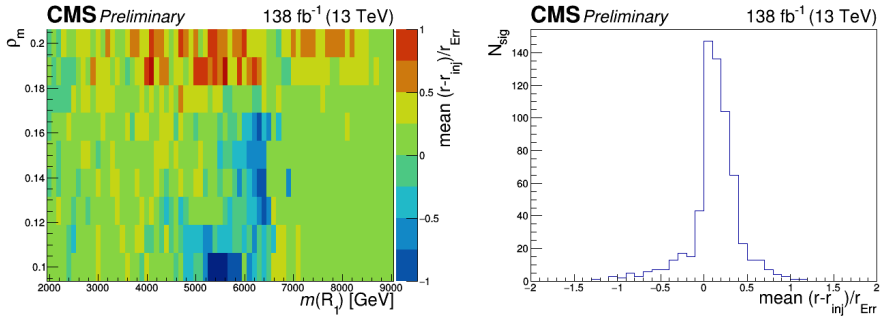

(a) No signal injection **(b)** bias histogram

Figure 7.33. Same as Fig. 7.32, but for test performed without the signal injection.

Chapter 8

Results and interpretation

In this Chapter we report the results of the search for signal processes involving the production of a new high-mass resonance (R_1), which decays into a parton and a second resonance (R_2), which in turns decay into two partons. The search uses the full dataset of pp collisions collected in the LHC Run 2, at $\sqrt{s} = 13\,\text{TeV}$, corresponding to an integrated luminosity of $138\,\text{fb}^{-1}$, and follows the strategy described in Ch. 7.

We tested for signal hypotheses with R_1 masses ($m(R_1)$) between 2 and 9 TeV, in steps of 0.1 TeV, and for ρ_m values between 0.1 and 0.2, in steps of 0.0125, where ρ_m is the ratio between the masses of the two resonances ($m(R_2)/m(R_1)$). The analysis is not sensitive to $m(G_{KK}) < 2\,\text{TeV}$, because of the trigger and event selection criteria discussed in Sec. 6.1, and larger values of ρ_m are not considered because of the small signal efficiency (Sec. 7.3.3.2).

The fit to the dijet mass (m_{jj}) spectra of the event categories defined in Sec. 7.2 has been performed following the method described in Sec. 7.3 for all the signal hypotheses considered. The evaluation of the significance of the observed excesses from the fit is reported in Sec. 8.1. No significant excess has been found above the SM background predictions.

The analysis sets limits on the benchmark warped extra dimension (WED) model introduced in Sec. 2.2.3. In this model R_1 is a KK gluon (G_{KK}), R_2 is a radion (ϕ) and the three partons produced in the decay are all gluons.

The analysis then set limits on the G_{KK} production cross section following the method described in Sec. 8.2. The resulting limits are reported in Sec. 8.2.2, as a function of $m(G_{KK})$ and ρ_m, and they are interpreted as limits on G_{KK} and ϕ masses. Our results are then compared to that provided by the latest CMS inclusive search for dijet resonances [30], showing the gain in sensitivity obtained with the analysis presented here.

8.1 Significance of observed excesses

8.1.1 Local significance

The local significance of the observed excesses is evaluated through an hypothesis test that quantifies the probability for the background to fluctuate, and give an excess of events as large, or larger, than the observed one.

For a given signal hypothesis with fixed $m(\mathrm{R}_1)$ and ρ_m, the test statistic used is the log-likelihood ratio:

$$q_0 = -2\ln\frac{L(\boldsymbol{x}|\mu=0,\hat{\boldsymbol{\theta}}_0)}{L(\boldsymbol{x}|\hat{\mu},\hat{\boldsymbol{\theta}})} \quad \text{and} \quad \hat{\mu}\geq 0. \tag{8.1}$$

The likelihood $L(\boldsymbol{x}|\mu,\boldsymbol{\theta})$ is the same defined in Eq. 7.2. Here we made explicit its dependence on the data $\boldsymbol{x}$, the signal strength modifier μ and the background parameters $\boldsymbol{\theta}$. $\hat{\boldsymbol{\theta}}_0$ refers to the set of θ values that maximizes the likelihood given $\mu = 0$. The parameter estimators $\hat{\mu}$ and $\hat{\boldsymbol{\theta}}$ correspond, instead, to the global maximum of the likelihood. The constraint $\hat{\mu}\geq 0$ limits the test statistic at zero for likelihoods with negative fluctuations of μ, since we are not interested in interpreting a deficit of events with respect to the expected background.

The distribution of the q_0 can be determined using Wilks' theorem [118] provided the number of analyzed events is large enough (i.e in the Asymptotic limit). Under this assumption, q_0 distribution asymptotically approaches a chi-squared (χ^2) distribution with 1 degree of freedom. We can then evaluate the p-value (p_0) corresponding to a given experimental observation of q_0^{obs} as:

$$p_0 = P(q_0\geq q_0^{\mathrm{obs}}) = \int_{q_0^{\mathrm{obs}}}^{\infty} f_k(q_0)dq_0 = \frac{1}{2}\left[1-\mathrm{Erf}\left(\sqrt{q_0^{\mathrm{obs}}/2}\right)\right] \tag{8.2}$$

where $f_k(q_0)$ is the distribution of a χ^2 with $k=1$ degrees of freedom and "Erf" is the error function. To convert the p-value into a significance S expressed as number of standard deviations σ, we adopt the convention of a "one-sided Gaussian tail":

$$p_0 = \int_{\mathrm{S}}^{\infty}\frac{1}{\sqrt{2\pi}}\exp(-x^2/2)dx \tag{8.3}$$

In high energy physics experiments, the value of $\mathrm{S}=5\sigma$, corresponding to $p_0 = 2.8\times10^{-7}$, is commonly considered the significance threshold to be passed by a signal to claim its discovery. For our analysis the value of the observed local significances is reported in Fig. 8.1, for all the signal hypotheses tested, as a function of $m(\mathrm{R}_1)$ ($= m(\mathrm{G_{KK}})$ in our benchmark model) and ρ_m.

No excess above $\mathrm{S}=5\sigma$ was found, with the two largest excesses corresponding to $\mathrm{S}=3.6$ and 2.8σ, respectively for $m(\mathrm{R}_1)=2.9$ and $4.2\,\mathrm{TeV}$, and $\rho_\mathrm{m}\approx 0.138$. The two excesses are surrounded by regions with similar observed significance. This is an expected consequence of the event categories definition and the fit method described in Sec. 7.2 and Sec. 7.3. The categories definition, in fact, is based on the value of the second resonance mass, $m(\mathrm{R}_2)$, in the signal hypothesis considered. Hence, two nearby signal hypotheses, with similar value of $m(\mathrm{R}_2)$, partially share the same events. For this reason they are affected by the same statistical fluctuations with respect to the expected background. Thus, the fit to data yields similar results for signal hypotheses which are close in the ρ_m vs. $m(\mathrm{R}_1)$ plane.

Figs. 8.2 and 8.3, show the background-only fit results, respectively for ($m(\mathrm{R}_1)=2.9, \rho_\mathrm{m}=0.138$) and ($m(\mathrm{R}_1)=4.2, \rho_\mathrm{m}=0.138$). The dijet mass spectra in data and the background-only fits are shown for the 20 categories used for the fit (2 categories are removed because of the $m_{\mathrm{jj}}^{\mathrm{thr}}$ requirements described in Sec. 7.3.2). The Figures also show, in the plot at the bottom of each category spectrum, the plot of the pulls,

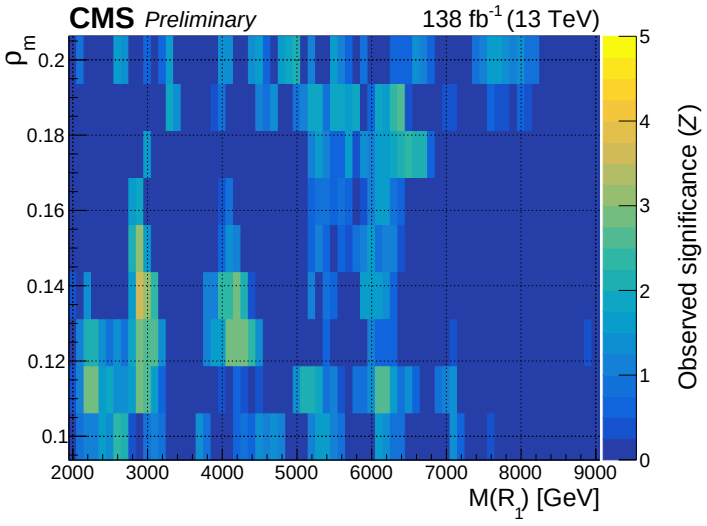

Figure 8.1. Observed local signal significance as a function of ρ_{m} and $m(\mathrm{R}_1)$. We identify two distinct regions around the two most significant excesses, which corresponds to $m(\mathrm{R}_1) = 2.9$ and 4.2 TeV, for $\rho_{\mathrm{m}} \approx 0.138$. The local significance is respectively $\mathrm{S} = 3.6\sigma$ and 2.8σ. The two most significant excesses are surrounded by regions because nearby categories in the plane partially share the same events.

defined as the difference between the data and the background yields in each bin, divided by the statistical uncertainty (assuming Poissonian fluctuation in each bin). These plots (called for simplicity ratio plots) show the agreement between the data and the background-only fit. The plots also shows the signal distributions for each category, normalized to a cross section equal to the observed 95% $\mathrm{CL_s}$ limit times the branching fraction (for a definition of the limits see Sec. 8.2).

The signal+background fit results, for the same two signal hypotheses, are reported in Figs. 8.4 and 8.5. In this case the signal is normalized to the fitted cross section, which are $\sigma_{\mathrm{fit}} = 30 \pm 9$ and 5 ± 2 fb, respectively for $m(\mathrm{R}_1) = 2.9$ and 4.2 TeV. The two values of the cross section are roughly consistent with the corresponding local significances of 3.6σ and 2.8σ, since $\sigma_{\mathrm{fit}}/\sigma_{\mathrm{err}} \approx 3.3$ and 2.5 respectively. The p-values from the goodness-of-fit tests of these two signal+background fits (evaluated with the method described in Sec. 7.3.4.1) are 0.21 and 0.23 respectively for $m(\mathrm{R}_1) = 2.9$ and 4.2 TeV. These values are larger than that of the corresponding background-only fits, which are 0.03 and 0.14, because the presence of a signal increase the agreement between the fit and the data.

For illustrative purposes, the m_{jj} spectra of the categories are combined in a single spectrum, for all the fits shown in Figs. from 8.2 to 8.5. The combination, shown in Fig. 8.6, is performed following the procedure of Ref. [119]. The spectra of the categories are combined through a weighted sum. The weight for the category i is equal to:

$$w_i = \frac{S_i}{S_i + B_i} \tag{8.4}$$

where S_i is the number of expected signal events in the category i and B_i the

number of expected background events. S_i is calculated as the integral of the signal event distribution in an m_{jj} interval of $\pm 20\%$ around the signal peak, assuming a signal cross section equal to the observed 95% CL upper limit for the background-only fits, and a signal cross section equal to the fitted one for the signal+background fits. B_i is defined as the integral of the background component of the fit, in the same m_{jj} interval.

The fit is displayed in the portion of the m_{jj} fit range common to all the categories, together with the signal peak normalized to the assumed cross section. Fig. 8.6 shows both the statistical uncertainty on data and the uncertainty on the fitted background distribution. For the evaluation of the latter:

- we generated $\sim$1000 toy datasets from the m_{jj} spectra from data (Poissonian fluctuation);
- we performed the fit for each of the generated toy datasets;
- we evaluated the bin content for each bin using the fitted background distribution;
- the root mean squares (RMS) of each bin is then the fit uncertainty for that bin.

This uncertainty is represented in Fig. 8.6 with a grey hatched band around the fit, which is barely visible in most of the combined spectra.

The Fig. 8.6 highlights the observed excesses for the two signal hypotheses, and allowing for a better comparison between the data and the fit. The blue distribution of the ratio plots (below each combined spectra) shows the signal significance in each bin (the number of signal events divided by the statistical uncertainty on the fitted background). The local signal significances of the signal hypotheses reported above (S = 3.6 and 2.8σ) is roughly consistent with the sum of the squares of the signal significance.

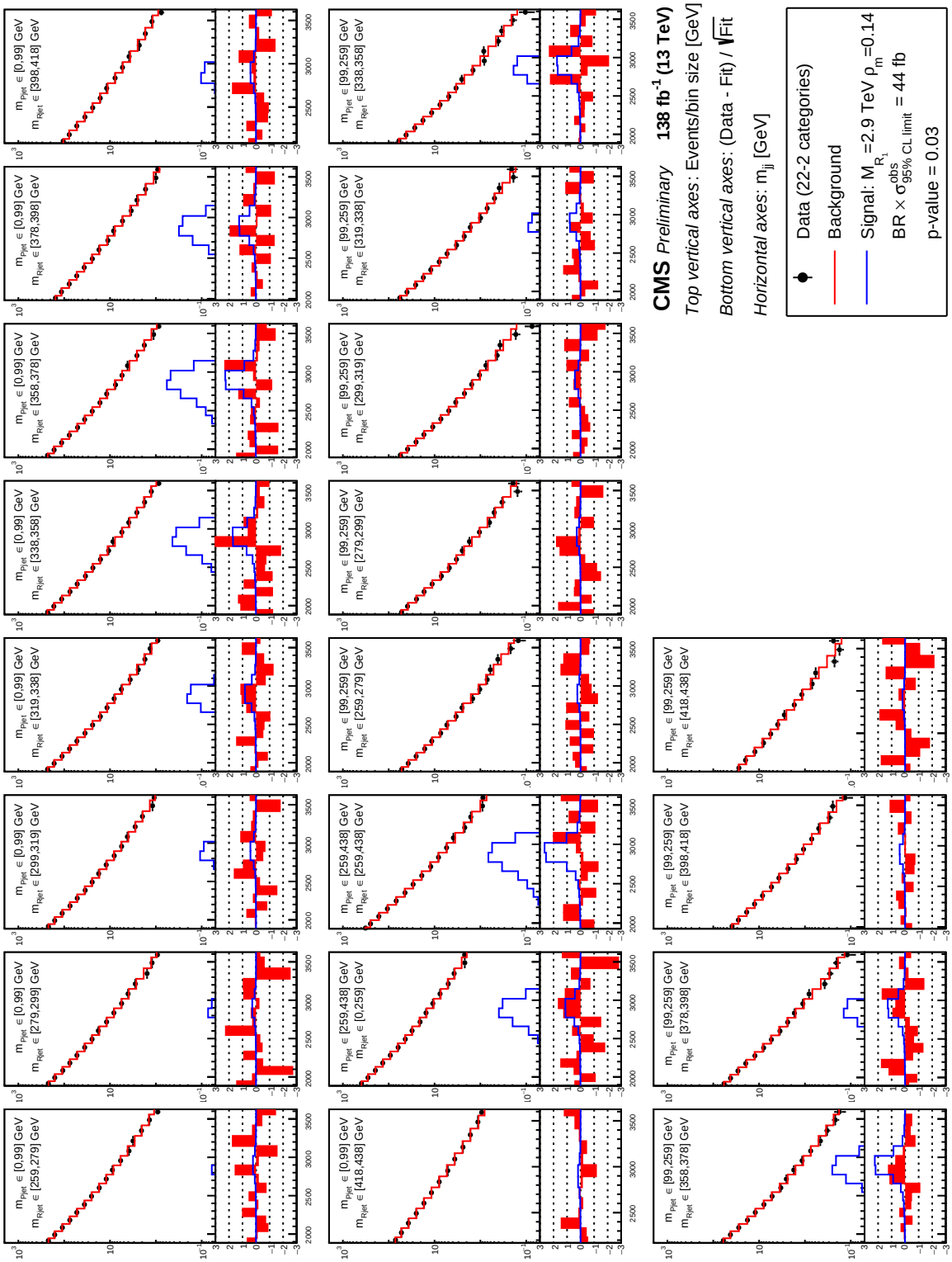

Figure 8.2. m_{jj} spectra (black points) from data, for 22 the categories corresponding a to signal hypothesis with $m(\mathrm{R}_1) = 2.9$ TeV and $\rho_{\mathrm{m}} = 0.138$. The resulting background-only fit is also shown (red line), together with a signal normalized to a cross section equal to the expected limit (blue line). The horizontal axis of each plot shows the value of m_{jj} in GeV. The vertical axis shows, in the top part of each plot, the bin event content divided by the bin width, and, in the bottom part, the difference between the simulated spectra and the fit divided by the statistical uncertainty for each bin. The p-value of the goodness of fit test for this fit is reported in the bottom-right part of the figure.

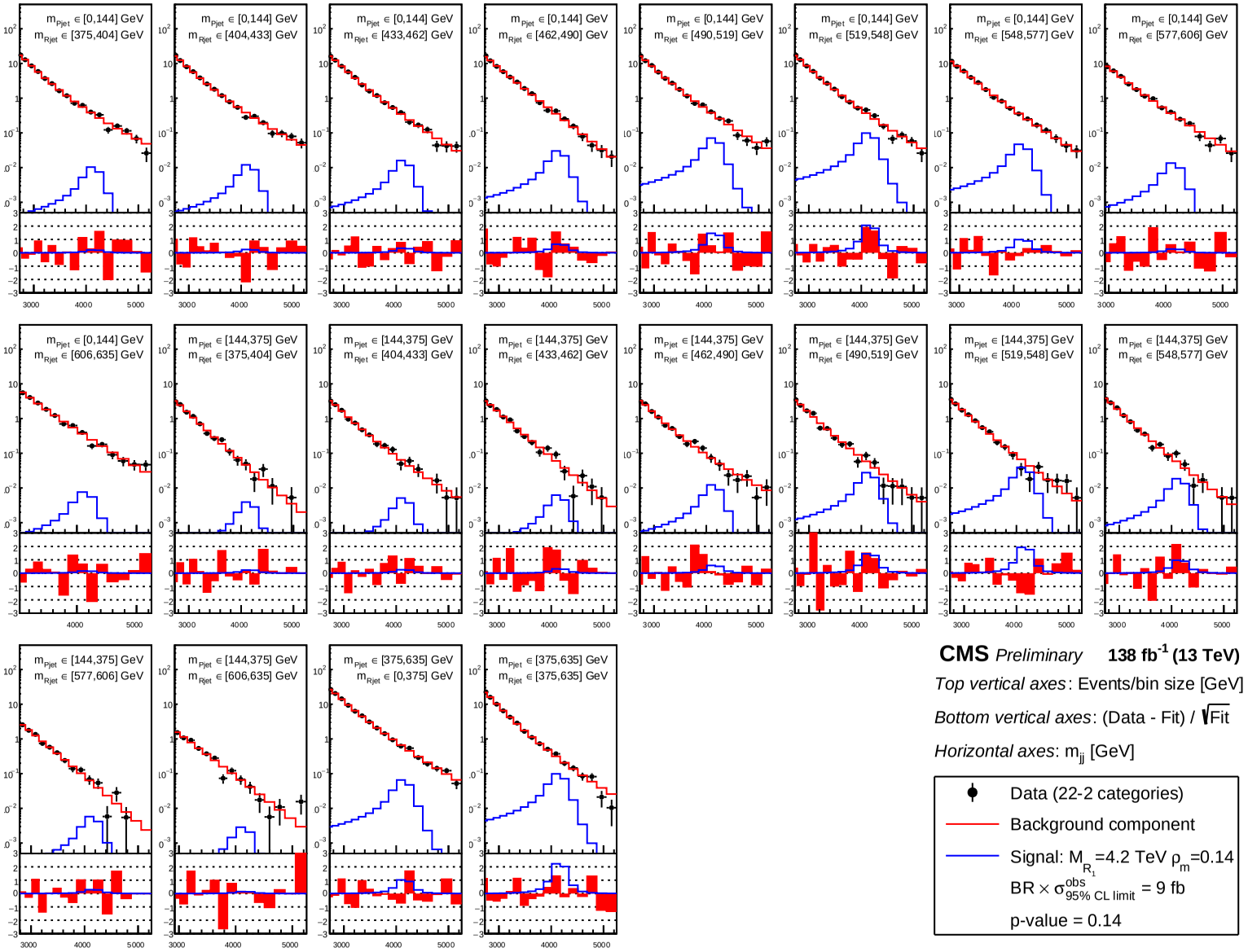

Figure 8.3. m_{jj} spectra (black points) from data, for 22 the categories corresponding a to signal hypothesis with $m(\mathrm{R}_1) = 4.2\,\mathrm{TeV}$ and $\rho_{\mathrm{m}} = 0.138$. The resulting background-only fit is also shown (red line), together with a signal normalized to a cross section equal to the expected limit (blue line). The horizontal axis of each plot shows the value of m_{jj} in GeV. The vertical axis shows, in the top part of each plot, the bin event content divided by the bin width, and, in the bottom part, the difference between the simulated spectra and the fit divided by the statistical uncertainty for each bin. The p-value of the goodness of fit test for this fit is reported in the bottom-right part of the figure.

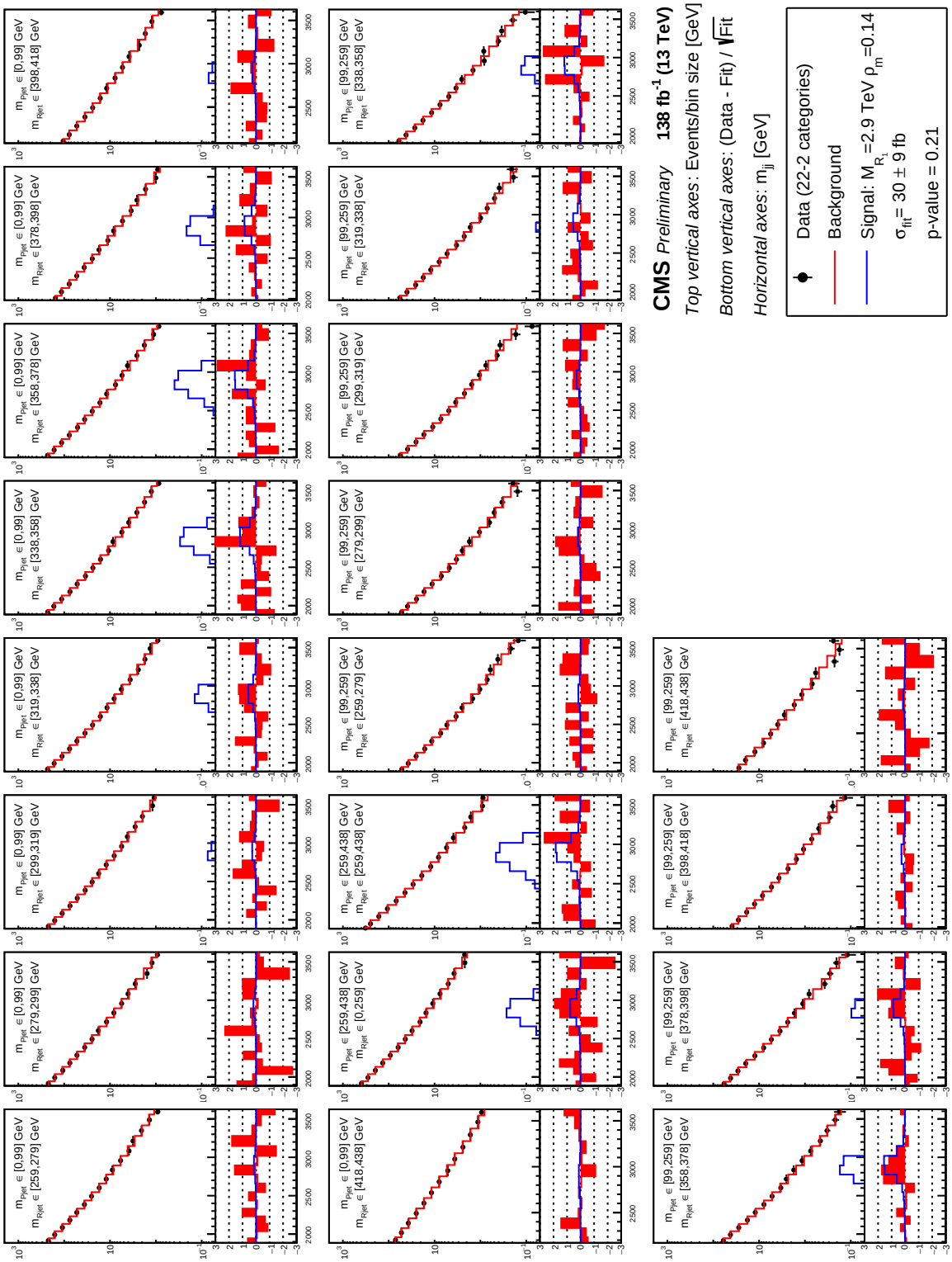

Figure 8.4. m_{jj} spectra (black points) from data, for 22 the categories corresponding a to signal hypothesis with $m(R_1) = 2.9$ TeV and $\rho_m = 0.138$. The resulting signal+background fit is also shown (red line), together with a signal normalized to the fitted cross section. The horizontal axis of each plot shows the value of m_{jj} in GeV. The vertical axis shows, in the top part of each plot, the bin event content divided by the bin width, and, in the bottom part, the difference between the simulated spectra and the fit divided by the statistical uncertainty for each bin. The p-value of the goodness of fit test for this fit is reported in the bottom-right part of the figure.

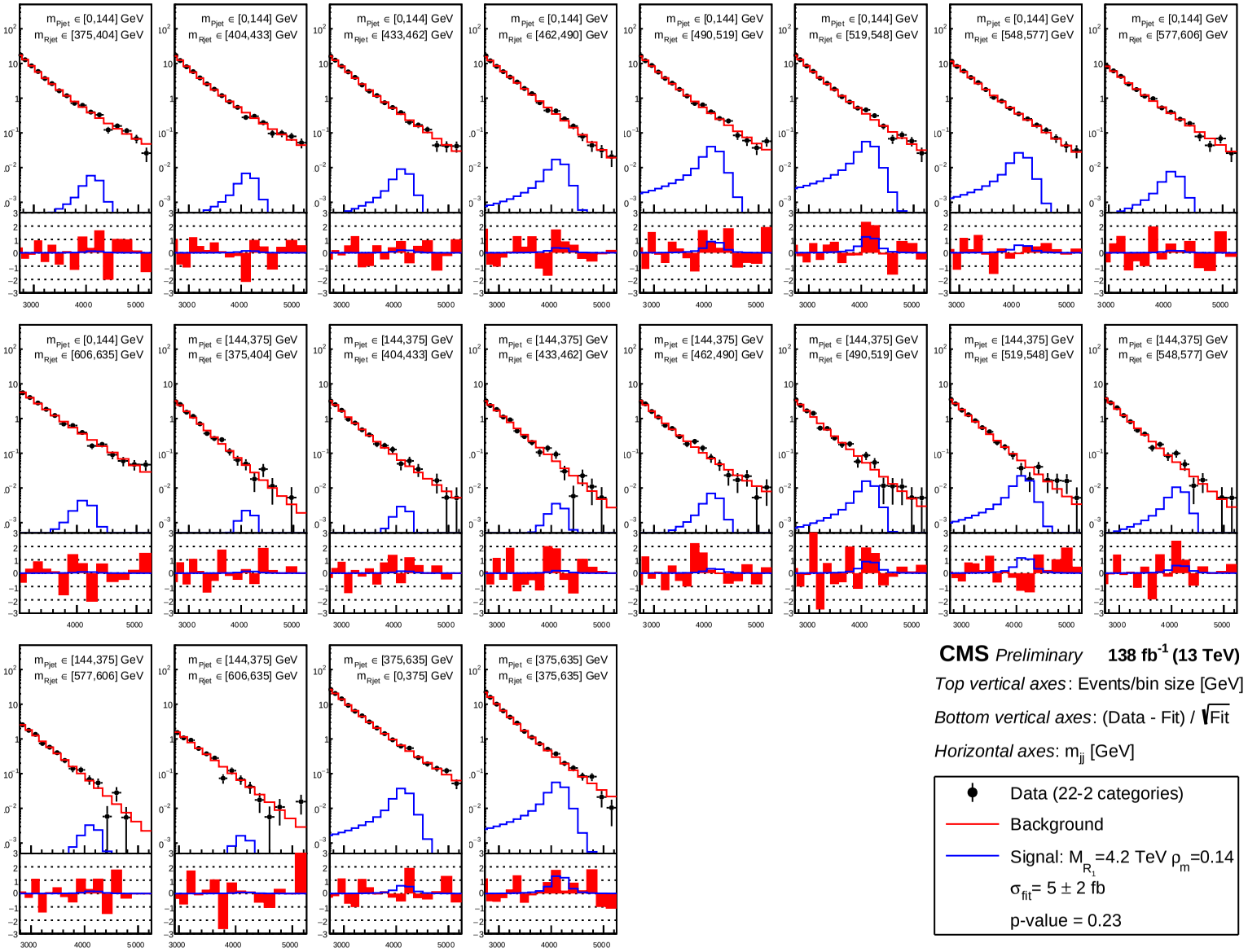

Figure 8.5. m_{jj} spectra (black points) from data, for 22 the categories corresponding a to signal hypothesis with $m(\mathrm{R}_1) = 4.2\,\mathrm{TeV}$ and $\rho_{\mathrm{m}} = 0.138$. The resulting signal+background fit is also shown (red line), together with a signal normalized to the fitted cross section. The horizontal axis of each plot shows the value of m_{jj} in GeV. The vertical axis shows, in the top part of each plot, the bin event content divided by the bin width, and, in the bottom part, the difference between the simulated spectra and the fit divided by the statistical uncertainty for each bin. The p-value of the goodness of fit test for this fit is reported in the bottom-right part of the figure.

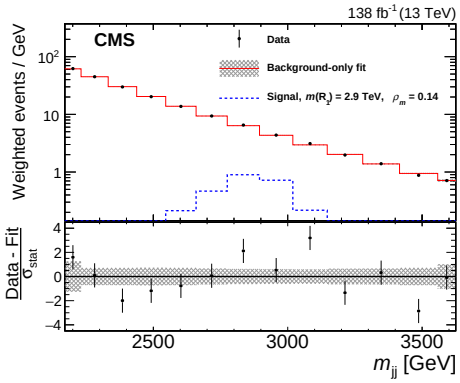

(a) $m(\mathrm{R}_1) = 2.9\,\mathrm{TeV}$, $\rho_\mathrm{m} = 0.138$, b-only fit

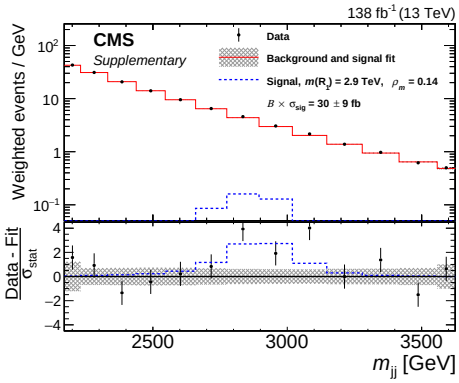

(b) $m(\mathrm{R}_1) = 2.9\,\mathrm{TeV}$, $\rho_\mathrm{m} = 0.138$, s+b fit

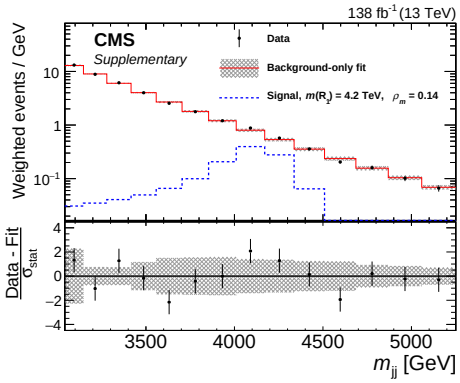

(c) $m(\mathrm{R}_1) = 4.2\,\mathrm{TeV}$, $\rho_\mathrm{m} = 0.138$, b-only fit

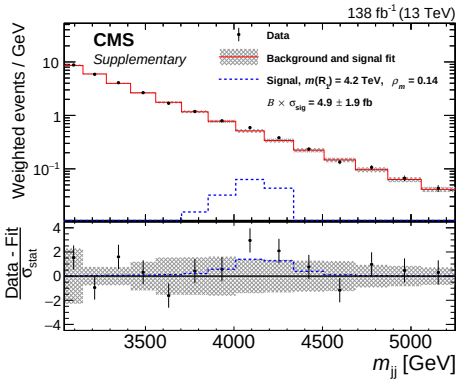

(d) $m(\mathrm{R}_1) = 4.2\,\mathrm{TeV}$, $\rho_\mathrm{m} = 0.138$, s+b fit

Figure 8.6. Dijet mass spectrum from the combination of th m_{jj} spectra from the different categories of the two signal hypotheses with the largest observed excesses. Both the background-only (b-only) and signal+background (s+b) fits are shown. Each figure shows the data (black points) with vertical bars representing the statistical uncertainty (σ_{stat}), the background component of the fit (red line) and its uncertainty (barely visible gray hatched area) together with the signal shape (dashed line) normalized to a cross section equal to the 95% $\mathrm{CL_s}$ upper limit (b-only fit) or to its post-fit value (s+b fit). The m_{jj} spectra of data, background and signal shapes of the different categories, are combined through the weighted sum discussed in the text. The lower panel shows the difference between the data and the background prediction (points), and the background uncertainty (hatched gray area), divided by the statistical uncertainty.

8.1.2 Global significance of largest excess

The significance of the largest excess has been also evaluated with toy experiments, without the asymptotic limit approximation. To perform this test we generated ∼10.000 toy datasets from the m_{jj} spectra of the categories of the corresponding signal hypothesis. We then fitted the generated m_{jj} spectra and evaluated the significance (S) for each toy dataset.

The result of this process is the distribution of S shown in Fig. 8.7. From this distribution, the p-value corresponding to $\mathrm{S} = 3.6\sigma$ is 6.5×10^{-41}. This value is higher than $\sim 2 \times 10^{-4}$, which would be the p-value corresponding to $\mathrm{S} = 3.6\sigma$ for a normal distribution. Converting the p-value from the simulated distribution in a number of standard deviations, the actual significance of the excess is $\mathrm{S} = 3.2\sigma$. We can conclude then that the asymptotic approximation provides a fair estimation of the significance of the most significant observed excess.

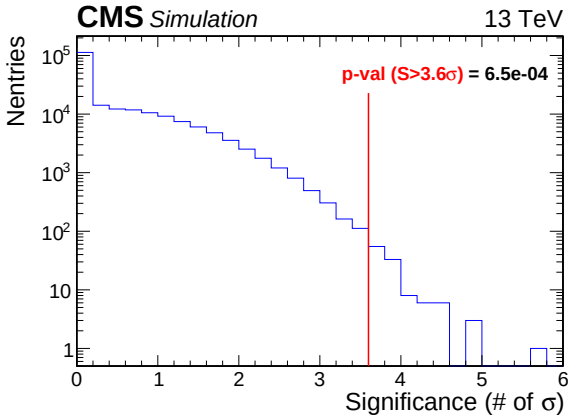

Figure 8.7. Distribution of the significance S obtained from ∼10.000 toy experiments. The two vertical lines mark the observed significance of the largest excess: 3.6σ.

Since the values of the two resonance masses are unknown, we test a broad range of $m(\mathrm{R}_1)$ and ρ_{m} hypotheses. When testing such a large number of hypotheses, an apparently statistically significant observation may have actually arisen by chance. For example, if one is performing n multiple independent tests, a p-value of $1/n$ is expected to occur once per n tests. We must then evaluate the probability that a fluctuation, similar or larger than the most significant one, can be obtained at least for one of the signal hypotheses tested. This significance "dilution" effect, associated with the multiple testing, is also known as a trial factor or look-elsewhere effect [120].

The significance, corrected for this effect, is called global significance. Here we report the evaluation of the global significance for the largest excess found, which corresponds to a local significance of $\mathrm{S}^{\mathrm{obs}} = 3.2\sigma$. The global significance is usually evaluated by generating a large number of toy experiments, calculating the local significance for all of the signal hypotheses considered, and taking the maximum value

[1] The use of the S distribution for this study is equivalent to the use of the q_0 distribution, since the two variables are connected by a monotonic relation: the higher is S, the higher is q_0. We chose S for this study because it was easier to evaluate with respect to q_0 with the program used for the analysis.

of S for each toy (S_{max}). The p-value evaluated integrating the S_{max} distribution for $S_{max} \geq S^{obs}$ would correspond to the global significance of the excess.

This approach is very time consuming, since it would require the generation of a large number of pseudodata samples. In fact, to take into account for the observed correlations in the evaluation of the local significance, a large number of pseudodatasets ($\boldsymbol{O}(10.000)$) should be generated by varying the data distribution in the 3 dimensional (3D) space formed by the variables: m_{jj}, m_{Rjet}, and m_{Pjet}, where the latter two are the masses of the two jets. Then, for each pseudodataset the full analysis needs to be rerun.

However, an upper limit on the global significance can be evaluated using a simplified approach. Since the largest excess has been found for $m(R_1) = 2.9\,\text{TeV}$, $\rho_m = 0.138$, we start by considering only signal hypotheses with $m(R_2) = m(R_1) \times \rho_m \simeq 400\,\text{GeV}$, which are located along an hyperbole in plane ρ_m vs $m(R_1)$ (Fig. 8.8).

Since the categories definition is based on the value of $m(R_2)$, the m_{jj} spectra of the event categories are the same for all the signals from this hyperbole. We can then sort the data into the categories, fit the m_{jj} spectra in the whole mass range and generate toys directly from the resulting background function. This approach avoids the complexity of a generation of a 3D distribution and produce a single set of m_{jj} spectra for all of the signal hypotheses with $m(R_2) = 400\,\text{GeV}$.

For each toy, then, we perform the fit and evaluate the local significance (in asymptotic approximation) for the 21 signal hypotheses belonging to this hyperbole, which correspond to different values of $m(R_1)$, from 2 to 4 TeV (100 GeV step). The plot in Fig. 8.8 shows an example of the local significance, evaluated for the signal hypotheses corresponding to this hyperbole, for a single toy.

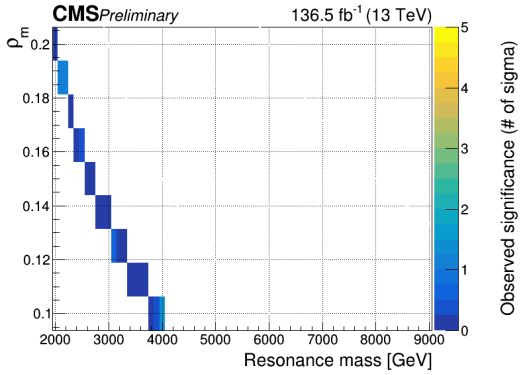

Figure 8.8. Local signal significance (asymptotic formulae) for one toy experiment, generating m_{jj} spectra for the categories corresponding to signal hypotheses with $m(R_2) = 400\,\text{GeV}$.

The maximum value of the asymptotic significance (S_{max}), among all the signals with different $m(R_1)$ probed, is then evaluated for each toy. After the generation of ~10.000 toy-datasets, we then built the S_{max} distribution shown in Fig. 8.9.

The global p-value p_g evaluated for $S_{max} \geq S^{obs} = 3.2\sigma$ is then $p_g \approx 1.1 \times 10^{-2}$. This means that the probability to observe a local significance above 3.2σ, among all the signal hypotheses with $m(R_2) = 400\,\text{GeV}$, is about 3.0%, which correspond to a significance of $\sim 1.9\sigma$.

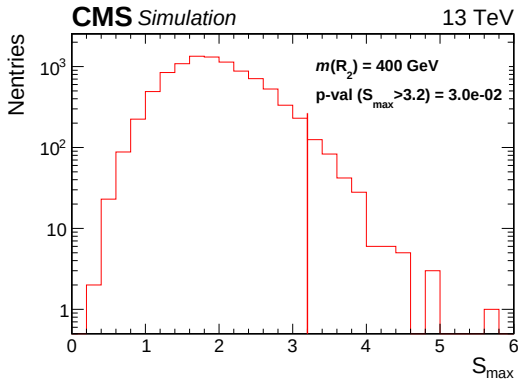

Figure 8.9. Distribution of the maximum local significance among the tested signal hypotheses with $m(\mathrm{R}_2) = 400\,\mathrm{GeV}$. The red line marks the value of the significance observed in data.

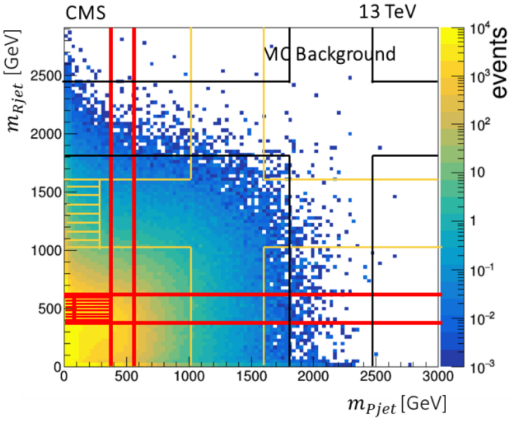

Figure 8.10. Schematic view of the three sets of categories in the m_{Rjet} vs. m_{Pjet} plane for $m(\mathrm{R}_2) = 0.4$ (red), 0.84 (yellow) and 1.44 TeV (black). The background event distribution from the QCD MC sample is also shown.

We can extend this reasoning by considering also signal hypotheses with other values of $m(\mathrm{R}_2)$, corresponding to other hyperboles in the ρ_{m} vs. $m(\mathrm{R}_1)$ plane. We chose to consider only other two values of $m(\mathrm{R}_2)$: 0.84 and 1.44 TeV. These values correspond to the event categories shown in Fig. 8.10, and are chosen in order to minimize the overlap in the plane. This choice minimize the correlation in data for the m_{jj} spectra of signal hypotheses belonging to different categories, therefore we are able generate the toy datasets independently for these other two values of $m(\mathrm{R}_2)$.

We then analyze the toy datasets to reproduce the $\mathrm{S}_{\mathrm{max}}$ distributions as done for $m(\mathrm{R}_2) = 0.4\,\mathrm{TeV}$. The resulting distributions are shown in Fig. 8.11, together with the relative p-values.

We can then evaluate the probability to observe one or more excesses with a local significance of 3.2σ in any of the 3 hyperboles by the combined probabilities of the p-values:

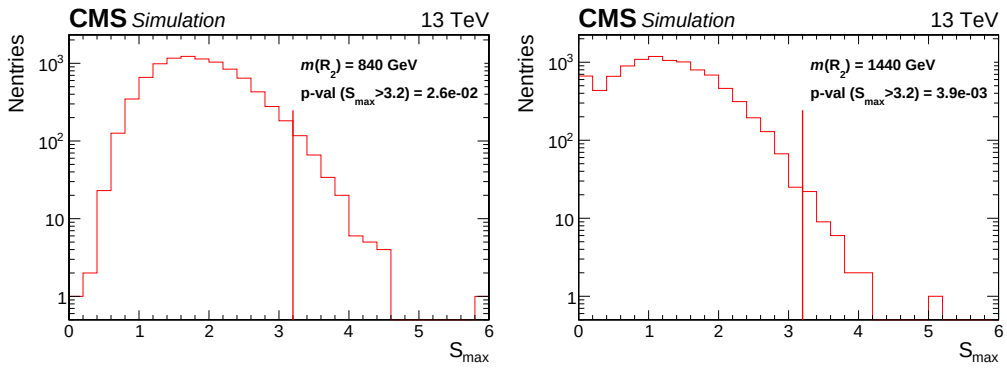

Figure 8.11. Distribution of the maximum local significance among the tested signal hypotheses with $m(\mathrm{R}_2) = 0.84$ (left) and 1.44 TeV (right). The red line marks the value of the significance observed in data.

$$P = 1 - \prod_{i=1}^{3} (1 - p_i) \approx 0.04 \tag{8.5}$$

Where p_i, with $i = 1, 2, 3$ are the p-values for the three hyperboles. The probability to observe an excess with a significance equal or larger than the observed one, in any of the three hyperboles, is then ≈4%, which corresponds to 1.6σ. This is an upper limit of the actual global significance, because it is evaluated on a restricted number of signal hypotheses. We can then conclude that the excess is not significant, having a global significance of $S^{global} \leq 1.6\sigma$.

8.2 Limits evaluation

Since no significative excess of events was observed in the fit, exclusion limits on the production cross section of an R_1 resonance decaying to R_2 and a parton are set.

The modified frequentist method (CL_s method)[121, 122] is used to set upper limits on the signal cross sections. The test statistic of the LHC CL_s procedure [123] is:

$$\tilde{q}_\mu = -2 \ln \frac{L(\boldsymbol{x}|\mu, \hat{\boldsymbol{\theta}}_\mu)}{L(\boldsymbol{x}|\hat{\mu}, \hat{\boldsymbol{\theta}})} \text{ and } 0 \leq \hat{\mu} \leq \mu. \tag{8.6}$$

where, as for the significance test statistic (Eq. 8.1), $\hat{\mu}$ and $\hat{\theta}$ maximize the likelihood L, and $\hat{\theta}_\mu$ maximizes L for a fixed value of μ. The lower constraint $0 \leq \hat{\mu}$ is dictated by physics (the signal rate is positive), while the upper constraint $\hat{\mu} \leq \mu$ is imposed by hand in order to guarantee a one-sided (not detached from zero) confidence interval. Physics-wise, this means that upward fluctuations of the data such that $\hat{\mu} > \mu$ are not considered as evidence against the signal hypothesis, namely a signal with strength μ.

In the evaluation of the CL_s limit, the probability density functions (*pdfs*) $f(\tilde{q}_\mu|\mu, \hat{\theta}_\mu^{obs})$ and $f(\tilde{q}_\mu|0, \hat{\theta}_0^{obs})$ are used. The first is the *pdf* of $\tilde{q}_\mu$ assuming a signal with strength μ in the signal+background hypothesis, while the second is for the background-only hypothesis ($\mu = 0$). The two *pdfs* are not known a priori, but the Asymptotic Formulae [124], valid in the limit of a large event sample, provide a useful approximation that avoid the estimation of them through the use of toy datasets.

Thus, two p-values are defined, associated with the actual observation for the signal+background and background-only hypotheses, p_μ and p_b:

$$\begin{aligned} p_\mu &= P(\hat{q}_\mu \geq \hat{q}_\mu^{obs}|\text{signal+background}) = \int_{\tilde{q}_\mu^{obs}}^{\infty} f(\tilde{q}_\mu|\mu, \hat{\theta}_\mu^{obs}) d\tilde{q}_\mu, \\ 1 - p_b &= P(\hat{q}_\mu \geq \hat{q}_\mu^{obs}|\text{background-only}) = \int_{\tilde{q}_0^{obs}}^{\infty} f(\hat{q}_\mu|0, \tilde{\theta}_0^{obs}) d\tilde{q}_\mu \end{aligned} \tag{8.7}$$

and $CL_s(\mu)$ is calculated from the ratio of these two p-values:

$$CL_s(\mu) = \frac{p_\mu}{1 - p_b} \tag{8.8}$$

The value of μ for which $CL_s = 0.05$ is the observed limit of our search, corresponding to an exclusion at 95% confidence level. Since $CL_s(\mu)$ is generally a increasing function of μ, lower values of μ are excluded with a even higher confidence level.

The expected CL_s limit on μ is evaluated by assuming $1 - p_b = 0.5$, i.e. the cumulative of the pdf for the background-only fit $f(\tilde{q}_\mu|0, \hat{\theta}_0^{obs})$ crosses the quantile of 50%, which corresponds to the median of $f(\tilde{q}_\mu|0, \hat{\theta}_0^{obs})$. The $\pm 1\sigma$ (68%) band is defined by the crossings of the 16% and 84% quantiles, while crossings at 2.5% and 97.5% define the $\pm 2\sigma$ (95%) band.

The expected and observed limits on the model under study are shown in Sec. 8.2.2 and discussed in detail, while the next Section is dedicated to the systematic uncertainties and their effects on the limits.

8.2.1 Systematic uncertainties

The systematic uncertainties are taken into account as nuisance parameters in the limit setting procedure. The dominant sources of systematic uncertainty are:

- Jet Energy Scale (JES);
- Jet Energy Resolution (JER);
- Jet Mass Scale (JMS);
- Jet Mass Resolution (JMR);
- N-subjettiness ratio uncertainty ($\delta\tau_{21}$);
- Standard deviation of the position ($\delta\mu$) and width ($\delta\sigma$) of the average shape;
- Luminosity.

Since the background shape is derived from data all of the uncertainties above are only considered for the resonance signal.

The JES and JER uncertainties (σ_{JES} and σ_{JER}) translate, respectively, into uncertainties in the position μ and the width σ of the average dijet mass shape for the signal. The effect of these uncertainties is propagated to the limits by shifting the dijet mass shape by $\pm 2\%$ and varying its reconstructed width by $\pm 8\%$ of the corresponding values. The values of these uncertainties has been evaluated by previous CMS analyses (for example Ref. [75]) for anti-k_{T} jets with a distance parameter $R = 0.8$ (AK8, see Sec. 5.2 for the definition of the different jet clustering algorithms). We performed a study to show that AK8 have similar performances on the reconstruction of the jet p_{T} with respect to the anti-k_{T} jets with $R = 1.5$ (AK15) used in this analysis. In this study, the p_{T} of reconstructed jets from MC simulation of signal events are compared with the p_{T} of the corresponding generated jets, for both AK15 and AK8 jets. An example of the resulting distributions for the jets p_{T} corresponding to two signal hypotheses with $m(\mathrm{R}_1) = 3\,\mathrm{TeV}$, $\rho_{\mathrm{m}} = 0.1$ and $m(\mathrm{R}_1) = 7\,\mathrm{TeV}$, $\rho_{\mathrm{m}} = 0.2$ is shown in Fig. 8.12. The p_{T} of the jets are respectively $\sim$1.5 and 3.5 TeV in the two cases.

The two distribution for AK15 and AK8 jets are nearly identical. The same study is repeated also for simulated signal samples with different $m(\mathrm{R}_1)$ and ρ_{m}, obtaining similar results. Hence, the JECs evaluated for the AK8 jets can be applied to the AK15 jet, assuming the same JEC uncertainty for AK8 and AK15 jets.

For the evaluation of the JMS and JMR, we applied the soft drop declustering algorithm (introduced in Sec. 5.5.1) to the AK15 jets and CA15 jets. We then compared the jet masses obtained in the two cases. In the first step of the soft drop mass algorithm the constituents of the AK15 jet are reclustered using CA15 algorithm. Therefore the soft drop mass algorithm should provide the same mass value for AK15 and CA15 jets. Figure 8.13 show the ratios between the AK15 and the

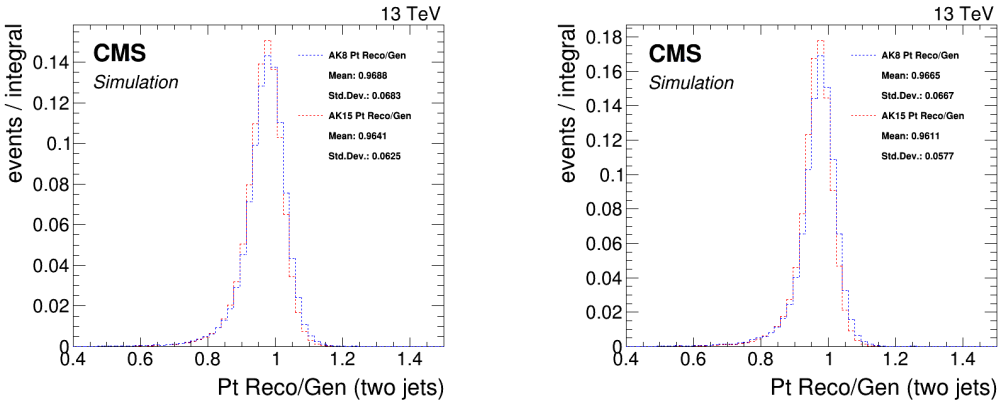

Figure 8.12. Distribution of the ratio between the reconstructed jet p_{T} and the generated jet p_{T} for AK8 jets(blue) and AK15 jets (red) for two simulated signal samples with $m(\mathrm{R}_1) = 3\,\mathrm{TeV}$, $\rho_{\mathrm{m}} = 0.1$ (left) and $m(\mathrm{R}_1) = 7\,\mathrm{TeV}$, $\rho_{\mathrm{m}} = 0.2$ (right).

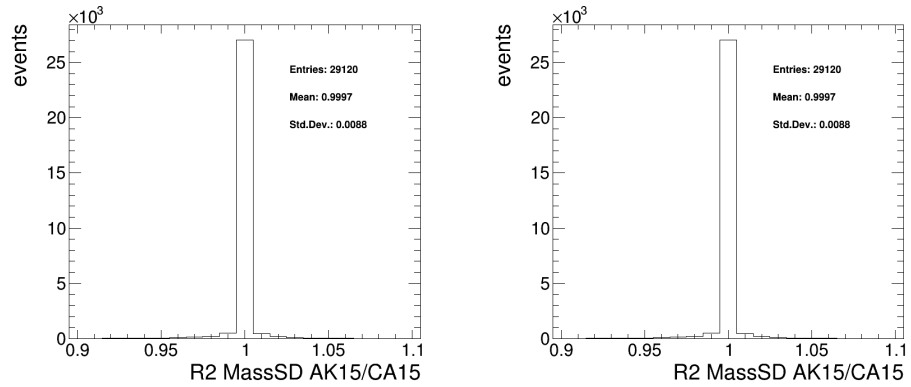

Figure 8.13. Ratio between the AK15 and CA15 soft drop jet masses, for a jet from R_2 decay (left) and a jet from the hadronization of a gluon (right). The comparison show that the resulting jet masses are the same for the two clustering algorithms.

CA15 jet masses, for a simulated jet coming from the decay of R_2 ($m(\mathrm{R}_2) = 300\,\mathrm{GeV}$) and a jet from the hadronization of a gluon.

The plots show indeed that the mass values obtained is the same in the two cases, except for a small fraction of events, attributable to errors in the algorithm. We performed this comparison also for other $m(\mathrm{R}_2)$ values, obtaining similar results. This comparison shows that we can apply, for the JMS and JMR, similar uncertainties as those used in previous CMS analyses which uses CA15 jets. An example is the analysis reported in Ref. [125], from which we derive a $\pm 3\%$ uncertainty on the JMS and a $\pm 10\%$ uncertainty on the JMR.

The uncertainty on τ_{21} is evaluated from the comparison between the simulated τ_{21} distribution and the same distribution in data, shown in Figs. 7.4a and 7.4b. These distributions suggest a systematic uncertainty on τ_{21} of $\sim$10%, from the smearing of the MC distribution to match the data.

Since the jet masses and τ_{21} are used in the selection of the events and their subsequent division into categories, the uncertainty on the JMS, JMR and τ_{21} cause

event migrations between categories. This effect results into uncertainties on the signal normalizations in each category. These uncertainties are propagated to the limits by varying the signal normalizations by a value that ranges between ±20% and ±50% (±1%–±50% for the τ_{21} uncertainty) of the central values obtained from the simulation, depending on the source of the uncertainty and on the category considered. It is important to stress that the event migration does not cause a global loss of signal efficiency, because signal events simply migrate between two categories. Hence, even if the uncertainty on the signal normalization uncertainty may seem large, it has small effect on the final limits.

The uncertainty on the integrated luminosity is 1.6% [9, 10, 11] and it is propagated to the normalization of the signal, in addition to the other uncertainties on the normalization.

The use of an average shape for all the event categories, as described in Sec. 7.3.3, introduces additional uncertainty on the position and the width of the signal peak, because of the differences between the average signal shape and the shapes of each category. The effect of these uncertainty sources are estimated from the simulation, evaluating the standard deviations of the shape parameters $\delta\mu$ and $\delta\sigma$, which are respectively ±2% and ±30% in the position μ and width σ of the signal peak. These uncertainties are combined with the JES and JER uncertainties as follows:

$$\begin{aligned} \sigma_\mu &= \sqrt{\sigma^2_{\text{JES}} + \delta\mu^2} \approx 2.8\% \\ \sigma_w &= \sqrt{\sigma^2_{\text{JER}} + \delta\sigma^2} \approx 31\% \end{aligned} \tag{8.9}$$

where σ_μ and σ_w are the total uncertainties on the central value and width of the signal peak, and are treated in the fit as uncorrelated uncertainties amongst different categories. The systematic uncertainties are summarized in Tab. 8.1. The combined effect of all the uncertainties above on the limit is estimated to be below ∼10%, for all the signal hypotheses considered.

Table 8.1. Summary of the systematic uncertainties propagated to the limit setting procedure

Systematic uncertainty source	Effect
JES	±2% shift of m_{jj} peak
JER	±8% of resolution
$\delta\mu$	±2% shift of m_{jj} peak
$\delta\sigma$	±30% of resolution
JMS	event migration between cat. (20%–50% on the normalization)
JMR	event migration between cat. (20%–50% on the normalization)
$\delta\tau_{21}$	event migration between cat. (up to 50% on the normalization)
Luminosity	±1.6% on the normalization

We do not consider additional uncertainty on the background shape parameters

because they are all considered as nuisance parameters distributed with a flat prior around the best fit values in a sufficiently large range, for which the limit is found to be stable.

A source of systematic uncertainty on the signal can arise from biases due to the choice of a specific functional form for the background modeling. In Sec. 7.3.4.2 we shown that the bias introduced by the chosen fit function is well below the 50% of the statistic uncertainty, therefore it is considered negligible for the reasons described in Sec. 7.3.4.2. Thus, we do not need to introduce systematic uncertainties to account for the bias.

8.2.2 Signal cross section limits

No significant excess is observed in data with respect to the background prediction. As we saw in Sec. 8.1 the largest observed excess in data occurs for a signal hypothesis with $m(\mathrm{R}_1) = 2.9\,\mathrm{TeV}$ and $\rho_\mathrm{m} = 0.138$, and has a local significance of $\sim 3.2\sigma$, which is less than 1.6σ when accounting for the look-elsewhere effect.

In this section we report the final results and the exclusion limits that our analysis can set on the signal model, introduced in Sec. 2.2.3, where the first resonance (R_1) is a KK gluon (G_KK) , the second resonance (R_2), is a radion (ϕ), and the three partons in the final state are all SM gluon (g)

In Figs. 8.14 and 8.15, we show the obtained limits on the product of the G_KK production cross section ($\sigma(\mathrm{G}_\mathrm{KK})$) and the branching fraction ($\mathcal{B}$). Each Figure shows the observed limit, the expected limit and its uncertainty bands as a function of the G_KK mass, $m(\mathrm{G}_\mathrm{KK}) = \mathrm{m}(\mathrm{R}_1)$, for the different ρ_m values tested.

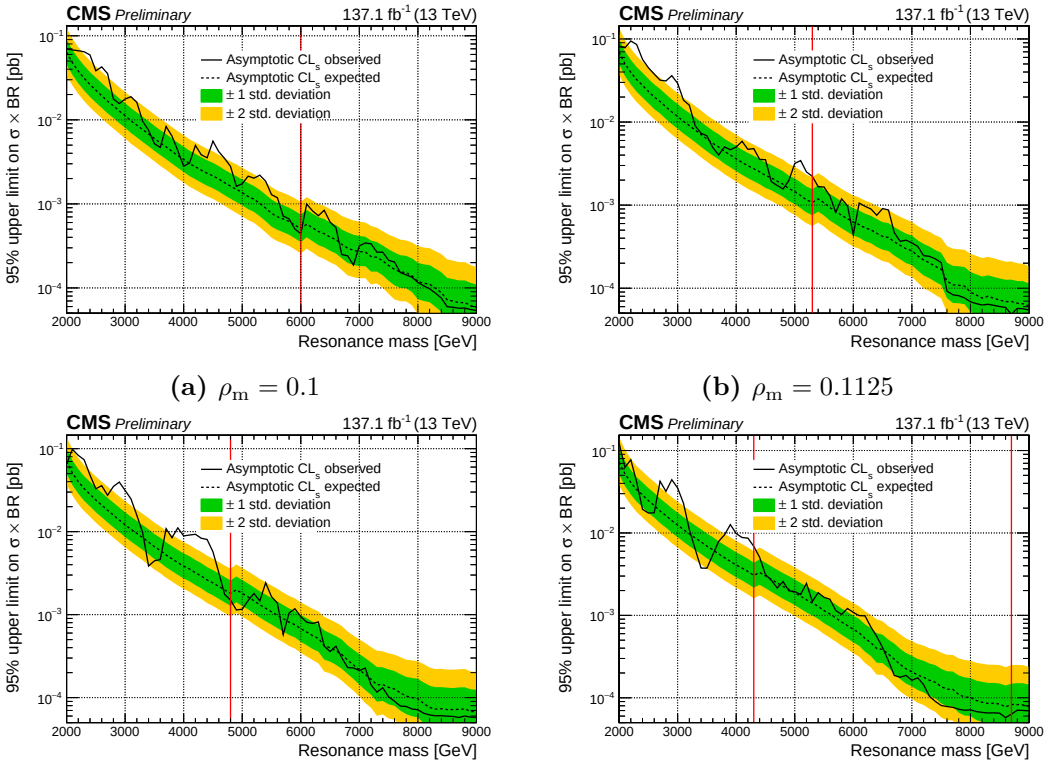

(a) $\rho_\mathrm{m} = 0.1$ **(b)** $\rho_\mathrm{m} = 0.1125$

(c) $\rho_\mathrm{m} = 0.125$ **(d)** $\rho_\mathrm{m} = 0.1375$

Figure 8.14. Expected (dashed line) and observed (solid line) 95% CL_s limits on $\sigma(\mathrm{G}_\mathrm{KK}) \times \mathcal{B} \times \mathrm{A}$ as a function of $m(\mathrm{R}_1)$, for fixed ρ_m. Uncertainty bands ($\pm 1\sigma$, $\pm 2\sigma$) on expected limits are also shown. Discontinuities in expected limits are present in the transition between sets with different number of categories (red lines).

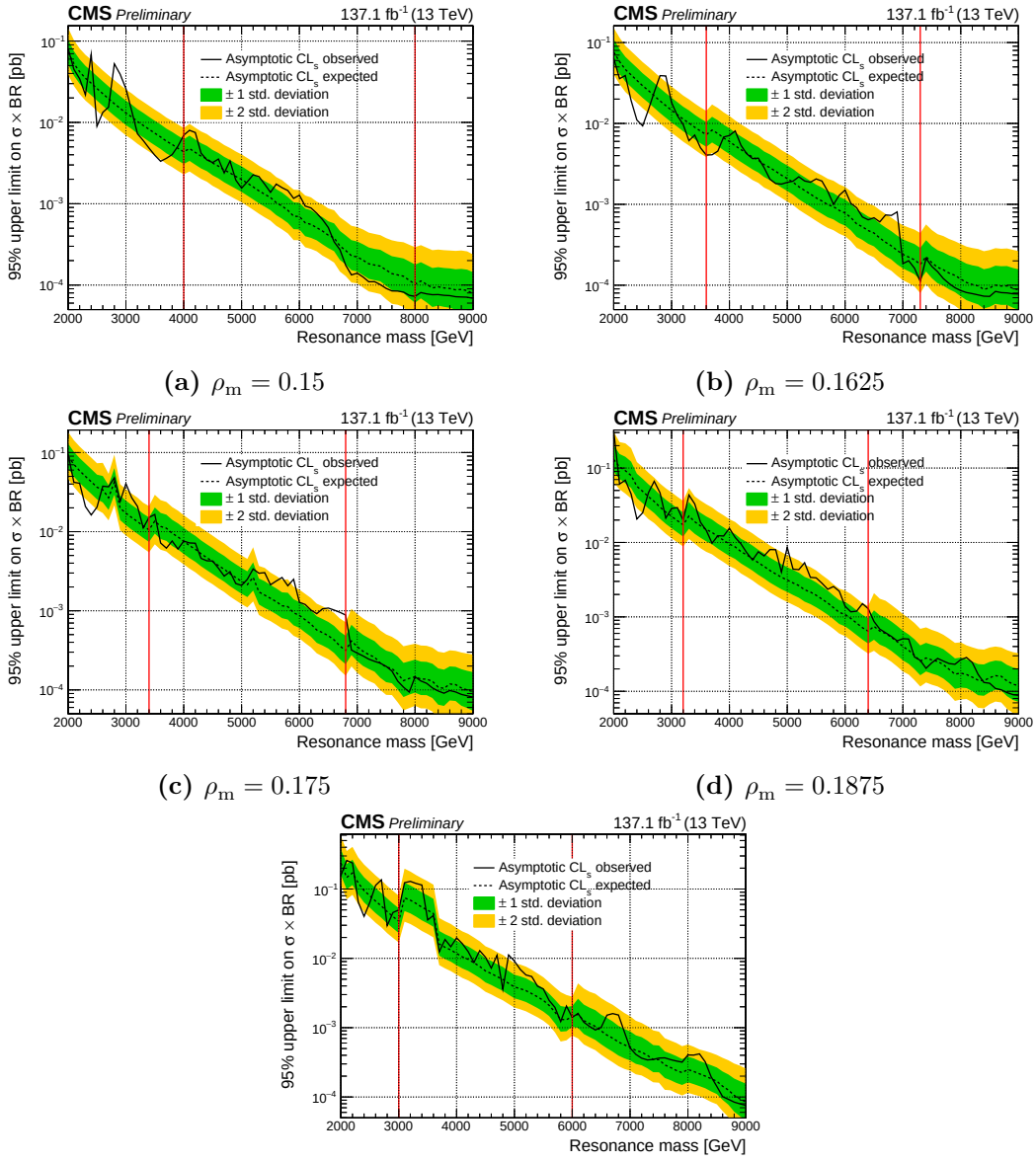

(a) $\rho_{\mathrm{m}} = 0.15$ **(b)** $\rho_{\mathrm{m}} = 0.1625$

(c) $\rho_{\mathrm{m}} = 0.175$ **(d)** $\rho_{\mathrm{m}} = 0.1875$

(e) $\rho_{\mathrm{m}} = 0.2$

Figure 8.15. Expected (dashed line) and observed (solid line) 95% $\mathrm{CL_s}$ limits on $\sigma(\mathrm{G_{KK}}) \times \mathcal{B} \times \mathrm{A}$ as a function of $m(\mathrm{R_1})$, for fixed ρ_{m}. Uncertainty bands ($\pm 1\sigma$, $\pm 2\sigma$) on expected limits are also shown. Discontinuities in expected limits are present in the transition between sets with different number of categories (red lines). The additional discontinuity for $\rho_{\mathrm{m}} = 0.2$ at $m(\mathrm{R_1}) \approx 3.6\,\mathrm{TeV}$ is caused by the removal of one category from the final fit, following the procedure described in Sec. 7.3.2.

The observed upper limits on $\sigma(\mathrm{G_{KK}}) \times \mathcal{B}$ are also shown in Fig. 8.16 as a function of ρ_m and $m(\mathrm{G_{KK}}) = \mathrm{m}(\mathrm{R_1})$. The black curve shown in the figure marks the contour of the region of the ρ_m-$m(\mathrm{R_1})$-plane corresponding to the signal hypotheses excluded by our search. The exclusion is obtained by the comparison of the observed limit with the theoretical prediction of $\sigma(\mathrm{G_{KK}})$ times the branching fraction $\mathcal{B}(\mathrm{G_{KK}} \to \phi\mathrm{g})$, which are evaluated for a specific choice of the couplings of the model, reported in Eq. 2.28. The signal hypotheses where the observed limits are below the theoretical predictions are excluded. Translating these limits as exclusion on the masses of the two new resonances, we can conclude that KK gluon masses up to 4.3 TeV are excluded at $\rho_\mathrm{m} \sim 0.1$, while at $\rho_\mathrm{m} \sim 0.2$ we can only exclude $m(\mathrm{G_{KK}})$ up to ∼3 TeV (not considering the isolated point at $m(\mathrm{G_{KK}}) = 3.7\,\mathrm{TeV}$). The reduction of the analysis sensitivity at $\rho_\mathrm{m} \sim 0.2$ is caused by the reduction of the signal efficiency in that region, as shown in Sec. 7.3.3.2. The dip in the expected and observed limit contours around $m(\mathrm{R_1}) \approx 3.4\,\mathrm{TeV}$ and $\rho_\mathrm{m} \approx 0.2$ is due to variations in the signal efficiency caused by the removal of categories in the fit, as described in Sec. 7.3.2. The two isolated excluded regions, occurring in the $m(\mathrm{R_1})$ interval between 4 and 5 TeV, are separated from the main excluded region at lower masses by a region where the observed limits are higher than expected, consistently with an upward statistical fluctuation within this intermediate region.

Also the expected upper limit has been compared with the theoretical predictions, the result is the exclusion area delimited by the violet dashed lines in Fig. 8.16, which is shown together with the $\pm 1\sigma$ uncertainty band. The area excluded by the observation is smaller than expected because of the aforementioned upward fluctuation around $m(\mathrm{R_1}) = 4.2\,\mathrm{TeV}$ and $\rho_\mathrm{m} = 0.138$. This effect is a direct consequence of the excess with a local significance of $\sim 2.8\sigma$ found for that signal hypothesis.

Figure 8.16 also shows, in red, the area excluded by the CMS dijet analysis [30], which is sensitive to the $\mathrm{G_{KK}} \to \mathrm{q\overline{q}}$ decay. This area is obtained after a reinterpretation of the observed limits from the dijet search, compared with the $\mathrm{G_{KK}}$ production cross section of the model under study, after taking into account for the branching fraction of $\mathrm{G_{KK}} \to \mathrm{q\overline{q}}$, which is estimated to be ∼50% for all $\mathrm{G_{KK}}$ masses. $\mathrm{G_{KK}}$ boson masses are excluded up to ∼3.2 TeV, a result that is in agreement with the interpretation of dijet limits reported in Ref. [34] (bottom plot of Fig. 5), which assumes slightly different couplings. The red area contour is almost a vertical line in the plane since the $\mathrm{G_{KK}} \to \mathrm{q\overline{q}}$ process is not sensitive to variation of ϕ mass, except for small effects caused by the variation of the phase space with $m(\phi)$.

The comparison between the black and the red line clearly shows that the analysis presented here is more sensitive to the model under study with respect to the CMS inclusive dijet search, especially for low values of ρ_m. For $\rho_\mathrm{m} \simeq 0.2$, the results of the two analyses are similar, because of the limited signal efficiency of our analysis, as described in Sec. 7.3.3.2.

In the WED model considered, only the gluon field among the SM gauge fields is allowed to propagate in the entire bulk. As a consequence, several constraints from existing searches do not apply since decays of the Kaluza-Klein gluon to a top quark-antiquark pair and Higgs boson pairs are suppressed, while radion decays to pairs of photons are forbidden.

We can conclude that the analysis here presented enhance the sensitivity to new

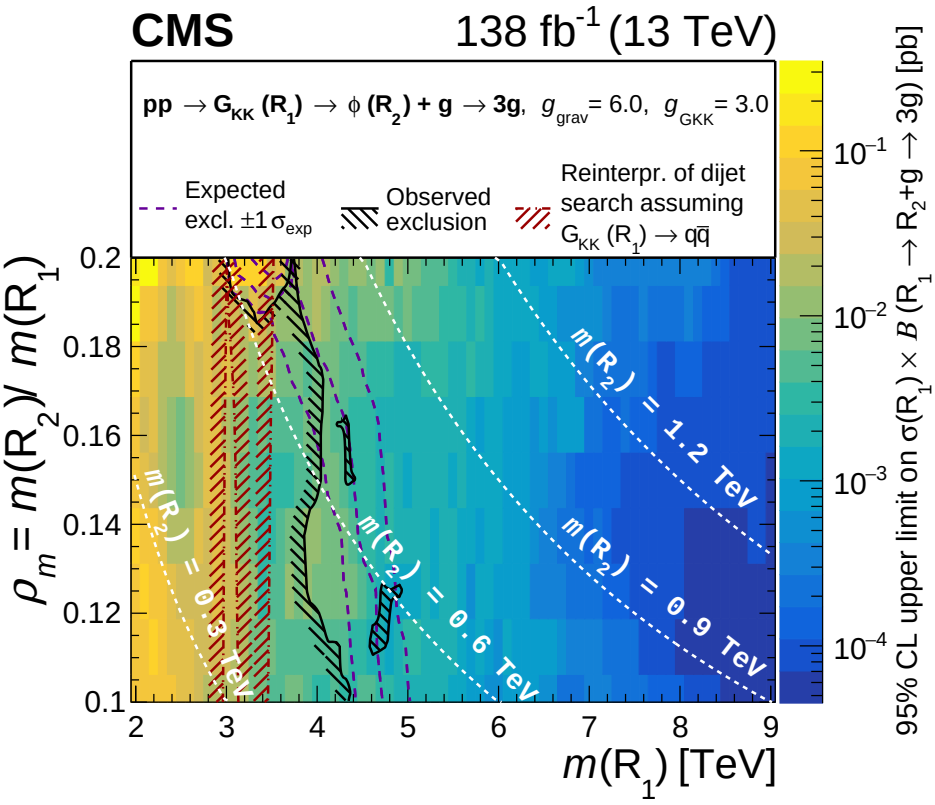

Figure 8.16. Observed upper limits on $\sigma(\mathrm{G_{KK}}) \times \mathcal{B}$, as a function of ρ_m vs. $m(\mathrm{R_1})$, for a resonance model with three gluons in the final state. The excluded regions from this search (black hatched) are optimized for the $\mathrm{G_{KK}} \to \phi + \mathrm{g} \to \mathrm{ggg}$ decay with $g_\mathrm{grav} = 6.0$ and $g_\mathrm{GKK} = 3.0$. These excluded regions are compared with those obtained from a reinterpretation of the inclusive CMS dijet resonance search [30], which is more sensitive to the decay channel $\mathrm{G_{KK}} \to \mathrm{qq}$ (red hatched). The vertical band between the $m(\mathrm{R_1})$ values of ≈3.0 and ≈3.1 TeV, for $\rho_\mathrm{m} \lesssim 0.19$, is not excluded by the dijet search because of an upward statistical fluctuation in the observed limit. The white, dashed lines represent a sample of curves corresponding to fixed $m(\mathrm{R_2})$ values.

resonances that follows the cascade decay chain $\mathrm{R_1} \to \mathrm{R_2} + \mathrm{P_3} \to \mathrm{P_1} + \mathrm{P_2} + \mathrm{P_3}$, introduced in Sec. 3.3, with respect to previous CMS searches. In the benchmark model studied, the excluded limit on the $\mathrm{G_{KK}}$ mass is extended by up to ∼1 TeV.

Chapter 9

Conclusions and perspectives for future analyses

In this dissertation a search for new phenomena beyond the Standard Model, involving the production of two hadronic resonances, is presented. The analysis uses data from proton-proton collisions produced at the CERN LHC at a center-of-mass energy of 13 TeV, and corresponding to a luminosity of $138\,\mathrm{fb}^{-1}$.

Searches for hadronic resonances by the CMS and ATLAS experiments typically assume the existence of a single new resonance that decays into two or more SM particles. Depending on the hypothesis it can be produced individually, in pairs or in association with other SM particles.

In this thesis we consider a new final state, not explored by previous searches. We consider the production of a first high-mass hadronic resonance (R_1) that decays into a parton and a second resonance (R_2), which in turn decays into a pair of partons.

The final state topology, resulting from the cascade decay, depends on the ratio between the masses of the two resonances: $\rho_\mathrm{m} = m(\mathrm{R}_2)\,/m(\mathrm{R}_1)$. This analysis assumes $m(\mathrm{R}_2)$ to be much lighter than $m(\mathrm{R}_1)$ ($\rho_\mathrm{m} \lesssim 0.2$). In this case the partons from the R_2 decay are collimated and can be reconstructed as a single jet. The resulting topology is then formed by a system of two jets (dijet), with an invariant mass (m_jj) distribution that peaks around the value of $m(\mathrm{R}_1)$. Moreover, the jet from the R_2 decay (R_2-jet) has a mass compatible with $m(\mathrm{R}_2)$ and the pattern of its constituents shows a dipolar substructure.

We analyze final states with a dijet-like topology, selecting events with two high-p_T jets, back-to-back in the plane orthogonal to the beam direction. In addition to the standard dijet selections, the properties of the R_2-jet are exploited to disentangle the signal from the background. The two-prong substructure of the R_2-jet is used for its identification. The events are then divided into categories based on the jet masses. We build then the m_jj spectra for the events of each category. A signal+background fit is used to search for excesses above the background predictions compatible with the presence of a signal peak. The R_1 and R_2 masses are unknown, therefore we scanned a wide range of values. For each $m(\mathrm{R}_2)$ value, different event categories are defined and the analysis is repeated on the selected events.

We searched R_1 resonances in the mass range between 2 and 9 TeV, for ρ_m values

between 0.1 and 0.2 ($m(\mathrm{R}_2)$ between 0.2 and 1.8 TeV). The CMS trigger thresholds prevent the search for resonances with mass below 2 TeV.

The largest excesses is found for $m(\mathrm{R}_1) = 2.9\,\mathrm{TeV}$ and $\rho_\mathrm{m} = 0.138$, and corresponds to a local significance of 3.2σ. Because of the large number of signal hypotheses tested, after correcting for the look-elsewhere effect, the global significance of the excess is below 1.6σ, and therefore the excess is not significant.

We derived the 95% $\mathrm{CL_s}$ upper limits on the production cross section of R_1 times the branching fraction of its decay into R_2 and a parton. The limits are also compared with the theoretical prediction for the decay of a Kaluza–Klein (KK) gluon ($\mathrm{G_{KK}}$) into a radion (ϕ) and a gluon, evaluated in the assumption WED benchmark model described in Sec. 2.2.3.

From the comparison, $\mathrm{G_{KK}}$ masses in the range from 2.0 to 4.3 TeV are excluded at 95% confidence level, together with radion masses in the range from 0.20 to 0.74 TeV. The excluded region is also compared to that obtained by a reinterpretation of the limits from the latest CMS dijet search [30] on the $\mathrm{G_{KK}} \to \mathrm{q\overline{q}}$ decay. We can conclude that the analysis presented here is more sensitive to the model under study, with an exclusion range on the $\mathrm{G_{KK}}$ mass extended by up to $\sim$1 TeV for low values of ρ_m.

The analysis results have been presented by the author of this thesis for the first time at the LHC Physics Conference on June 9, 2021 [126], and are reported in a paper submitted to the Physics Letter B journal on January, 2022 [127].

We conclude this thesis with an outlook on possible upgrades of this analysis and possible extensions to similar decay chains.

The extension of the search in the mass region below 2 TeV could be obtained by using the CMS scouting technique. This data acquisition strategy allow to lower the jet trigger thresholds by storing a minimal amount of data at trigger level.

New searches, with a different analysis strategy, are possible for models with ρ_m values above 0.2. In this regime the R_2 resonance does not have a large Lorentz-boost anymore and the final state presents three resolved jets. Initial studies are ongoing on this research within the CMS experiment.

The WED model foresees the existence of other KK partners of SM gauge bosons, besides the KK gluon studied in this thesis. Some of these searches are currently performed within the CMS collaboration. One example is the search for $\mathrm{W_{KK}}$ boson which decays to 3 W bosons, the search is performed in both the semileptonic and fully hadronic final states [36, 35]. These searches can be extended to $\mathrm{Z_{KK}}$ or γ_KK. The latter particle, for example, would decay in the process $\gamma_\mathrm{KK} \to \phi\gamma \to \gamma\gamma\gamma$. The signature would be a peak in the invariant mass of three photons, which is little explored by searches at the LHC.

Appendix A

The Kaluza–Klein theory

The first formulation of a theory of gravity with an extra spatial dimension was made by the German mathematician and physicist Theodor Kaluza in 1921 [128] (see also [129] for a recent translation of the original paper), followed by the Swedish physicist Oskar Klein in 1926 [130], which postulated the extra dimension to be "curled up", or compactified.

This work is generally known as the Kaluza–Klein theory, and provides an extension of the General Relativity (GR) to 5 dimensions, which also offer a possibility for the unification of the GR and the electromagnetism. The general scheme of a space with a compact dimension is show in Fig. A.1, where the vertical axis of the cylinder stands for the traditional 4 dimensions (time + 3 spatial dimensions), which are infinite and flat. The fifth dimension is finite, and compactified on a circle of radius R. The universe corresponds then to the surface of the cylinder, with nothing inside or outside of it. The most relevant aspect of the KK 5D theory of gravity is that it can be used to construct a 4D effective theory with an infinite spectrum of 4D fields. This is known as the KK decomposition and it is described in the next Section.

A.1 The Kaluza–Klein decomposition scheme

The KK decomposition, which is essentially a normal mode expansion, converts a 5D Lagrangian into a 4D Lagrangian with an infinite spectrum of 4D particles. This allows to convert the 5D theory in a 4D effective theory, integrating out the extra dimensions from their equation of motion (EOM).

For simplicity, we will show this process on a scalar field φ with null potential. The action of the 5D theory is of the form:

$$\begin{aligned} S &= \int d^4x dy \frac{1}{2} \partial_M \varphi(x,y) \partial^M \varphi(x,y) \\ &= \int d^4x dy \frac{1}{2} \left[(\partial_\mu \varphi)^2 - (\partial_y \varphi)^2 \right] \end{aligned} \tag{A.1}$$

with $M = 0, 1, 2, 3, 4$ and the extra dimension is $x_4 = y$. The variation of this action gives the following EOM for φ:

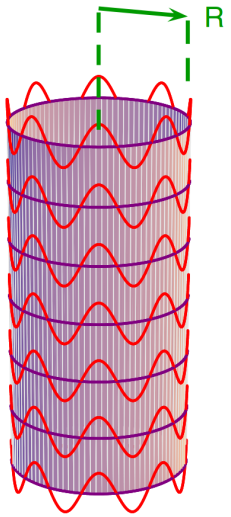

Figure A.1. Representation of KK space with a compact dimension. The vertical axis represent the $3+1$ traditional dimension, while the fifth dimension is curled up in a circle of radius R. The 5d fields are quantized along the compact dimension generating massive 4-dimensional fields.

$$\partial_\mu^2 \varphi - \partial_y^2 \varphi = 0 \tag{A.2}$$

Since the y dimension is compactified on a circle, we can introduce periodic boundary conditions. As a consequence, the EOM for φ admits periodic solutions along the y direction that can be decomposed in a Fourier series of the form:

$$\varphi(x,y) = \frac{1}{\sqrt{2\pi R}} \sum_{n=-\infty}^{\infty} \varphi^{(n)}(x) e^{i\frac{n}{R}y} \tag{A.3}$$

with $\varphi^{(n)*} = \varphi^{(-n)}$ in order to guarantee that φ is real. Replacing this expression of φ back into Eq. A.2 and using the orthogonality relations of the Fourier modes we obtain

$$S = \int d^4x \sum_{n>0} \partial_\mu \varphi^{(n)\dagger} \partial^\mu \varphi^{(n)} - \frac{n^2}{R^2} |\varphi^{(n)}|^2 \tag{A.4}$$

The momentum along the compact direction is then quantized by the boundary conditions, and its spectrum appears as a 4D tower of particle with masses $m_n = n/R$. Unfortunately the KK theory is not able to describe the SM as we know it today, because the SM fermions are chiral under the SM gauge group, while KK decomposition give rise to a vector-like fermion spectrum. Nonetheless, it probes that theories with extra dimensions provide an intriguing way to achieve the unification of apparently disparate forces, by obtaining 4D massive fields from a 5D theory.

Appendix B

ECAL Endcaps intercalibration with $Z \to e^+e^-$ events

This Chapter reports my study about the inter-calibration of the CMS electromagnetic calorimeter (ECAL). All the procedures and techniques adopted by CMS for the ECAL calibration are briefly introduced, giving more details about one specific method, which exploits electron-positron pairs (ee) from Z bosons decays.

The excellent performance in the reconstruction and identification of high energy photons and electrons has played a key role in the observation of the Higgs boson and the study of its properties during the LHC Run 1.

The LHC Run 2 represented a challenge for the detector, which has been successfully passed. In fact, the ECAL ensured its reliability on the energy reconstruction, even in the harsher environment of the Run 2, where the LHC achieved a stable instantaneous luminosity of $2 \times 10^{34}\,\mathrm{cm}^{-2}\,\mathrm{s}^{-1}$, twice the design value.

Maintaining and improving the ECAL performance also in Run 3 is vital for all the physics analyses that include photons and/or electrons in their final state. The materials of which the ECAL is composed, in fact, tend to degrade because of the radiation damage that affects both the crystals and the photodetectors, causing their response to change with time. Achieving stable energy reconstruction performances requires then a continuous effort in the operation, monitoring, and calibration of the calorimeter.

In the next sections we will briefly discuss the ECAL energy reconstruction and calibration techniques, while the results of my study will be discussed in Sec. B.4.

B.1 ECAL energy reconstruction

The first step of the ECAL energy reconstruction is the identification of the group of crystals (a "supercluster") in which an electromagnetic particle deposited energy. Electrons and positrons bend along the azimuthal ϕ-coordinate with respect to the longitudinal magnetic field of CMS, and release *bremsstrahlung* photons spread in ϕ, which are recovered by the supercluster algorithm [131] in combination to the photon conversion energy. The reconstructed energy is then calculated as a sum of the signals from all crystals within this supercluster (SC):

$$E_{\mathrm{e},\gamma} = F_{\mathrm{e},\gamma} \times \left[G(\eta) \times \{ \sum_{i \in SC} S_i(t) \times C_i \times A_i \} + E_{\mathrm{preshower}} \right] \tag{B.1}$$

Here, the factors A_i are the raw pulse amplitudes of the signals from the ECAL read-out electronics, which are proportional to the energy deposited by the particle in the ECAL crystals. A detailed description of the raw amplitudes can be found in Ref. [132]. $G(\eta)$ contains the conversion factor from the amplitude of the signal: from counts from the analogue-to-digital converter (ADC) to GeV. It is η-dependent to incorporate geometry effects. The factor $F_{\mathrm{e},\gamma}$ corrects for imperfect clustering and other geometry effects, and depends on the particle type. For electrons and photons incident on the endcaps, $E_{\mathrm{preshower}}$ contains an estimate of the energy absorbed by the ECAL preshower. The factors $S_i(t)$ are correction factors that account for the different crystal response to the incoming particle. They are evaluated using a laser system as discussed in Sec. B.2. The inter-calibration coefficients C_i, instead, are used to set an energy scale at the granularity of a single crystal, accounting for small differences between crystals that are not corrected by the laser corrections; the procedure for obtaining these coefficients is discussed in Sec. B.3.

B.2 Crystal response to the scintillation signal

The response of each ECAL crystal to a scintillation signal varies with time. In order to monitor this response, ECAL operates a dedicated laser system [133] which shines laser light into all ECAL crystals and measures the response. For ECAL crystals, the scintillation signal drift, S_i in Eq. B.1, is assumed to be related to the laser monitoring signal L by a power law:

$$\frac{S}{S_0} = \left(\frac{L}{L_0} \right)^{\alpha} \tag{B.2}$$

The evolution of the ECAL response to the laser pulse L/L_0 is shown in Fig. B.1. The response decrease during the data taking because of radiation damage, that reduces the crystal transparency to scintillation light. After ∼6 years of LHC activity, this loss is significant and it is very large especially at high $|\eta|$.

The Figure shows also how, during the LHC shutdown, there is a partial recovery of the transparency at room temperature. Fluctuations due to these trends affect the crystal response on short time-scales as well; the response of crystals to scintillation can vary significantly within an LHC fill.

The laser-correction procedure works well for short-term drifts in the response to the scintillation signal, but there still remains a long-term residual drift that cannot be picked up by the laser monitoring. For example, α varies slightly from crystal to crystal, and there are residual aging effects that affect each crystal differently. To compensate for all these additional factors, we include the crystal-dependent inter-calibration coefficients C_i, which are the subject of the next Section.

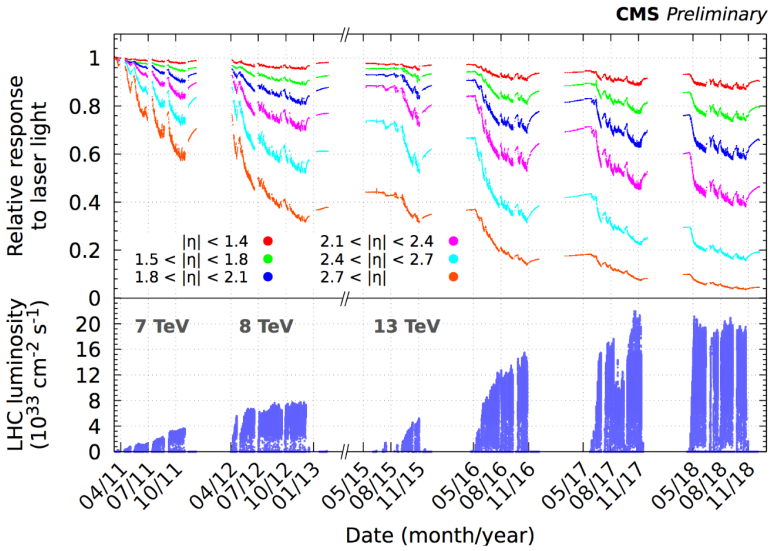

Figure B.1. Evolution of the ECAL channel response to laser light versus time since 2011. The channels are subdivided in ranges of $|\eta|$. The bottom panel shows the instantaneous luminosity delivered by the LHC in the same time period.

B.3 Inter-calibration coefficients evaluation

The evaluation of the inter-calibration coefficients C_i exploits several physics signals:

- azimuthal symmetry of minimum bias events;
- photons from π^0 decays;
- comparison between particles energy and momentum (E/p ratio);
- electron pairs from Z boson decays.

Dedicated reduced data streams are saved for each type of event. The following sections briefly describe each calibration method, while Sec. B.3.5 describes the combination of the inter-calibrations from the various methods. For more information on these topics, see Ref. [134]

B.3.1 Inter-calibration from azimuthal symmetry of minimum bias events

A first method of calculating the inter-calibration coefficients C_i is the ϕ–symmetry method, which exploits the intrinsic symmetry of the energy deposits in rings of fixed azimuthal angle (ϕ) in minimum bias collision events. The latter are inelastic events from soft interactions of the colliding partons, selected by triggers with loose requirements that introduce as little bias as possible. This method enables us to set the relative inter-calibration coefficients for crystals at the same η, because these minimum bias events are highly sensitive to geometric effects, including some absorption in the tracker, the precision of the coefficients obtained using this technique is lower than that achieved with other available methods.

In the ϕ–symmetry procedure ECAL hits between a minimum and a maximum threshold are summed for each crystal for a given period. The energy sums are equalized between crystals in the same η ring. This method can provide a measurement of C_i per crystal every few tens of minutes. However, it is very sensitive to the energy thresholds. Since the noise evolves in the ECAL, due to transparency changes in the crystals and photodetector radiation damage, the accuracy of this method was worse than the other methods in Run 2. Therefore it was mostly used to monitor the single crystal response and to spot anomalous channels, rather than to derive crystal inter-calibrations.

B.3.2 Inter-calibration using $\pi^0 \to \gamma\gamma$ decay

At the end of each year the full statistics of the $\pi^0 \to \gamma\gamma$ data is used to compute channel-to-channel intercalibration. For each crystal, events with one hit in that crystal are selected, and the $\gamma\gamma$ invariant mass distribution is fitted separately with this selection. Because each fit depends on the inter-calibration coefficients of all crystals, the true values are obtained following an iterative process in which the coefficients at iteration n are obtained from the coefficients at iteration $n-1$; after a sufficient number of iterations, the peak of the fitted distributions for all crystals converges to the value of the π^0 mass, as shown in Fig. B.2. In Ref. [135] this technique is described for the Z $\to$ ee inter-calibrations, but it can be applied more generally to $\pi^0 \to \gamma\gamma$.

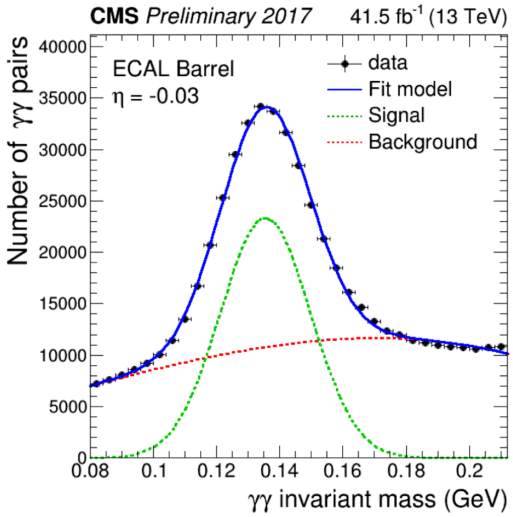

Figure B.2. Reconstructed invariant mass distribution of photon pairs around the π^0 mass peak for one barrel crystal in 2017.

At iteration n,

$$C_i = \prod_{\text{iteration } j=1}^{n} \left[1 + \frac{1}{2} \left\{ \left(\frac{m^j_{\gamma\gamma}(\text{events with crystal i})}{m^{\text{PDG}}_{\gamma\gamma}} \right)^2 - 1 \right\} \right]^{-1} \tag{B.3}$$

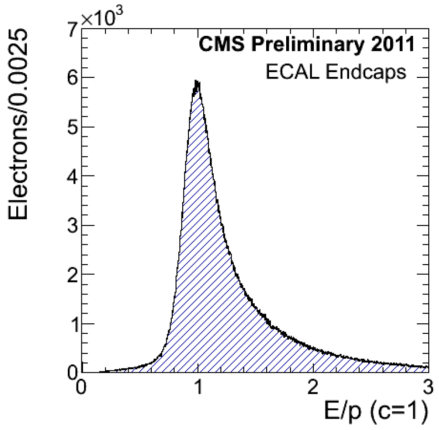

Figure B.3. Template used in 2012 for the distribution of the fraction E/p for the ECAL endcaps.

The final C_i for a crystal is normalized to the η–ring average, because the η–scale correction is found to be much more precise when done with the $Z \to ee$ method described in Sec. B.3.4.

B.3.3 Inter-calibration using E/p ratio

The CMS tracker provides an independent measurement of the momentum of a charged particle by reconstructing its track and obtaining its curvature in the magnetic field. Specifically, the ratio E/p, where E= ECAL supercluster energy (which depends on the inter-calibration factors) and p = tracker momentum, should remain stable over time. We first obtain the E/p templates from a high purity sample of high energy electrons from W/Z decay. These templates vary with η; one example template, used in 2012 for all endcap electrons, is shown in Fig. B.3. Next, the inter-calibration coefficients are derived using an iterative approach which ensures that the observed E/p distribution matches these templates.

B.3.4 Inter-calibration using $Z \to ee$

In this technique, the inter-calibration constants are chosen such that the overall Z-peak, reconstructed from $Z \to ee$ decays in all crystals, yields the correct mass and lifetime. We perform a maximum likelihood fit of the data to a Voigtian, a convolution of the natural Z-shape (which depends on Z-mass and lifetime), and a Gaussian spread due to resolution effects:

$$L = \prod_{Z \to ee\ events} Voigt(m_{ee}, \sigma_{ee}, M_Z, \Gamma_Z) \tag{B.4}$$

where

$$
\begin{aligned}
m_{\mathrm{e_1e_2}} &= \sqrt{2 \times E_{\mathrm{corrected}}(\mathrm{e}_1) \times E_{\mathrm{corrected}}(\mathrm{e}_2) \times (1 - \cos\theta_{12})} \\
\sigma_{\mathrm{e_1e_2}} &= \frac{1}{2} \times M_{\mathrm{Z}} \times \sqrt{\left(\frac{\sigma_E}{E}\right)^2 (\mathrm{e}_1) + \left(\frac{\sigma_E}{E}\right)^2 (\mathrm{e}_2)} \\
E_{\mathrm{corrected}} &= \frac{E_{\mathrm{ECAL}}}{r(\eta)} + E_{\mathrm{preshower}}
\end{aligned}
\tag{B.5}
$$

Here, $r(\eta)$ is an η-dependent correction which is equivalent to normalizing correctly between all bins in η. The inter-calibration coefficients, which affect the reconstructed energy, are parameters that are evaluated from the fit, which maximizes the likelihood comparing the reconstructed mass distribution with that predicted by Monte Carlo simulation. The method can also be used to calculate the inter-calibrations in crystal rings, to estimate the energy resolution of electrons in different η regions and to equalize the response of the different rings (absolute energy calibration). The software that has been developed for this is called iJAZZ [136]. Since 2016, because of the larger integrated luminosity, this method is used to inter-calibrate the ECAL channels at the single crystal level. Typically, for this task the fit of the Z $\to$ ee peak requires the full data sample collected in one year, but in my study reported in Sec. B.4 I show that only a fraction of one year of data-taking is enough for the intercalibration of only the ECAL region corresponding to $|\eta| > 2.5$.

B.3.5 Combined estimation of the inter-calibration coefficients and their uncertainty

Having three independent measurements of the inter-calibration coefficients for each crystal, it is possible to combine them in a single value with a smaller uncertainty with respect to the single measures.

At first the uncertainty on the inter-calibration coefficients from the three methods, $\sigma_1, \sigma_2, \sigma_3$, are evaluated from the data. We construct the three distribution of the differences between the intercalibration coefficients obtained with the different methods. Assuming that the three measurements methods are uncorrelated, the spread of these distributions is connected to $\sigma_1, \sigma_2, \sigma_3$ by:

$$
\begin{aligned}
\sigma_1^2 + \sigma_2^2 &= \sigma_{1\text{-}2}^2 \\
\sigma_1^2 + \sigma_3^2 &= \sigma_{1\text{-}3}^2 \\
\sigma_2^2 + \sigma_3^2 &= \sigma_{2\text{-}3}^2
\end{aligned}
\tag{B.6}
$$

The values of the spread in the difference $\sigma_{i\text{-}j}^2$ can be determined by the distribution of these differences evaluated from data. The values of $\sigma_1, \sigma_2, \sigma_3$ can be then obtained by:

$$
\begin{aligned}
\sigma_1^2 &= \tfrac{1}{2}\left(\sigma_{1\text{-}2}^2 + \sigma_{1\text{-}3}^2 - \sigma_{2\text{-}3}^2\right) \\
\sigma_2^2 &= \tfrac{1}{2}\left(\sigma_{1\text{-}2}^2 + \sigma_{2\text{-}3}^2 - \sigma_{1\text{-}3}^2\right) \\
\sigma_3^2 &= \tfrac{1}{2}\left(\sigma_{1\text{-}3}^2 + \sigma_{2\text{-}3}^2 - \sigma_{1\text{-}2}^2\right)
\end{aligned}
\tag{B.7}
$$

This provides estimates of the uncertainty due to each method individually. Note that both the statistical and systematic uncertainties are accounted for in this

estimate of the factors σ_i. The combined inter-calibration coefficient for each crystal is then obtained as the mean of the coefficients obtained by each individual method weighted by $1/\sigma_i^2$. The residual uncertainty in the inter-calibration coefficients is shown in Fig. B.4 for 2017 data. In the barrel region, the E/p method has the best precision (0.4-0.6%), while the π^0 and Z $\rightarrow$ ee methods have comparable performance (0.5-1%). In the endcaps, the π^0 method works well for $|\eta| < 2$ with an accuracy of $\sim$3%, the E/p method has an accuracy of 1.5% and the Z $\rightarrow$ ee method has the best accuracy. The Z $\rightarrow$ ee method is the only one used to calibrate the crystals in the endcap region $|\eta| > 2.5$ crystals, therefore its precision is fully determined from the fit to the Z-peak. The black points represent the combined weighted precision. As shown, with the increased statistics available in 2017, the precision of the inter-calibration is now at the sub-percent level throughout the barrel.

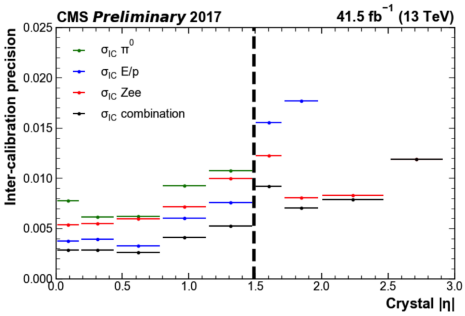

Figure B.4. Final individual and combined inter-calibration precision for 2017.

B.4 Monitoring of inter-calibration coefficients of ECAL forward endcaps

In the sections above we discussed the algorithm of the ECAL energy reconstruction and on its calibration. In particular, Sec. B.3 is dedicated to the evaluation of the crystal inter-calibration coefficients (ICs) that correct for residual differences between the response of different ECAL crystals, after the application of the laser corrections.

During Run 1 and Run 2, ECAL data have been first reconstructed applying only the laser corrections, and released every 48 hours (prompt reconstruction). The evaluation of the ICs, and the resulting re-calibration of ECAL energy, has been done only at the end of each year of data-taking. This approach has been adopted both because the energy precision of prompt data is sufficient for most of the CMS analyses, and because the use of the methods for IC evaluation described above require the analysis of a sufficiently large data sample.

However, this would not be necessarily true during the Run 3 of the LHC, especially in the forward region of the ECAL endcaps. As shown in Fig-B.1, in fact, the region corresponding to $|\eta| > 2.5$ shows the worst degradation in terms of ECAL response to the laser pulse. This means that in Run 3, where the luminosity of the LHC will further increase above its current value of $2 \times 10^{34}\,\mathrm{cm}^{-2}\,\mathrm{s}^{-1}$, the ECAL performances on the energy reconstruction will change rapidly with time.

To make sure ECAL maintains its performances during Run 3, also in the $|\eta| > 2.5$ region, it could be possible to evaluate the ICs multiple times during the year in order to monitor their values. In this forward region the Z → ee method is the only one that can be used. We already said that this method requires the analysis of a data sample as large as that collected in one year of data-taking. However, since most of the electrons from the Z decay hit the forward region of the ECAL detector, this region can be calibrated even analyzing only a fraction of the data, corresponding to an integrated luminosity of few fb^{-1}.

In the study reported in this section, I analyzed the evolution of the crystals IC in the forward region of the ECAL endcaps during 2017 and 2018. For this study I divided the 2017 and 2018 datasets in sub-datasets corresponding to luminosity intervals of $\sim 5\,\text{fb}^{-1}$ (Tabs. B.1 and B.2). I used prompt data, where the only energy correction applied is that from the laser corrections. I used the iJAZZ software to evaluate the IC with the Z → ee method, for each sub-dataset individually.

Table B.1. 2017 sub-datasets

Label	L_{int} [fb^{-1}]	Start date
2017B_1	4.80	16/06/2017
2017C_1	4.99	18/07/2017
2017C_2	4.59	07/08/2017
2017D_1	4.25	30/08/2017
2017E_1	5.01	24/09/2017
2017E_2	4.31	04/10/2017
2017F_1	5.38	13/10/2017
2017F_2	5.30	22/10/2017
2017F_3	2.86	03/11/2017

Table B.2. 2018 sub-datasets

Label	L_{int} [fb^{-1}]	Start date
2018A_1	5.13	03/05/2018
2018A_2	5.28	14/05/2018
2018A_3	3.13	23/05/2018
2018B_1	5.07	04/06/2018
2018B_2	1.71	15/06/2018
2018C_1	5.01	14/07/2018
2018C_2	1.60	22/07/2018
2018D_1	5.38	07/08/2018
2018D_2	5.28	17/08/2018
2018D_3	5.00	28/08/2018
2018D_4	5.27	06/09/2018
2018D_5	5.03	30/09/2018
2018D_6	5.97	16/10/2018

It is possible then to plot the single-crystal ICs from each luminosity interval against the time of the data-taking to study the evolution of the IC during 2017 and 2018. Figure B.5 shows the IC evolution over time for a single ECAL crystal in the forward region of one of the two endcaps. The IC value significantly drifts from its initial value during one year.

This result shows that in principle, it is possible to evaluate the IC for crystals in the $|\eta| > 2.5$ region every $\sim 5\,\text{fb}^{-1}$ of integrated luminosity collected, which correspond to roughly 2 weeks of data-taking, and monitor the IC evolution with time. This would allow to achieve better performances on the ECAL energy calibration, and improve the quality of the prompt data of ECAL. Finally, Fig. B.6 shows an estimation of the uncertainty on the IC value (σ_{IC}) averaged over crystals in the same $|\eta|$ region. The values reported show that the precision of the IC, when evaluated using only the Z → ee, is below 2% for $|\eta| < 2.5$, and below 10% elsewhere.

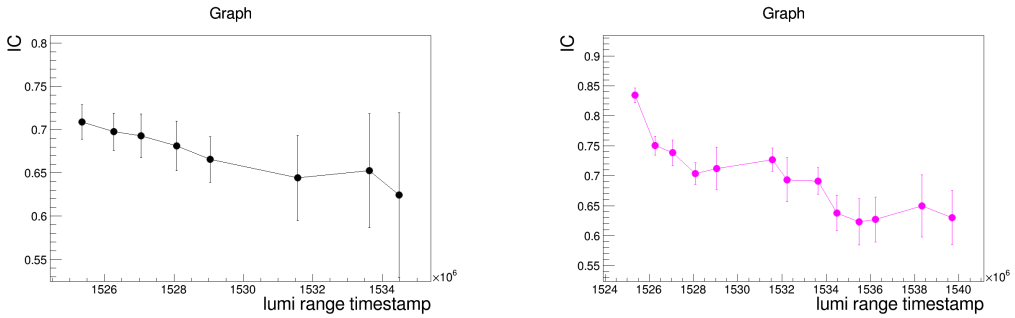

(a) 2017 **(b)** 2018

Figure B.5. Evolution over time during two years of data-taking for the IC of a single ECAL crystal. The IC evaluated for each luminosity interval of Tabs. B.1 and B.1 are plotted against the timestamp corresponding to the starting date of the data-taking. The timestamp is a progressive integer number that mark the time from the start of LHC activity.

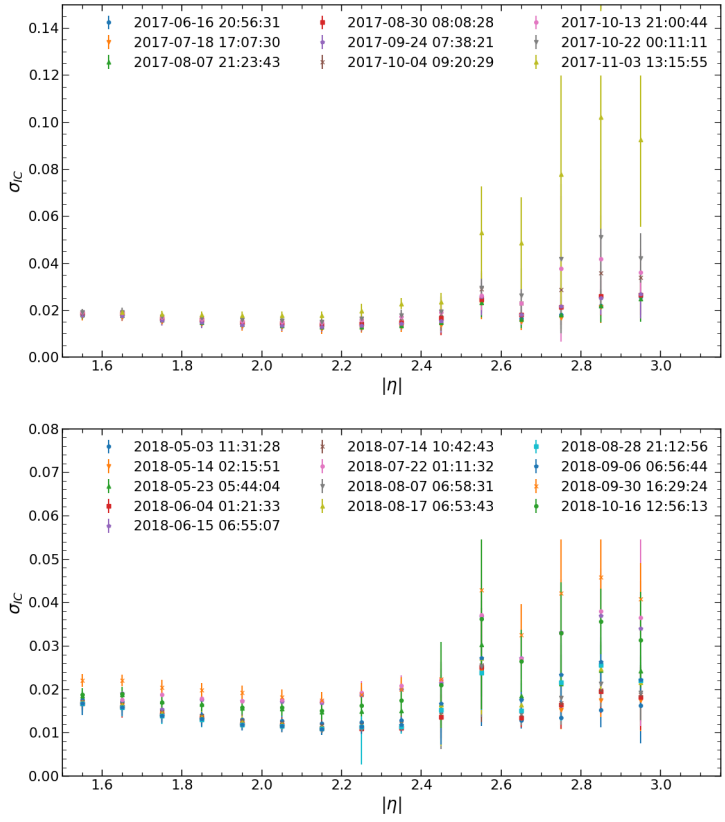

Figure B.6. IC error (σ_{IC}) averaged over crystals in the same $|\eta|$ region, for crystals in the endcaps and for different luminosity intervals from 2017 (top) and 2018 (bottom) data. The average precision of the IC, evaluated from the fit, using the Z $\rightarrow$ ee method is below 2% for $|\eta| < 2.5$ and below 10% elsewhere.

Appendix C

Fisher tests for background parameterization choice

In this Section we report the study carried out for the choice of the number of parameters of the background fit function. We performed the test using simulated QCD multijet events and looked at fits to the dijet mass spectrum in all event categories individually, for a selection of 6 signal hypotheses. This procedure allows us to test the fit function independently in all categories, which may have very different event yields. The test procedure starts from general assumption. Lets assume we have two fit models, M_0 and M_1, with n and $n+1$ parameters:

$$M_0 : (\theta_0, ..., \theta_n) \text{ and } M_1 : (\theta_0, ..., \theta_{n+1}) \tag{C.1}$$

Given the set of observation $\boldsymbol{y}$, the post-fit likelihoods for the two models are:

$$L(\boldsymbol{y}|M_0, \hat{\theta_0}, ..., \hat{\theta_n}) \text{ and } L(\boldsymbol{y}|M_1, \hat{\theta_0}, ..., \hat{\theta_n}, \hat{\theta_{n+1}}) \tag{C.2}$$

For the *Neyman-Pearson lemma* [137], the best discriminating variable for the comparisons of the goodness of the two fits is the likelihood ratio:

$$LR(\theta_{n+1}) = \frac{L(\mathbf{y}|M_1, \hat{\theta_0}, ..., \hat{\theta_n}, \hat{\theta_{n+1}})}{L(\mathbf{y}|M_0, \hat{\theta_0}, ..., \hat{\theta_n})} \tag{C.3}$$

If we assume, in our model, that the errors on each of the observation y_i are Gaussian, the two likelihoods are simply the product of Gaussian distributions:

$$LR(\theta_{n+1}) = \prod_i \frac{\exp\left(-\frac{y_i - \mu_i(M_1)}{2\sigma_i}\right)^2}{\exp\left(\frac{y_i - \mu_i(M_0)}{2\sigma_i}\right)^2} \tag{C.4}$$

where y_i are the observed data, σ_{y_i} are the Gaussian errors, and $\mu_i(M_0)$ and $\mu_i(M_1)$ are the prediction for M_0 and M_1 respectively. Since the logarithm is a monotonic function, we can take the logarithm of Eq. C.3 and multiply by -2. Therefore, we can re-write the expression above as:

$$LLR = -2\log LR(\theta_{n+1}) = \sum_i \left(\frac{y_i - \mu_y(M_1)}{\sigma_i}\right)^2 - \sum_i \left(\frac{y_i - \mu_y(M_0)}{\sigma_i}\right)^2 \\ = \chi^2(\nu_\theta = n+1) - \chi^2(\nu_\theta = n) = \chi^2(\nu = 1) \tag{C.5}$$

where ν_θ is the number of fit parameters, and $\nu = 1$ the degrees of freedom. LLR is then written as the difference between χ^2 from fits with the two models. The result is a random variable which follows a χ^2 distribution with 1 degree of freedom. The p-value (right tail) of the LLR distribution has the following meaning:

- p-value $\geqslant 0.05$: The difference between chi squares is not statistically relevant. The model with lower number of parameters is generally preferred.
- p-value < 0.05: Model M_1 performs better than M_0.

We perform the study using three functions with a different number of parameters. All functions tested are members of the standard dijet family and are reported in Tab. C.1 where $x = \frac{m_{jj}}{\sqrt{s}}$. The study has been performed as follows:

- the events from the simulated background sample (QCD multijet events) have been divided into categories following the procedure described in Sec. 7.2, under 6 different signal hypotheses: $m(\mathrm{R}_1) = 3$, 4, 5 TeV for both $\rho_\mathrm{m} = 0.1$ and 0.2;
- the m_jj spectra from each category, for all the signal hypotheses, have been simultaneously fitted with the method described in Sec. 7.3, using the three functions of Tab. C.1;
- the χ^2 of the fits has been evaluated for each category, assuming Gaussian uncertainties on the m_jj bins of $\sigma_i = \sqrt{N_i}$, where N_i is the content of the i-th bin;
- We then evaluated the two LLR, using Eq. C.5, for the comparison between f_{2par} and f_{3par}, and between f_{3par} and f_{4par}.
- The resulting p-values of the LLR obtained are shown in Figs. from C.1 to C.6, for the categories belonging to the 6 different signal hypotheses.

Table C.1. Standard dijet fit functions tested.

number of parameters	function
f_{2par}	$p_0(1-x)^{p_1}$
f_{3par}	$\frac{p_0(1-x)^{p_1}}{x^{p_2}}$
f_{4par}	$\frac{p_0(1-x)^{p_1}}{x^{p_2+p3\log x}}$

The left parts of Figs. from C.1 to C.6 show the p-value from the comparison between f_{2par} and f_{3par}. The test show that, especially at low $m(\mathrm{R}_1)$, the f_{3par}

performs better than f_{2par} in almost half of the cases. Instead, the comparison of f_{3par} with f_{4par}, in the right parts of the same Figures, show that the addition of a fourth parameter does not significantly improve the goodness of the fit in almost all cases.

After these considerations, we decided to use the 3-parameters function to fit the m_{jj} spectra of the categories of all the signal hypotheses. There are some cases (Fig. C.1a, C.2a, C.3a, C.4a, C.5a, C.6a) where the fit with 2 parameters is as good as the fit with 3 parameters, but we decided to maintain the use of f_{3par} for all the categories, to keep more simple the fit procedure without degrading its performances.

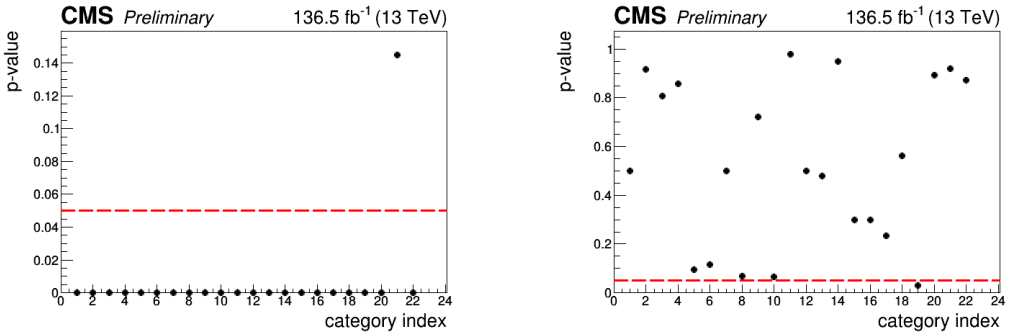

(a) f_{2par} vs. f_{3par} **(b)** f_{3par} vs. f_{4par}

Figure C.1. background fit function test for $m(\mathrm{R}_1) = 3\,\mathrm{TeV}$ and $\rho_{\mathrm{m}} = 0.1$.

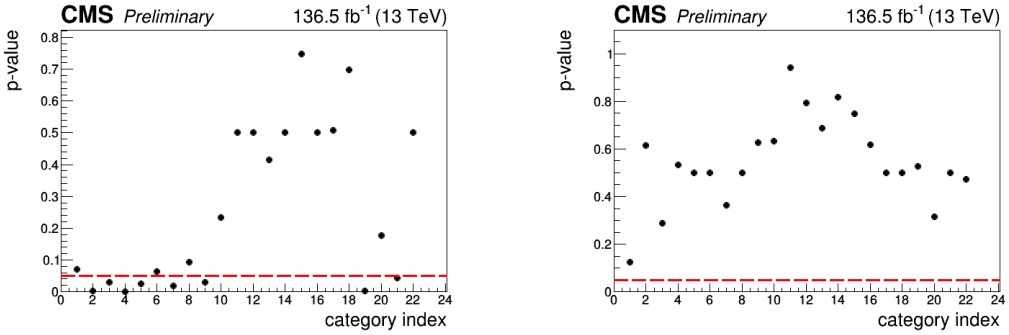

(a) f_{2par} vs f_{3par} **(b)** f_{3par} vs f_{4par}

Figure C.2. background fit function test for $m(\mathrm{R}_1) = 5\,\mathrm{TeV}$ and $\rho_{\mathrm{m}} = 0.1$.

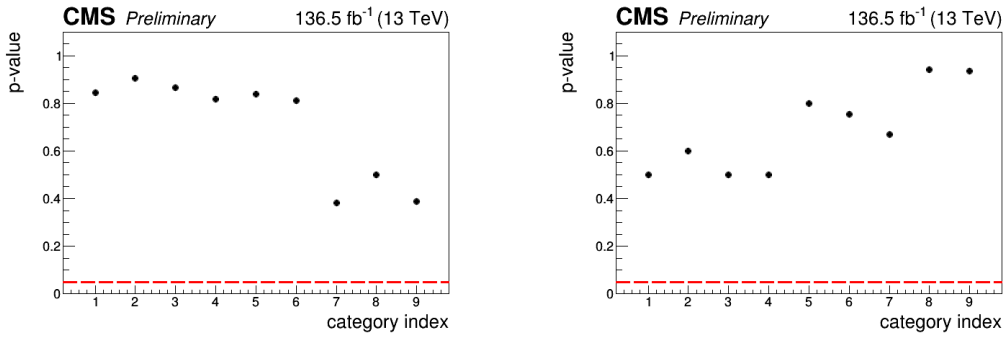

(a) f_{2par} vs f_{3par} **(b)** f_{3par} vs f_{4par}

Figure C.3. background fit function test for $m(\mathrm{R}_1) = 7\,\mathrm{TeV}$ and $\rho_\mathrm{m} = 0.1$.

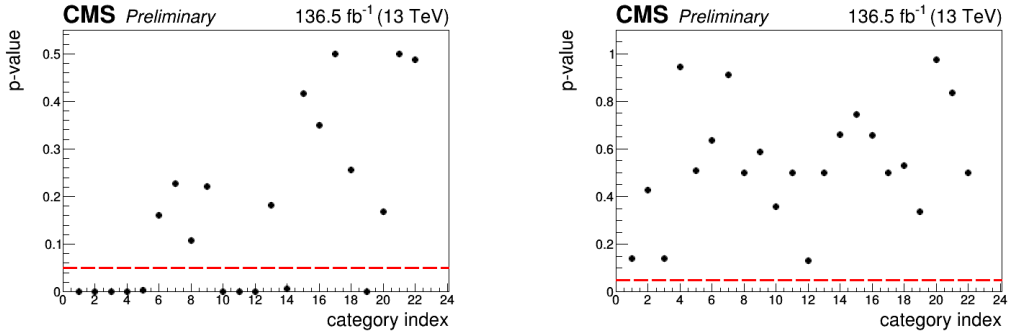

(a) f_{2par} vs f_{3par} **(b)** f_{3par} vs f_{4par}

Figure C.4. background fit function test for $m(\mathrm{R}_1) = 3\,\mathrm{TeV}$ and $\rho_\mathrm{m} = 0.2$.

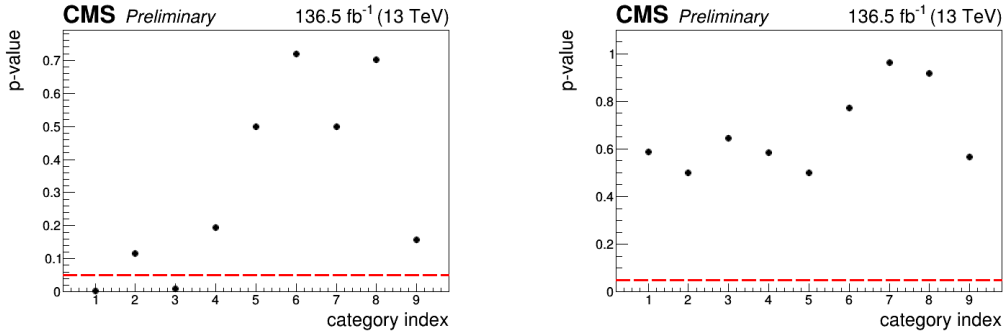

(a) f_{2par} vs f_{3par} **(b)** f_{3par} vs f_{4par}

Figure C.5. background fit function test for $m(\mathrm{R}_1) = 5\,\mathrm{TeV}$ and $\rho_\mathrm{m} = 0.2$.

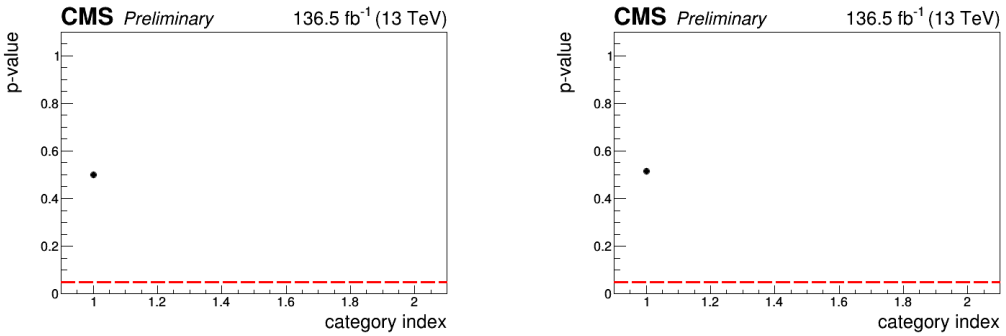

(a) f_{2par} vs f_{3par} **(b)** f_{3par} vs f_{4par}

Figure C.6. background fit function test for $m(\mathrm{R}_1) = 7\,\mathrm{TeV}$ and $\rho_\mathrm{m} = 0.2$.

Appendix D

Binning for m_{jj} spectra

For the m_{jj} spectra shown in this thesis we chose the following binning:

$$\begin{aligned}\text{bin edges} = [&1, 3, 6, 10, 16, 23, 31, 40, 50, 61, 74, 88, 103, 119, 137, 156, 176, 197, 220, 244,\\ &270, 296, 325, 354, 386, 419, 453, 489, 526, 565, 606, 649, 693, 740, 788, 838,\\ &890, 944, 1000, 1058, 1118, 1181, 1246, 1313, 1383, 1455, 1530, 1607, 1687, 1770,\\ &1856, 1945, 2037, 2132, 2231, 2332, 2438, 2546, 2659, 2775, 2895, 3019, 3147, 3279,\\ &3416, 3558, 3704, 3854, 4010, 4171, 4337, 4509, 4686, 4869, 5058, 5253, 5455, 5663,\\ &5877, 6099, 6328, 6564, 6808, 7150, 7500, 7850, 8250, 8650, 8999, 9500, 9999]\end{aligned} \tag{D.1}$$

The binning has been fixed in the previous dijet analysis in CMS and the bin size corresponds roughly to the experimental resolution at that mass.

Bibliography

[1] S. L. Glashow. "Partial-symmetries of weak interactions". In: *Nuclear Physics* 22 (1961), p. 579. DOI: 10.1016/0029-5582(61)90469-2.

[2] S. Weinberg. "A Model of Leptons". In: *Phys. Rev. Lett.* 19 (1967), p. 1264. DOI: 10.1103/PhysRevLett.19.1264.

[3] A. Salam. "Weak and Electromagnetic Interactions". In: *Conf. Proc. C* 680519 (1968), p. 367. DOI: 10.1142/9789812795915_0034.

[4] F. Englert and R. Brout. "Broken Symmetry and the Mass of Gauge Vector Mesons". In: *Phys. Rev. Lett.* 13 (1964), p. 321. DOI: 10.1103/PhysRevLett.13.321.

[5] P.W Higgs. "Broken symmetries, massless particles and gauge fields". In: *Physics Letters* 12 (1964), p. 132. DOI: https://doi.org/10.1016/0031-9163(64)91136-9.

[6] R. K. Ellis, W. J. Stirling, and B. R. Webber. *QCD and collider physics*. 2003.

[7] G. Dissertori, M. Schmelling, and I.G. Knowles. *Quantum chromodynamics: high energy experiments and theory.* 2009.

[8] S. van der Meer. *Calibration of the effective beam height in the ISR*. Tech. rep. Technical report. 1968. URL: https://cds.cern.ch/record/296752.

[9] CMS collaboration. "Precision luminosity measurement in proton-proton collisions at $\sqrt{s} = 13$ TeV in 2015 and 2016 at CMS". In: *Eur. Phys. J. C* 81.9 (2021), p. 800. DOI: 10.1140/epjc/s10052-021-09538-2. arXiv: 2104.01927 [hep-ex].

[10] CMS Collaboration. *CMS luminosity measurement for the 2017 data-taking period at $\sqrt{s} = 13$ TeV*. CMS Physics Analysis Summary CMS-PAS-LUM-17-004. 2018. URL: https://cds.cern.ch/record/2621960/.

[11] CMS Collaboration. *CMS luminosity measurement for the 2018 data-taking period at $\sqrt{s} = 13$ TeV*. CMS Physics Analysis Summary CMS-PAS-LUM-18-002. 2019. URL: https://cds.cern.ch/record/2676164/.

[12] Csaba Csáki, Salvator Lombardo, and Ofri Telem. *TASI Lectures on Non-Supersymmetric BSM Models*. 2018. arXiv: 1811.04279 [hep-ph].

[13] Richard P. Feynman. *Feynman Lectures on Gravitation.* Addison-Wesley., p. 136. ISBN: 0-201-62734-5.

[14] N. Arkani–Hamed, S. Dimopoulos, and G. Dvali. "The hierarchy problem and new dimensions at a millimeter". In: *Phys. Lett. B* 429 (1998), p. 263. DOI: 10.1016/S0370-2693(98)00466-3. arXiv: hep-ph/9803315 [hep-ph].

[15] J.C. Long, H.W. Chan, and J.C. Price. "Experimental status of gravitational-strength forces in the sub-centimeter regime". In: *Nuclear Physics B* 539 (1999), p. 23. DOI: 10.1016/s0550-3213(98)00711-1. arXiv: hep-ph/9805217 ["hep-ph"].

[16] ATLAS collaboration. "Search for new phenomena in high-mass diphoton final states using 37 fb^{-1} of proton–proton collisions collected at $\sqrt{s} = 13\,\mathrm{TeV}$ with the ATLAS detector". In: *Phys. Lett. B* 775 (2017), p. 105. DOI: 10.1016/j.physletb.2017.10.039. arXiv: 1707.04147 [hep-ex].

[17] CMS collaboration. "Search for physics beyond the standard model in high-mass diphoton events from proton-proton collisions at $\sqrt{s} = 13\,\mathrm{TeV}$". In: *Phys. Rev. D* 98.9 (2018), p. 092001. DOI: 10.1103/PhysRevD.98.092001. arXiv: 1809.00327 [hep-ex].

[18] CMS collaboration. "Search for contact interactions and large extra dimensions in the dilepton mass spectra from proton-proton collisions at $\sqrt{s} = 13$ TeV". In: *Journal of High Energy Physics* 2019 (2019), p. 114. DOI: 10.1007/jhep04(2019)114. arXiv: 1812.10443 ["hep-ex"].

[19] S. Dimopoulos and G. L. Landsberg. "Black holes at the LHC". In: *Phys. Rev. Lett.* 87 (2001), p. 161602. DOI: 10.1103/PhysRevLett.87.161602. arXiv: hep-ph/0106295.

[20] ATLAS collaboration. "Search for TeV-scale gravity signatures in high-mass final states with leptons and jets with the ATLAS detector at $\sqrt{s} = 13$ TeV". In: *Physics Letters B* 760 (2016), p. 520. DOI: 10.1016/j.physletb.2016.07.030. arXiv: 1606.02265 ["hep-ex"].

[21] CMS collaboration. "Search for lepton-flavor violating decays of heavy resonances and quantum black holes to eμ final states in proton-proton collisions at $\sqrt{s} = 13$ TeV". In: *Journal of High Energy Physics* 2018 (2018), p. 073. DOI: 10.1007/jhep04(2018)073. arXiv: 1802.01122 ["hep-ex"].

[22] L. Randall and R. Sundrum. "Large Mass Hierarchy from a Small Extra Dimension". In: *Phys. Rev. Lett.* 83 (17 1999), p. 3370. DOI: 10.1103/PhysRevLett.83.3370. arXiv: hep-ph/9905221 [hep-ph].

[23] L. Randall and R. Sundrum. "An Alternative to Compactification". In: *Phys. Rev. Lett.* 83 (23 Dec. 1999), p. 4690. DOI: 10.1103/PhysRevLett.83.4690. arXiv: hep-ph/9906064 [hep-ph].

[24] W. D. Goldberger and M. B. Wise. "Modulus Stabilization with Bulk Fields". In: *Phys. Rev. Lett.* 83 (1999), p. 4922. DOI: 10.1103/PhysRevLett.83.4922. arXiv: hep-ph/9907447 [hep-ph].

[25] K. Agashe et al. "RS1, custodial isospin and precision tests". In: *Journal of High Energy Physics* 2003 (2003), p. 050. DOI: 10.1088/1126-6708/2003/08/050. arXiv: hep-ph/0308036 [hep-ph].

[26] K. Agashe et al. "CERN LHC signals from warped extra dimensions". In: *Phys. Rev. D* 77 (2008), p. 015003. DOI: 10.1103/PhysRevD.77.015003. arXiv: hep-ph/0612015 [hep-ph].

[27] ATLAS collaboration. "Search for $t\bar{t}$ resonances in fully hadronic final states in pp collisions at $\sqrt{s} = 13$ TeV with the ATLAS detector". In: *Journal of High Energy Phys.* 10 (2020), p. 061. DOI: 10.1007/JHEP10(2020)061. arXiv: 2005.05138 [hep-ex].

[28] CMS collaboration. "Search for resonant $t\bar{t}$ production in proton-proton collisions at $\sqrt{s} = 13$ TeV". In: *Journal of High Energy Phys.* 4 (2019), p. 031. DOI: 10.1007/jhep04(2019)031. arXiv: 1810.05905 [hep-ex].

[29] G. Aad et al. "Search for new resonances in mass distributions of jet pairs using 139 fb^{-1} of pp collisions at $\sqrt{s} = 13$ TeV with the ATLAS detector". In: *JHEP* 03 (2020), p. 145. DOI: 10.1007/JHEP03(2020)145. arXiv: 1910.08447 [hep-ex].

[30] Albert M Sirunyan et al. "Search for high mass dijet resonances with a new background prediction method in proton-proton collisions at $\sqrt{s} = 13$ TeV". In: *JHEP* 05 (2020), p. 033. DOI: 10.1007/JHEP05(2020)033. arXiv: 1911.03947 [hep-ex].

[31] Kaustubh S. Agashe et al. "LHC Signals from Cascade Decays of Warped Vector Resonances". In: *JHEP* 05 (2017). Including private communications with authors., p. 078. DOI: 10.1007/JHEP05(2017)078. arXiv: 1612.00047 [hep-ph].

[32] ATLAS collaboration. "Search for resonances in diphoton events at $\sqrt{s}$=13 TeV with the ATLAS detector". In: *JHEP* 09 (2016), p. 001. DOI: 10.1007/JHEP09(2016)001. arXiv: 1606.03833 [hep-ex].

[33] CMS collaboration. "Search for high-mass diphoton resonances in proton–proton collisions at 13 TeV and combination with 8 TeV search". In: *Physics Letters B* 767 (2017), p. 147. DOI: https://doi.org/10.1016/j.physletb.2017.01.027. arXiv: 1609.02507 [hep-ex].

[34] Kaustubh Agashe et al. "LHC Signals for KK Graviton from an Extended Warped Extra Dimension". In: *JHEP* 11 (2020), p. 109. DOI: 10.1007/JHEP11(2020)109. arXiv: 2008.06480 [hep-ph].

[35] CMS Collaboration. *Search for resonances decaying to three W bosons in the hadronic final state in proton-proton collisions at $\sqrt{s}$ = 13 TeV*. 2021. arXiv: 2112.13090 [hep-ex].

[36] CMS Collaboration. *Search for resonances decaying to three W bosons in proton-proton collisions at $\sqrt{s}$ = 13 TeV*. 2022. arXiv: 2201.08476 [hep-ex].

[37] U. Baur, I. Hinchliffe, and D. Zeppenfeld. "Excited Quark Production at Hadron Colliders". In: *Int. J. Mod. Phys. A* 2 (1987), p. 1285. DOI: 10.1142/S0217751X87000661.

[38] Paul H. Frampton and Sheldon L. Glashow. "Chiral Color: An Alternative to the Standard Model". In: *Phys. Lett. B* 190 (1987), p. 157. DOI: 10.1016/0370-2693(87)90859-8.

[39] R.S. Chivukula, A.G. Cohen, and E.H. Simmons. "New strong interactions at the Tevatron?" In: *Physics Letters B* 380 (1996), p. 92. DOI: 10.1016/0370-2693(96)00464-9. arXiv: hep-ph/9603311 [hep-ph].

[40] T. Han, I. Lewis, and Z. Liu. "Colored resonant signals at the LHC: largest rate and simplest topology". In: *Journal of High Energy Physics* 12 (2010), p. 085. DOI: 10.1007/jhep12(2010)085. arXiv: 1010.4309 [hep-ph].

[41] E. Eichten et al. "Super Collider Physics". In: *Rev. Mod. Phys.* 56 (1984). [Addendum: Rev.Mod.Phys. 58, 1065–1073 (1986)], pp. 579–. DOI: 10.1103/RevModPhys.56.579.

[42] J. L. Hewett and T. G. Rizzo. "Low-Energy Phenomenology of Superstring Inspired E(6) Models". In: *Phys. Rept.* 183 (1989), p. 193. DOI: 10.1016/0370-1573(89)90071-9.

[43] L. A. Anchordoqui et al. "Dijet Signals for Low Mass Strings at the Large Hadron Collider". In: *Physical Review Letters* 101 (2008), p. 241803. DOI: 10.1103/physrevlett.101.241803. arXiv: 10.1103 [hep-ph].

[44] M. Chala et al. "Constraining dark sectors with monojets and dijets". In: *Journal of High Energy Physics* 7 (2015), p. 089. DOI: 10.1007/jhep07(2015)089. arXiv: 1503.05916 [hep-ph].

[45] D. et al. Abercrombie. "Dark Matter benchmark models for early LHC Run-2 Searches: Report of the ATLAS/CMS Dark Matter Forum". In: *Physics of the Dark Universe* 27 (2020), p. 100371. DOI: 10.1016/j.dark.2019.100371. arXiv: 1507.00966 [hep-ph].

[46] J. et al. Abdallah. "Simplified models for dark matter searches at the LHC". In: *Physics of the Dark Universe* 9-10 (2015), p. 8. DOI: 10.1016/j.dark.2015.08.001. arXiv: 1506.03116 [hep-ph].

[47] CDF collaboration. "Global search for new physics with $2.0\,\mathrm{fb}^{-1}$ at CDF". In: *Physical Review D* 79 (2009), p. 011101. DOI: 10.1103/physrevd.79.011101. arXiv: 0809.3781 [hep-ex].

[48] G. Choudalakis. *On hypothesis testing, trials factor, hypertests and the BumpHunter*. 2011. arXiv: 1101.0390 [physics.data-an].

[49] Javier Duarte. "Fast Reconstruction and Data Scouting". In: *4th International Workshop Connecting The Dots*. 2018. arXiv: 1808.00902 [hep-ex].

[50] S. Mukherjee. *Data Scouting : A New Trigger Paradigm*. 2017. arXiv: 1708.06925 [hep-ex].

[51] ATLAS collaboration. "Search for Low-Mass Dijet Resonances Using Trigger-Level Jets with the ATLAS Detector in pp collisions at $\sqrt{s} = 13\,\mathrm{TeV}$". In: *Physical Review Letters* 121 (2018), p. 081801. DOI: 10.1103/physrevlett.121.081801. arXiv: 1804.03496 [hep-ex].

[52] CMS collaboration. "Search for narrow and broad dijet resonances in proton-proton collisions at $\sqrt{s} = 13$ TeV and constraints on dark matter mediators and other new particles". In: *Journal of High Energy Physics* 08 (2018), p. 130. DOI: 10.1007/jhep08(2018)130. arXiv: 1806.00843 [hep-ex].

[53] CMS collaboration. "Search for dijet resonances in proton–proton collisions at $\sqrt{s} = 13\,\text{TeV}$ and constraints on dark matter and other models". In: *Physics Letters B* 769 (2017), p. 520. DOI: 10.1016/j.physletb.2017.02.012. arXiv: 1611.03568 [hep-ex].

[54] CMS Collaboration. *Search for heavy resonances decaying to b quarks in proton-proton collisions at sqrt s=13 TeV*. Tech. rep. 2021. URL: https://cds.cern.ch/record/2776798.

[55] J. L. Rosner. "Prominent decay modes of a leptophobic Z'". In: *Physics Letters B* 387 (1996), p. 113. DOI: 10.1016/0370-2693(96)01022-2. arXiv: hep-ph/9607207 [hep-ph].

[56] M. Carena et al. "Z' gauge bosons at the Fermilab Tevatron". In: *Physical Review D* 70 (2004), p. 093009. DOI: 10.1103/physrevd.70.093009. arXiv: hep-ph/0408098 [hep-ph].

[57] D. Dicus, A. Stange, and S. Willenbrock. "Higgs decay to top quarks at hadron colliders". In: *Physics Letters B* 333 (1994), p. 126. DOI: 10.1016/0370-2693(94)91017-0. arXiv: hep-ph/9404359 [hep-ph].

[58] R. M. Harris and S. Jain. "Cross sections for leptophobic topcolor Z' decaying to top-antitop". In: *The European Physical Journal C* 72 (2012), p. 2072. DOI: 10.1140/epjc/s10052-012-2072-4. arXiv: 1112.4928 [hep-ph].

[59] Albert M Sirunyan et al. "Search for dijet resonances using events with three jets in proton-proton collisions at $\sqrt{s} = 13$ TeV". In: *Phys. Lett. B* 805 (2020), p. 135448. DOI: 10.1016/j.physletb.2020.135448. arXiv: 1911.03761 [hep-ex].

[60] Albert M Sirunyan et al. "Search for low mass vector resonances decaying into quark-antiquark pairs in proton-proton collisions at $\sqrt{s} = 13$ TeV". In: *Phys. Rev. D* 100 (2019), p. 112007. DOI: 10.1103/PhysRevD.100.112007. arXiv: 1909.04114 [hep-ex].

[61] Morad Aaboud et al. "Search for light resonances decaying to boosted quark pairs and produced in association with a photon or a jet in proton-proton collisions at $\sqrt{s} = 13$ TeV with the ATLAS detector". In: *Phys. Lett. B* 788 (2019), p. 316. DOI: 10.1016/j.physletb.2018.09.062. arXiv: 1801.08769 [hep-ex].

[62] A. Sirunyan et al. "Search for low-mass quark-antiquark resonances produced in association with a photon at $\sqrt{s} = 13$ TeV". In: *Phys. Rev. Lett.* 123 (2019), p. 231803. DOI: 10.1103/PhysRevLett.123.231803. arXiv: 1905.10331 [hep-ex].

[63] Morad Aaboud et al. "Search for low-mass resonances decaying into two jets and produced in association with a photon using pp collisions at $\sqrt{s} = 13$ TeV with the ATLAS detector". In: *Phys. Lett. B* 795 (2019), p. 56. DOI: 10.1016/j.physletb.2019.03.067. arXiv: 1901.10917 [hep-ex].

[64] G. Aad et al. "Search for dijet resonances in events with an isolated charged lepton using $\sqrt{s} = 13$ TeV proton−proton collision data collected by the ATLAS detector". In: *JHEP* 06 (2020), p. 151. DOI: 10.1007/JHEP06(2020)151. arXiv: 2002.11325 [hep-ex].

[65] Morad Aaboud et al. "A search for pair-produced resonances in four-jet final states at $\sqrt{s} = 13$ TeV with the ATLAS detector". In: *Eur. Phys. J. C* 78 (2018), p. 250. DOI: 10.1140/epjc/s10052-018-5693-4. arXiv: 1710.07171 [hep-ex].

[66] Albert M Sirunyan et al. "Search for pair-produced resonances decaying to quark pairs in proton-proton collisions at $\sqrt{s} = 13$ TeV". In: *Phys. Rev. D* 98 (2018), p. 112014. DOI: 10.1103/PhysRevD.98.112014. arXiv: 1808.03124 [hep-ex].

[67] Albert M. Sirunyan et al. "Search for pair-produced resonances each decaying into at least four quarks in proton-proton collisions at $\sqrt{s} = 13$ TeV". In: *Phys. Rev. Lett.* 121 (2018), p. 141802. DOI: 10.1103/PhysRevLett.121.141802. arXiv: 1806.01058 [hep-ex].

[68] Morad Aaboud et al. "Search for R-parity-violating supersymmetric particles in multi-jet final states produced in *p*-*p* collisions at $\sqrt{s} = 13$ TeV using the ATLAS detector at the LHC". In: *Phys. Lett. B* 785 (2018), p. 136. DOI: 10.1016/j.physletb.2018.08.021. arXiv: 1804.03568 [hep-ex].

[69] CMS collaboration. "Search for massive resonances decaying into WW, WZ, ZZ, qW, and qZ with dijet final states at $\sqrt{s} = 13$ TeV". In: *Phys. Rev. D* 97.7 (2018), p. 072006. DOI: 10.1103/PhysRevD.97.072006. arXiv: 1708.05379 [hep-ex].

[70] ATLAS collaboration. "Search for diboson resonances in hadronic final states in 139 fb^{-1} of pp collisions at $\sqrt{s} = 13$ TeV with the ATLAS detector". In: *JHEP* 09 (2019). [Erratum: JHEP 06, 042 (2020)], p. 091. DOI: 10.1007/JHEP09(2019)091. arXiv: 1906.08589 [hep-ex].

[71] CMS collaboration. "Search for a massive resonance decaying to a pair of Higgs bosons in the four b quark final state in proton-proton collisions at $\sqrt{s} =$ 13 TeV". In: *Phys. Lett. B* 781 (2018), p. 244. DOI: 10.1016/j.physletb.2018.03.084. arXiv: 1710.04960 [hep-ex].

[72] ATLAS collaboration. "Search for resonant pair production of Higgs bosons in the $b\bar{b}b\bar{b}$ final state using pp collisions at $\sqrt{s} = 13$ TeV with the ATLAS detector". In: (2022). arXiv: 2202.07288 [hep-ex].

[73] ATLAS collaboration. "Search for resonances decaying into a weak vector boson and a Higgs boson in the fully hadronic final state produced in proton−proton collisions at $\sqrt{s} = 13$ TeV with the ATLAS detector". In: *Phys. Rev. D* 102.11 (2020), p. 112008. DOI: 10.1103/PhysRevD.102.112008. arXiv: 2007.05293 [hep-ex].

[74] CMS collaboration. "Search for a heavy vector resonance decaying to a Z boson and a Higgs boson in proton-proton collisions at $\sqrt{s} = 13$ TeV". In: *Eur. Phys. J. C* 81.8 (2021), p. 688. DOI: 10.1140/epjc/s10052-021-09348-6. arXiv: 2102.08198 [hep-ex].

[75] CMS collaboration. "A multi-dimensional search for new heavy resonances decaying to boosted WW, WZ, or ZZ boson pairs in the dijet final state at 13 TeV". In: *Eur. Phys. J. C* 80.3 (2020), p. 237. DOI: 10.1140/epjc/s10052-020-7773-5. arXiv: 1906.05977 [hep-ex].

[76] ATLAS collaboration. "The ATLAS Experiment at the CERN Large Hadron Collider". In: *JINST* 3 (2008), S08003. DOI: 10.1088/1748-0221/3/08/S08003.

[77] CMS collaboration. "The CMS Experiment at the CERN LHC". In: *JINST* 3 (2008), S08004. DOI: 10.1088/1748-0221/3/08/S08004.

[78] ALICE Collaboration. "The ALICE experiment at the CERN LHC". In: *JINST* 3 (2008), S08002. DOI: 10.1088/1748-0221/3/08/s08002.

[79] LHCb collaboration. "The LHCb Detector at the LHC". In: *JINST* 3 (2008), S08005. DOI: 10.1088/1748-0221/3/08/S08005.

[80] ATLAS collaboration. "Observation of a new particle in the search for the Standard Model Higgs boson with the ATLAS detector at the LHC". In: *Phys. Lett. B* 716 (2012), p. 1. DOI: 10.1016/j.physletb.2012.08.020. arXiv: 1207.7214 [hep-ex].

[81] CMS collaboration. "Observation of a New Boson at a Mass of 125 GeV with the CMS Experiment at the LHC". In: *Phys. Lett. B* 716 (2012), p. 30. DOI: 10.1016/j.physletb.2012.08.021. arXiv: 1207.7235 [hep-ex].

[82] CMS collaboration. *The CMS magnet project: Technical Design Report*. Technical design report. CMS. Geneva: CERN, 1997. URL: https://cds.cern.ch/record/331056.

[83] CMS Collaboration. "Precise Mapping of the Magnetic Field in the CMS Barrel Yoke using Cosmic Rays". In: *JINST* 5 (2010), T03021. DOI: 10.1088/1748-0221/5/03/T03021. arXiv: 0910.5530 [physics.ins-det].

[84] CMS collaboration. *The CMS tracker system project: Technical Design Report*. Technical design report. CMS. Geneva: CERN, 1997. URL: https://cds.cern.ch/record/368412.

[85] CMS Collaboration. *The CMS electromagnetic calorimeter project: Technical Design Report*. Technical design report. CMS. Geneva: CERN, 1997. URL: https://cds.cern.ch/record/349375.

[86] CMS Collaboration. *The CMS hadron calorimeter project: Technical Design Report*. Technical design report. CMS. Geneva: CERN, 1997. URL: https://cds.cern.ch/record/357153.

[87] CMS Collaboration. *The CMS muon project: Technical Design Report*. Technical design report. CMS. Geneva: CERN, 1997. URL: https://cds.cern.ch/record/343814.

[88] CMS collaboration. "The CMS trigger system". In: *JINST* 12 (2017), P01020. DOI: 10.1088/1748-0221/12/01/P01020. arXiv: 1609.02366 [physics.ins-det].

[89] CMS collaboration. "Particle-flow reconstruction and global event description with the CMS detector". In: *JINST* 12 (2017), P10003. DOI: 10.1088/1748-0221/12/10/P10003. arXiv: 1706.04965 [physics.ins-det].

[90] S. D. Ellis and D. E. Soper. "Successive combination jet algorithm for hadron collisions". In: *Physical Review D* 48 (1993), p. 3160. DOI: 10.1103/physrevd.48.3160. arXiv: hep-ph/9305266 [hep-ph].

[91] Yu .L Dokshitzer et al. "Better jet clustering algorithms". In: *Journal of High Energy Physics* 1997 (1997), p. 001. DOI: 10.1088/1126-6708/1997/08/001. arXiv: hep-ph/9707323 [hep-ph].

[92] M. Cacciari, G. P. Salam, and G. Soyez. "The anti-k_{T} jet clustering algorithm". In: *JHEP* 04 (2008), p. 63. DOI: 10.1088/1126-6708/2008/04/063. arXiv: 0802.1189 [hep-ph].

[93] M. Cacciari, G. P. Salam, and G. Soyez. "FastJet User Manual". In: *Eur. Phys. J. C* 72 (2012), p. 1896. DOI: 10.1140/epjc/s10052-012-1896-2. arXiv: 1111.6097 [hep-ph].

[94] D. Bertolini et al. "Pileup Per Particle Identification". In: *JHEP* 10 (2014), p. 059. DOI: 10.1007/JHEP10(2014)059. arXiv: 1407.6013 [hep-ph].

[95] CMS collaboration. "Pileup mitigation at CMS in 13 TeV data". In: *Journal of Instrumentation* 15.09 (Sept. 2020), P09018. DOI: 10.1088/1748-0221/15/09/p09018. arXiv: 2003.00503 [hep-ex].

[96] CMS collaboration. "Pileup measurement and mitigation techniques in CMS". In: *Journal of Physics: Conference Series* 404 (2012), p. 012045. DOI: 10.1088/1742-6596/404/1/012045.

[97] CMS collaboration. "Jet energy scale and resolution in the CMS experiment in pp collisions at 8 TeV". In: *JINST* 12 (2017), P02014. DOI: 10.1088/1748-0221/12/02/P02014. arXiv: 1607.03663 [hep-ex].

[98] CMS Collaboration. "Jet energy scale and resolution performance with 13 TeV data collected by CMS in 2016-2018". In: (2020). URL: http://cds.cern.ch/record/2715872.

[99] CMS collaboration. "Determination of jet energy calibration and transverse momentum resolution in CMS". In: *Journal of Instrumentation* 6 (Nov. 2011), P11002. DOI: 10.1088/1748-0221/6/11/p11002. arXiv: 1107.4277 [physycs.ins-det].

[100] A. J. Larkoski et al. "Soft drop". In: *Journal of High Energy Physics* 2014 (2014), p. 146. DOI: 10.1007/jhep05(2014)146. arXiv: 1402.2657 [hep-ph].

[101] J. Thaler and K. Van Tilburg. "Identifying Boosted Objects with N-subjettiness". In: *JHEP* 03 (2011), p. 015. DOI: 10.1007/JHEP03(2011)015. arXiv: 1011.2268 [hep-ph].

[102] S. D. Ellis and D. E. Soper. "Successive combination jet algorithm for hadron collisions". In: *Physical Review D* 48 (1993), p. 3160. DOI: 10.1103/physrevd.48.3160. arXiv: hep-ph/9305266 [hep-ph].

[103] "Longitudinally-invariant $k_{\perp}$-clustering algorithms for hadron-hadron collisions". In: *Nuclear Physics B* 406 (1993), p. 187. DOI: https://doi.org/10.1016/0550-3213(93)90166-M.

[104] G. Franzoni. "Dataset definition for CMS operations and physics analyses". In: *Nucl. Part. Phys. Proc.* 273-275 (2016), p. 929. DOI: 10.1016/j.nuclphysbps.2015.09.144.

[105] D. Krohn, J. Thaler, and L. T. Wang. "Jet Trimming". In: *JHEP* 02 (2010), p. 084. DOI: 10.1007/JHEP02(2010)084. arXiv: 0912.1342 [hep-ph].

[106] J. et al. Alwall. "The automated computation of tree-level and next-to-leading order differential cross sections, and their matching to parton shower simulations". In: *Journal of High Energy Physics* 07 (2014), p. 079. ISSN: 1029-8479. DOI: 10.1007/jhep07(2014)079. arXiv: 1405.0301 [hep-ph].

[107] R. D. et al. Ball. "Parton distributions from high-precision collider data". In: *The European Physical Journal C* 77 (2017), p. 663. DOI: 10.1140/epjc/s10052-017-5199-5. arXiv: 1706.00428 [hep-ph].

[108] Torbjörn et al. Sjöstrand. "An introduction to PYTHIA 8.2". In: *Comput. Phys. Commun.* 191 (2015), p. 159. DOI: 10.1016/j.cpc.2015.01.024. arXiv: 1410.3012 [hep-ph].

[109] CMS collaboration. "Extraction and validation of a new set of CMS PYTHIA8 tunes from underlying-event measurements". In: *Eur. Phys. J. C* 80.1 (2020), p. 4. DOI: 10.1140/epjc/s10052-019-7499-4. arXiv: 1903.12179 [hep-ex].

[110] S. et al. Agostinelli. "GEANT4–a simulation toolkit". In: *Nucl. Instrum. Meth. A* 506 (2003), p. 250. DOI: 10.1016/S0168-9002(03)01368-8.

[111] CMS collaboraiton. "Performance of the CMS Level-1 trigger in proton-proton collisions at $\sqrt{s} = 13$ TeV". In: *JINST* 15.10 (2020), P10017. DOI: 10.1088/1748-0221/15/10/P10017. arXiv: 2006.10165 [hep-ex].

[112] CMS collaboration. "Search for Narrow Resonances Using the Dijet Mass Spectrum in *pp* Collisions at $\sqrt{s}$=8 TeV". In: *Phys. Rev. D* 87.11 (2013), p. 114015. DOI: 10.1103/PhysRevD.87.114015. arXiv: 1302.4794 [hep-ex].

[113] CMS collaboration. "Search for Resonances in the Dijet Mass Spectrum from 7 TeV pp Collisions at CMS". In: *Phys. Lett. B* 704 (2011), p. 123. DOI: 10.1016/j.physletb.2011.09.015. arXiv: 1107.4771 [hep-ex].

[114] M. J. Oreglia. "A study of the reactions $\psi' \to \gamma\gamma\psi$". SLAC Report SLAC-R-236. PhD thesis. Stanford University, 1980. URL: http://www.slac.stanford.edu/cgi-wrap/getdoc/slac-r-236.pdf.

[115] J. E. Gaiser. "Charmonium spectroscopy from radiative decays of the J/ψ and ψ'". SLAC Report SLAC-R-255. PhD thesis. Stanford University, 1982. URL: https://www.slac.stanford.edu/cgi-bin/getdoc/slac-r-255.pdf.

[116] A.L Read. "Linear interpolation of histograms". In: *Nuclear Instruments and Methods in Physics Research Section A: Accelerators, Spectrometers, Detectors and Associated Equipment* 425 (1999), p. 357. DOI: https://doi.org/10.1016/S0168-9002(98)01347-3.

[117] Robert D. Cousins. "Generalization of Chisquare Goodness-of-Fit Test for Binned Data Using Saturated Models, with Application to Histograms". In: *UCLA website* (2013). URL: http://www.physics.ucla.edu/~cousins/stats/cousins_saturated.pdf.

[118] S. S. Wilks. "The Large-Sample Distribution of the Likelihood Ratio for Testing Composite Hypotheses". In: *The Annals of Mathematical Statistics* 9.1 (1938), p. 60. DOI: 10.1214/aoms/1177732360.

[119] R. Barlow. "Event classification using weighting methods". In: *J. Comp. Phys.* 72 (1987), p. 202. DOI: 10.1016/0021-9991(87)90078-7.

[120] L. Demortier. "P values and nuisance parameters". In: *Statistical issues for LHC physics. Proceedings, Workshop, PHYSTAT-LHC, Geneva, Switzerland, June 27-29, 2007*. 2008, p. 23. DOI: 10.5170/CERN-2008-001.

[121] T. Junk. "Confidence level computation for combining searches with small statistics". In: *Nucl. Instrum. Meth. A* 434 (1999), p. 435. DOI: 10.1016/S0168-9002(99)00498-2. arXiv: hep-ex/9902006.

[122] A. L. Read. "Presentation of search results: The CL(s) technique". In: *J. Phys. G* 28 (2002), p. 2693. DOI: 10.1088/0954-3899/28/10/313.

[123] LHC Higgs Combination Group ATLAS Collaboration CMS Collaboration. *Procedure for the LHC Higgs boson search combination in Summer 2011*. Tech. rep. Geneva: CERN, 2011. URL: http://cds.cern.ch/record/1379837.

[124] G. Cowan et al. "Asymptotic formulae for likelihood-based tests of new physics". In: *Eur. Phys. J. C* 71 (2011). [Erratum: Eur.Phys.J.C 73, 2501 (2013)], p. 1554. DOI: 10.1140/epjc/s10052-011-1554-0. arXiv: 1007.1727 [physics.data-an].

[125] CMS collaboration. "Search for low mass vector resonances decaying into quark-antiquark pairs in proton-proton collisions at $\sqrt{s} = 13$ TeV". In: *Phys. Rev. D* 100.11 (2019), p. 112007. DOI: 10.1103/PhysRevD.100.112007. arXiv: 1909.04114 [hep-ex].

[126] Claudio Quaranta. "Search for high mass mediators in ATLAS and CMS. 9th Edition of the Large Hadron Collider Physics Conference". In: (June 2021). URL: https://cds.cern.ch/record/2772301.

[127] CMS Collaboration. *Search for high-mass resonances decaying to a jet and a Lorentz-boosted resonance in proton-proton collisions at $\sqrt{s} = 13$ TeV*. 2022. arXiv: 2201.02140 [hep-ex].

[128] Kaluza T. "On the Problem of Unity in Physics". In: *Math. Phys.* 966 (1921).

[129] T. Kaluza. "On the Unification Problem in Physics". In: *International Journal of Modern Physics D* 27.14 (2018), p. 1870001. DOI: 10.1142/s0218271818700017.

[130] Klein O. "Quantum Theory and Five-Dimensional Theory of Relativity". In: *Z. Phys.* 37 (1926), p. 895.

[131] CMS collaboration. "Performance of Electron Reconstruction and Selection with the CMS Detector in Proton-Proton Collisions at $\sqrt{s} = 8$ TeV". In: *JINST* 10 (2015), P06005. DOI: 10.1088/1748-0221/10/06/P06005. arXiv: 1502.02701 [physics.ins-det].

[132] P. Adzic et al. "Reconstruction of the signal amplitude of the CMS electromagnetic calorimeter". In: *Eur. Phys. J. C* 46S1 (2006), p. 23. DOI: 10.1140/epjcd/s2006-02-002-x.

[133] M. Anfreville et al. "Laser monitoring system for the CMS lead tungstate crystal calorimeter". In: *Nucl. Instrum. Meth. A* 594 (2008), p. 292. DOI: 10.1016/j.nima.2008.01.104.

[134] CMS collaboration. "Energy Calibration and Resolution of the CMS Electromagnetic Calorimeter in *pp* Collisions at $\sqrt{s} = 7\,\text{TeV}$". In: *JINST* 8 (2013), P09009. DOI: 10.1088/1748-0221/8/09/P09009. arXiv: 1306.2016 [hep-ex].

[135] P. Meridiani and R. Paramatti. "On the use of $Z \to e^+e^-$ events for ECAL calibration". In: (Jan. 2006).

[136] F. Couderc. "Quest for the Higgs boson(s) from D0 to CMS experiments". PhD thesis. SORBONNE UNIVERSITE, 2018. URL: https://tel.archives-ouvertes.fr/tel-02106984.

[137] Jerzy Neyman and Egon Sharpe Pearson. "On the Problem of the Most Efficient Tests of Statistical Hypotheses". In: *Phil. Trans. Roy. Soc. Lond. A* 231.694-706 (1933), p. 289. DOI: 10.1098/rsta.1933.0009.